

Compositional and textural analysis of host-rock diamictite matrix at the Kakula
copper deposit, Democratic Republic of Congo

by

Quinn Dabros

A thesis submitted in partial fulfillment
of the requirements for the degree of
Master of Science (MSc) in Geology

The Faculty of Graduate Studies
Laurentian University
Sudbury, Ontario, Canada

© Quinn Dabros, 2019

THESIS DEFENCE COMMITTEE/COMITÉ DE SOUTENANCE DE THÈSE
Laurentian Université/Université Laurentienne
Faculty of Graduate Studies/Faculté des études supérieures

Title of Thesis Titre de la thèse	Compositional and textural analysis of host-rock diamictite matrix at the Kakula copper deposit, Democratic Republic of Congo		
Name of Candidate Nom du candidat	Dabros, Quinn		
Degree Diplôme	Master of Science		
Department/Program Département/Programme	Geology	Date of Defence Date de la soutenance	October 11, 2019

APPROVED/APPROUVÉ

Thesis Examiners/Examineurs de thèse:

Dr. Elizabeth C. Turner
(Supervisor/Directrice de thèse)

Dr. David Broughton
(Committee member/Membre du comité)

Dr. Dan Kontak
(Committee member/Membre du comité)

Dr. David Burrows
(External Examiner/Examineur externe)

Approved for the Faculty of Graduate Studies
Approuvé pour la Faculté des études supérieures
Dr. David Lesbarrères
Monsieur David Lesbarrères
Dean, Faculty of Graduate Studies
Doyen, Faculté des études supérieures

ACCESSIBILITY CLAUSE AND PERMISSION TO USE

I, **Quinn Dabros**, hereby grant to Laurentian University and/or its agents the non-exclusive license to archive and make accessible my thesis, dissertation, or project report in whole or in part in all forms of media, now or for the duration of my copyright ownership. I retain all other ownership rights to the copyright of the thesis, dissertation or project report. I also reserve the right to use in future works (such as articles or books) all or part of this thesis, dissertation, or project report. I further agree that permission for copying of this thesis in any manner, in whole or in part, for scholarly purposes may be granted by the professor or professors who supervised my thesis work or, in their absence, by the Head of the Department in which my thesis work was done. It is understood that any copying or publication or use of this thesis or parts thereof for financial gain shall not be allowed without my written permission. It is also understood that this copy is being made available in this form by the authority of the copyright owner solely for the purpose of private study and research and may not be copied or reproduced except as permitted by the copyright laws without written authority from the copyright owner.

Abstract

The Kakula deposit is a high-grade sedimentary-rock-hosted Cu deposit (628 Mt, 2.72% Cu indicated resource, 1% cut-off) ~10 km south of the Kamoia deposit (759 Mt, 2.57% Cu indicated resource, 1% cut-off) in the central African copperbelt, Democratic Republic of Congo. Copper-sulphide ore (chalcocite, bornite, chalcopyrite) at Kakula is predominantly disseminated in the fine-grained matrix of clast-poor ($\leq 20\%$ clasts ≥ 2 mm) subaqueous debrite (diamictite), at the base of the nearly flat-lying mid-Neoproterozoic “grand congrégat” (Mwale formation). Scanning electron microscopy was used to document matrix texture and composition to develop a matrix paragenesis, recorded in five phases of the matrix evolution: sedimentation, pre-ore diagenesis, main-ore mineralisation, post-ore alteration, and weak tectonism. The ore-zone matrix is porous, up to 12.5%, and consists of clay- to silt-sized muscovite, quartz, chlorite, K-feldspar, dolomite, and biotite, whereas least-altered matrix, several hundred metres above copper-sulphide mineralisation, consists of clay- to silt-sized quartz, albite, chlorite, K-feldspar, calcite, and dolomite. Copper-sulphide precipitation is contemporaneous with chlorite and biotite (+/- hematite, quartz, and K-feldspar) and fit in a paragenetic sequence between diagenetic pyrite (\pm Fe-dolomite) and later muscovite. Hematite is ore-stage and most abundant in areas containing chalcocite. Areas of mm- to cm-scale “aligned” matrix (nearly vertical microfabric of aligned, elongated grains) consists of a higher abundance of muscovite, locally elongated copper-sulphides, and a lower concentration of copper than non-aligned matrix, suggesting that copper-sulphide development pre-dated fabric development and that copper-sulphide grains were later

dissolved and possibly remobilised. Although determining the original mineralogy and texture of the diamictite matrix is challenging, the depositional matrix characteristics (clast-rich versus clast-poor diamictite) and the availability of reactive agents (e.g., diagenetic pyrite) may have been important controls on copper grade and distribution. More work is required to constrain the absolute timing of mineralisation, which is a major debate at Kakula and Kamoia.

Acknowledgements

First and foremost, I would like to thank my supervisor, Dr. Elizabeth Turner, for the opportunity to work on such an interesting project. Thank you for your guidance and for sharing your knowledge and expertise throughout the project, and of course, for your hard work editing this thesis to make it the best product possible.

I would like to express my thanks to Drs. Dan Kontak and David Broughton for helpful discussions and guidance; Dr. Bruno Lafrance for helpful discussions; David Edwards, Franck Twite, and other Ivanhoe staff for on-site help; and Ivanhoe and NSERC for funding this project and making it all possible. Thank you to Willard Desjardin for instruction and preparing my thin sections, and thank you William Zhe and Dr. Andy McDonald for help and instruction using analytical equipment and techniques. Thank you to the rest of the geology graduate students at Laurentian University and departmental staff for making this a smooth process.

Last but not least, I would like to thank my wonderful family and friends for all the fun, love, and support along the way. This was a very rewarding experience for me, and I could not have done it without you.

Table of Contents

Abstract.....	iii
Acknowledgements	v
List of Figures.....	ix
List of tables	xii
Appendices.....	xiv
Chapter 1	1
1. Introduction to Thesis.....	1
1.1 Introduction	1
1.2 Research questions	4
1.3 Structure of thesis	5
1.4 Statement of responsibilities.....	6
1.5 References	8
Chapter 2	9
2. Compositional and textural analysis of the high-grade Kakula copper deposit diamictite matrix, Democratic Republic of Congo.....	9
2.1 Abstract.....	9
2.2 Introduction	11
2.3 Geologic setting.....	13
2.3.1 Regional geology.....	13
2.3.2 Local geology	16
2.3.3 Local stratigraphy.....	18
2.3.4 Depositional environment	20
2.3.5 Mineralisation.....	23
2.4 Methods	26
2.4.1 Samples	26
2.4.2 Analytical techniques	27
2.5 Results	31
2.5.1 Stratigraphy	31
2.5.2 Diamictite characteristics	32
2.5.3 Least-altered matrix.....	35
2.5.3.1 Matrix minerals	35

2.5.3.2	Matrix texture.....	38
2.5.4	Ore-zone matrix.....	39
2.5.4.1	Matrix minerals.....	39
2.5.4.2	Matrix texture.....	43
2.5.5	Bulk and mineral compositions.....	44
2.5.5.1	Matrix bulk composition.....	45
2.5.5.2	Aligned versus non-aligned matrix.....	46
2.5.5.3	Chlorite, biotite, and muscovite composition.....	47
2.5.6	Whole-rock geochemistry.....	49
2.5.6.1	Major elements.....	49
2.5.6.2	Trace elements.....	50
2.6	Interpretation.....	51
2.6.1	Matrix composition.....	51
2.6.1.1	Matrix “bulk” composition.....	51
2.6.1.2	Aligned versus non-aligned matrix.....	53
2.6.1.3	Chlorite, biotite, and muscovite composition.....	54
2.6.2	Matrix evolution and paragenesis.....	55
2.6.2.1	Sedimentation and source material.....	56
2.6.2.2	Diagenesis.....	59
2.6.2.3	Main- and post-ore.....	61
2.6.2.4	Tectonism.....	64
2.6.3	Matrix alignment origin.....	66
2.7	Discussion.....	69
2.7.1	Influence of matrix on mineralisation.....	69
2.7.2	Kamoā and Kakula comparison.....	72
2.7.3	Other deposits.....	74
2.7.4	Timing of mineralisation.....	76

2.8	Summary.....	80
2.9	References	82
Chapter 3	91
3. Concluding statements	91
Figures	94
Tables	137
Appendix A	161
Appendix B	168

List of Figures

Figure 1 Regional geology map of the central African copperbelt after François (1993) and Cailteux (1994).

Figure 2 Simplified stratigraphy of the Katanga Supergroup and its subdivisions

Figure 3 Local geology map of the Kamoia and Kakula area

Figure 4 Map and cross sections of the Kakula deposit with sample locations

Figure 5 Stratigraphic subdivisions of the grand conglomerat used at Kamoia and Kakula

Figure 6 Stratigraphic logs of DKMC_DD1012, DKMC_DD975, and DKMC_DD1001 showing their spatial relationships

Figure 7 Stratigraphic log for Kakula high-grade drill-hole DKMC_DD1012

Figure 8 Stratigraphic log for Kakula low-grade drill-hole DKMC_DD975

Figure 9 Stratigraphic log for Kakula medium-grade drill-hole DKMC_DD1001

Figure 10 Stratigraphic log for Kamoia high-grade drill-hole DKMC_DD627

Figure 11 Stratigraphic log for Kamoia high-grade drill-hole DKMC_DD793

Figure 12 Stratigraphic log for Kakula low-grade drill-hole DKMC_DD1161

Figure 13 Images of drill-core slabs of clast-rich and clast-poor diamictite of the basal diamictite at Kakula

Figure 14 Images of drill-core slabs of maroon and grey-green diamictite of the basal diamictite at Kakula

Figure 15 Images of drill-core slabs of clast-rich and clast-poor diamictite of the basal diamictite at Kamoia

Figure 16 Image of drill-core slab of the middle diamictite at Kakula

Figure 17 Petrographic images of matrix in clast-poor and clast-rich diamictite at Kakula

Figure 18 SEM and petrographic images of aligned versus non-aligned matrix at Kakula

Figure 19 SEM images of least-altered matrix sample DKMC-DD1012_16 at Kakula

Figure 20 SEM images of least-altered matrix sample DKMC-DD1012_16 at Kakula

Figure 21 SEM images of least-altered matrix sample DKMC-DD1161_3 at Kakula

Figure 22 SEM images of least-altered matrix sample DKMC-DD1161_3 at Kakula

Figure 23 SEM images of least-altered matrix sample DKMC-DD1161_6 at Kakula

Figure 24 Petrographic and SEM images showing the composition in aligned versus non-aligned matrix of ore-zone matrix at Kakula

Figure 25 SEM images of quartz in ore-zone matrix of clast-rich diamictite at Kakula

Figure 26 SEM images of dolomite and ferroan dolomite in ore-zone matrix at Kakula

Figure 27 SEM images of ore-zone matrix showing paragenetic relationships, characteristics, and associations of ore-zone matrix components at Kakula

Figure 28 SEM images showing paragenetic relationships, characteristics, and associations of ore-zone matrix components with copper-sulphides at Kakula

Figure 29 SEM images showing paragenetic relationships, characteristics, and associations of ore-zone matrix components at Kakula

Figure 30 SEM images showing paragenetic relationships, characteristics, and associations of ore-zone matrix components at Kakula

Figure 31 SEM images of disseminated copper-sulphides in non-aligned matrix from the ore-zone matrix at Kakula

Figure 32 SEM images of disseminated copper-sulphide in aligned matrix of ore-zone matrix at Kakula

Figure 33 SEM and petrographic images showing the morphology, paragenesis, and relationships of pyrite and chalcopyrite in ore-zone matrix at Kakula

Figure 34 Petrographic images showing the morphology, paragenesis, and relationships of copper-sulphides and hematite in ore-zone matrix at Kakula

Figure 35 SEM and petrographic images showing the morphology, paragenesis, and relationships of copper-sulphides and hematite in ore-zone matrix at Kakula

Figure 36 Chemical analysis of FeO versus MgO of matrix, chlorite, biotite, and muscovite according to depth for high-grade drill-hole DKMC_DD1012 at Kakula

Figure 37 Scatter plot of FeO versus MgO of matrix, chlorite, biotite, and muscovite according to depth for low-grade drill-hole DKMC_DD975 at Kakula

Figure 38 Chemical analysis of FeO versus MgO of matrix, chlorite, and muscovite according to depth for high-grade drill-hole DKMC_DD627 at Kamoia

Figure 39 Copper grade in aligned versus non-aligned matrix for high-grade drill-hole DKMC_DD1012 at Kakula

Figure 40 Copper grade in aligned versus non-aligned matrix for low-grade drill-hole DKMC_DD975 at Kakula

Figure 41 Copper grade in aligned versus non-aligned matrix for high-grade drill-hole DKMC_DD627 at Kamoia

Figure 42 Paragenetic table and summary diagram illustrating the evolution of ore-zone diamictite matrix at Kakula

List of tables

Table 1 Complete list of samples collected for this study

Table 2 Diamictite grain-size (clay-silt, sand, larger) proportions and porosity percentage

Table 3 Diamictite matrix average grain size for samples analysed with the SEM

Table 4 Summary of typical minerals present in least-altered matrix and their characteristics

Table 5 Summary of typical mineral distributions and associations in least-altered matrix

Table 6 Summary of typical minerals present in ore-zone matrix and their characteristics

Table 7 Summary of typical mineral distributions and associations in ore-zone matrix.

Table 8 SEM average oxide concentrations from high-grade drill-hole DKMC_DD1012 at Kakula

Table 9 Standard deviations for the SEM compositional analysis of high-grade drill-hole DKMC_DD1012 at Kakula

Table 10 SEM average oxide concentrations from high-grade drill-hole DKMC_DD975 at Kakula

Table 11 Standard deviations for the SEM compositional analysis of high-grade drill-hole DKMC_DD975 at Kakula

Table 12 SEM average oxide concentrations from high-grade drill-hole DKMC_DD627 at Kamoia

Table 13 Standard deviations for the SEM compositional analysis of high-grade drill-hole DKMC_DD627 at Kamoia

Table 14 SEM average oxide concentrations from high-grade drill-hole DKMC_DD1161 at Kakula

Table 15 Standard deviations for the SEM compositional analysis of high-grade drill-hole DKMC_DD1161 at Kakula

Table 16 SEM average oxide concentrations for various minerals at Kakula

Table 17 Standard deviations for the SEM compositional analysis of various minerals
Kakula

Appendices

Appendix A

Figure A.1 XRD pattern and mineral identification of sample DD1012_16 of least-altered diamictite matrix at Kakula

Figure A.2 XRD pattern and mineral identification of sample DD1161_6 of least-altered diamictite matrix at Kakula

Figure A.3 XRD pattern and mineral identification of sample DD1161_3 of least-altered diamictite matrix at Kakula

Figure A.4 XRD pattern and mineral identification of sample DD1012_13 of ore-zone diamictite matrix at Kakula.

Figure A.5 XRD pattern and mineral identification of sample DD975_10 of ore-zone diamictite matrix at Kakula.

Figure A.6 XRD pattern and mineral identification of sample DD1012_7 of ore-zone diamictite matrix at Kakula.

Figure A.7 XRD pattern and mineral identification of sample DD975_4 of ore-zone diamictite matrix at Kakula.

Appendix B

Table B.1 Whole-rock geochemistry analyses with major oxide concentrations of different samples

Table B.2 Whole-rock geochemistry analyses with trace element concentrations of different samples

Figure B.1 Concentrations (log scale) of major oxides for the average of least-altered and ore-zone matrix samples

Figure B.2 Concentrations (log scale) of major oxides for the average of least-altered and ore-zone matrix samples normalised to local mafic rock

Figure B.3 Concentrations (log-scale) of major oxides for the average of least-altered and ore-zone matrix samples normalised to mafic clasts

Figure B.4 Concentrations (log-scale) of major oxides for the average of least-altered and ore-zone matrix samples normalised to average crust

Figure B.5 Concentrations (log-scale) of major oxides for the average of least-altered and ore-zone matrix samples normalised to mafic rock

Figure B.6 Concentrations (log-scale) of major oxides for the average of least-altered and ore-zone matrix samples normalised to silicic rock

Figure B.7 Concentrations (log-scale) of trace elements for the average of least-altered and ore-zone matrix samples

Figure B.8 Concentrations (log-scale) of trace elements for the average of least-altered and ore-zone matrix samples normalised to MORB

Figure B.9 Concentrations (log-scale) of trace elements for the average of least-altered and ore-zone matrix samples normalised to local mafics

Figure B.10 Concentrations (log-scale) of trace elements for the average of least-altered and ore-zone matrix samples normalised to mafic clasts

Figure B.11 Concentrations (log-scale) of trace elements for the average of least-altered and ore-zone matrix samples normalised to bulk crust

Figure B.12 Concentrations (log-scale) of trace elements for the average of least-altered and ore-zone matrix samples normalised to sediment.

Figure B.13 Concentrations (log-scale) of trace elements for the average of least-altered and ore-zone matrix samples normalised to upper crust

Chapter 1

1. Introduction to Thesis

1.1 Introduction

The Kakula (628 Mt, 2.72% indicated Cu resource at 1% cut-off grade) and Kamoia (759 Mt at 2.57% indicated Cu resource at 1% cut-off grade) deposits are world-class sedimentary-rock-hosted copper deposits in the central African copperbelt (CACB) discovered in 2015 and 2006, respectively. These deposits are hosted in the Neoproterozoic Katanga Supergroup, a thick (~7.5 km) sedimentary succession deposited in intracontinental rift basins and a later foreland basin (Cailteux, 1994; Batumike et al., 2006). A study by Kennedy et al. (2018) of the ore-hosting grand conglomérat interpreted it to have been deposited entirely by subaqueous mass flows (predominantly debrites) in the Kamoia sub-basin of the Katanga basin. The majority of copper-sulphides at Kamoia and Kakula are present as fine-grained disseminations in matrix of subaqueous diamictite and siltstone of the basal diamictite unit of the grand conglomérat (Mwale formation; Broughton and Rogers, 2010; Schmandt et al., 2013; Twite, 2016; Twite et al., 2019). A diamictite is a textural term for a sedimentary rock with clasts of various sizes dispersed in a fine-grained matrix, whereas a debrite is an interpretive term for the lithified deposit of a debris flow. The grand conglomérat is located stratigraphically above the majority of the 'traditional' copper deposits in the CACB and was previously considered to be devoid of mineral potential (Broughton and Rogers, 2010). The much smaller Kashime (Fishtie) and Lonshi deposits in Zambia and the newly discovered Makoko deposit, west of the Kamoia and Kakula deposits, are also hosted by the grand conglomérat. The Shanika

syncline copper occurrence, in the Tenke Fungurume mining district in DRC, is also hosted by the grand conglomérat, but mineralisation is mainly vein-hosted. The base of the grand conglomérat, especially in the western foreland in DRC, is now recognised as an important exploration target for sedimentary-rock-hosted copper mineralisation.

Kakula and Kamoia are collectively considered the largest undeveloped copper deposit in the world and the largest high-grade (>2.5%) copper deposit ever discovered (Ivanhoe Mines Ltd. website). The current understanding of the deposits is limited because of their recent discovery, geographic location, and poor surficial expression. The fine-grained nature of the diamictite matrix ($\leq 65 \mu\text{m}$) makes studying its textural and compositional attributes, and determining the timing of mineralisation, challenging. A recent study at Kamoia suggested that mineralisation was emplaced relatively early in the rock's history, during diagenesis, primarily based on the fine-grained, disseminated nature of copper-sulphides in the matrix (Schmandt et al., 2013). Despite the rocks at Kamoia and Kakula being relatively unmetamorphosed, undeformed, and free of mineralised veins, another study at Kamoia (Twite, 2016) focussed on structural controls on mineralisation and areas with a tectonic fabric (aligned matrix) inferred to have developed roughly 150 to 200 m.y. after sedimentation, during the Lufilian orogeny.

Copper-sulphides at Kakula and Kamoia are primarily disseminated and stratiform, and show a zonation in ore-grade and mineral species vertically from chalcocite to bornite to chalcopyrite. The copper-sulphides at Kakula are essentially all hypogene, well below surface (100 – 1000 m), and locally extend up to 60 m above the base of the grand conglomérat. Diamictite at Kakula and Kamoia is classified based on the percentage of large clasts ($\geq 2 \text{ mm}$) it contains. Clast-rich diamictite contains 20 – 40% clasts and a

generally silty and sandy matrix, whereas clast-poor diamictite contains <20% clasts and a muddy matrix. The clast-rich diamictite is more common near the base of the grand congolomérat and generally has a lower grade than clast-poor diamictite, suggesting a possible textural and/or compositional control on copper grade and distribution. Prior to this study, the textural and compositional influence of diamictite matrix on mineralisation had not been aggressively examined. Overall, there is a poor understanding of the host-rock's evolution through time, and of the timing of copper mineralisation relative to sediment deposition, diagenesis, hydrothermal alteration, deformation, and possible low-grade regional metamorphism.

The Kakula-Kamoa project is a multi-year academic study funded through Ivanhoe Mines Ltd. and NSERC, and is based at Laurentian University in Sudbury, Ontario. This study focusses primarily on diamictite matrix of the Kakula deposit, with a minor focus on the Kamoa deposit. As a detailed study, this project relies heavily on scanning electron microscopy (SEM) for textural and compositional analysis. The main objective of this study is to document and interpret the compositional and textural attributes of the diamictite matrix and to develop a paragenesis that deciphers the evolution of mineralised matrix since sedimentation. To be successful, this project compares matrix from diamictite samples in and outside of the ore zone and from high- and low-grade copper zones laterally and vertically. This study also compares matrix that is essentially textureless (non-aligned matrix) with matrix containing locally elongated and aligned components (aligned matrix). In so doing, this project evaluates the origin of compositional and textural attributes of diamictite matrix and the relationship of matrix characteristics with the grade and distribution of copper-sulphides. By constraining the

mineralisation processes and relationships in host rock at Kakula, this work contributes to a better understanding of sedimentary-rock-hosted copper deposits.

1.2 Research questions

- *What is the composition of the matrix? Are there vertical or lateral compositional differences?*
- *What are the textures of the matrix and how/when did they develop? What is the origin of the “aligned matrix”?*
- *Which matrix minerals are depositional, diagenetic, hydrothermal, or possibly deformational, or metamorphic?*
- *What is the paragenesis and relative timing of copper mineralisation?*
- *Are there relationships between matrix characteristics and ore grade?*

1.3 Structure of thesis

This thesis is written as three separate chapters. Chapter 1 is an introductory chapter that describes and introduces the background geology, project objectives, research questions, responsibilities of the candidate, and methods used in the study. Chapter 2 is written as a manuscript entitled: “**Compositional and textural analysis of the high-grade Kakula copper deposit diamictite matrix, Democratic Republic of Congo**”. This chapter presents the regional and local geologic background, methods, results, interpretations, and discussion of the study. Chapter 3 is a conclusion chapter that covers concluding statements of the study and possible future work.

1.4 Statement of responsibilities

Core-logging and sample collection was completed by the candidate at Ivanhoe Mines Ltd.'s Kakula-Kamoa camp in DRC in September, 2016, and supplementary samples were collected in September, 2017. For Kakula, drill-core samples were collected from three drill-holes along an approximately northwest-southwest fence from a relatively high-grade (DKMC_DD1012), medium-grade (DKMC_DD1001), and low-grade (DKMC_DD975) zones. Fewer samples were also collected from a second low-grade drill-hole (DKMC_DD1161) in a different location, to the west, at Kakula. For Kamoa, samples were collected from two high-grade drill-holes: (DKMC_DD793) and (DKMC_DD627). A total of 67 samples were cut by Ivanhoe Mines Ltd. personnel and shipped to Canada as rock-core slabs. Stratigraphic logs were constructed by the candidate. Fifty-four thin-section chips were cut by the candidate at Laurentian University, and standard polished thin sections (30 µm thickness) were prepared by Willard Desjardins. Polished thin-sections were carbon-coated by William Zhe for SEM analysis. Petrography and SEM analysis was undertaken by the candidate at Laurentian University. The initial diamictite characterisation involved documenting composition, texture, grain size, sorting, and mineralisation using transmitted- and reflected-light petrography using an Olympus BX-51 petrographic microscope equipped with Q-imaging. Thirty-two polished thin-sections were examined using a JEOL 6400 SEM with Oxford INCA EDS detector at Laurentian University. Samples were also selected and prepared for X-ray powder diffraction and whole-rock geochemistry (major and trace elements) by the candidate. The main interpretations and conclusions were made by the candidate with guidance and background knowledge provided by Dr. Elizabeth Turner.

The many manuscript drafts were written and organised by the candidate with editing by Dr. Elizabeth Turner.

1.5 References

- Batumike, M. J., Kampunzu, A. B., and Cailteux, J., 2006. Petrology and Geochemistry of the Neoproterozoic Nguba and Kundelungu Groups, Katangan Supergroup, Southeast Congo. Implications for Provenance, Paleoweathering and Geotectonic Setting. *Journal of African Earth Sciences*, 44, p. 97–115.
- Broughton, D. W., and Rogers, T., 2010. Discovery of the Kamao Copper Deposit, Central African Copperbelt, D.R.C. *Society of Economic Geologists, Special Publication 15*, p. 287–297.
- Cailteux, J., 1994. Lithostratigraphy of the Neoproterozoic Shaba-Type (Zaire) Roan Supergroup and Metallogenesis of Associated Stratiform Mineralization. *Journal of African Earth Sciences*, 19 (4), p. 279–301.
- Kennedy, K., Eyles, N., Broughton, D., 2018. Basinal setting and origin of thick (1.8 km) mass-flow dominated Grand Conglomérat diamictites, Kamao, Democratic Republic of Congo: Resolving climate and tectonic controls during Neoproterozoic glaciations. *Sedimentology*, 66 (2).
- Schmandt, D., Broughton, D., Hitzman, M., Bjorklund, P. P., and Edwards, D., 2013. The Kamao Copper Deposit, Democratic Republic of Congo: Stratigraphy, Diagenetic and Hydrothermal Alteration, and Mineralization. *Economic Geology*, 108, p. 1301–1324.
- Twite, F., 2016. Controls of Sulphide Mineralization at the Kamao Copper Deposit, with an Emphasis on Structural Controls, Democratic Republic of Congo. Unpublished MSc Thesis. University of Witwatersrand, South Africa. 288 pages.
- Twite, F., Broughton, D., Nex, P., Kinnaird, J., and Gilchrist, G., 2019. Lithostratigraphic and structural controls on sulphide mineralisation at the Kamao copper deposit, Democratic Republic of Congo. *Journal of African Earth Sciences*, 151, p. 212 – 224.

Chapter 2

2. **Compositional and textural analysis of the high-grade Kakula copper deposit diamictite matrix, Democratic Republic of Congo**

2.1 **Abstract**

The Kakula deposit is a high-grade sedimentary-rock-hosted Cu deposit (628 Mt, 2.72% Cu indicated resource, 1% cut-off) in the central African copperbelt, Democratic Republic of Congo, and ~10 km to the south of the Kamao deposit (759 Mt, 2.57% Cu indicated resource, 1% cut-off). Copper-sulphide ore (chalcocite, bornite, chalcopyrite) at Kakula is predominantly disseminated in the fine-grained matrix of clast-poor ($\leq 20\%$ clasts ≥ 2 mm) subaqueous debris (diamictite), at the base of the nearly flat-lying mid-Neoproterozoic “grand conglomérat” (Mwale formation). Matrix texture and composition was documented using scanning electron microscopy to unravel the matrix’s evolution, recorded in five phases in the matrix paragenesis: sedimentation, pre-ore diagenesis, main-ore mineralisation, post-ore alteration, and weak tectonism. Samples from several hundred metres above the ore-zone, as least-altered matrix, samples from Kamao, and mm- to cm-scale areas of “aligned” (nearly vertical microfabric of aligned, elongated grains) versus “non-aligned” (textureless) matrix were also analysed and compared. The ore-zone matrix has up to 12.5% porosity and consists of clay- to silt-sized muscovite, quartz, chlorite, K-feldspar, dolomite, and biotite, whereas least-altered matrix consists of clay- to silt-sized quartz, albite, chlorite, K-feldspar, calcite, and dolomite. Copper-sulphides, along with chlorite and biotite (+/- hematite, quartz, and K-feldspar), fit in a paragenetic sequence between diagenetic pyrite (\pm Fe-dolomite) and later muscovite.

Hematite is most abundant in areas containing chalcocite. Chlorite and biotite have a systematic decrease in MgO and increase in FeO up-section, which, together with textural relationships with copper-sulphides, suggest that their formation was contemporaneous with copper-sulphide precipitation. Aligned matrix consists of a higher abundance of muscovite, locally elongated copper-sulphides, and a lower concentration of copper than non-aligned matrix, which suggests copper-sulphides were locally dissolved and possibly remobilised during fabric development. Although determining the rock's original composition is challenging, a mixed source of mafic and felsic-derived rock is proposed based on the composition of large clasts and whole-rock geochemistry analyses of major and trace elements. Moreover, original matrix characteristics from deposition (clast-rich versus clast-poor diamictite) and the availability of reactive agents (e.g. diagenetic pyrite) may have been important controls on copper grade and distribution at Kakula. More work is required to constrain the absolute timing of mineralisation, which continues to be a major debate.

2.2 Introduction

The central African copperbelt (CACB), divided geographically into the Congolese copperbelt in the Democratic Republic of Congo (DRC) and the Zambian copperbelt in Zambia, is the largest and highest-grade sedimentary-rock-hosted copper province in the world (Cailteux et al., 2007; Hitzman et al., 2010). Not only is the CACB an impressive copper producer containing many identified sedimentary-rock-hosted copper deposit resources (approximately 85; Zientek et al., 2014), it also contains some of the largest and highest-grade copper deposits (e.g., Kamoia and Kakula). The Kakula and Kamoia deposits are located approximately 25 km west of the copper-cobalt mining district of Kolwezi, DRC (Fig. 1). The Kakula deposit was discovered in 2015, approximately 10 km south-southwest of the Kamoia deposit. The Kamoia deposit, which was discovered nearly a decade before the Kakula deposit, was discovered through surface work, geophysical surveys, and drilling (Broughton and Rogers, 2010).

The Kakula deposit, the main focus of this study, is present at the same inferred redox boundary as the Kamoia deposit, at the base of the mid-Neoproterozoic grand conglom rat (Mwale formation) of the Katanga Supergroup (Fig. 2). More specifically, Kamoia and Kakula are hosted by the basal diamictite unit of the grand conglom rat. At Kakula and Kamoia, hypogene copper-sulphide ore (chalcocite, bornite, chalcopyrite) is predominantly disseminated in the fine-grained matrix of nearly-flat-lying subaqueous debrites (diamictite), and siltstone. Sand-sized (65 μm – 2 mm) clasts are considered diamictite matrix because they act as supporting material for larger clasts (≥ 2 mm); this

study focusses primarily on the abundant clay- to silt-sized material ($\leq 65 \mu\text{m}$) that is characteristic of the diamictite matrix.

The Kakula deposit is as yet unstudied. There is considerable controversy over the timing of mineralisation at Kamoia and Kakula; relatively early diagenetic (Schmandt et al., 2013) and relatively late orogenic (Twite, 2016) origins have been proposed. Studying the diamictite matrix is challenging because of its fine-grained nature, but is essential in understanding the origin and timing of these deposits because (a) most of the mineralisation is contained in the diamictite matrix, and (b) the matrix contains mineral species capable of recording diagenetic, hydrothermal, and structural events. This study relies heavily on SEM imaging and analysis to evaluate the compositional and micro-textural attributes of the diamictite matrix, and develop a paragenesis that conveys the evolution of mineralised matrix since its deposition as sediment. By studying diamictite samples from within and outside of the ore-zone, this study helps illuminate how and if matrix characteristics influenced or were influenced by the copper-mineralising process, and evaluates the relative timing of mineralisation.

2.3 Geologic setting

2.3.1 Regional geology

The Katanga Supergroup is an approximately 7.5-km-thick Neoproterozoic succession that hosts the sedimentary-rock-hosted copper deposits of the CACB (Batumike et al., 2007; Cailteux and De Putter, 2018). It overlies Paleoproterozoic (2081 – 1790 Ma) and Mesoproterozoic to early-Neoproterozoic (1300 – 900 Ma) metasedimentary and granitic basement rocks (Rainaud et al., 2005; Master et al., 2005). In ascending stratigraphic order, the Katanga Supergroup is subdivided into three groups with corresponding subgroups: Roan (R.A.T or “roches argilo-talqueuses”, Mines, Dipeta, and Mwashya Subgroups), Nguba (Muombe and Bunkeya subgroups), and Kundelungu (Gombela, Ngule and Bianco subgroups) groups (Fig. 2; François, 1993; Cailteux, 1994; Cailteux et al., 2005; Selley et al., 2005; Batumike et al., 2006; Cailteux and De Putter, 2019). The Roan and Nguba groups were deposited in intracontinental rift basins (“Katanga rift aulocogen”) associated with the breakup of supercontinent Rodinia (Cailteux, 1994; Batumike et al., 2006) and mafic volcanism (Key et al., 2001; Master and Wendorff, 2011). Neoproterozoic rifting of Rodinia began at roughly 879 ± 16 Ma based on ages extracted from the Kafue rhyolite at the base of the Katanga Supergroup (Armstrong et al., 2005). Roan Group deposition involved initial rift-stage siliciclastic rocks and post-rift evaporitic carbonate rocks, whereas Nguba Group deposition involved a second rifting stage of siliciclastic and carbonate rocks with syndepositional mafic volcanism (Cailteux, 1994; Batumike et al., 2006). The Kundelungu Group consists of siliciclastic

and carbonate rocks that were deposited in a foreland basin (Cailteux, 1994; Batumike et al., 2006).

The Katanga Supergroup's depositional history extends from approximately 880 to 573 Ma (Master et al., 2005; Wendorff and Key, 2009). Lithoclasts and zircon from the Nchanga granite ($^{207}\text{Pb}/^{206}\text{Pb}$ on zircon 883 \pm 10 Ma) from the basement in Zambia are present in the basal Katanga Supergroup and provide a maximum age for the onset of sediment deposition in the Katanga basin (Armstrong et al., 2005; Wendorff and Key 2009). Argon-argon dating of detrital muscovite collected at the top of the Katanga Supergroup in DRC provides the best estimate for their maximum possible depositional age at 573 ± 5 Ma (Master et al., 2005). The depositional age of the grand conglomérat is constrained by mafic sills and flows in the upper Roan and lower Nguba groups dated from 765–735 Ma in the Mwinilunga area of northwestern Zambia (Kampunzu et al., 1993, 2000; Wendorff and Key, 2009). However, the oldest maximum possible age of deposition for the grand conglomérat has been updated to 727 ± 5 Ma with Re-Os dating of black shale of the Mwashya subgroup just below the grand conglomérat (Rooney et al., 2015). This suggests that the grand conglomérat may be younger than previously thought.

Tectonic compression during collision of the Congo and Kalahari cratons during the 590 – 530 Ma Lufilian orogeny (pan-African orogeny) variably deformed and metamorphosed the rocks of the Katanga Supergroup (Hanson et al., 1993; John et al., 2004; Selley et al., 2005; Rainaud et al., 2005). Uranium-lead dating of monazite constrained peak metamorphism to 545 – 530 Ma (Steven and Armstrong, 2003; John et al., 2004; Turlin et al., 2016; Selley et al., 2018). Most of the Katanga Supergroup

underwent subgreenschist- to greenschist-grade metamorphism, whereas part of the succession in Zambia records amphibolite-grade metamorphism. Metamorphic grades are generally sub-greenschist in the northern part of the Lufilian arc in DRC (Cosi et al., 1992; Broughton et al., 2002; Selley et al., 2018). The Lufilian orogeny resulted in the incorporation of rocks of the Katanga Supergroup into the Lufilian arc, an approximately 750 km-long orogenic belt (Cosi et al., 1992; Cailteux et al., 2007). The Lufilian arc is bounded by the Paleoproterozoic Bangweulu block to the east and the Mesoproterozoic Kibaran belt to the west. The Lufilian arc is divided into the domes region, external fold-and-thrust belt, and western foreland tectonic domains (Fig. 1; Porada and Berhorst, 2000; Key et al., 2001; Selley et al., 2005; Zientek et al., 2014). The external fold-and-thrust belt is to the north of the domes region; it is characterised by folded Katanga Supergroup rocks and includes the Congolese copperbelt and the Kafue anticline of the Zambian copperbelt. It has been proposed that halokinesis (salt tectonics) was responsible for local fragmentation and diapiric extrusion of Roan Group rocks in the Congolese copperbelt (Jackson et al., 2003). Salt tectonics were considered fundamental in the structural evolution of the Lufilian arc, especially the northern part of the CACB (Selley et al., 2018). The Nzilo block of basement rock, northwest of Kolwezi, DRC, is the approximate northwestern limit of the fold-and-thrust belt (Broughton and Rogers, 2010). The western foreland, which extends along the west side of the copperbelt, is relatively undeformed and unmetamorphosed (Key et al., 2001; Broughton and Rogers, 2010; Schmandt et al., 2013; Twite et al., 2019).

Sedimentary-rock-hosted copper deposits in the CACB vary significantly according to stratigraphic level, mineralisation style, timing, extent of deformation, and host-rock

lithology. The deposits in the Zambian copperbelt are hosted primarily in mudstone and arenite units that are variably folded but relatively undeformed. Mineralisation in the Zambian copperbelt is dominated by pre-folding, disseminated copper-cobalt-sulphides, and to a lesser extent, post-orogenic vein-hosted copper-cobalt sulphides (Selley et al., 2005; Broughton and Rogers, 2010). In the Congolese copperbelt, copper deposits are primarily hosted in km-long megabreccias of the Mines Subgroup (Cailteux, 1994; Cailteux et al., 2005). Unlike the other deposits of the Congolese copperbelt, Kakula and Kamoia are in the relatively undeformed and unmetamorphosed part of the western foreland, outside of the classical CACB boundary (Broughton and Rogers, 2010; Schmandt et al., 2013; Twite et al., 2019).

2.3.2 *Local geology*

The subsurface Kakula and Kamoia deposits are in areas with virtually no outcrop and veneered by Tertiary cover, so almost all geological information has been gathered from drill-core. For many years prior to the discoveries, the overburden and presumed inappropriateness of rocks of the area were significant disincentives for copper exploration (Broughton and Rogers, 2010). The deposits are hosted by strata of the Kamoia sub-basin recently investigated by Kennedy et al. (2018), located in the northwestern part of the western foreland tectonic domain (Fig. 3; Broughton and Rogers, 2010). The Kamoia sub-basin, a western offshoot of the Katanga basin, is a rift basin extension confined by metamorphic Kibaran basement outcropping to the north and west (Kennedy et al., 2018). Distance above basement is generally unknown in the Kakula and

Kamoa area because drill-holes usually terminate at the Mwashya subgroup footwall of the deposits. Although the rocks in the Kamoa area are relatively undeformed and unmetamorphosed (Broughton and Rogers, 2010; Schmandt et al., 2013), shear fabrics are locally present in the southern parts of the Kamoa sub-basin (Twite, 2016; Kennedy et al., 2018). Tectonically, the Kakula and Kamoa deposits are delimited to the east by the Kansoko structure (Fig. 3), which parallels the external fold-and-thrust belt of the Lufilian arc. The Kansoko structure is interpreted from aeromagnetic data depicting a north-northwest-trending east-side-down normal fault (Schmandt et al. 2013; Twite, 2016; Kennedy et al. 2018). The west scarp fault marks the western limit of Kamoa, and cuts through the centre of the Kakula deposit to the south (Figs. 3, 4). The west scarp fault is a north-northeast-trending west-side-down fault that post-dated deposition of the Nguba Group based on facies and thickness similarities on both sides of the structure (Schmandt et al., 2013; Twite et al., 2019). This structure is associated with other similar-trending local structures, which dip at approximately 75° to the west and jointly account for an offset of 200 m (Fig. 4; OreWin, 2018). At Kakula and Kamoa, low-amplitude folds are the principal structural effect of the Lufilian orogeny (OreWin, 2018). The Kakula-Kamoa antiform axis, represented by erosional windows of anticlinally-folded, uplifted areas of Mwashya Subgroup rock (domes), trends northeast through the Kamoa and Kakula area (Figs. 3, 4). The rocks in the area dip gently ($\leq 5^\circ$) away from the Kamoa, Makalu, Kakula northeast, and Kakula domes (Figs. 3, 4; Schmandt et al., 2013; Kennedy et al., 2018; Twite et al., 2019). The Mupaka fault (Fig. 3), a pervasive north-northwest-trending structure at Kamoa, was interpreted as a synsedimentary normal fault based on facies and thickness differences across the fault and the presence of steeply

dipping bedding, synsedimentary mesoscopic faults, and soft-sediment deformation in the vicinity of the structure. The Mupaka fault and other possible synsedimentary normal faults may have formed during northeast-southwest extension during early rifting (Twite, 2016; Twite et al., 2019).

2.3.3 *Local stratigraphy*

The strata in the Kamoia sub-basin consist of three major stratigraphic units from base to top: conglomerate and breccia (“poudingue”), sandstone of the Mwashya subgroup, diamictite and siltstone of the grand conglomérat, and minor stromatolitic siltstone of the Kakontwe Formation (Nguba Group; Kennedy et al., 2018). Diamictite of the grand conglomérat represents most of the total stratigraphic thickness in the Kamoia area (67% of total logged; Kennedy et al., 2018). The “poudingue” unconformably overlies basement and outcrops north of the Kamoia deposit at the flank of the Nzilo block (Fig. 3; Kennedy et al., 2018). The Nzilo block consists predominantly of Kibaran quartzite and smaller amounts of pelite, metaconglomerate, and basalt (Kokonyangi et al., 2006; Kennedy et al., 2018). Sandstone of the Mwashya subgroup is generally thinly to thickly bedded, graded to weakly laminated, and has minor laminated siltstone interbeds (Schmandt et al., 2013; Kennedy et al., 2018). The “grand conglomérat” conformably but sharply overlies the Mwashya subgroup (Kennedy et al., 2018). Diamictite is generally massive, but it has rare (<1%) laminated or normally graded facies. In general, individual diamictite beds are poorly defined or unrecognisable, probably because they represent

thick depositional units and/or bed amalgamation (Kennedy et al., 2018). Mafic volcanic rocks in the Kamoia area are intercalated with diamictite and siltstone interbeds; they include coherent basalt, pillow basalt, and peperite facies. Diamictite clasts have variable shapes and sizes, were subject to little to no abrasion during transport, and have similar composition to detritus in the “poudingue” and Mwashya subgroup, which are predominantly locally derived clasts of Kibaran basement. Most clasts are quartzite and basalt cobbles and freshly fractured peperite basalt clasts with lesser siltstone, dolostone, granitoid, schist, and argillite clasts (Kennedy et al., 2018).

Starting at the Mwashya - grand conglomérat contact, which is thought to be a major redox boundary (Broughton et al., 2010; Schmandt et al., 2013), the Kakula - Kamoia rock units have been stratigraphically subdivided by Ivanhoe Mines Ltd. (Fig. 5), yielding a scheme also used by Schmandt et al. (2013), Twite (2016), Kennedy et al. (2018), and Twite et al. (2019). The classification scheme is based on lithostratigraphic units and their positions above the contact with the Mwashya subgroup (Rn.4). As shown in Fig. 5, the units include the basal diamictite (Ng.1.1.1), lower laminated pyritic siltstone (Ng.1.1.2), middle diamictite (Ng.1.1.3), upper laminated pyritic siltstone (Ng.1.1.4), upper diamictite (Ng.1.1.5), and uppermost diamictite (Ng.1.1.6). The thickness and continuity of the different units vary according to location (Schmandt et al., 2013; Twite, 2016; Kennedy et al., 2018), which makes correlation of units across the Kakula and Kamoia deposits difficult. The basal diamictite (Ng 1.1.1) of the grand conglomérat coincides with the ore-zone and is further subdivided into three parts: lower basal diamictite (Ng.1.1.1.1), intercalated siltstone (Ng.1.1.1.2), and upper basal diamictite (Ng.1.1.1.3). The lower basal diamictite is generally dominated by clast-rich

diamictite, an informal term indicating diamictite containing 20 - 40% clasts that are ≥ 2 mm. The upper basal diamictite is dominated by clast-poor diamictite that has less than 20% clasts ≥ 2 mm. The intercalated siltstone (Ng. 1.1.1.2) is massive to laminated and locally interlayered with subordinate clast-poor diamictite units. At Kakula, there is significant thickening of the siltstone and clast-poor diamictite units relative to Kamoia. Mineralisation at Kakula and Kamoia is in the basal diamictite (Ng. 1.1.1), whereas the lower laminated pyritic siltstone (Ng. 1.1.2) coincides with the upper limit of the ore-zone at Kamoia. Unlike at Kamoia, a laminated pyritic siltstone is located significantly higher above the Mwashya-“grand-conglom rat” contact at Kakula. The middle diamictite (Ng. 1.1.3) lies above the Kamoia pyritic siltstone but is not part of the ore-zone at either of the deposits. Depocentres for subaqueous mass flows in the Kamoia sub-basin varied because of synsedimentary faulting and/or subaqueous basaltic eruptions, which led to variations in unit thickness and facies (Kennedy et al., 2018). Thickness variations of units were also noted by Schmandt et al. (2013), Twite (2016), and Twite et al. (2019) at Kamoia and are considered to be the result of local synsedimentary faulting.

2.3.4 *Depositional environment*

The sedimentological study by Kennedy et al. (2018) provides insightful information on the depositional environment in the Kamoia sub-basin and the broader tectonic extensional setting. Sedimentation in the Kamoia sub-basin was structurally controlled and represent three phases of a rift cycle: (1) segmented basement faulting, (2) fault

linkage and rapid subsidence, and (3) slow thermal subsidence. The first phase is expressed by “poudingue” and Mwashya subgroup deposition during synsedimentary basement faulting, and the second phase involved rapid subsidence during significant accumulation of sediment of the grand conglomerat. The third phase is interpreted as slow thermal subsidence that eventually resulted in shallowing and transition in the grand conglomerat from subaqueous debrites to siltstone (Kakontwe formation). Although paleocurrent data are rare in the Kamoia area, weak clast imbrication and cross-bedding in conglomerate and sandstone units, especially near the Nzilo block north of Kamoia and Kakula, suggest south-southeast transport directions, away from the modern exposure of the Kibaran basement. This is further supported by Mwashya sandstone turbidites that fine towards the southeast (Kennedy et al., 2018).

All sedimentary facies present in the Kakula and Kamoia area, minus the Kakontwe formation, are the result of deep-water subaqueous mass-flows accompanied by episodic mafic volcanism. Synsedimentary pillow basalt and peperite indicate that basaltic magma was extruded in a subaqueous environment. Debris flows were probably triggered along oversteepened basin margins by faulting and seismic activity. Unstable, shallow-water rift-basin marginal detritus was progressively reworked downslope, which explains the lack of shallow-water deposits or basin-margin facies (Kennedy et al., 2018). Subaqueous conglomerate facies of the “poudingue” probably represent gravelly fan-deltas, whereas breccias of the “poudingue” are probably talus slope deposits generated by faults along the Nzilo basement. The sandstone turbidites of the Mwashya subgroup were probably deposited into deep water in front of a prograding fan-delta. Contrary to previous assumptions, Mwashya and “poudingue” units are coeval, lateral equivalents in this part

of the basin because their facies are intermixed or interdigitate (Kennedy et al., 2018). The most voluminous sedimentary facies in the Kamoia area, diamictite of the grand conglomérat, was deposited by subaqueous debris flows in relatively deep and quiescent parts of the basin (Schmandt et al., 2013; Kennedy et al., 2018). It was deposited by mixing and homogenisation of previously deposited “poudingue” and Mwashya sediments (Kennedy et al., 2018). Interbedded thinly bedded turbidites in the grand conglomérat probably filled in topography over debrites on the basin floor. Large slumps could have further directed subsequent debris-flows. Local basin-floor topography could have also been created by faulting and contemporaneous mafic volcanism (Kennedy et al., 2018).

Prior to the study of Kennedy et al. (2018), the rift in which the grand conglomérat accumulated was thought to have resulted from a different tectonic episode than the one in which the “poudingue” and Mwashya Subgroup accumulated (Roan Group; Cailteux et al., 2007). The contact between the Mwashya Subgroup and grand conglomérat at Kamoia was once thought to represent an unconformity (Schmandt et al., 2013). However, Kennedy et al. (2018) proposed a genetic and temporal relationship between the grand conglomérat and the Mwashya subgroup, as previously suggested by Wendorff (2003). The diamictite of the grand conglomérat does not record direct glacial deposition or glacially-influenced mass-flows along glacier margins (Selley et al., 2005; Wendorff and Key, 2009; Master and Wendorff, 2011), but rather deep-water subaqueous debrites deposited during active rifting and subsidence (Schermerhorn, 1974; Kennedy et al., 2018). The presence of lone oversized clasts (possibly dropstones) and striated clasts in fine-grained units, although rare, is commonly ascribed to glacial activity, but outrunner

clasts and/or tectonic rotation and clast collision during debris flow events are possible alternatives that cannot be discounted. Therefore, although glaciers and glaciofluvial processes probably provided some of the sediment to the basin margins, glacial influence on deposition was considered to be weak and distal (Kennedy et al., 2018).

2.3.5 *Mineralisation*

Sedimentary-rock-hosted copper deposits, like Kakula and Kamoia, form at the boundary between reduced and oxidised sedimentary rocks. Copper-sulphides of sedimentary-rock-hosted copper deposits precipitate from low- to moderate-temperature, moderate- to high-salinity oxidised fluids (Kirkham, 1989; Hitzman et al., 2005; 2010). Mineralisation at Kakula and Kamoia is predominantly disseminated chalcocite, bornite, and chalcopyrite in diamictite and lesser siltstone units of the lower basal diamictite (Ng.1.1.1). Interestingly, mineralisation at Kamoia and Kakula is poorly developed in the clast-rich diamictite but is well developed in siltstone and clast-poor diamictite. This phenomenon is especially apparent at Kamoia, where a strong textural distinction can be drawn between the clast-poor and clast-rich diamictite units. The presence and thickness of these units appear to have exerted an important control on ore-grade and stratigraphic position of ore above the lower contact of the grand conglom rat (Twite, 2016).

The copper-sulphides at Kakula are almost exclusively hypogene, present well below surface (100 – 1000 m), and locally extend up to 60 m above the base of the grand conglom rat (Fig. 4; OreWin, 2018). Although hypogene copper-sulphides also dominate at Kamoia, minor supergene enrichment and copper leaching is identified in parts of the

deposit that reach surface, especially near the uplifted areas and localised along fractures or structures that extend into the subsurface (Schmandt et al., 2013; Twite, 2016).

Vertical zonation in ore grade and copper-sulphide mineral species goes from chalcocite to bornite to chalcopyrite at both deposits, but lateral zonation is currently poorly understood. At Kakula, the most abundant copper-sulphide is chalcocite and represents the thickest copper-sulphide zone, whereas bornite and chalcopyrite are less abundant and have relatively thinner zones. At Kamoia, chalcopyrite is the dominant copper-sulphide, whereas chalcocite and bornite are less abundant or absent and have relatively thin vertical extents (OreWin, 2018).

Copper mineralisation at Kakula and Kamoia has been identified across an irregularly shaped area of over 500 km² (27 x 21 km; OreWin, 2018). The copper grade, thickness, and stratigraphic positions of ore show mosaic patterns, termed mosaic pieces, which represent areas of roughly consistent copper grades, thickness, and stratigraphic position (Fig. 3). The mosaic pieces are generally non-linear, with irregular shapes; the reason(s) for the distribution of ore and grade throughout the deposits is unclear (OreWin, 2018). However, the presence of synsedimentary structures, such as the Mupaka fault at Kamoia, appears to coincide with linear zones of relatively high copper grades (Fig. 3; Twite, 2016; Twite et al., 2019). At Kakula and Kamoia, mineralisation is predominantly stratiform and conforms to the shallow ($\leq 5^\circ$) dips of the sedimentary units of the area, but locally exhibits greater dips on the flanks of uplifted domes (Fig. 4). The Kamoia deposit occupies a shallowly plunging anticline looking north, and is contained in a horst between the west-scarp fault to the west and the Kansoko structure to the east (Schmandt et al., 2013). At the Kakula deposit, gentle folding of the units and the ore-zone are also

present (Fig. 4), but the west side of the deposit is in a graben, where the deposit is offset, up to 200 m collectively, by the west scarp fault and associated parallel structures in its vicinity (OreWin, 2018).

2.4 Methods

Detailed logging was primarily focussed on the ore-zone of each drill-hole (i.e. above the Mwashya subgroup) for DKMC_DD1012, DKMC_DD975, DKMC_DD1001 at Kakula and DKMC_DD627 and DKMC_DD793 at Kamoia. However, drill-holes DKMC_DD1012, DKMC_DD793, and DKMC_DD1161 include units several hundred metres above the ore-zone because samples were collected from these drill-holes at higher stratigraphic levels. Detailed logging was not undertaken for drill-hole DKMC_DD1161. The sedimentary units were divided into lithofacies: sandstone, siltstone, and diamictite. Diamictite was further subdivided based on the percentage of large clasts (≥ 2 mm), as clast-rich (20 – 40%) and clast-poor ($\leq 20\%$) varieties. The numerical stratigraphic codes used by Ivanhoe Mines Ltd. for subdivision of the grand conglomerat are not particularly useful at Kakula because sediment mass-flow deposits interdigitate, producing a stratigraphy composed of interleaved wedges, tongues, lenses, and aprons of diamictite, rather than consistent layers.

2.4.1 Samples

Oriented rock samples were collected at regular intervals through the mineralised zone at Kakula and Kamoia and from areas vertically and laterally away from copper mineralisation (Figs. 3, 4). At Kakula, samples were collected from three drill-holes along a northeast-southwest fence from a high-grade (DKMC_DD1012), medium-grade (DKMC_DD1001), and low-grade (DKMC_DD975) copper areas. Samples were also collected from a second low-grade drill-hole (DKMC_DD1161) in a different area at

Kakula (Figs. 3, 4). Samples from two high-grade drill-holes (DKMC_DD793 and DKMC_DD627) were collected from Kamoia. Samples were cut and made into oriented polished thin-sections (30 µm thickness), and some were carbon-coated for SEM analysis. The samples subjected to SEM analysis were selected from roughly equal depth intervals in and above the ore-zone for DKMC_DD1012 and DKMC_DD975 for Kakula, and from DKMC_DD627 for Kamoia (for comparison). Diamictite samples from well above (several hundred metres) the ore-zones were also examined for comparison in DKMC_DD1012, DKMC_DD1161 and DKMC_DD793. All samples examined with the SEM are diamictite except for the lowermost sample from DKMC_DD1012, which is a siltstone sample. Although some samples were collected from the middle (Ng.1.1.3) and upper diamictite units (Ng. 1.1.5), most diamictite samples used in this study were collected from the basal diamictite (Ng. 1.1.1). A complete sample list and information regarding the samples and analyses performed is found in Table 1.

2.4.2 *Analytical techniques*

Transmitted- and reflected-light petrography was performed using an Olympus BX-51 petrographic microscope equipped with Q-imaging at Laurentian University.

Petrography was important in the initial characterisation and selection of samples for further examination with the SEM. Laurentian University's JEOL-6400 SEM with Oxford INCA EDS detector was used with the following operating conditions for all analyses: 20 kV accelerating potential, 1.005 nA beam current, and a 5-second count

time. The spot size for spot analyses was at an estimated 5 μm . All SEM analyses are considered semi-quantitative, with minimum detection limits generally at 0.15 wt.%. Negative values and values below the general detection limit are not reliable or meaningful. For samples analysed with the SEM, the percentages of large clasts (≥ 2 mm), sand (65 μm – 2 mm), and matrix (≤ 65 μm) were visually estimated using scanned thin-section and BS-SEM images (Table 2). Backscattered-SEM images were also used for point-counting matrix grains to calculate the average grain size of different samples. Matrix grains were subjected to 100 point counts for every sample for grain size and averaged (Table 3). The SEM was used to image and examine matrix for texture and composition, produce EDS element maps, and perform compositional point and area “bulk” analyses to determine mineralogy and composition. “Bulk” area analyses were performed as square or rectangular shapes, generally from 1 - 4 mm^2 , that encompass as much matrix material as possible without containing relatively large clasts (≥ 2 mm). Backscattered-SEM images of high resolution and high magnification were also imported into ImageJ software to calculate the porosity percentage using greyscale shades in the images. This was performed for three images for each SEM sample to calculate an approximate average porosity (Table 2).

The “bulk” matrix area analysis was conducted to produce an average composition for diamictite matrix among drill-holes, stratigraphic levels, and aligned versus non-aligned matrix. The matrix phyllosilicate minerals (chlorite, biotite, muscovite) were analysed and compiled to produce compositional averages. Examples of other minerals, such as K-feldspar, albite, calcite, and dolomite were also analysed to show the elemental stoichiometry of the different minerals. Compositional results of matrix and mineral

analyses were imported from INCA software to Microsoft Excel as raw elemental data to be analysed and compared, and tables and graphs were created in Microsoft Excel. The elements that were imported into Excel were O, Na, Mg, Al, Si, S, K, Ca, Ti, Mn, Fe, and Cu. The SEM compositional analyses were converted to oxides using element-to-stoichiometric oxide conversion factors; this was performed by multiplying wt% element by the conversion factors for the equivalent expressed as oxide. The resulting compositional information was in the form of Na₂O, MgO, Al₂O₃, SiO₂, SO₃, K₂O, CaO, TiO₂, MnO, FeO, and CuO. Data were normalised to 100% for matrix analyses and normalised to 88, 98, and 96% for chlorite, biotite, and muscovite, respectively, to account for H₂O. The compositional average for each oxide for a particular population (sample, matrix, mineral) was calculated in Excel by dividing the sum of the population by the number of analyses (n). The population standard deviation for each oxide for each particular population (sample matrix, mineral) was also calculated in Excel.

X-ray powder diffraction (XRD) was performed using a Scintag XDS2000 diffractometer with Cu radiation and Ni filter, and it was performed on Kakula diamictite matrix samples to confirm that the minerals analysed on the SEM were identified correctly. Seven samples were analysed from Kakula, from different drill-holes and parts of the stratigraphy relative to the ore-zone. The samples analysed were DD1012_16, DD1161_6, DD1161_3, DD1012_7, DD1012_13, DD975_4, and DD975_10. Prior to the analyses, the samples were finely ground using a ring-and-puck laboratory pulveriser at Laurentian University. The XRD analyses were performed at Laurentian University, and minerals were identified using HighScore Plus XRD software.

Whole-rock geochemistry for major and trace elements was performed on seven Kakula diamictite matrix and three mafic clasts from the diamictite. The samples were pulverised and analysed by ALS Minerals. The samples analysed were the same as the XRD analyses with the addition of three mafic clasts from DD975_4 and DD1161_2 from Kakula, and DD627_4 from Kamoā. Diamictite matrix material submitted to the lab contained as little volume of large clasts (2 mm) as possible. For mafic clast analyses, large (cm-scale) mafic clasts were cut out from the diamictite to avoid contamination by matrix material. The geochemical data were used to compare the major oxides and trace elements in diamictite matrix to local mafic rock (basement and flows) and mafic clasts from the diamictite. The concentrations of major oxides were normalised to standards for mafic rock, silicic (felsic) rock, and continental crust (Pakiser and Robinson, 1967), and the concentrations of trace elements were normalised to MORB (mid-ocean ridge basalt; Taylor and McLennan, 1985; 2001), continental crust, upper continental crust (Taylor and McLennan, 1995; 2001), and sediment (weighted average based on relative distribution of sedimentary lithologies; primarily mud or equivalent mudrock; McLennan and Murray, 1999; Taylor and McLennan, 2001).

2.5 Results

2.5.1 Stratigraphy

The elevation relative to sea level of the Mwashya subgroup - grand-conglomérat contact and copper level at Kakula varies from one drill-hole to another (Fig. 6). Along the southeast-northwest fence at Kakula, the contact in the high-grade drill-hole (DKMC_DD1012) is at a lower elevation than the low-grade (DKMC_DD975) and medium-grade (DKMC_DD1001) drill-holes to the southwest and northeast, respectively (Figs. 4, 6). There are also notable differences in lithofacies thickness and presence among the drill-holes, especially in the lowermost diamictite units that contain mineralisation. All drill-holes end in the sandstone of the Mwashya subgroup just below the lower contact of the grand conglomérat.

The Kakula high-grade hole (DKMC_DD1012; Fig. 7) contains a relatively thin clast-rich diamictite that is directly overlain by a pervasively mineralised siltstone unit. Clast-poor diamictite includes the rest of the ore-zone and represents most of the thickness of the logged section. The Kakula low-grade drill-hole (DKMC_DD975; Fig. 8) has a relatively thick clast-rich diamictite and is overlain by a siltstone unit of similar thickness to the siltstone of drill-hole DKMC_DD1012. The rest of the logged part of the drill-hole consists of clast-poor diamictite. The Kakula medium-grade drill-hole (DKMC_DD1001; Fig. 9) contains a relatively thick clast-rich diamictite and no thick siltstone units as in drill-holes DKMC_DD1012 and DKMC_DD975. It does, however, contain a thin siltstone unit in clast-rich diamictite just above the basal contact of the grand

conglomérat. The rest of the drill-hole examined is predominantly clast-poor diamictite. In the Kamoia high-grade drill-hole (DKMC_DD627; Fig. 10), clast-rich diamictite is poorly mineralised and directly overlain by clast-poor diamictite that is more heavily mineralised. The only siltstone identified was the typical lower pyritic siltstone (Ng.1.1.2) unit that is present at Kamoia above the clast-poor diamictite. In the second high-grade drill-hole at Kamoia (DKMC_DD793; Fig. 11), there is a roughly equal thickness of clast-rich diamictite, siltstone, and clast-poor diamictite, which is then overlain by typical lower laminated pyritic siltstone of Kamoia. Unlike the Kakula drill-holes, the lower laminated pyritic siltstone (Ng.1.1.2) at Kamoia is located closer to the lower contact of the grand conglomerat. For the second Kakula low-grade drill-hole (DKMC_DD1161; Fig. 12), the units are simply divided from bottom to top into sandstone, diamictite, and siltstone based on the samples collected and the Ivanhoe Mines Ltd. geology log for the drill-hole. This drill-hole intersects the Mwashya subgroup - grand conglomerat contact at a greater depth than the other drill-holes studied.

2.5.2 *Diamictite characteristics*

Characterisation of diamictite through logging was based on the percentage of large clasts (≥ 2 mm). The diamictite units are predominantly textureless and unbedded at all scales. A variety of clast lithologies is identified in the diamictite units, but the majority are quartzite, with moderate volumes of altered mafic volcanic rock, and smaller volumes of pelite, dolostone, and granitoid clasts. Diamictite matrix descriptions are limited in hand sample because of the rock's fine-grained nature. The percentage of large clasts (≥ 2 mm)

is the only requirement in the distinction between clast-rich (Fig. 13a) and clast-poor (Figs. 13b, 14) diamictite, with the division at 20%. Matrix colour varies throughout the stratigraphy and is not obviously stratigraphically meaningful; colour is, however, compositionally meaningful. In the basal diamictite, matrix colour ranges regionally from maroon-grey to grey to green-grey, but is generally maroon to green-grey at Kakula (Figs. 13, 14) and grey to grey-green at Kamoia (Fig. 15). In hand sample, samples collected from the middle diamictite (Fig. 16) and upper diamictite look similar to grey to green-grey basal diamictite and are both clast-poor and clast-rich, but all samples collected for this study are clast-poor. Locally, diamictite samples exhibit macroscopic nearly vertical fabric (alignment and elongation of matrix minerals and clasts; Figs. 14a, 15b), although it is weak to absent in the samples investigated for this study. The fabric is generally more easily characterised under magnification in the matrix (aligned matrix; Fig. 17). The fine-grained matrix mineralogy is hard to identify with the petrographic microscope, and in plane-polarised light, is pale brown to colourless with indistinct boundaries among its component particles (Fig. 18). Percentage estimations show that clast-rich diamictite (Figs. 18a, 18b) has a higher percentage of sand-sized clasts ($65\ \mu\text{m} - 2\ \text{mm}$; 22.5 – 32.5%; Table 2), and consequently, a lower percentage of matrix (material $\leq 65\ \mu\text{m}$) than clast-poor diamictite (12.5 – 25%; Figs. 18c, 18d; Table 2). Visual estimates of the percentage of large clasts ($\geq 2\ \text{mm}$), sand ($65\ \mu\text{m} - 2\ \text{mm}$), matrix ($\leq 65\ \mu\text{m}$), and porosity for all samples analysed with the SEM are in Table 2. Importantly, the lower percentage of large clasts and sand-sized particles in clast-poor diamictite correlates with higher copper grades.

Copper-sulphide mineralisation is hypogene, stratiform, and variably present in siltstone and clast-rich and clast-poor diamictite, but it is generally higher-grade in siltstone and clast-poor diamictite based on calculated SEM “bulk” analyses and as shown in Ivanhoe Mines Ltd. assay results. Copper grade is commonly much higher than visually estimated in drill-core because grade is conferred predominantly by fine-grained (clay- and silt-sized) sulphide disseminated in the diamictite matrix. Coarse-grained copper sulphides (sand-sized and larger), however, are visually striking. Copper-sulphides locally fully replace clasts and form rims around them, whereas larger clasts (≥ 2 mm) are locally replaced along their edges and have copper-sulphide rims. Copper-sulphides also form caps on the stratigraphic tops of clasts and less commonly form “beards” on their undersides. Large caps are up to a few centimetres thick, and are generally proportional to the size of the clast on which they developed. Chalcocite disseminated in the matrix is especially hard to see in hand sample because its colour is well camouflaged by the medium to dark matrix colour. At Kakula, there is a prominent upward zonation of copper-sulphides in the ore zone (Figs. 7, 8, 9), from chalcocite to bornite to chalcopyrite, yet an overlap among the copper-sulphide species is also present. At Kakula, chalcocite and bornite are generally more abundant than chalcopyrite, whereas chalcopyrite is more abundant at Kamoia. Sulphide-gangue caps at Kamoia are larger than those at Kakula, and commonly consist of chalcopyrite, whereas the caps at Kakula are smaller and generally consist of chalcocite and bornite.

Although unidentifiable through core-logging and hand sample examination, significant compositional and textural differences between matrix in and around the mineralised zone (ore-zone matrix) and in matrix in areas well outside of the ore-zone (least-altered

matrix) are discernable using SEM imaging. Ore-zone matrix defined here is not exclusively where there are copper-sulphides; it also includes the areas extending away from the ore-zone that have the same mineral assemblages as matrix containing copper-sulphides. Least-altered matrix is identified in only three of the thin-sections examined from a few hundred metres above the mineralised zone at Kakula, in drill-holes DKMC_DD1012 and DKMC_DD1161. Samples of least-altered matrix coincide with the middle and upper diamictite units of the grand conglomérat (Figs. 7, 12). The uppermost sample collected from drill-hole DKMC_DD1161 would be considered farthest from the ore-zone vertically and laterally. Least-altered matrix was not identified in any of the samples from Kamoá, even from the diamictite sample collected from DKMC_DD793, in the middle diamictite unit (Ng.1.1.3), over 250 m above the base of the grand conglomérat. This suggests that the particular unit of the grand conglomérat may be irrelevant in the distinction between least-altered and ore-zone matrix. However, it is unclear how and where the ore-zone matrix transitions into the “least-altered” matrix. Unfortunately, no samples that were collected from the Kakula or Kamoá area can be considered completely unaltered. Great drilling success by Ivanhoe Mines Ltd. in hitting mineralised areas means that completely unaltered rock is essentially unavailable.

2.5.3 *Least-altered matrix*

2.5.3.1 *Matrix minerals*

The Kakula least-altered diamictite matrix consists predominantly of quartz (30 – 60% volume), albite (20 – 50% volume), chlorite (15 – 40% volume), and K-feldspar (5 – 15% volume; Table 4). The presence of albite and the lack of muscovite are the major distinguishing characteristics of least-altered matrix as compared ore-zone matrix. Other than in rare detrital clasts, biotite and muscovite were not identified in least-altered matrix, and carbonate particles (Fe-dolomite and calcite) are minor components ($\leq 5\%$ volume). Pyroxene, anorthite, and clay minerals were not identified in this study. A small increase in chlorite abundance and relative decrease in abundance of other minerals is evident in aligned matrix versus and non-aligned matrix of least-altered sample DD1012_16. However, only weak matrix alignment was identified in this sample, whereas no aligned matrix was identified in the other least-altered samples.

There are differences in mineral presence and abundance among the three least-altered matrix samples. For example, sample DD1012_16 (Figs. 19, 20) contains calcite as its only carbonate mineral, whereas samples DD1161_3 (Figs. 21, 22) and DD1161_6 contain ferroan dolomite instead of calcite. Pure dolomite was not identified in any of the least-altered samples. The matrix of DD1161_6 (Fig. 23) appears to contain more albite and less quartz and K-feldspar than the other least-altered samples. Matrix from DD1012_16 appears to contain more chlorite than the other least-altered matrix samples.

Matrix grains of albite (typically 1 - 65 μm), quartz (typically 1 - 65 μm), and K-feldspar (typically 1 - 65 μm) in the least-altered matrix has various sizes and shapes (Fig. 21). Smaller grains locally have indistinct grain boundaries, especially in DD1161_6 (Fig. 23). Equant, rounded to subrounded albite, quartz, and K-feldspar are probably detrital.

Albite grains appear to have been locally altered to K-feldspar (Figs. 19b, 21c, 21d), and chlorite and calcite also appear to grow locally on albite and K-feldspar in DD1012_16 (Fig. 19). Calcite (typically 1 – 20 μm) from DD1012_16 appears to be partially dissolved, contains pores (Fig. 19), and is typically equant and subrounded to angular. Ferroan dolomite (typically 1 – 20 μm) is typically equant to elongated, subangular to angular, and is generally present between relatively larger matrix components (Fig. 22). Quartz locally overgrows albite and K-feldspar and may be an important cementing component of the rocks (Fig. 20).

Chlorite grains (typically 1 – 20 μm) in the matrix are subangular to elongated (Figs. 19b, 21c) and are locally present along the edges of albite, quartz, and K-feldspar (Figs. 19b, 21c). Other than fine-grained rutile, pyrite is the only opaque mineral phase in least-altered matrix; no copper-sulphides or hematite are present. Pyrite generally represents 1 – 3% total volume, but has a relatively high abundance in sample DD1012_16, at up to 5%. Disseminated pyrite is predominantly framboidal and a few microns in diameter (Figs. 19, 20); some pyrite euhedra (Figs. 22, 23d) are locally present. Some pyrite appears to form along the edges of pores (Fig. 22), whereas some pyrite appears to be locally enclosed by or tightly surrounded by other matrix minerals, commonly quartz (Fig. 20) and albite (Fig. 23). Rutile is a minor component of the matrix ($\leq 1\%$), and its morphology is typically elongated and angular. A summary of typical mineral distributions and associations in least-altered matrix is found in Table 5.

X-ray powder diffraction analyses (Appendix A; Figs. A1 - A3) confirm the mineralogy of least-altered matrix identified with the SEM. It also confirms that there are no clay

minerals in the matrix. Quartz, chlorite, albite, K-feldspar, and carbonate (Fe-dolomite, dolomite, calcite, or ankerite) were identified. Some discrepancies for carbonate minerals exist between the SEM and XRD analyses. Ankerite, for example, was never identified by SEM analyses. Minor components of biotite and muscovite in some samples is consistent with a minor detrital component that was identified with the SEM. The XRD analysis of DD1012_16 identified pyrite because of its relatively high abundance compared to other least-altered diamictite samples analysed. Notably, the XRD analysis for DD1161_6 reveals that there is ferropargasite (amphibole) present in the sample. However, based on limited SEM point analyses, stoichiometry suggests the mineral is ferropumpellyite. These grains are rare and are generally equant and rounded to subrounded, suggesting they are probably detrital.

2.5.3.2 *Matrix texture*

The least-altered matrix is generally textureless (non-aligned), but local areas of vertical matrix elongation and alignment are present in sample KAK1012_16. Matrix alignment appears to be absent in KAK1161_3 and KAK1161_6. Aligned matrix is less well developed and less common in the least-altered matrix versus ore-zone matrix. Aligned matrix is spatially limited on a micro-scale and has gradational contacts with non-aligned matrix. Alignment is strongest and most common beside large clasts, whereas stratigraphic tops and bottoms of large clasts are commonly non-aligned matrix. Similar to the ore-zone matrix described below, there is little to no evidence of horizontal matrix alignment that could be related to burial compaction. The least-altered matrix contains a

full spectrum of clay- and silt-sized components, but point-counting measurements for DD1012_16 of matrix material yielded an average of 7 μm (fine-silt; Table 3). Although the average grain size of the least-altered matrix is slightly larger than ore-zone matrix, their grain sizes are similar.

Following the mudrock pore classification scheme of Loucks et al. (2012), Kakula least-altered matrix has interparticle pores (pores among particles; common in Fig. 22) with a smaller volume of intraparticle pores (pores in an individual particle; Fig. 20). The shape and size of pores in the matrix vary, but intraparticle pores are usually smallest. The porosity percentage in the least-altered diamictite matrix of DD1012_16 is measured at 8.3%, which is lower than what is typical for ore-zone matrix (Table 2). No difference in overall pore shape and size among samples could be identified. Where matrix grain edges are locally indistinct, in DD1012_16 and DD1161_6, this gives the least-altered matrix a “cemented” look (Figs. 19, 23). The “cemented” look is locally present in sample DD1012_16 and DD1161_6, but less so in DD1161_3. Overall, the least-altered matrix has somewhat different texture or appearance from ore-zone matrix.

2.5.4 *Ore-zone matrix*

2.5.4.1 *Matrix minerals*

The Kakula ore-zone diamictite matrix is dominated by muscovite (40 - 80% volume) and quartz (20 - 40% volume), with lower amounts of chlorite (5 – 20% volume), K-

feldspar (5 – 20% volume), dolomite (1 – 5% volume), ferroan dolomite (1 – 5% volume) and biotite $\leq 3\%$ volume; Table 6). Rare detrital apatite and tourmaline are also present in the matrix. Aligned and non-aligned matrix contain the same minerals, but the mineral abundances are different (Table 6). Muscovite is significantly more abundant in aligned matrix than in non-aligned matrix (Fig. 24b), which corresponds with a lower percentage of other matrix minerals, such as quartz, K-feldspar, chlorite, biotite, and dolomite. The mineralogy of all ore-zone matrix samples is consistent, except for the opaque mineral phases. Opaque minerals locally represent over 5% of the matrix volume and include chalcopyrite, bornite, chalcocite, hematite, and rutile in the copper-sulphide zone, and pyrite and rutile outside of the copper-sulphide zone (Figs. 6 - 9). A higher abundance of copper-sulphides is present in non-aligned matrix, whereas a lower abundance of copper-sulphides and a higher abundance of hematite and rutile is evident in aligned matrix (Fig. 24c). Rutile has a low abundance ($\leq 1\%$).

Quartz (typically 1 – 65 μm) and K-feldspar (typically 1 – 65 μm) grains in the ore-zone matrix locally show evidence of dissolution along their edges and have various shapes and sizes, but they are generally equant and rounded to subangular in non-aligned matrix, whereas they are locally elongated and angular in aligned matrix (Table 6). Much of the quartz in the matrix is detrital because of its relatively large grain sizes and rounded morphologies (Fig. 25). Quartz overgrowths on detrital quartz grains are rare and difficult to identify in the matrix. Potassium-feldspar is the only feldspar mineral present in ore-zone matrix. Pure dolomite (typically 1 – 65 μm) is present only as rounded to subrounded cores in iron- and manganese-bearing dolomite overgrowths (Fig. 26; ≤ 8 wt% FeO and ≤ 2 wt% MnO). Ferroan dolomite (typically 1 – 20 μm) is also present

without pure-dolomite cores in the matrix (Fig. 26) and has a similar composition to ferroan dolomite overgrowths. Locally, the boundary between pure dolomite and the ferroan dolomite overgrowth is irregular (Fig. 26c). No calcite or ankerite was identified in ore-zone matrix.

Chlorite (typically 1 – 20 μm) and biotite (typically 1 – 20 μm) in the diamictite matrix are typically elongated and subangular to angular. Chlorite is present on quartz and K-feldspar, ferroan-dolomite overgrowths (Figs. 27a, 27b), and pyrite (Fig. 27c). Chlorite locally co-occurs with K-feldspar (Fig. 27d). Chlorite is far more abundant than biotite, but is commonly intergrown with biotite (Fig. 28a) and adjacent to copper-sulphides in the matrix (Fig. 28). Copper-sulphides are locally present along chlorite mineral cleavage (Figs. 28a, 28c). Muscovite has similar size and shape to chlorite and biotite, and locally replaces and forms on quartz (Fig. 29a), K-feldspar (Fig. 29c), ferroan dolomite (Fig. 29d), biotite (Fig. 29a), and chlorite (Figs. 27a, 29a). Muscovite appears to have locally formed at sites of dissolved chlorite and biotite (Figs. 30a, 30b) and replaces chlorite along mineral cleavage (Fig. 30c).

Copper-sulphides (chalcocite, bornite, chalcopyrite) are predominantly disseminated in the matrix as round and equant crystals, but locally have irregular shapes (Fig. 31). Disseminated copper-sulphides are generally $\leq 5 \mu\text{m}$ in diameter, smaller than other matrix minerals on average, and commonly adhere to the walls of matrix pores (Fig. 31). Like other minerals in aligned matrix, copper-sulphides are locally elongated and oriented parallel to matrix fabric (Fig. 32). Copper-sulphides in aligned matrix appear to

be tightly surrounded by or completely enclosed by other matrix minerals (Fig. 32).

Copper-sulphides rarely form μm - to mm-scale veinlets in the matrix.

Pyrite (typically less than $\leq 5 \mu\text{m}$) is predominantly framboidal and commonly adheres to the margins of matrix pores (Fig. 33a). Pyrite euhedra are also present in the matrix and are commonly much larger than framboidal pyrite (Fig. 33b). There is textural evidence of pyrite overgrown by chalcopyrite in low-grade copper zones (Fig. 33c), where the sizes and shapes of disseminated pyrite are similar to those of copper sulphides (Fig. 33d). Locally, chalcopyrite replacement by bornite was followed by bornite replacement by chalcocite (Fig. 34). Hematite (typically $\leq 5 \mu\text{m}$; Fig. 24) co-occurs with chalcocite (and bornite) only at certain stratigraphic levels at Kakula (Figs. 6 - 9), and is rare at Kamoia. Hematite locally contains inclusions of copper-sulphide, most commonly chalcopyrite and bornite (Figs. 34a, 34b, 35), and locally cross-cuts copper-sulphides (Fig. 34a, 34b). Copper-sulphide and hematite grain sizes may be locally large, especially where they are replacing or forming on relatively large clasts in the matrix. Rutile is a minor component of the matrix, and its morphology is locally equant and rounded but is typically elongated and angular. Unlike copper sulphides and locally pyrite, rutile and hematite are not significant cap- and rim-forming minerals on clasts. A summary of typical mineral distributions and associations in least-altered matrix is found in table 7.

X-ray powder diffraction analyses (Appendix A; Figs. A4 – A7) confirms the mineralogy of least-altered matrix identified here with the SEM. It also confirms that there are no clay minerals in the matrix. Quartz, muscovite, chlorite, K-feldspar, dolomite (or Fe-

dolomite), and biotite were identified. X-ray powder diffraction analyses of matrix suggest the chlorite species present is clinochlore.

2.5.4.2 *Matrix texture*

Matrix of the ore-zone is generally textureless (non-aligned matrix), but aligned matrix is more common in ore-zone matrix than in least-altered matrix. As it is for least-altered matrix, aligned matrix of ore-zone matrix is spatially limited on a micro-scale (areas of aligned matrix are generally $\geq 100 \mu\text{m}$), with sharp to gradual contacts with non-aligned matrix. This spatial limitation of aligned matrix on a micro-scale is strongly controlled by the abundance of relatively large clasts in the area. The alignment is strongest and most common beside large clasts (Fig. 17), and follows clast edges and commonly converges on the stratigraphic tops and bottoms of clasts. Matrix at the stratigraphic tops and bottoms of large clasts are generally areas of non-aligned matrix (Fig. 17). Aligned matrix is commonly highlighted by dark material in plane-polarised light (Fig. 17a). In crossed-polarised light, aligned matrix has more colourfully birefringent material than non-aligned matrix, which implies a difference in composition (Fig. 17b).

The matrix always contains a full spectrum of clay- and silt-sized particles; point-counting measurements of individual matrix components yielded an average size of 4-8 μm (fine silt; Table 3) in all ore-zone matrix samples. The total percentage of sand-sized (65 μm – 2 mm) material varies also, especially between clast-rich and clast-poor diamictite (Figs, 13, 15, 18). Grain shapes are commonly variable because of mineralogy

and whether the grains are in non-aligned or aligned matrix. Phyllosilicate minerals (muscovite, chlorite, biotite) are commonly elongated and are in contact with each other less in non-aligned matrix than in aligned matrix. Non-aligned matrix in the ore-zone diamictite matrix has a porosity variation from 8 – 12.5% spanning all ore-zone diamictite SEM samples (Table 2). The only siltstone sample (DD1012_3.5) had the highest measured porosity at 13.8%. In general, aligned matrix has lower porosity than non-aligned matrix. For example, 11.9% porosity for non-aligned matrix (Fig. 31) and 7.4% porosity for aligned matrix (Fig. 32) was measured in the same sample (DD1012_6). Similar to least-altered diamictite matrix, the ore-zone matrix at Kakula is dominated by interparticle pores rather than intraparticle pores. Porosity is also evident along cleavage planes of chlorite, biotite, and muscovite, but most common in mineral rims (Fig. 30c). No variation in overall pore shape and size among ore-zone matrix samples was identified. Moreover, there is no obvious cement phase present in ore-zone matrix.

2.5.5 Bulk and mineral compositions

The SEM compositional analysis results for the Kakula high-grade drill-hole (DKMC_DD1012), Kakula low-grade drill-hole (DKMC_DD975), and Kamoia high-grade drill-hole (DKMC_DD627) are summarised in Tables 8 and 9, 10 and 11, and 12 and 13, respectively. The compositional analysis for the second Kakula low-grade drill-hole (DKMC_DD1161) is found in Tables 14 and 15. The total wt% for chlorite, biotite, and muscovite were normalised to 88, 98, and 96%, respectively, to account for the

approximate H₂O component of each mineral. Scatter plots of individual area analyses for “bulk” matrix and individual point analyses for chlorite, biotite, and muscovite of the ore-zone matrix were created for DKMC_DD1012 (Fig. 36), DKMC_DD975 (Fig. 37). Scatter plots for DKMC_DD627 (Fig. 38) were created only for “bulk” matrix, chlorite, and muscovite because not enough biotite is present in DKMC_DD627.

2.5.5.1 *Matrix bulk composition*

The least-altered and ore-zone matrix consist of varying amounts quartz, chlorite, K-feldspar, and dolomite, whereas least-altered matrix contains albite (and calcite) instead of muscovite and biotite. Pyrite is present in least-altered matrix and locally in ore-zone matrix outside of heavily mineralised zones. As it is reflected by the observed mineralogy, bulk composition for the least-altered matrix of drill-hole DKMC_DD1012 has less Al₂O₃, SiO₂ and K₂O, more Na₂O, SO₃ and FeO, and similar CaO, TiO₂, and MgO to ore-zone matrix. The least-altered samples contain Na₂O, whereas Na₂O is low and near detection limit in ore-zone matrix. The least-altered matrix sample DD1161_6 farthest from the mineralisation, both laterally and vertically, has similar composition as DD1012_16 and DD1161_3, but contains more Na₂O.

Whether from the Kakula high- or low-grade drill-holes, there is only minor variability in the wt% of different elements among ore-zone matrix samples (Tables 8, 10). However, even though there is some variability in FeO and MgO wt% among samples, FeO and MgO maintain a roughly consistent ratio (Figs. 36, 37). The lowermost sample of

diamictite (KAK1012_6) from drill-hole DKMC_DD1012 coincides with the most copper, and copper grades decrease up-section from there (Fig. 39). The siltstone sample (KAK1012_3.5), the lowermost sample that was analysed from the drill-hole, has a similar composition to diamictite matrix, but contains more copper and SO₃, and notably more K₂O, similar Al₂O₃, and less MgO, CaO, MnO, and FeO (Table 8).

Other than the relatively low copper content in ore-zone matrix of low-grade drill-holes (DKMC_DD975 and DKMC_DD1161) at Kakula, the wt% of elements from samples in the high-grade Kakula drill-hole (DKMC_DD1012) are comparable to those of the low-grade drill-holes. In the low-grade drill-hole (DKMC_DD975), the matrix copper grades are relatively low in samples from the clast-rich diamictite towards the base of the drill-hole and are higher in clast-poor diamictite above (Fig. 40; Table 10). The SO₃ content is also higher in the clast-poor diamictite samples than the other samples.

Similarly to the “bulk” matrix samples of ore-zone matrix of the Kakula holes, there is variability in the wt% of elements among samples at Kamoia in the high-grade drill-hole (DKMC_DD627; Table 12). Overall, the element wt% values are similar to those of the Kakula samples. Copper grades are low in the lowermost sample of clast-rich diamictite, and they are highest towards the base of the clast-poor diamictite and then decrease up-section (Fig. 41). The clast-rich diamictite sample has relatively low SO₃ wt% and relatively elevated SiO₂ wt% compared to other samples.

2.5.5.2 *Aligned versus non-aligned matrix*

In the “least-altered” matrix sample (KAK1012_16), aligned matrix is poorly developed but still locally present; alignment is absent in KAK1161_3 and KAK1161_6. Moreover, alignment was not identified in sample KAK1161_1 of the ore-zone matrix or in the siltstone sample analysed from DKMC_DD1012. Aligned matrix of the least-altered material has lower Na₂O, SiO₂ and CaO wt% than non-aligned matrix, but higher Al₂O₃, K₂O, MgO, FeO, TiO₂, and SO₃ (sample DD1012_16; Table 8). In ore-zone matrix, aligned matrix has higher Al₂O₃, K₂O, TiO₂, and FeO wt% than non-aligned matrix, lower SiO₂, and similar CaO and MgO (Tables 8, 10). Matrix element differences in aligned versus non-aligned matrix are similar for ore-zone matrix and least-altered matrix for Al₂O₃, K₂O, FeO and TiO₂ and SiO₂. However, in least-altered matrix, MgO increases and CaO decreases, whereas MgO and CaO are roughly uniform in aligned ore-zone matrix. In ore-zone matrix containing pyrite instead of copper-sulphides, an increase or a comparable value of SO₃ in aligned matrix versus non-aligned matrix is present. In the ore-zone matrix samples containing copper-sulphides instead of pyrite, aligned matrix has lower SO₃ than non-aligned matrix. Most notably, there is a lower copper grade in aligned matrix as compared to non-aligned matrix of ore-zone matrix. This contrast is most dramatic at Kakula in DKMC_DD1012 (Fig. 39) and DKMC_DD975 (Fig. 40) but is also evident in DKMC_DD627 (Fig. 41) at Kamoia.

2.5.5.3 *Chlorite, biotite, and muscovite composition*

In the high-grade Kakula (DKMC_DD1012) drill-hole, there is a linear compositional decrease of MgO wt% and increase of FeO wt% in chlorite and biotite up-section (Fig.

36). For example, the average chlorite MgO content goes from 23.77 to 15.12% in ore-zone matrix and decreases to 13.61% in sample DD1012_16 of least-altered matrix (Table 8). Chlorite from least-altered matrix is more Fe-rich than ore-zone matrix. Relatively Mg-rich chlorite and biotite are present in areas containing copper-sulphides. The trend in MgO and FeO wt% ratios in chlorite and biotite in the low-grade Kakula hole (DKMC_DD975; Fig. 37) is also present, but it is not as drastic as in the high-grade Kakula hole over a similar depth interval. The FeO and MgO wt% ratios in chlorite and biotite change over a short depth interval, and are present irrespective of the roughly consistent FeO and MgO wt% ratios of “bulk” matrix for the same samples. An increase in FeO wt% in chlorite and biotite is accompanied by a nearly proportional decrease in MgO and a small decrease in SiO₂ (Tables 8, 10). Chlorite and biotite composition is roughly homogeneous in a given sample (Figs. 36, 37). The least-altered matrix does not contain biotite or muscovite, but has chlorite with relatively high FeO wt%.

In the high-grade hole from Kamoia (DKMC_DD627), chlorite is more Fe-rich in the relatively copper-poor clast-rich diamictite, becomes Mg-rich in the copper-rich clast-poor diamictite, and then becomes Fe-rich upwards away from copper mineralisation (Table 12). These characteristics resulted in an overlap in the analyses in the scatter plot of chlorite (Fig. 38). In ore-zone matrix, the chlorite and biotite in the low-grade drill-hole (DKMC_DD975; Table 10) is relatively Mg-poor compared to chlorite and biotite from the high-grade drill-hole (DKMC_DD1012; Table 8) at a similar vertical distance above the basal contact of the grand conglomerat. Although the chlorite and biotite analysed were predominantly from the matrix, analyses of chlorite and biotite in coarse-

grained mineral caps highlighted the same composition as the chlorite and biotite from the matrix in the same sample.

Muscovite is exclusively present in ore-zone matrix and contains significant MgO (≤ 3 wt%) and FeO (≤ 6 wt%; Tables 8, 10). However, unlike chlorite and biotite, muscovite does not show a compositional trend in FeO and MgO wt% up-section (Figs. 36, 37). Individual muscovite crystals have heterogeneous compositions within a given sample, particularly for FeO and MgO wt%, yet the overall FeO to MgO wt% ratio is generally 2:1 (Figs. 36, 37). A higher combined FeO + MgO wt% in muscovite results in a proportional decrease in Al₂O₃ wt%. The muscovite composition at Kamoia (DKMC_DD627; Fig. 38) is also heterogeneous, but there is more variability in the FeO to MgO wt% ratio than there is in muscovite at Kakula. Muscovite composition is similar in aligned and non-aligned matrix of all ore-zone samples analysed.

2.5.6 Whole-rock geochemistry

2.5.6.1 Major elements

Analysis by whole-rock geochemistry (see Appendix B) yielded similar results for major element concentrations to SEM bulk matrix analyses. The iron content is given as Fe₂O₃, rather than FeO. Ore-zone matrix is depleted in Na₂O and enriched in K₂O compared to least-altered matrix, as it is for the mafic clasts. Least-altered and ore-zone matrix are enriched in TiO₂, Fe₂O₃, and MgO relative to the average silicic rock, but are slightly depleted in these elements relative to the average mafic rock and the average for local

mafic rock (basement and flows). The TiO₂, Fe₂O₃, and MgO concentrations of least-altered and ore-zone matrix is comparable to the average continental crust. Least-altered matrix has similar Na₂O content as silicic rock, mafic rock, and average crust. Because K₂O and Na₂O concentrations vary significantly from least-altered matrix to ore-zone matrix, these oxides cannot be used as a good proxy for original depositional makeup.

2.5.6.2 *Trace elements*

Trace element concentrations are similar in least-altered and ore-zone matrix, except for Sr, V, Rb, and Cs. Least-altered matrix contains more Sr and V, but has less Rb and Cs than ore-zone matrix. In general, least-altered and ore-zone matrix are enriched in trace elements relative to the local mafic rock, mafic clasts, average crust, and MORB, but are depleted in Cr, Sr, and W. Matrix trace element patterns and concentrations resemble more closely those of the average upper crust and average sediment. However, matrix has elevated V and Cr concentrations relative to average sediment and upper crust. Notably, the concentration of Cr is very similar in both matrix types and is elevated in both mafic clasts and local mafic rocks. Least-altered and ore-zone matrix have similar REE concentrations and patterns, with relatively enriched LREEs.

2.6 Interpretation

2.6.1 *Matrix composition*

2.6.1.1 *Matrix “bulk” composition*

Least-altered matrix consists of quartz, chlorite, albite, K-feldspar, dolomite or calcite, pyrite, and rutile. Ore-zone matrix consists of muscovite, quartz, chlorite, K-feldspar, dolomite, Fe-dolomite, biotite, rutile, whereas the presence of pyrite, copper-sulphides, and hematite varies locally. The difference in mineralogy between least-altered and ore-zone matrix is important because it illustrates the effects of alteration on mineralogy in the ore-zone versus least-altered matrix following deposition. Compositional variations of bulk matrix among samples is a function of the relative abundance of minerals and mineral compositions. The possible compositional variability of the original diamictite sediment at different stratigraphic levels makes it challenging to use bulk matrix composition as a baseline for post-depositional, alteration-induced compositional changes. Nonetheless, the significant compositional and mineralogical differences between ore-zone matrix and least-altered matrix may be, at least in part, the result of alteration. For example, the complete absence of albite in ore-zone matrix and its abundance in least-altered matrix suggests addition, or at least the preservation, of Na_2O in the least-altered matrix and the dissolution and removal of albite in ore-zone matrix. The ore-zone matrix has significantly more K_2O than least-altered matrix, and this relative enrichment of K_2O in the ore-zone matrix suggests the addition of K_2O , as was

suggested by Schmandt et al. (2013). There may have also been addition of MgO during alteration, or the preservation of MgO from detrital mafic material.

Variability in composition among samples may be from alteration, whereas some may be a function of variability in original bulk sediment composition. Variations in SiO₂ “bulk” matrix content in a given sample can be explained by the abundance of quartz. Given that FeO to MgO wt% ratios are roughly consistent among bulk matrix analyses, the variability in elemental wt% is probably a reflection of the abundance of FeO- and MgO-bearing minerals. Pyrite, chalcopyrite, bornite, and chalcocite contain approximately 53, 35, 26, and 20 wt% elemental sulphur, respectively. The sulphur content of the ore-zone diamictite matrix increases up-section away from mineralisation, which suggests that sulphur may have been released during the replacement of pyrite by relatively sulphur-poor copper-sulphides. However, the lowermost sample of the high-grade drill-hole (DKMC_DD1012), a siltstone sample (DD1012_3.5), contains significant sulphur but has even more copper. Samples containing pyrite rather than copper-sulphides, both in ore-zone and least-altered matrix, generally contain more sulphur. The abundance of sulphur in least-altered diamictite matrix and the increase in sulphur away from mineralisation in ore-zone diamictite matrix suggests that an external source of sulphur was not necessary for copper-sulphide formation.

The bulk matrix copper grade is a reflection of the abundance of copper-sulphides and the particular copper-sulphide species present at a given stratigraphic level. Chalcocite, bornite, and chalcopyrite contain approximately 80, 63, and 35 wt% elemental copper, respectively, and bornite and chalcopyrite containing approximately 11 and 30 wt%

elemental iron, respectively. The upward zonation of copper-sulphides from chalcocite to bornite to chalcopyrite is well documented in sedimentary-rock-hosted copper deposits in general. This zonation can be explained by an upward-migrating fluid becoming gradually copper-depleted as copper-sulphides are precipitated in the lower, reduced stratigraphic units (Hitzman et al., 2005; 2012). The degree of oxidation by the copper-mineralising fluid may have also played a role in the zonation and stability of the copper-sulphide species at Kakula and Kamoia.

2.6.1.2 *Aligned versus non-aligned matrix*

Aligned and non-aligned matrix contain the same mineral assemblages, but are compositionally different owing to different mineral abundances. Element wt% differences between the two matrix types can be explained by the removal of elements and/or the concentration and/or addition of elements during the matrix alignment process. In ore-zone matrix, there is a higher abundance of muscovite in aligned matrix than in non-aligned matrix (Fig. 24). The higher abundance of muscovite and the correspondingly diminished relative abundance of other matrix minerals is consistent with the increase in K_2O and Al_2O_3 in aligned matrix. The relative increase in K_2O , Al_2O_3 , FeO, and MgO in least-altered matrix of aligned matrix can be attributed to a lower abundance of quartz. Increased FeO and MgO would be proportional to a relative increase in chlorite content. Lower SiO_2 content in aligned matrix in the ore-zone matrix is consistent with the lower abundance of quartz in aligned matrix of least-altered and ore-zone matrix. A decrease in the amount of albite and calcite can also explain the

decrease in Na₂O and CaO, respectively, of aligned matrix in least-altered matrix from DD1012_16.

As shown by copper versus depth plots for Kakula (Figs. 39, 40), there is less copper in aligned matrix than in non-aligned matrix. Although not as dramatic, this pattern is also present at Kamoia (Fig. 41). The lower copper grade in aligned matrix correlates with the visually lower abundance of copper-sulphides in aligned matrix than non-aligned matrix (Fig. 24). This suggests that some copper-sulphides were dissolved or possibly replaced during the development of aligned matrix. The lower abundance of copper-sulphides in aligned matrix is also consistent with the decrease in SO₃ in aligned matrix compared to non-aligned matrix. However, areas with pyrite in the ore-zone matrix and least-altered matrix have a minor increase in the concentration of SO₃ in aligned matrix than non-aligned matrix. Although the reason for this is not as clear, it is possible that pyrite was better preserved in aligned matrix than other minerals, which resulted in the concentration of those elements.

2.6.1.3 *Chlorite, biotite, and muscovite composition*

The composition of chlorite and biotite, notably their FeO to MgO wt% ratios, change systematically over short vertical distances irrespective of “bulk” matrix FeO to MgO wt% ratios. The composition of chlorite and biotite is more likely controlled, primarily, by the composition and characteristics of a migrating fluid rather than bulk-rock composition. Relatively Mg-rich chlorite and biotite in high-grade copper zones suggests

that chlorite and biotite formed cogenetically with copper-sulphides. The physiochemical factor(s) responsible for this trend are difficult to determine, but it is possible that copper-sulphides competed with chlorite and biotite for iron during the copper-mineralising fluid event, resulting in relatively Fe-poor chlorite and biotite in mineralised zones. Although chalcocite is a copper-sulphide with no iron, it is commonly present in the same zone as hematite. A single generation of chlorite and biotite is suggested because chlorite and biotite composition are roughly homogeneous in a given sample.

The chlorite and biotite FeO and MgO wt% trend may be expressed laterally as well as vertically, but is poorly understood, as is lateral copper-sulphide zonation. Because muscovite does not follow the FeO and MgO wt% trend expressed by chlorite and biotite, muscovite probably formed separately from chlorite and biotite. Relatively elevated FeO and MgO wt% in muscovite suggests replacement of Fe- and Mg-rich minerals (e.g., chlorite, biotite, dolomite, and ferroan dolomite), whereas muscovite with lower FeO and MgO wt% may have formed from the breakdown and/or replacement of Fe-Mg-poor matrix material (e.g., quartz, K-feldspar, detrital muscovite). Muscovite MgO and FeO wt% heterogeneity may have resulted from alteration reactions that involved many different minerals.

2.6.2 *Matrix evolution and paragenesis*

The diamictite matrix changed significantly since sediment deposition. Its evolution can be summarised into five main paragenetic phases: sedimentation, diagenesis, main-ore,

post-ore, and tectonism (Fig. 42). The absolute timing and extent of the matrix evolution phases and transition from one to the next are still unclear, but the relative timing is now well established. The textural and compositional information used to develop the ore-zone matrix paragenesis is consistent in all drill-holes studied at the Kakula deposit.

2.6.2.1 *Sedimentation and source material*

Deposition by subaqueous debris flows is the essential first phase in the history of the diamictite and its matrix. Subaqueous debrites are generally textureless, yet subtle depositional microstructures, such as clast rotation, are known from modern diamictons (Guvard et al., 2016). In areas of non-aligned matrix, evidence of clast rotation is rare at Kakula, and such structures, when present, cannot be distinguished from diagenetically or tectonically induced clast rotation. Determining the original composition of the matrix is challenging, and so several different approaches were used in this study: comparing matrix composition to that of large diamictite clasts, and comparing ore-zone matrix to “least-altered” matrix for detrital minerals and bulk composition.

Detrital matrix minerals are distinguished from later mineral phases based on their rounded morphologies and the relatively large sizes of some components (e.g., quartz; Fig. 25). The clay- to fine-silt-sized matrix components cannot easily or assertively be identified as detrital because they are fine-grained and could have been altered relatively easily. However, the composition of large clasts (≥ 2 mm), although locally altered, is good proxy of the original matrix composition from sediment deposition (if not for the

relative proportions of its constituent minerals). In ore-zone matrix, the most abundant and identifiable detrital mineral is quartz, with less abundant K-feldspar and dolomite, and minor muscovite and chlorite. As was identified by Kennedy et al. (2018) for Kamoia, the large diamictite clasts at Kakula are composed predominantly of quartzite and altered mafic volcanic rock. Mafic minerals are generally more easily altered than minerals such as quartz. In least-altered matrix, the mafic material was altered to an assemblage of chlorite with less abundant biotite, ferroan dolomite, quartz, and Cu-sulphides in ore-zone matrix, and albite, chlorite, and a smaller volume of quartz, calcite or ferroan dolomite in least-altered matrix. Detrital albite, which is present only in least-altered matrix, and mafic and/or altered mafic minerals, must have been originally present in the initial sediment of the ore-zone matrix.

Although post-depositional alteration is evident in the matrix, it is not clear if the mafic detritus was altered prior to sediment deposition, or if it was deposited as primary mafic minerals, such as pyroxene and anorthite. Basalt, such as that from the mid-Atlantic ridge, can be quickly altered in active oceanic ridges by seawater at greenschist-facies temperatures (Humphris and Thompson, 1977). The mineralogical transformations during the alteration of basalt are the alteration of plagioclase (anorthite) to an assemblage of albite, chlorite, and epidote, and the alteration of pyroxene to chlorite, epidote, and actinolite. Quartz and pyrite are minor accessory minerals during the alteration process (Humphris and Thompson, 1977).

Whole-rock major and trace element results also support the presence of a mafic-derived sediment component. Trace elements are well suited for discrimination of provenance

because they generally have low mobility during sedimentary processes, and therefore represent the signature of source rock composition (Taylor and McLennan, 1985). The enrichment in TiO₂, Fe₂O₃, and MgO relative to the average silicic rock, whether in in least-altered and ore-zone matrix, suggests the presence of a mafic component. Any effects of post-depositional alteration can be dismissed, because the concentrations of these oxides are similar in both least-altered and ore-zone matrix. The TiO₂, Fe₂O₃, and MgO concentrations of least-altered and ore-zone matrix is comparable to the average continental crust, whose composition is said to be loosely derived from mixing of approximately equal parts of mafic and felsic igneous rock (Taylor, 1964).

The higher abundance of most trace elements is consistent with the upper crust and sediment, except for V and Cr (Taylor and McLennan, 1985; 1995; 2001; and McLennan and Murray, 1999). The elevated V and Cr concentrations in matrix relative to average sediment and upper crust is a strong indication of mafic source rock. Chromium is especially important, because the concentration of Cr is very similar in least-altered and ore-zone matrix and is especially elevated in mafic clasts and in samples of local mafic rock. Overall, the original composition of the matrix cannot currently be determined with certainty, but it is thought to have had an overwhelming component of fine-grained quartz and mafic (primarily pyroxene and anorthite) and/or altered-mafic (primarily chlorite, albite, epidote) minerals with relatively minor K-feldspar and carbonate minerals.

2.6.2.2 *Diagenesis*

The pre-ore, diagenetic phase of the matrix evolution predated deposition and main-ore hydrothermal alteration and copper mineralisation and spanned an unknown length of time. The matrix compositional and textural changes associated with diagenesis prior to hydrothermal mineralisation at Kakula are difficult to identify and interpret. It is also not clear why horizontal fabric from burial compaction is absent the diamictite matrix.

Although there is no obvious cement phase in the ore-zone matrix currently, cementation cannot be ruled out in the early history of the matrix, especially because some samples of least-altered matrix exhibit local “cementation”. Horizontal fabric development from burial compaction may have been hindered by early diagenetic cementation or regional overpressuring with elevated fluid pore pressures that exceed lithostatic pressure (Boggs, 2009; Ulmer-Scholle et al., 2014). It is also possible that hydrothermal mineralisation or late reorientation of matrix components during deformation obliterated any such evidence of an early horizontal fabric. Diagenesis is a complex mix of processes and brings significant physical (compaction and porosity loss) and compositional/mineralogical changes to sediment (Boggs, 2009). Generally, mudrock porosity and permeability decrease significantly and rapidly because of cementation and burial compaction (Boggs, 2009; Loucks et al., 2012), and so the absence of evidence of either compaction or cementation in the matrix is strange and possibly meaningful.

Few diagenetic studies have been conducted on diamictite. Diamictite diagenesis should resemble that of fine-grained sedimentary rocks more widely studied in oil and gas industry contexts. The only mineral that is comfortably assigned a diagenetic, pre-ore

origin at Kakula is framboidal pyrite (Fig. 42), but it is present only in least-altered matrix and in parts of ore-zone matrix where there are few to no copper-sulphides. Framboidal pyrite (Fig. 33a) is characteristically diagenetic and generally forms by bacterial sulphate reduction at low temperatures (Berner, 1970). Euhedral pyrite also forms during diagenesis (Berner, 1970), but it is not clear whether all pyrites with euhedral to subhedral morphology at Kakula are diagenetic, or if some formed during the copper-mineralising event. Diagenetic pyrite and ore-stage pyrite are common throughout much of the CACB (Cailteux et al., 2005; Hitzman et al., 2012; Muchez et al., 2015). In the study of Schmandt et al. (2013), the majority of pyrite, especially framboidal pyrite, was considered to be pre-ore and diagenetic, whereas some pyrite, more commonly euhedral, was given a hydrothermal origin. Minor dolomite, diagenetic quartz, and chlorite were speculatively considered by Schmandt et al (2013) to be diagenetic minerals based on what is common in mudrock diagenesis. Likewise, a diagenetic origin for small proportions of chlorite, quartz, K-feldspar, and dolomite cannot be discounted in this study.

During diagenesis of mudrock, precipitation of feldspar, quartz, and carbonate cements can form at virtually any stage, from early syn-sedimentary conditions to deep burial (Boggs, 2009; Ulmer-Scholle et al., 2014). Ferroan-dolomite rims on pure dolomite, which resemble those from Kakula (Fig. 26), have been recognised in mudstone diagenesis in marine sedimentary rocks. For example, ferroan dolomite overgrowths are common in the Midland basin's lower Permian Wolfcamp siliciclastic and calcareous mudstones in Texas (Wickard, 2016). Ferroan dolomite and other matrix mineral overgrowths appear to have formed after pyrite because the overgrowths locally enclose

or nucleate on pyrite. At Kakula, ferroan dolomite probably formed towards the end of the diagenetic phase (Fig. 42) because it is overgrown by other matrix minerals, such as chlorite, that are main-ore stage minerals. Although ferroan dolomite could also have had a partly hydrothermal origin because of dolomite's logical association with the magnesian alteration that is common in the CACB (Cailteux et al., 2005; Selley et al., 2005; Hitzman et al., 2012), textural relationships argue for an earlier origin.

2.6.2.3 *Main- and post-ore*

The main-ore phase is the most conspicuously expressed phase of the matrix in the ore-zone (Fig. 42). Main-ore phase hydrothermal minerals were identified based on compositional and textural relationships with copper-sulphides, and in some cases, the presence of minerals in ore-zone matrix but not in least-altered matrix. Textural and compositional relationships suggest that the matrix evolved under increasingly oxidised and acidic conditions during progressive hydrothermal alteration. Chlorite and biotite are considered main-ore phase (Fig. 42), and they may have formed from the replacement and/or recrystallisation of original detrital mafic (or altered mafic) material during hydrothermal alteration. Although some chlorite formation during diagenesis cannot be completely discounted, the homogeneous composition of chlorite in any given sample suggests one single generation of chlorite (Figs. 36, 37). Chlorite overlies ferroan-dolomite overgrowths (Figs. 26a, b), indicating that it formed after ferroan dolomite. As was already suggested by the relationship of MgO and FeO wt% of chlorite and biotite

with copper-grade, copper-sulphides are spatially associated with and intergrown with chlorite and biotite in the matrix (Fig. 28). Texturally, copper-sulphides are present in chlorite mineral cleavage (Figs. 28a, 28c). Although copper-sulphide mineralisation is associated with chlorite, it is not clear whether copper-sulphide formation outlasted the formation of chlorite (Fig. 42). Potassium feldspar also appears to have locally formed with chlorite (Fig. 27d) but also appears with quartz where K-feldspar overgrows biotite (Fig. 29c). Some quartz and K-feldspar may be products of hydrothermal alteration, but the timing and the extent are not as clear as in the case of chlorite (Fig. 42). The addition, or at least the preservation, of MgO and K₂O in ore-zone matrix during alteration probably took place during this main-ore phase, as indicated by compositional matrix data and the mineral assemblages, and relatively low K₂O content in least-altered matrix.

A major part of the main-ore phase involved the replacement of pre-ore diagenetic framboidal pyrite by copper-sulphides, as suggested by Schmandt et al. (2013), because (a) the ore-zone is devoid of pyrite, (b) copper-sulphides in the ore-zone have similar sizes and shapes as pyrite outside the ore-zone, and (c) there is textural evidence of copper-sulphide replacement of pyrite (Fig. 33c). Textural relationships indicate progressive copper enrichment of copper-sulphides as replacement of chalcopyrite by bornite and then by chalcocite (Fig. 34). Hematite generally post-dates copper-sulphides, especially chalcopyrite and bornite (Fig. 42), because it replaces and overgrows copper-sulphides and cross-cuts and contains inclusions of copper-sulphides (Fig. 34). Chalcocite is the most oxidised copper-sulphide species in the ore-zone, and its stratigraphic association with ore-stage hematite suggests that the matrix in the high-grade ore zones was significantly oxidised at Kakula during progressive hydrothermal mineralisation.

This is logical because reduced agents, such as diagenetic pyrite, would be consumed during protracted mineralisation. Notably, the replacement of chalcopyrite by bornite and by chalcocite releases significant sulphur, which can be used to produce more copper-sulphides. Because some copper-sulphides are present at the edges of matrix pores (Fig. 31), it is not clear if some copper-sulphides precipitated in pores or if some pores are secondary and formed by mineral dissolution.

Muscovite is considered to be hydrothermal because of its spatial limitation to ore-zone matrix and absence from least-altered matrix; moreover, muscovite is not a mineral that forms during conventional diagenesis. Muscovite may have started to form towards the end of the main-ore phase but formed primarily in the post-ore phase (Fig. 42), as the matrix was subjected to increasingly acidic conditions. Muscovite formation at the expense of feldspar has been attributed to acidic conditions at other deposits in the central African copperbelt (Selley et al., 2005; Hitzman et al., 2012). Acidic conditions could also result in dolomite dissolution. Muscovite is relatively late in the matrix paragenesis because it replaces chlorite along mineral cleavage (Fig. 30c), and commonly overgrows, replaces, and/or corrodes the edges of other matrix minerals such as quartz, K-feldspar, and dolomite (Figs. 29, 30). Additionally, the heterogeneous FeO and MgO wt% composition of muscovite (Figs. 36, 37), unlike chlorite and biotite, suggest that muscovite formed independently from chlorite and biotite formation. Given that muscovite is the most abundant matrix mineral in ore-zone matrix and its increasing abundance resulted in the decrease in abundance of the other matrix minerals, it is very important in the evolution of ore-zone matrix. Although the addition of K₂O may have been involved in the formation of muscovite, it is possible that there was enough K₂O

already present in the matrix prior to muscovite formation from minerals such as K-feldspar and biotite. The acidic conditions responsible for muscovite formation may have developed from H₂S generated by the release of sulphur during the breakdown and replacement of diagenetic pyrite and relatively sulphur-rich copper-sulphides such as bornite and chalcopyrite. This phenomenon has been proposed for other sedimentary-rock-hosted copper deposits in the CACB that contained a high abundance of pre-ore diagenetic pyrite (Hoy, 1989; Hitzman et al., 2005). However, muscovite is present in ore-zone matrix that does not contain copper-sulphides, which suggests that acidic conditions extended spatially beyond the sites containing copper-sulphides to a limited extent. Secondary porosity may have formed in ore-zone matrix during this time through dissolution (Fig. 30 a, 30b). This is also possibly supported by the least-altered matrix having relatively lower porosities than ore-zone matrix and a locally “cemented” appearance. Although there are no identifiable textural indications for the relative timing of the rutile that is present throughout the ore-zone matrix, some rutile may have formed through the hydrothermal breakdown of biotite. Some hematite may have also formed from the breakdown of iron-bearing minerals such as chlorite and biotite.

2.6.2.4 *Tectonism*

The formation of aligned matrix during tectonism appears to have been the most informative part of the post-ore phase. The textural and compositional changes in non-aligned matrix during this phase are hard to determine, but aligned fabric development is

an important part of the matrix evolution because it appears to have had an influence on localised compositional and textural changes (Figs. 17, 24). The timing between main- and post-ore phases and whether there is an interval of no change to the matrix is unclear. Not only were many of the matrix components locally aligned and stretched during fabric development, many of them (quartz, K-feldspar, dolomite, chlorite, biotite) seem to have been replaced or dissolved completely, suggesting they pre-date fabric development (Fig. 42). This phenomenon is also supported by the relatively high abundance of muscovite in aligned matrix versus non-aligned matrix (Fig. 24). Because there is a lower abundance of copper-sulphides and lower copper content measured in aligned versus non-aligned matrix (Figs. 24c, 39, 40), copper-sulphides are also thought to pre-date the formation of aligned matrix and were dissolved during the process. Copper-sulphide mineralisation prior to fabric development is also supported by the elongation or stretching of copper-sulphides in aligned matrix (Fig. 32) but not in non-aligned matrix (Fig. 31). Large copper-sulphide minerals are locally elongated parallel to fabric, in an example for Kamoā (Fig. 15b). Notably, fine-grained copper-sulphides are also tightly surrounded by muscovite crystals, especially in aligned matrix, and although it could not be determined with certainty, some appear to be enclosed by individual muscovite crystals (Fig. 32). Even though the interpreted origin of muscovite in the matrix is predominantly hydrothermal, the higher abundance of muscovite in aligned matrix than non-aligned matrix suggests a possible association between muscovite and fabric development. The higher abundance of muscovite in aligned matrix may be because of the recrystallisation and concentration of precursor hydrothermal muscovite when other minerals were being dissolved (Fig. 42). However, new muscovite growth would be considered relatively

minor because there is no muscovite in least-altered matrix, whether in aligned or non-aligned matrix. Although the ore-zone matrix has significant porosity (Fig. 31), aligned matrix development resulted in a relative decrease in porosity (Fig. 32). Overall, the abundance of matrix porosity suggests that the rock was not significantly metamorphosed. Even if some porosity formed through secondary processes, it would have happened prior to the development of aligned matrix.

2.6.3 *Matrix alignment origin*

Aligned matrix is interpreted as a tectonic fabric that formed through weak deformation during the Lufilian orogeny, some 150 to 200 m.y. after sediment deposition, as it was suggested by Twite (2016). Conversely, although aligned matrix at Kamoia was not a focus of Schmandt et al. (2013), it was interpreted to have formed via localised early-diagenetic fluid-escape because the aligned fabric was notably stronger and more pervasive in the ore-zone. Twite (2016) noted that the tectonic fabric has a regionally consistent orientation, is axial-planar to the gentle folding, and cross-cuts early synsedimentary features such as slump folds, microscopic normal faults, and bedding. Stronger matrix alignment expressed in the vicinity of large diamictite clasts was inferred to reflect areas of higher stress during weak deformation. Large clasts in the diamictite are unlikely to develop a tectonic fabric under weak deformation because they are generally more competent, have coarser constituent crystals, and generally contain few platy minerals as compared to matrix (Twite, 2016).

Least-altered diamictite matrix examined in this study contains little to no aligned matrix and a paucity of platy minerals such as muscovite. Under weak deformation conditions, fabric development would be poor to non-existent in areas containing few to no platy minerals. In ore-zone diamictite matrix, although quartz, chlorite, K-feldspar, dolomite, and biotite are less common in areas of aligned matrix than non-aligned matrix, when present, they are commonly elongated in the same orientation as muscovite crystals (Figs. 24, 32). The alignment of some elongated grains can be explained by the rotation of elongated grains to align themselves vertically and normal to the shortening direction during deformation. However, the high abundance of elongated grains in aligned matrix relative to non-aligned matrix suggests that the morphology of some matrix grains changed and was stretched during deformation. Pressure-solution along grain contacts was probably an important aspect of fabric development (Passchier and Trouw, 2005; Twite, 2016).

Aligned matrix has compositional differences from adjacent non-aligned matrix material. For example, a higher abundance of muscovite in aligned matrix than non-aligned matrix. Local compositional differences such as this are commonly documented in spaced foliations in low-grade metamorphic rocks (Passchier and Trouw, 2005). For example, tectonic fabric of the Ordovician to Early Carboniferous Dwyka diamictite matrix in South Africa formed during horizontal shortening during the development of the late Paleozoic Cape fold belt under relatively low-temperature sub-greenschist metamorphic conditions (Fagereng, 2014). The Dwyka diamictite matrix is dominated by quartz and feldspar, with minor chlorite and muscovite. The fabric is vertically oriented and is defined in plane-polarised light as being relatively phyllosilicate-rich and containing

dark, insoluble material. Pressure-solution was interpreted to be the main process in fabric development, producing localised dissolution and removal of relatively mobile elements and concentration of relatively immobile elements. Compositionally, electron backscatter images revealed that the fabric had relatively low Si concentrations, and relatively high K, Al, Fe, and Ti concentrations (Fagereng, 2014). The appearance and compositional characteristics of the fabric described in the Dwyka diamictite matrix resembles many of the characteristics of aligned matrix at Kamoia and Kakula.

2.7 Discussion

The effects of alteration coupled with the fine-grained nature of the diamictite matrix make it difficult to distinguish detrital versus early-diagenetic components and to evaluate the later possible effect of upper-diagenetic to subgreenschist regional metamorphism during the Lufilian orogeny. Diagenesis has many definitions; it can be considered all changes occurring in the process of sedimentary rock lithification in temperature and pressure conditions below metamorphism (Boggs, 2009). The diagenesis to metamorphic boundary is not well defined and is generally arbitrary and subjective, but it is commonly placed at 200 to 250 °C and less than 5 kb (Robb, 2005; Boggs, 2009). Fluid inclusion data of Schmandt et al. (2013) at Kamoa from syn-copper-mineralisation ankerite yielded an approximate temperature of 225°C. However, no other geothermometry work has been conducted for Kamoa or Kakula to date. Hydrothermal alteration can take place under a range of temperatures, and can trigger diagenetic or metamorphic reactions (Robb, 2005).

2.7.1 *Influence of matrix on mineralisation*

The proposed precipitation mechanism of copper-sulphides in sedimentary-rock-hosted copper deposits, such as Kamoa and Kakula, is by the interaction of an oxidised copper-bearing fluid with reduced stratigraphic units (Kirkham, 1989; Hitzman et al., 2005; 2010). For mineralised fluids to enter the reduced grand conglomérat, the distance from

fluid conduits, such as synsedimentary normal faults, would be a crucial first-order control on copper-grade distribution. The vertical distance above the redox interface is also important because copper precipitates in the lowest reduced units that the fluid encounters. However, copper-sulphide distribution is stratiform and preferentially disposed in certain stratigraphic units, especially clast-poor diamictite (and siltstone) units rather than clast-rich diamictite. This phenomenon leads to complex copper-grade profiles. Matrix characteristics are, therefore, probably important secondary, localised controls on mineralisation. A few factors are probably intricately related on a micro-scale, such as texture (grain-size, porosity, permeability) and composition, especially the abundance of reactive agents such as diagenetic pyrite.

The stratigraphic abundance of diagenetic pyrite prior to copper mineralisation is thought to have been critical to the precipitation of copper-sulphides. Diagenetic pyrite has been identified as an essential chemical trap for copper-sulphide precipitation (Hitzman et al., 2005; 2010). Pyrite was considered to be the primary reactive agent at Kamo a by Schmandt et al. (2013) based on its apparent replacement by copper-sulphides, lack of pyrite in the ore-zone, and similar sulphur isotope values in pyrite and copper-sulphide minerals. It is not clear whether diagenetic pyrite was the only reducing agent at Kamo a and Kakula or if organic matter and/or H₂S were also involved in copper-sulphide precipitation. The reason(s) behind original pyrite and/or other reactive agent concentrations not currently understood. However, the availability of organic matter to be metabolised by sulphate-reducing bacteria is a crucial factor in the formation of diagenetic pyrite (Berner, 1970). It appears that the clast-rich diamictite units were not as reduced as the clast-poor diamictite units.

Although there is a full spectrum of clay- to silt-sized particles in the matrix, and the average grain-size of ore-zone matrix does not vary much among samples, the percentage of sand and larger clasts does vary. Many large clasts (≥ 2 mm) and sand-sized clasts are quartz-rich, making them chemically resistant and not commonly replaced by copper-sulphides. The higher percentage of large clasts and sand in clast-rich diamictite as compared to clast-poor diamictite is mirrored by a relatively lower percentage of matrix, and therefore, a lower percentage of the rock that can be easily mineralised. Although some large clasts did get replaced, commonly along their edges, much of the copper mineralisation is in the matrix. The percentage estimations illustrate the relationship among higher matrix percentage and higher copper grade for Kamoia and Kakula (Table 2). The siltstone sample (KAK1012_3.5) had the highest copper-grade, the finest grain-size on average, and contains only rare sand-sized clasts.

Porosity and permeability are also important to consider because these characteristics influence fluid-rock interactions and the ability of copper-bearing fluids to flow. The porosity in mudrock is a topic of much research because its connectivity defines permeability, an important implication for gas flow in unconventional mudrock hydrocarbon reservoirs. Mudrock lithification and its influence on porosity is complicated by the overlapping influences of mineralogy, rate and depth of burial compaction, texture, cementation, and fluid compositions (Loucks et al., 2012). The presence of copper-sulphides locally at the margins of matrix pores highlights the importance of porosity at Kakula and Kamoia. Moreover, H_2S could have been an important reducing agent occupying porosity, whether in primary or secondary porosity. Because the matrix underwent alteration-related compositional and textural changes, it is

difficult to distinguish between primary depositional pores and pores associated with secondary processes (dissolution or mineralogical changes). It is also difficult to determine the matrix permeability because pores form intricate networks in three dimensions, a phenomenon that was beyond the scope of this study to investigate. Collectively, the variation in matrix texture (grain-size and porosity) and abundance of reducing agents are thought to have been important controls on copper mineralisation up-section in different units above the Mwashya-“grand-conglomérat” contact, but also laterally between high- and low-grade copper zones.

2.7.2 *Kamoa and Kakula comparison*

The paragenesis developed by Schmandt et al. (2013) for Kamoa relied heavily on large clast rims and caps rather than fine-grained matrix, yet the paragenesis of large clast rims does not necessarily mimic matrix paragenesis. The study of fine-grained matrix by Schmandt et al. (2013) was limited to the petrographic microscope and QEMSCAN. In Schmandt et al. (2013), muscovite, quartz, K-feldspar, ankerite, and biotite were all considered to be syn-mineralisation hydrothermal minerals. Chlorite was considered late relative to copper-mineralisation because chlorite was shown to be limited to outsides of larger clast mineral rims. Although ankerite was not identified in the current study at Kamoa or Kakula, ferroan dolomite versus ankerite terminology is commonly confused because definitions vary, and the terms are sometimes used interchangeably (Ulmer-Scholle et al., 2014). The paragenetically late position of chlorite relative to copper-

sulphide mineralisation in Schmandt et al. (2013) is different from the paragenesis identified in the current study, in which chlorite is considered to be syn-mineralisation and relatively early in the paragenesis. Although the current study focussed primarily on Kakula, comparison between ore-zone matrix characteristics at Kamoia and Kakula yielded similar textural and compositional characteristics: similarities were drawn for mineral abundances, mineral composition composition, “bulk” non-aligned and aligned matrix composition, and the textural relationships among matrix minerals. The abundance of matrix biotite is low at Kakula and Kamoia, but Kakula may have more biotite than Kamoia, suggesting that Kakula may have been subject to slightly higher temperatures than Kamoia. The main mineralogical difference between the two deposits is expressed in the abundance of copper-sulphide mineral species and the higher abundance of hematite at Kakula (locally as distinctly maroon-coloured matrix). Although large mineral caps and rims at both Kamoia and Kakula were not a focus of this study, copper-sulphide caps and rims on clasts at Kakula are generally smaller than those at Kamoia. The generally higher grade at Kakula versus Kamoia is mainly conferred by the higher abundance of the relatively copper-rich copper-sulphide, chalcocite. One of many possibilities for the abundance of chalcocite is a higher degree of copper input into the matrix. Also, chalcocite and hematite are more oxidised than chalcopyrite and bornite, and their higher abundance at Kakula than at Kamoia suggests that the host-rock was subject to a higher degree of oxidation by the mineralising fluid. Considering this, it is possible that the copper-mineralising fluid event did not last as long at Kamoia as at Kakula, that it was not as intense, or that the fluid was less oxidised or more effectively buffered by the host

rocks at Kamoia. Perhaps the original copper “source” was closer to the Kakula deposit than the Kamoia deposit.

2.7.3 *Other deposits*

Similarities can be drawn between Kamoia-Kakula and other deposits in the central African copperbelt. For example, the Kashime (Fishtie) deposit in Zambia has significantly lower grade and tonnage than Kamoia and Kakula, but is hosted in the same rock unit (grand conglomérat) and has a similar composition and mineralisation style as Kamoia and Kakula. For example, copper mineralisation is predominantly fine-grained and disseminated in diamictite and siltstone. Although fine-grained diamictite matrix analysis in the study of Hendrickson (2015) for Kashime was limited to optical petrography and QEMSCAN, as in Schmandt et al. (2013) for Kamoia, many aspects of the mineral paragenesis resemble that established for Kakula in the present study. As at Kakula, chlorite, biotite, and muscovite at Kashime were interpreted as hydrothermal minerals. Dolomite was relatively early at Kashime, and chlorite was found to have the closest temporal and spatial association with copper-sulphides (Hendrickson, 2015). The association of chlorite with copper-sulphides at Kakula was identified by textural relationships and compositional trends, yet at Kashime it was identified by textural relationships but mostly by the higher abundance of chlorite in high-grade copper zones. Potassium feldspar at Kashime is locally intergrown with copper-sulphides and formed at the same time as muscovite, which formed prior to most of the copper-sulphide minerals and chlorite (Hendrickson, 2015). At Kakula, most muscovite formed late relative to

chlorite and copper-sulphide minerals. At a larger scale, the chlorite zone at Kashime is localised to areas containing copper-sulphides, whereas muscovite is more widespread (Hendrickson, 2015). This is the opposite of what was identified by Schmandt et al. (2013) for Kamoia, and in this study for Kakula. At Kakula, muscovite is limited to the ore-zone matrix, whereas chlorite is more widespread and extends into least-altered matrix.

Copper-sulphide mineralisation at the Shanika syncline, in the Tenke Fungurume mining district in DRC, is also hosted by the grand conglomérat, but this area is significantly deformed and mineralisation is of a different style. In the Shanika syncline, subordinate disseminated mineralisation in diamictite, sandstone, and siltstone host-rock was identified, but the majority of the mineralisation is hosted by dolomite-chlorite veins. Potassic alteration was evident as K-feldspar, but is interpreted to be relatively early because it is cross-cut by the mineralised veins (Mambwe et al., 2017). Magnesian and potassic alteration is commonly identified in the Congolese and Zambian copperbelts, and is almost always attributed to the passage of evaporite-sourced brines (Selley et al., 2005; El Desouky et al., 2009; Hitzman et al., 2012; Selley et al., 2018). Magnesian alteration (chlorite, dolomite) is widespread in the Congolese copperbelt and commonly associated with copper mineralisation in the Mines subgroup (Cailteux et al., 2005; El Desouky et al., 2009; Hitzman, 2012; Fay and Barton, 2012). Moreover, in the Kolwezi area, DRC, just 25 km east of the Kamoia and Kakula deposits, copper-sulphide mineralisation is broadly associated with chlorite (Muechez et al., 2010; Hitzman et al., 2012). Potassic alteration is widespread and associated with copper-sulphide mineralisation in the Zambian copperbelt (Hitzman et al., 2012; Selley et al., 2018).

Overall, alteration in the CACB is commonly regional and cannot be used as an effective vector for ore (Hitzman et al., 2012; Selley et al., 2018). The current study indicates localised potassic and magnesian alteration at Kamoia/Kakula; there may be a temporal overlap between the two, as suggested by the matrix paragenesis. Because dolomite and chlorite are early in the Kakula matrix paragenesis and muscovite is relatively late, the bulk of potassic alteration may have been relatively late or outlasted magnesian alteration. However, muscovite formation may have been derived from K-feldspar that formed previously. The area at Kakula containing albite (“least-altered” matrix) may represent an outer sodic alteration halo to the deposit. Sodic alteration is common in the Mwashya subgroup and lower Nguba Group in Zambia (Hitzman et al., 2012). Because many deposits in the Congolese copperbelt are deformed and metamorphosed, the Kamoia and Kakula deposits more closely resemble deposits of the Zambian copperbelt, but the association of copper mineralisation with chlorite bears more similarities to the bulk of the deposits nearby in the Congolese copperbelt.

2.7.4 *Timing of mineralisation*

The timing of mineralisation remains controversial at Kamoia and Kakula, as it is for much of the CACB as a whole. In the CACB, syn-sedimentary, early- to late-diagenetic, (Selley et al., 2005; Cailteux et al., 2005; Hitzman et al., 2012), syn- to post-orogenic origins (El Desouky et al., 2009; Sillitoe et al., 2017, Santilian et al., 2018), and remobilisation (Haest and Muchez, 2011; Turlin et al., 2016) have been proposed based on a combination of structural, textural, isotopic, and geochronological approaches.

Although a distinct and narrow mineralisation window may be the case for some deposits, others may have experienced repeated episodes of mineralisation and/or remobilisation (Dewaele et al., 2006; Selley et al., 2005; Hitzman et al., 2012; Selley et al., 2018). Some have suggested that the CACB as whole probably formed over a 400-million-year span and through multiple phases (Haest and Muchez, 2011; Hitzman et al., 2012). However, the narrow distribution of sulphur isotope values at Kamoia is consistent with one large single-stage copper mineralising event (Schmandt et al., 2013).

It was suggested by Schmandt et al. (2013) that mineralisation was relatively early at Kamoia because of the fine-grained, disseminated nature of the copper-sulphides and the paucity of mineralised veins. It was even posited that the sediment may have been unlithified, and although this is possible, a study at the Coates Lake deposit, Redstone Copperbelt, Canada, shows that copper mineralising fluids can infiltrate and form pervasive stratiform and disseminated mineralisation in rocks deposited over 100 m.y. earlier (Milton et al., 2017). Mineralisation at the Coates Lake deposit was dated at 635 ± 13 Ma by U-Pb dating on monazite overgrowths cogenetic with copper mineralisation. Strata hosting the Redstone copperbelt include diamictite of the Sayunei Formation (Rapitan Group), which has a similar depositional age to that of the grand conglomerat (<711 Ma; U/Pb detrital zircon age; Baldwin et al., 2016).

The identification of some copper-sulphides in the current study at the margins of pores complicates the interpretation of the relative timing of mineralisation. For the copper-sulphides present in matrix pores, some may have precipitated directly in pores, whereas some of the porosity may be secondary and formed relatively late; it has not been

possible to distinguish depositional from secondary pores using any approach applied in this study. Contrarily to the study of Schmandt et al. (2013), relatively late Lufilian timing for the bulk of the copper mineralisation at Kamoia was suggested Twite (2016), who focussed on structural controls on mineralisation, copper-sulphide caps on clasts, and the local elongation of copper sulphides parallel to tectonic fabric. It is important to note, for that study, that samples were purposely sampled in and around faults. It was interpreted by Twite (2016) that the aligned, elongated copper sulphide minerals in the matrix were emplaced (not merely deformed or remobilised) during the formation of the tectonic fabric during the Lufilian orogeny. The alignment and elongation of copper-sulphide minerals in the matrix is interpreted differently in the present study than it was by Twite (2016): the alignment and elongation of copper-sulphide minerals and lower abundance of copper in aligned matrix suggests that the copper mineralising event predated fabric development of the Lufilian orogeny. Although direct textural evidence of copper remobilisation could not be identified in the present study, the possibility of some copper-sulphide remobilisation during fabric development is granted by the lower abundance of copper-sulphides both documented visually and calculated in aligned versus non-aligned matrix.

Although the study by Twite (2016) proposed a Lufilian-aged mineralising event, that study also identified a synsedimentary normal fault, the Mupaka fault, associated with areas of relatively high copper grade (Twite, 2016; Twite et al., 2019). The association of the structures with high copper grade does not necessarily specify a time of mineralisation, but there is a common association between relatively early copper orebodies and synsedimentary normal faults in the Zambian copperbelt (Selley et al.,

2005; Hitzman et al., 2012). Synsedimentary faults can be reactivated during later deformation, but no evidence was presented in the studies of Twite (2016) and Twite et al. (2019) to suggest this happened. Nonetheless, the identification of synsedimentary normal faults at Kamoā accentuates the importance of extensional faulting for the localisation of copper ore bodies.

2.8 Summary

Textural and compositional analysis of the ore-hosting diamictite matrix of the world-class Kakula copper deposit shows that least-altered diamictite matrix was originally derived from quartzose metasedimentary rock and altered mafic rock; although only some original matrix is preserved, it probably consisted of quartz, albite, K-feldspar, chlorite, and minor carbonate minerals (dolomite, calcite), muscovite, and biotite in a textureless arrangement. It is unclear whether material derived from mafic sources was already altered at the time of sedimentation. Diagenesis at an uncertain time produced diverse effects on matrix texture and minerals, such as overgrowth of Fe-dolomite on dolomite, diagenetic pyrite formation, and possible cementation between matrix grains by quartz, but no compaction-related texture is present. The main ore-forming event caused precipitation of copper-sulphides in the lowermost reduced units during upwards migration of an oxidised, copper-rich fluid. Ore-stage hematite also formed, locally with bladed morphologies, primarily in association with chalcocite. Chlorite (and minor biotite) precipitation, or at least recrystallisation, was temporally and texturally associated with mineralisation. Chlorite and biotite are hydrothermal minerals that have roughly homogenous composition in a given sample and their quickly-changing MgO and FeO ratios up-section according to copper grade, and irrespective of roughly consistent MgO and FeO bulk matrix composition. The fluid, which was oxidised enough to form chalcocite and hematite, was also locally acidic, probably because of diagenetic pyrite replacement and progressive copper-sulphide mineralisation. The interaction of the acidic fluid with minerals (e.g., quartz, albite, chlorite, biotite, K-feldspar, dolomite) in the ore-zone resulted in the formation of muscovite and possibly the formation of secondary

porosity. Potassium was either recycled from the breakdown of K-feldspar and biotite, or it was added by the fluid during muscovite formation. Tectonism (the presumed Lufilian event) produced faint, microscopic alignment of elongate matrix minerals along the sides of diamictite clasts >2 mm in diameter, but not at their tops or bases, probably through pressure-solution and reprecipitation under a subtle regional Lufilian stress field.

Development of mineral alignment is associated with lowered copper-sulphide content in ore-zone areas of aligned matrix versus ore-zone areas of textureless matrix, indicating that the ore-forming event took place prior to Lufilian deformation, but that ore minerals could have been remobilised by Lufilian deformation. It is possible that the ore sulphides that were pressure-solved in the immediate vicinity of diamictite clasts during the Lufilian event contributed to the development of the sulphide 'caps' that are the hallmark macroscopic characteristic of ore in the Kamo-a-Kakula district.

2.9 References

- Armstrong, R. A., Master, S., Robb, L. J., 2005. Geochronology of the Nchanga Granite, and constraints on the maximum age of the Katanga Supergroup, Zambian Copperbelt. *Journal of African Earth Sciences*, 42, p. 32 – 40.
- Baldwin, G. J., Turner, E. C., and Kamber, B. S., 2016. Tectonic controls on distribution and stratigraphy of the Cryogenian Rapitan iron formation, northwestern Canada. *Precambrian Research*, 278, p. 303 - 322.
- Batumike, M. J., Kampunzu, A. B., and Cailteux, J., 2006. Petrology and Geochemistry of the Neoproterozoic Nguba and Kundelungu Groups, Katangan Supergroup, Southeast Congo. Implications for Provenance, Paleoweathering and Geotectonic Setting. *Journal of African Earth Sciences*, 44, p. 97–115.
- Batumike, M. J., Cailteux, J., and Kampunzu, A. B., 2007. Lithostratigraphy, base metal deposits, and regional correlations of the Neoproterozoic Nguba and Kundelungu rock successions, Central African Copperbelt. *Gondwana Research*, 11 (3), p. 432-447.
- Berner, R. A., 1970. Sedimentary Pyrite Formation. *American Journal of Science*, 268, p.1–23.
- Boggs, S., 2009. *Petrology of Sedimentary Rocks*. Second Edition. United States of America Cambridge University Press, New York. 612 pages.
- Broughton, D. W., and Rogers, T., 2010. Discovery of the Kamao Copper Deposit, Central African Copperbelt, D.R.C. *Society of Economic Geologists, Special Publication 15*, p. 287–297.
- Broughton, D., Hitzman, M., and Stephens, A. J., 2002. Exploration history and geology of the Kansanshi Cu-(Au) deposit, Zambia. *Society of Economic Geologists, Special Publication*, 9, p. 141-153.

- Cailteux, J., 1994. Lithostratigraphy of the Neoproterozoic Shaba-Type (Zaire) Roan Supergroup and Metallogenesis of Associated Stratiform Mineralization. *Journal of African Earth Sciences*, 19 (4), p. 279–301.
- Cailteux, J., and De Putter, T., 2019. The Neoproterozoic Katanga Supergroup (D. R. Congo): State-of-the-art and revisions of the lithostratigraphy, sedimentary basin and geodynamic evolution. *Journal of African Earth Sciences*, 150, p. 522-531.
- Cailteux, J., Kampunzu, A. B., and Lerouge, C., 2007. The Neoproterozoic Mwashya-Kansuki Sedimentary Rock Succession in the Central African Copperbelt, Its Cu-Co Mineralisation, and Regional Correlations. *Gondwana Research*, 11 (3), p. 414–431.
- Cailteux, J., Kampunzu, A.B., Lerouge, C., Kaputo, A.K., Milesi, J.P., 2005. Genesis of sediment-hosted stratiform copper–cobalt deposits, central African Copperbelt. *Journal of African Earth Sciences*, 42 (1-5), p. 134–158.
- Cosi, M., De Bonis, A., Gosso, G., Hunziker, J., Martinotti, G., Moratto, S., Robert, J.P. and Ruhlman, F., 1992. Late Proterozoic thrust tectonics, high-pressure metamorphism and uranium mineralization in the Domes area, Lufilian Arc, northwest Zambia. *Precambrian Research*, 58, p. 215-240.
- Dewaele, S., Muchez, Ph., Vets, J., Fernandez-Alonzo, M., Tack, L., 2006. Multiphase origin of the Cu–Co ore deposits in the western part of the Lufilian fold-and-thrust belt, Katanga (Democratic Republic of Congo). *Journal of African Earth Sciences*, 46, p. 455–469.
- El Desouky, H.A., Muchez, P., and Cailteux, J., 2009. Two Cu-Co phases and contrasting fluid systems in the Katanga Copperbelt, Democratic Republic of Congo. *Ore Geology Reviews*, 36, p. 315–332.
- El Desouky, H. A., Muchez, Ph., Boyce, A., Schneider, J., Cailteux, J., Dewaele, S., Von Quadt, A., 2010. Genesis of sediment-hosted stratiform copper-cobalt mineralization at Luiswishi and Kamoto, Katanga Copperbelt (Democratic Republic of Congo). *Mineral Deposita*, 45, p. 735–763.

- Fagereng, A., 2014. Significant shortening by pressure solution creep in the Dwyka diamictite, Cape Fold Belt, South African Journal of African Earth Sciences, 97, p. 9-18.
- Fay, I., Barton, M., 2012. Alteration and ore distribution in the Proterozoic Mines Series, Tenke Fungurume Cu–Co district, Democratic Republic of Congo. Mineralium Deposita, 47, p. 501-519.
- François, A., 1993. The tectonic structure of the Katanguien in the area of Kolwezi (Shaba, Zaire). Annales de la Société Géologique de Belgique, p. 87–104.
- Gromet, L.P, Dymek, R.F, Haskin, L.A, and Korotev, R.L. 1984. The “North American shale composite”: its compilation, major and trace element characteristics. Geochimica et Cosmochimica Acta, 48, p 2469 – 2482.
- Guyard, H., Francus, P., St-Onge, G., Hausmann, S., and Pienitz, R., 2014. Microfacies and microstructures of subglacial and deglacial sediments from the Pingualuit Crater Lake (Ungava Peninsula, Canada). Canadian Journal of Earth Sciences, 51, p. 1084–1096.
- Haest, M., and Muchez, P., 2011. Stratiform and vein-type deposits in the Pan-African Orogeny in Central and Southern Africa. Evidence for multiphase mineralization. Geologica Belgica, 14, p. 23-44.
- Hanson, R.E., Wardlaw, M.S., Wilson, T.J., and Mwale, G., 1993. U-Pb zircon ages from the Hook granite massif and Mwembeshi dislocation: Constraints on Pan-African deformation, plutonism and transcurrent shearing in central Zambia. Precambrian Research, 63, p. 189–209.
- Hendrickson, M. D., 2015. Geology of the Fishtie Deposit, Central Province, Zambia: Iron Oxide and Copper Mineralization in Nguba Group Metasedimentary Rocks. Mineralium Deposita, 50, p. 717–37.
- Hitzman, M., Selley, D., and Bull, S., 2010. Formation of Sedimentary Rock-Hosted Stratiform Copper Deposits through Earth History. Economic Geology, 105, p. 627–639.

- Hitzman, M., Kirkham, D., Broughton, D., Thorson, J., and Selley, D., 2005. The Sediment-Hosted Stratiform Copper Ore System. *Economic Geology* 100th Anniversary, p. 609–642.
- Hitzman, M., Broughton, D., Selley, D., Woodhead, J., Wood, D., and Bull, S., 2012. The Central African Copperbelt: Diverse stratigraphic, structural, and temporal settings in the world's largest sedimentary copper district: *Society of Economic Geologists Special Publication*, 16. p. 487–514.
- Hoy, L. D., 1989. Geochemical investigations of the redbed-associated stratiform copper mineralization at Kamoto Principal (Central African Copperbelt), Zaire. Unpublished PhD thesis, University Park, Pennsylvania State University.
- Humphris, S.E., Thompson, G., 1978. Hydrothermal alteration of oceanic basalts by seawater. *Geochimica et Cosmochimica Acta*, 42, p. 107 – 125.
- Jackson, M. P., Warin, A., Woad, G. M., and Hudec, M. R., 2003. Neoproterozoic Allochthonous Salt Tectonics during the Lufilian Orogeny in the Katangan Copperbelt, Central Africa. *Bulletin of the Geological Society of America*, 115, p. 314–330.
- John, T., Schenk, V., Mezger, K., Tembo, F., 2004. Timing and P–T evolution of whiteschist metamorphism in the Lufilian arc- Zambezi belt orogen (Zambia): Implication for the assembly of Gondwana. *The Journal of Geology*, 112, p. 71–90.
- Kampunzu, A. B., Kapenda, D., and Manteka, B., 1991. Basic magmatism and geotectonic evolution of the Pan African belt in Central Africa: Evidence from the Katanga and West Congolian segments. *Tectonophysics*, 90, p. 363– 371.
- Kampunzu, A. B., Kanika, M., Kapenda, D., Tshimanga, K., 1993. Geochemistry and geotectonic evolution of late Proterozoic Katangan basic rocks from the Kibambale in central Shaba (Congo). *Geologische Rundschau*, 82 (4), p. 619–630.
- Kampunzu, A. B., Tembo, F., Matheis, G., Kapenda, D., Huntsman-Mapila, P., 2000. Geochemistry and tectonic setting of mafic igneous units in the Neoproterozoic

- Katangan Basin, Central Africa: implications for Rodinia break-up. *Gondwana Research*, 3, p. 125–153.
- Kennedy, K., Eyles, N., Broughton, D., 2018. Basinal setting and origin of thick (1.8 km) mass-flow dominated Grand Conglomérat diamictites, Kamao, Democratic Republic of Congo: Resolving climate and tectonic controls during Neoproterozoic glaciations. *Sedimentology*, 66 (2).
- Key, R. M., Liyungu, A. K., Njamu, F. M., Somwe, V., Banda, J., Mosley, P. N., Armstrong, R. A., 2001. The western arm of the Lufilian Arc in NW Zambia and its potential for copper mineralization. *Journal of African Earth Sciences*, 33, p. 503–528.
- Kirkham, R.V., 1989. Distribution, Setting, and Genesis of Sediment-hosted Stratiform Copper Deposits in Boyle. R.W., Brown. A.C., Jefferson, C.W., Howett, E.C. and Kirkham, R.V. *Sediment-hosted Stratiform Copper Deposits. Geological Association of Canada, Special Paper 36*, p. 3-38.
- Kokonyangi, J.W., Kampunzu, A.B., Armstrong, R., Yoshida, M., Okudaira, T., Arima, M., and Ngulube, D.A., 2006. The Mesoproterozoic Kibaride Belt (Katanga, SE D.R. Congo). *Journal of African Earth Sciences*, 46, p. 1 – 35.
- Kretz, R., 1983. Symbols for rock-forming minerals. *American Mineralogist*, 68, p. 277 – 279.
- Loucks, R.G, Reed, R.M., Ruppel, S. C., and Hammes, U., 2012. Spectrum of Pore Types and Networks in Mudrocks and a Descriptive Classification for Matrix-Related Mudrock Pores. *AAPG Bulletin* 96, p. 1071–1098.
- Mambwe, P., Milan, L., Batumike, J., Lavoie, S., Jébrak, M., Kipata, L., Chabu, M., Mulongo, S., Lubala, T., Delvaux, D., and Muchez, P., 2017. Lithology, petrography and Cu occurrence of the Neoproterozoic glacial Mwale Formation at the Shanika Syncline (Tenke Fungurume, Congo Copperbelt; Democratic Republic of Congo. *Journal of African Earth Sciences*, 129, p. 898 – 909.

- Master, S., and Wendorff, M., 2011. Neoproterozoic glaciogenic diamictites of the Katanga Supergroup, Central Africa. *Geological Society of London*, 36. p. 173 – 184.
- Master, S., Rainaud, C., Armstrong, R. A., Phillips, D., and Robb, L. J., 2005. Provenance Ages of the Neoproterozoic Katanga Supergroup (Central African Copperbelt), with Implications for Basin Evolution. *Journal of African Earth Sciences*, 42, p. 41–60.
- McLennan, S.M., and Murray, R.W., 1999. *Geochemistry of Sediments*. In: Marshall, C.P. and Fairbridge, R.W. *Encyclopedia of geochemistry*. 714 pages.
- Milton, J. E., Hickey, K. A., Gleeson, S.A., Falek, H., and Allaz, J., 2017. In Situ Monazite Dating of Sediment-Hosted Stratiform Copper Mineralization in the Redstone Copper Belt, Northwest Territories, Canada: Cupriferous Fluid Flow Late in the Evolution of a Neoproterozoic Sedimentary Basin. *Economic Geology*, 112, p. 1773–1806.
- Muchez, P., André-Mayer, A.S., El Desouky, A. H., Reisberg, L., 2015. Diagenetic origin of the stratiform Cu–Co deposit at Kamoto in the Central African Copperbelt. *Mineralium Deposita*, 50, p. 437 – 447.
- OreWin Pty Ltd., Amec Foster Wheeler E&C Services Inc. and Amec Foster Wheeler Australia Pty Ltd (collectively Amec Foster Wheeler), MDM (Technical) Africa Pty Ltd (MDM), Stantec Consulting International LLC (Stantec Consulting), and SRK Consulting (South Africa) Pty Ltd (SRK)., 2018. Kamoia-Kakula Project Resource Update. Prepared for Ivanhoe Mines Ltd., Mar 8, 2018, 617 pages.
- Pakiser, L.C., and Robinson, R., 1967. Composition of the continental crust as estimated from seismic observations. In Steinhart, J.S. and Smith, T.J., 2013. *The earth beneath the continents*. *Geophysical Monograph Series*, 10, p. 620-626.
- Passchier, C. W., Trouw, R. A. J., 2005. *Microtectonics*. Second Edition, Springer Verlag, Berlin, 371 pages.
- Rainaud, C., Master, S., Armstrong, R. A., and Robb, L. J., 2005. Geochronology and Nature of the Palaeoproterozoic Basement in the Central African Copperbelt

- (Zambia and the Democratic Republic of Congo), with Regional Implications. *Journal of African Earth Sciences*, 42, p.1–31.
- Robb, L. J., 2005. *Introduction to Ore-Forming Processes*. Blackwell Publishing, 386 pages.
- Rooney, A. D., Strauss, J. V., Brandon, A. D. and Macdonald, F. A., 2015. A Cryogenian chronology: Two long-lasting synchronous Neoproterozoic glaciations. *Geology*, 43 (5) p. 459 – 462.
- Saintilan, N. J., Selby, D., Creaser, R. A., and Dewaele, S., 2018. Sulphide Re-Os geochronology links orogenesis, salt and Cu-Co ores in the Central African Copperbelt. *Scientific Reports* 8, 14946. 8 pages.
- Sillitoe, R. H., Perelló, J., Creaser, R. A., Wilton, J., Wilson, A. L., and Dawborn, T., 2017. Age of the Zambian Copperbelt. *Mineralium Deposita*, 52, p. 1245 – 1268.
- Schermerhorn, L. J. G., 1974. Late Precambrian mixites: Glacial and/or nonglacial? *American Journal of Science*, 274, p. 673–824.
- Schmandt, D., Broughton, D., Hitzman, M., Bjorklund, P. P., and Edwards, D., 2013. The Kamao Copper Deposit, Democratic Republic of Congo: Stratigraphy, Diagenetic and Hydrothermal Alteration, and Mineralization. *Economic Geology*, 108, p. 1301–1324.
- Selley, D., Broughton, D., Scott, R., Hitzman, M., Bull, S.W., Large, R.R., McGoldrick, P.J., Croaker, M., Pollington, N., and Barra, F., 2005. A new look at the geology of the Zambian Copperbelt. *Economic Geology*. 100th Anniversary Volume, p. 965 – 1000.
- Steven, N., and Armstrong, R., 2003. A metamorphosed Proterozoic carbonaceous shale-hosted Co-Ni-Cu deposit at Kalumbila, Kabompo dome: The Copperbelt Ore Shale in northwestern Zambia. *Economic Geology*, 98, p. 893–909.
- Taylor, S.R., 1964. Abundance of chemical elements in the continental crust: a new table. *Geochimica et Cosmochimica Acta*, 28, p. 1273 – 1285.

- Taylor, S.R. and McLennan, S.M., 1985. "The Continental Crust: Its Composition and Evolution," Blackwell, Oxford, 312 pages.
- Taylor, S.R. and McLennan, S.M., 1995. The geochemical evolution of the continental crust. *Reviews of Geophysics*, 33, p 241 – 265.
- Taylor, S.R. and McLennan, S.M., 2001. Chemical composition and element distribution in the Earth's crust. Unknown publisher, p. 697 – 719.
- Turlin, F., Eglinger, A., Vanderhaeghe, O., Andre-Mayer, A., Poujol, M., Bartlett, R., and Mercadier, J., 2016. Synmetamorphic Cu remobilization during the Pan-African orogeny: Microstructural, petrological and geochronological data on the kyanite-micaschists hosting the Cu (-U) Lumwana deposit in the Western Zambian Copperbelt of the Lufilian belt. *Ore Geology Reviews*, 75, p. 52–75.
- Twite, F., 2016. Controls of Sulphide Mineralization at the Kamao Copper Deposit, with an Emphasis on Structural Controls, Democratic Republic of Congo. Unpublished MSc Thesis. University of Witwatersrand, South Africa. 288 pages.
- Twite, F., Broughton, D., Nex, P., Kinnaird, J., and Gilchrist, G., 2019. Lithostratigraphic and structural controls on sulphide mineralisation at the Kamao copper deposit, Democratic Republic of Congo. *Journal of African Earth Sciences*, 151, p. 212 – 224.
- Ulmer-Scholle, D. S., Scholle, P. A., Schieber, J., and Raine, R. J., 2014. A Color Guide to the Petrography of Sandstones, Siltstones, Shales and Associated Rocks. The American Association of Petroleum Geologists, Memoir 109, 525 pages.
- Wendorff, M., 2003. Stratigraphy of the Fungurume Group - evolving foreland basin succession in the Lufilian fold-thrust belt, Neoproterozoic-Lower Palaeozoic, Democratic Republic of Congo. *South African Journal of Geology*, 106, p. 17-34.
- Wendorff, M., and Key, R. M., 2009. The Relevance of the Sedimentary History of the Grand Conglomerat Formation (Central Africa) to the Interpretation of the Climate during a Major Cryogenian Glacial Event. *Precambrian Research*, 172, p. 127–142.

Wickard, A., 2016. A diagenetic study of the wolfcamp shale in the midland basin, West Texas. Unpublished MSc Thesis. University of Oklahoma, 83 pages.

Zientek, M.L., Bliss, J.D., Broughton, D.W., Christie, Michael, Denning, P.D., Hayes, T.S., Hitzman, M., Horton, J.D., Frost-Killian, S., Jack, D.J., Master, S., Parks, H.L., Taylor, C.D., Wilson, A.B., Wintzer, N.E., and Woodhead, J., 2014. Sediment-Hosted Stratabound Copper Assessment of the Neoproterozoic Roan Group, Central African Copperbelt, Katanga Basin, Democratic Republic of the Congo and Zambia. U.S. Geological Survey Scientific Investigations Report 2010-5090-T, 178 pages.

Chapter 3

3. Concluding statements

The Kakula deposit is a world-class sedimentary-rock-hosted copper deposits with stratiform and fine-grained, disseminated copper-sulphide mineralisation. Mineralisation is predominantly hosted by fine-grained matrix of clast-poor subaqueous debrite (diamictite) of the lower grand conglomerat. This study used SEM to document textural and chemical characteristics of the diamictite matrix. The ore-zone matrix consists of muscovite, quartz, K-feldspar, chlorite, dolomite (and Fe-dolomite), and relatively less biotite, copper-sulphides, hematite, and rutile. Pyrite is present outside of heavily mineralised zones. Matrix from outside of the ore-zone, as least-altered matrix, does not contain muscovite, and unlike the ore-zone matrix, it contains albite. The evolution of matrix in the ore-zone matrix is recorded by five paragenetic phases: sedimentation, diagenesis (pre-ore), main-ore, post ore alteration, and tectonism. The original composition of the matrix from deposition could not be determined with certainty because of extensive alteration, but it is thought to have been predominantly composed of detrital quartz and mafic and/or altered mafic minerals, and smaller amounts of K-feldspar, muscovite and carbonate minerals. Copper-sulphides (chalcopyrite, bornite, chalcocite) fit into a paragenetic sequence between pre-ore diagenetic pyrite (\pm Fe-dolomite) and muscovite, and they are associated with relatively Mg-rich chlorite and biotite (\pm hematite, K-feldspar, and quartz). Chlorite and biotite have textural relationships with copper-sulphides and have FeO and MgO wt% compositional trends despite a roughly uniform “bulk” matrix composition. The trends, which are highlighted by Fe-poor chlorite and biotite in more heavily mineralised zones, may be the result of

chlorite, biotite, and copper-sulphides competing for iron during their formation.

Although the diamictite is relatively undeformed and unmetamorphosed, aligned matrix formed during weak tectonism of the Lufilian orogeny and is characterised by elongated and aligned matrix components, including copper sulphides. Aligned matrix is relatively muscovite-rich and copper-depleted compared to non-aligned matrix in any given sample of ore-zone matrix, suggesting that alignment post-dated copper mineralisation. Clast-poor diamictite matrix characteristics, which include a lower abundance of large clasts and sand grains, appears to have influenced mineralisation because it correlates with higher copper-grade levels. Even though siltstone does not make up a significant total stratigraphic thickness compared to diamictite, it contains elevated copper grades.

Although only one sample of mineralised siltstone was examined, it contained the highest porosity, highest copper grade, no discernible fabric, and the finest average grain size of all of the samples. Overall, the Kamoia and Kakula deposits are very similar in terms of ore-zone matrix compositional and textural characteristics, other than the higher abundance of chalcocite and hematite at Kakula. Kamoia and Kakula appear to share similarities with the Kashime (Fishtie) deposit in Zambia and have characteristics consistent with the magnesian and potassic alteration commonly documented in the CACB. Although the grand congoloméat west of Kolwezi, DRC, was once considered unsuitable for copper exploration, it has proven to be one of the most prospective high-grade and high-tonnage stratiform copper areas in the world. Future detailed work at Kamoia and Kakula could include: (1) trace element geochemistry and isotopes on individual minerals, such as copper sulphides, to complement the limited trace element analyses performed in this study; (2) total organic carbon (TOC) analysis to see if there is

organic carbon in the rock outside of the ore-zone, to further explore possible reducing agents; (3) detailed study of pyrite to determine its significance in copper-grade and possible secondary ore-stage pyrite formation; (4) detailed study of matrix porosity and its possible implications for permeability and pervasive hydrothermal fluid migration; and (5) radiometric dating to constrain the timing of copper mineralisation better.

Figures

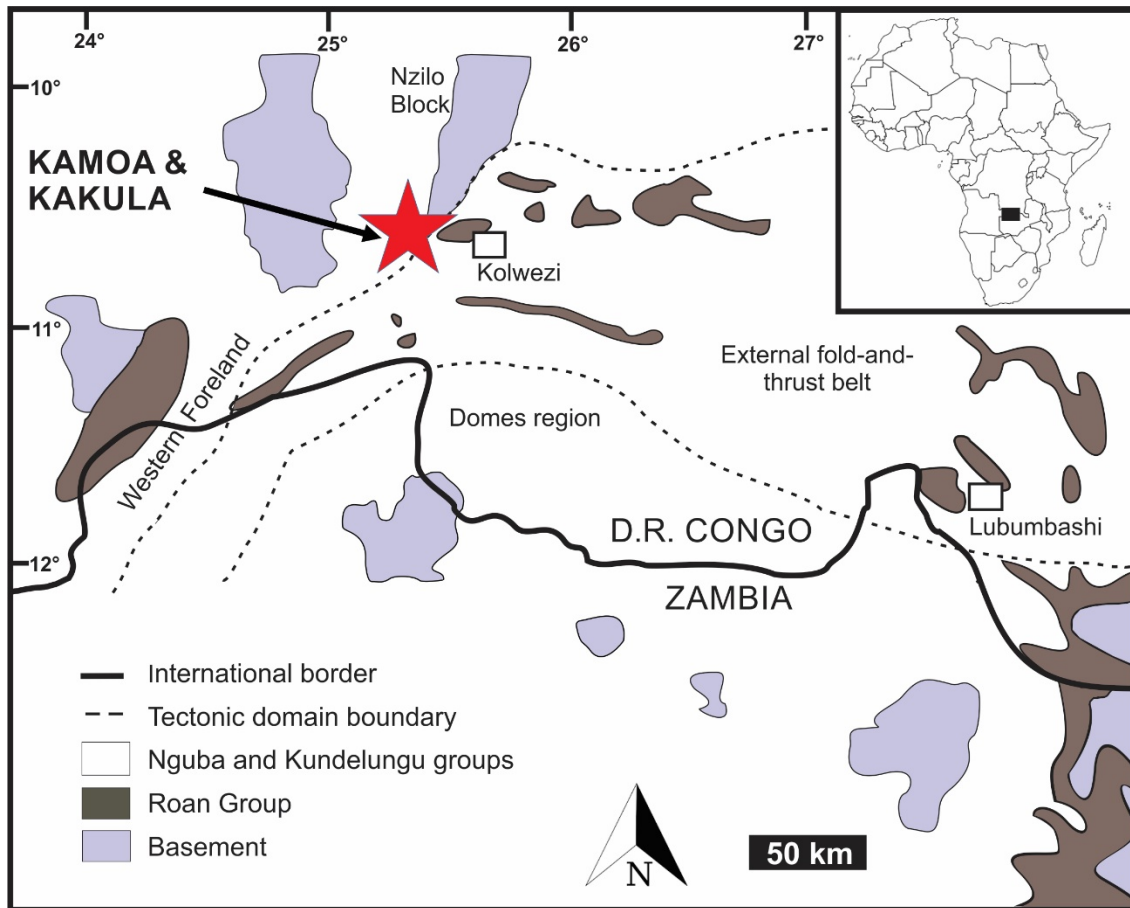


Figure 1: Simplified regional geology map of the central African copperbelt showing tectonic domains, rock types, and location of the Kamoia and Kakula sedimentary-rock-hosted copper deposits (red star). The Kamoia and Kakula deposits are located in the northern extension of the western foreland tectonic domain west of Kolwezi, Democratic Republic of Congo. The external fold-and-thrust belt and domes regions east and south of Kamoia and Kakula host the majority of the copper deposits of the central African copperbelt. After François (1993) and Cailteux (1994).


Katanga Supergroup	Kundelungu Group	Biano Subgroup
		Ngule Subgroup
		Gombela Subgroup
	Nguba Group	Bunkeya Subgroup
		Muombe Subgroup
		“grand conglomérat” 
		Mwashya Subgroup
	Roan Group	Dipeta Subgroup
		Mines Subgroup
		R.A.T Subgroup
		Pre-Katanga basement

Figure 2: Simplified stratigraphy of the Katanga Supergroup and its groups and subgroups above pre-Katanga basement rock (François, 1993; Cailteux, 1994; Cailteux et al., 2005; Selley et al., 2005; Batumike et al., 2006; Cailteux and De Putter, 2019). The basal contact between the Roan Group (R.A.T. subgroup) and pre-Katanga basement is unknown. The Roan and Nguba groups were deposited in Neoproterozoic intracratonic rift basins, whereas the Kundelungu Group was deposited in a foreland basin. The grand conglomérat (Mwale formation) of the Muombe subgroup marks the base of the Nguba Group and hosts the Kamoia and Kakula deposits (red star).

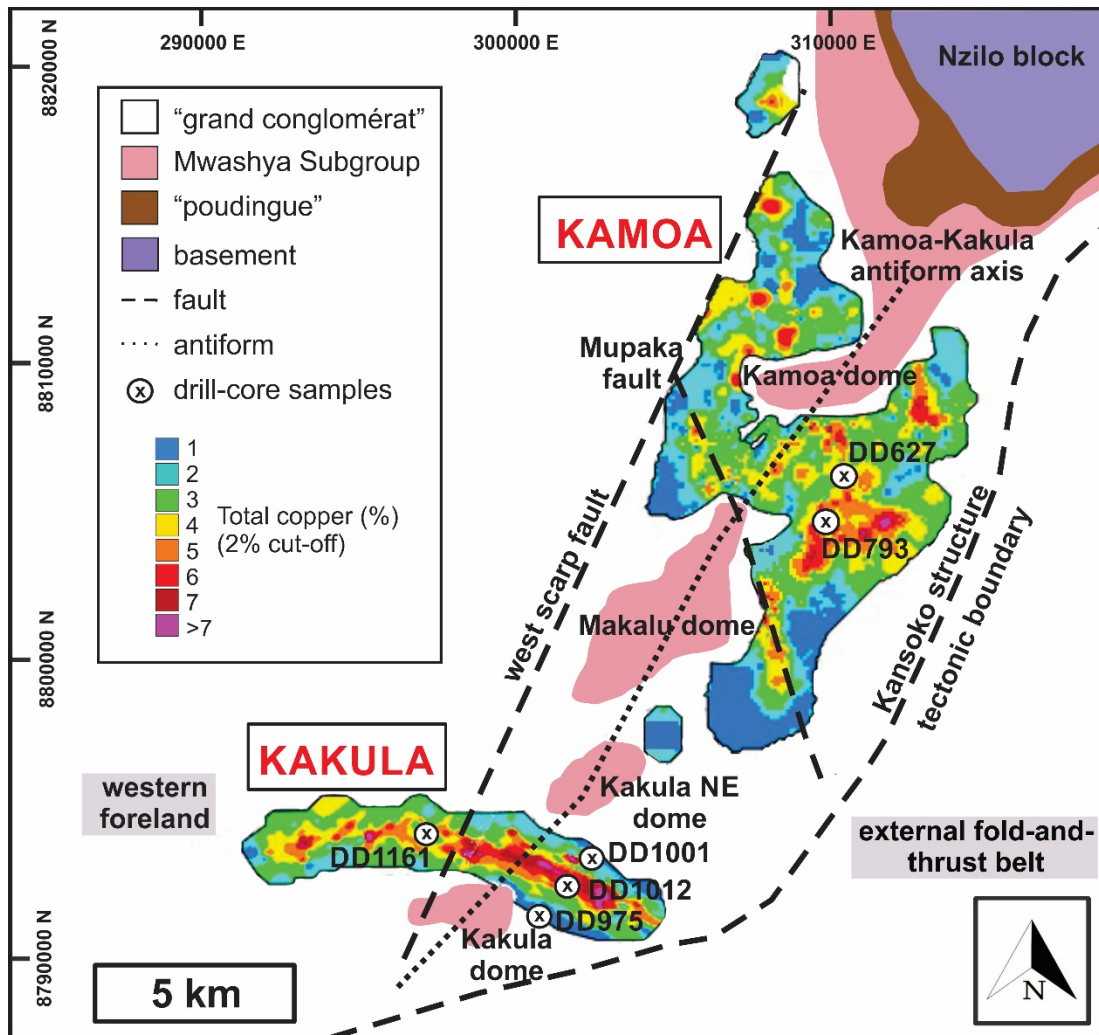


Figure 3: Local geology map of the Kamoia and Kakula area. Current copper resource areas with total copper percentage (2% cut-off) projected to surface, rock types, tectonic domains, structures, and the locations of the drill-holes studied are indicated. The only exposure of basement rock in the area is the Nzilo block to the north. The resource area is dominated by rock of the grand conglomérat, whereas areas along the Kamoia-Kakula antiform axis reveal rock of the Mwashya Subgroup and “poudingue” to the north. Surface expression and bedrock in the area are poorly expressed. The Kamoia and Kakula deposits are delineated to the east by the Kansoko structure, which separates younger rock of the western foreland from older, relatively deformed Katanga Supergroup strata of the external fold-and-thrust belt. Other notable structures in the Kamoia and Kakula area include the Mupaka fault (Twite, 2016; Twite et al., 2019) and the west scarp fault (Schmandt et al., 2013). Map after Schmandt et al. (2013), Twite (2016), Kennedy et al. (2018), OreWin (2018), and Ivanhoe Mines Ltd. website.

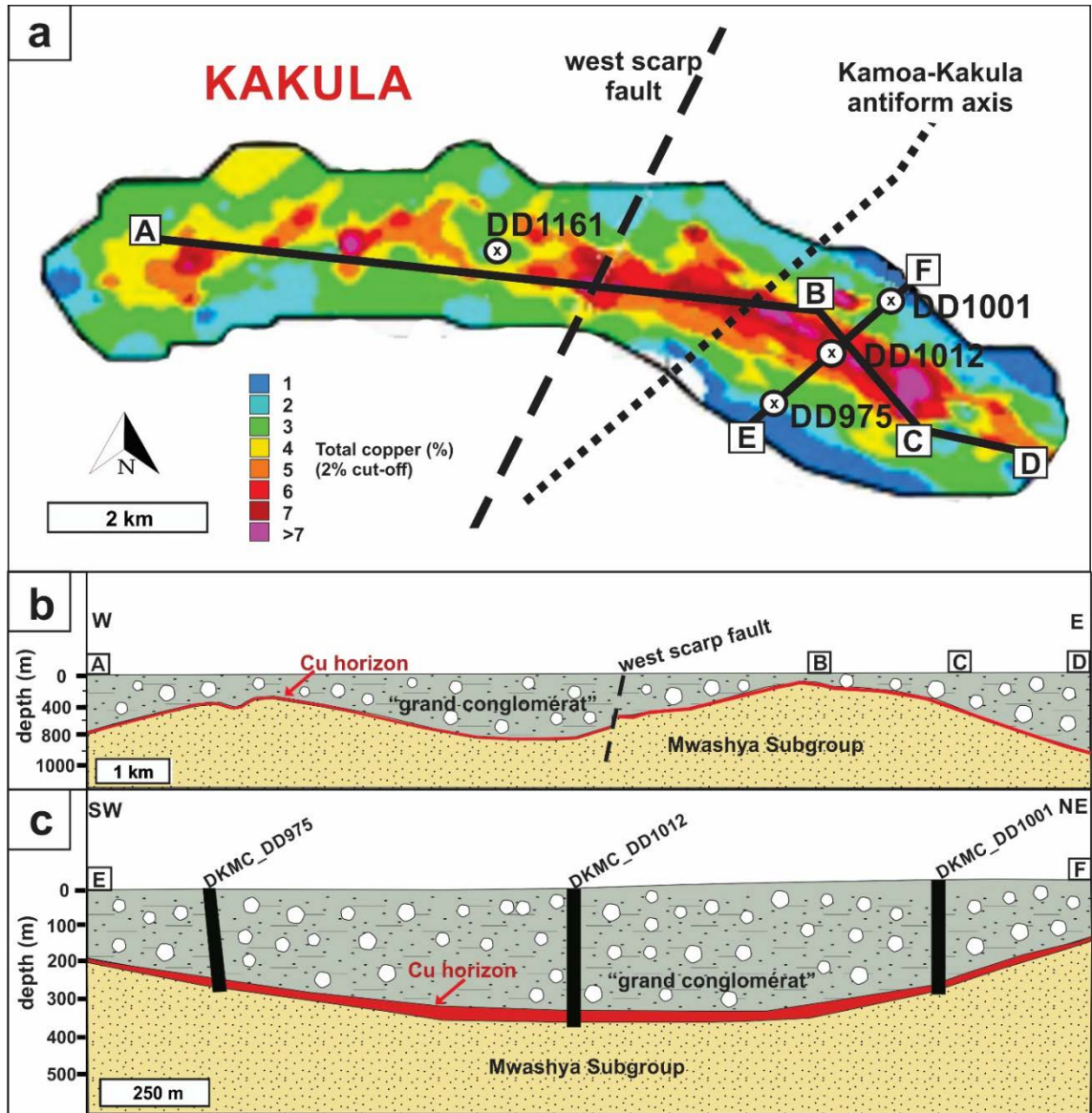


Figure 4: Map and cross-sections of the Kakula deposit resource area. (a) Map of the total copper percent (2% cut-off) grades projected to surface, approximate location of the west scarp fault and Kamoia-Kakula antiform axis, and approximate location of drill-holes studied. (b) Cross-section A-B-C-D is an approximate west-east section across the Kakula deposit that illustrates the depth of the grand conglomérat-Mwashya Subgroup contact and copper ore-zone, and structure and general architecture across the deposit. (c) Cross-section E-F shows three drill-holes (DKMC_DD975, DKMC_DD1012, DKMC_DD1001) studied at Kakula from an approximate southwest-northeast fence. Map and cross-sections after Ivanhoe Mines Ltd. website.

“grand congrlomérat”	Uppermost diamictite (Ng.1.1.6)	
	Upper diamictite (Ng.1.1.5)	
	Upper laminated pyritic siltstone (Ng.1.1.4)	
	Middle diamictite (Ng.1.1.3)	
	Lower laminated pyritic siltstone (Ng.1.1.2)	
	Basal diamictite (Ng.1.1.1)	Upper basal diamictite (Ng.1.1.1.3)
		Intercalated siltstone (Ng.1.1.1.2)
Lower basal diamictite (Ng.1.1.1.1)		
Mwashya Subgroup	R4.2	

Figure 5: Stratigraphic subdivisions of the grand congrlomérat used at Kamoia and Kakula. The basal diamictite hosts the ore-zones at Kakula and Kamoia and is further subdivided into the lower basal diamictite, intercalated siltstone, and upper basal diamictite. The ore is hosted by the basal diamictite (primarily by the upper basal diamictite, intercalated siltstone, and to a lesser extent the lower basal diamictite). The lower basal diamictite is predominantly clast-rich ($\geq 20\%$ clasts larger than 2 mm) with a sandy matrix, whereas the upper basal diamictite is commonly clast-poor ($\leq 20\%$ clasts larger than 2 mm) with a muddy matrix. The numerical stratigraphic codes used by Ivanhoe Mines Ltd. for subdivisions for the grand congrlomérat is not particularly useful at Kakula because stratigraphy of sediment mass flow deposits interdigitate and is not always layer-cake type. Moreover, the thickness and lateral continuity of units vary according to location and make detailed correlation between Kamoia and Kakula difficult.

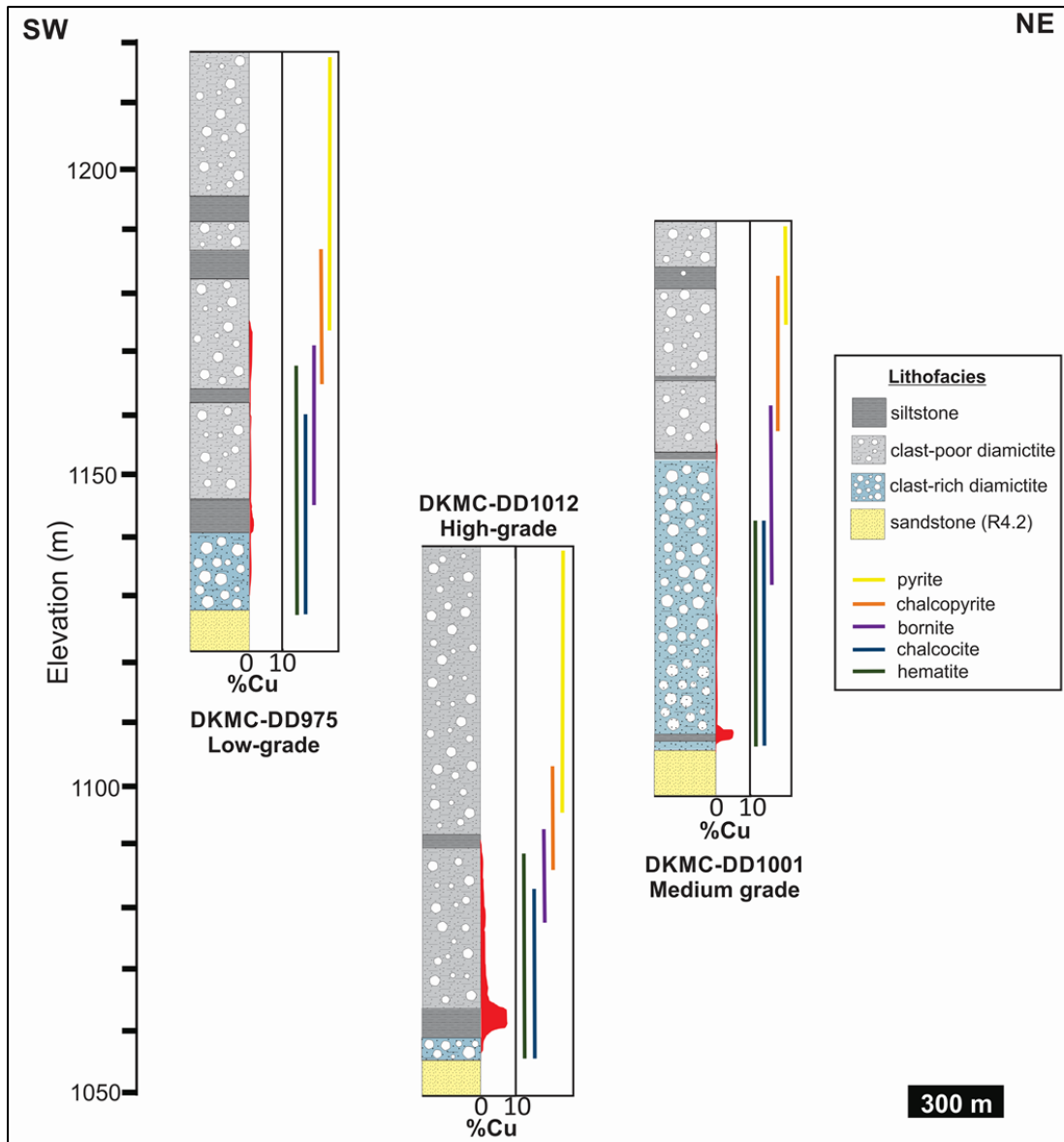


Figure 6: Stratigraphic logs of low-grade, high-grade, and medium-grade drill-holes studied from an approximately SW-NE fence at Kakula showing their relative elevations and positions at 20x vertical exaggeration. Sedimentary facies, approximate copper-grades from Ivanhoe Mines Ltd. assay results, and opaque mineral distributions are indicated. Diamictite and siltstone belong to the grand conglomerat, whereas the sandstone belongs to the Mwashya subgroup (R4.2).

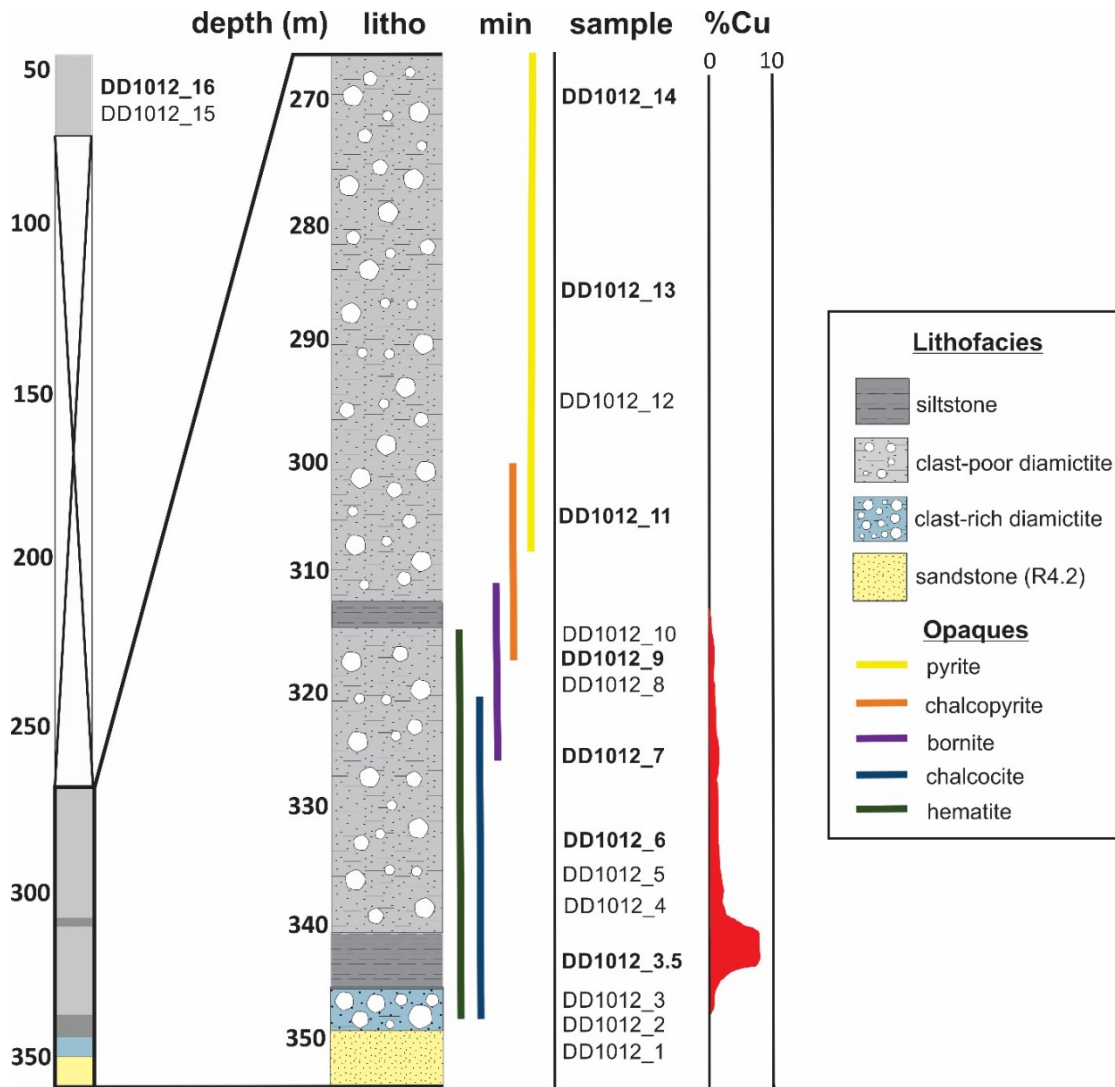


Figure 7: Stratigraphic log of high-grade drill-hole DKMC_DD1012 at Kakula, with focus on the ore-zone. This log includes sedimentary facies, sample IDs and locations, and approximate copper grades (% Cu) from Ivanhoe Mines Ltd. assay results. The opaque mineral phases and their approximate stratigraphic distributions are based on their presence, rather than abundance and copper grade. The presence of hematite, chalcocite, bornite, chalcopyrite, and pyrite has been approximated from visual logging, petrography, and Ivanhoe Mines Ltd. assay results. Diamictite and siltstone belong to the grand conglomérat, whereas the sandstone belongs to the Mwashya subgroup (R4.2). The uppermost samples (DD1012_15 and DD1012_16) are from the middle diamictite (Ng.1.1.3). Samples examined under the SEM are in bold.

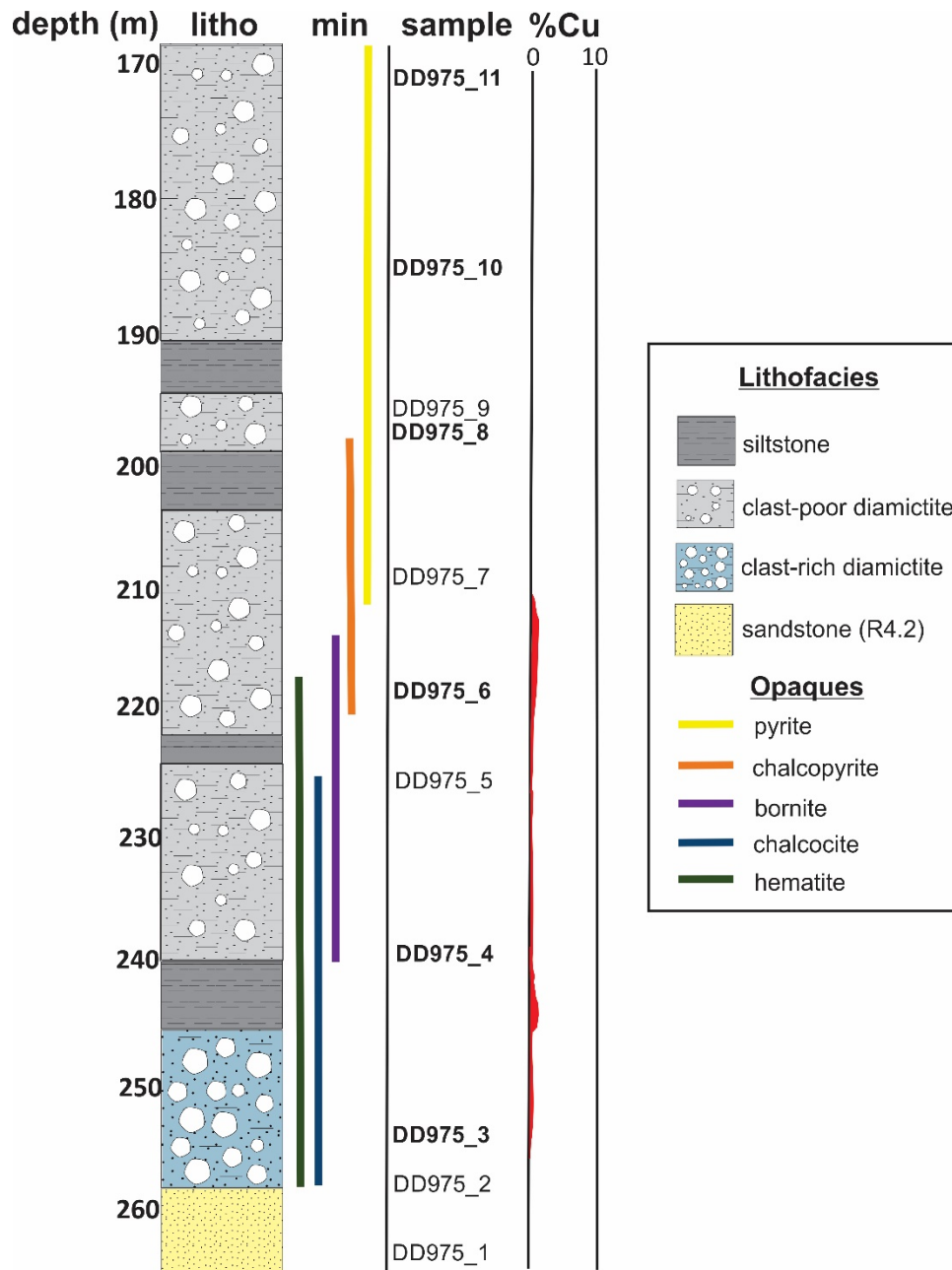


Figure 8: Stratigraphic log of low-grade drill-hole DKMC_DD975 at Kakula, with focus on the ore-zone. This log includes sedimentary facies, sample IDs and locations, and approximate copper grades (% Cu) from Ivanhoe Mines Ltd. assay results. The opaque mineral phases and their approximate stratigraphic distributions are based on their presence, rather than abundance and copper grade. The presence of hematite, chalcocite, bornite, chalcopyrite, and pyrite has been approximated from visual logging, petrography, and Ivanhoe Mines Ltd. assay results. Diamictite and siltstone belong to the grand conglomérat, whereas the sandstone belongs to the Mwashya subgroup (R4.2). Samples examined under the SEM are in bold.

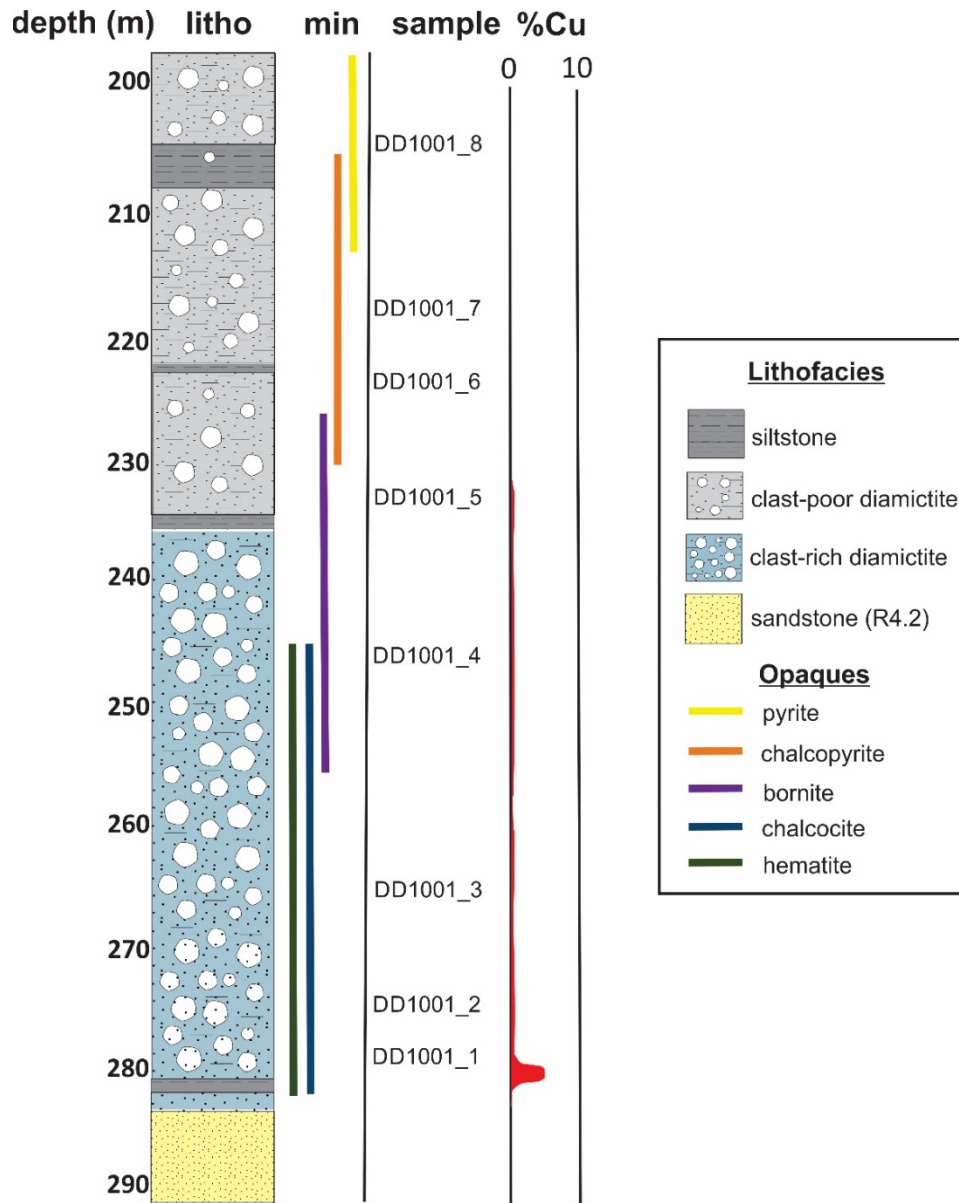


Figure 9: Stratigraphic log of medium-grade drill-hole DKMC_DD1001 at Kakula, with focus on the ore-zone. This log includes sedimentary facies, sample IDs and locations, and approximate copper grades (% Cu) from Ivanhoe Mines Ltd. assay results. The opaque mineral phases and their approximate stratigraphic distributions are based on their presence, rather than abundance and copper grade. The presence of hematite, chalcocite, bornite, chalcopyrite, and pyrite has been approximated from visual logging, petrography, and Ivanhoe Mines Ltd. assay results. Diamictite and siltstone belong to the grand conglomérat, whereas the sandstone belongs to the Mwashya subgroup (R4.2). Samples from this drill-hole were not subject to SEM analysis.

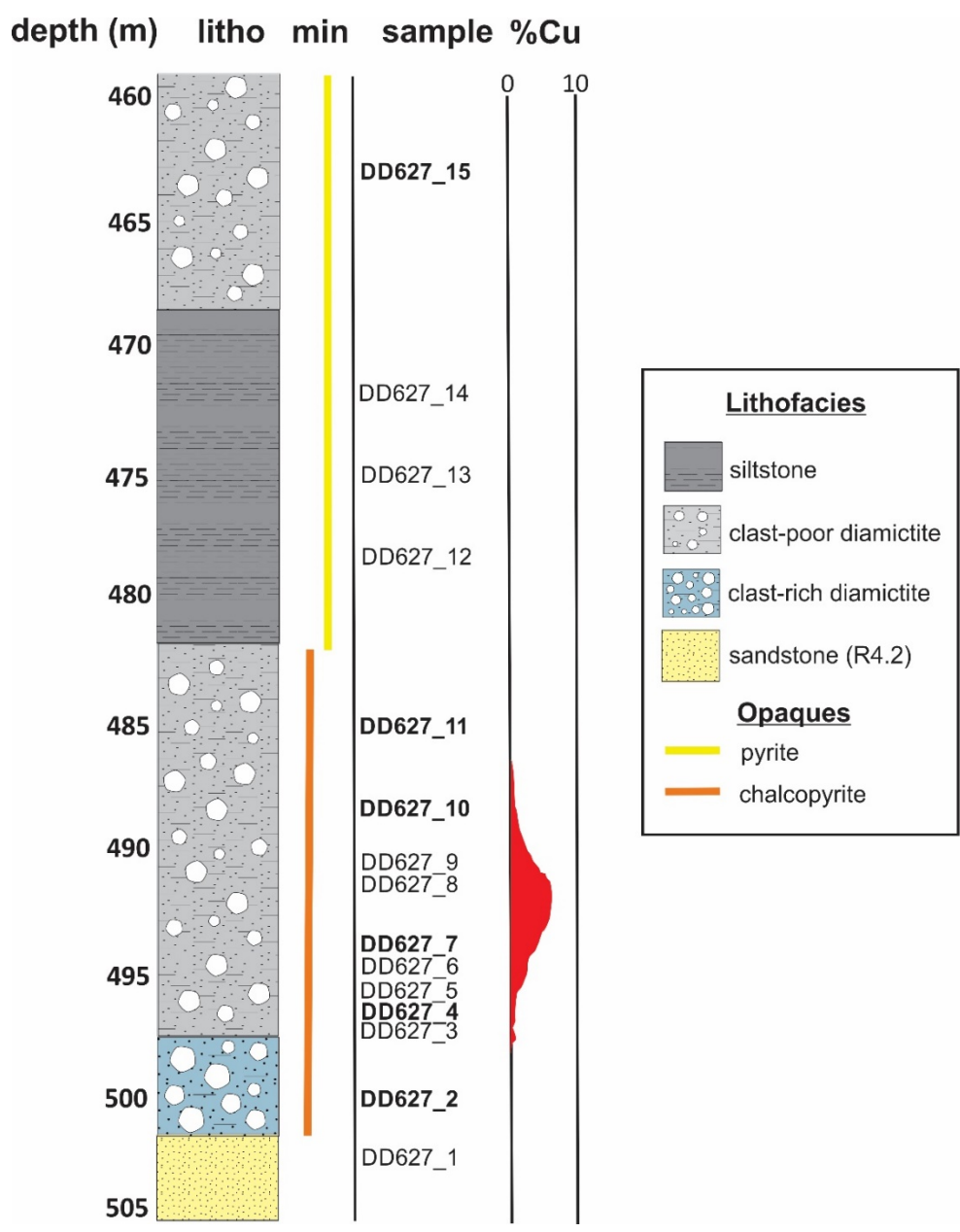


Figure 10: Stratigraphic log of high-grade drill-hole DKMC_DD627 at Kamoia, with focus on the ore-zone. This log includes sedimentary facies, sample IDs and locations, and approximate copper grades (% Cu) from Ivanhoe Mines Ltd. assay results. The opaque mineral phases and their approximate stratigraphic distributions are based on their presence, rather than abundance and copper grade. The presence chalcopyrite and pyrite has been approximated from visual logging, petrography, and Ivanhoe Mines Ltd. assay results. Diamictite and siltstone belong to the grand conglomérat, whereas the sandstone belongs to the Mwashya subgroup (R4.2). Samples examined under the SEM are in bold.

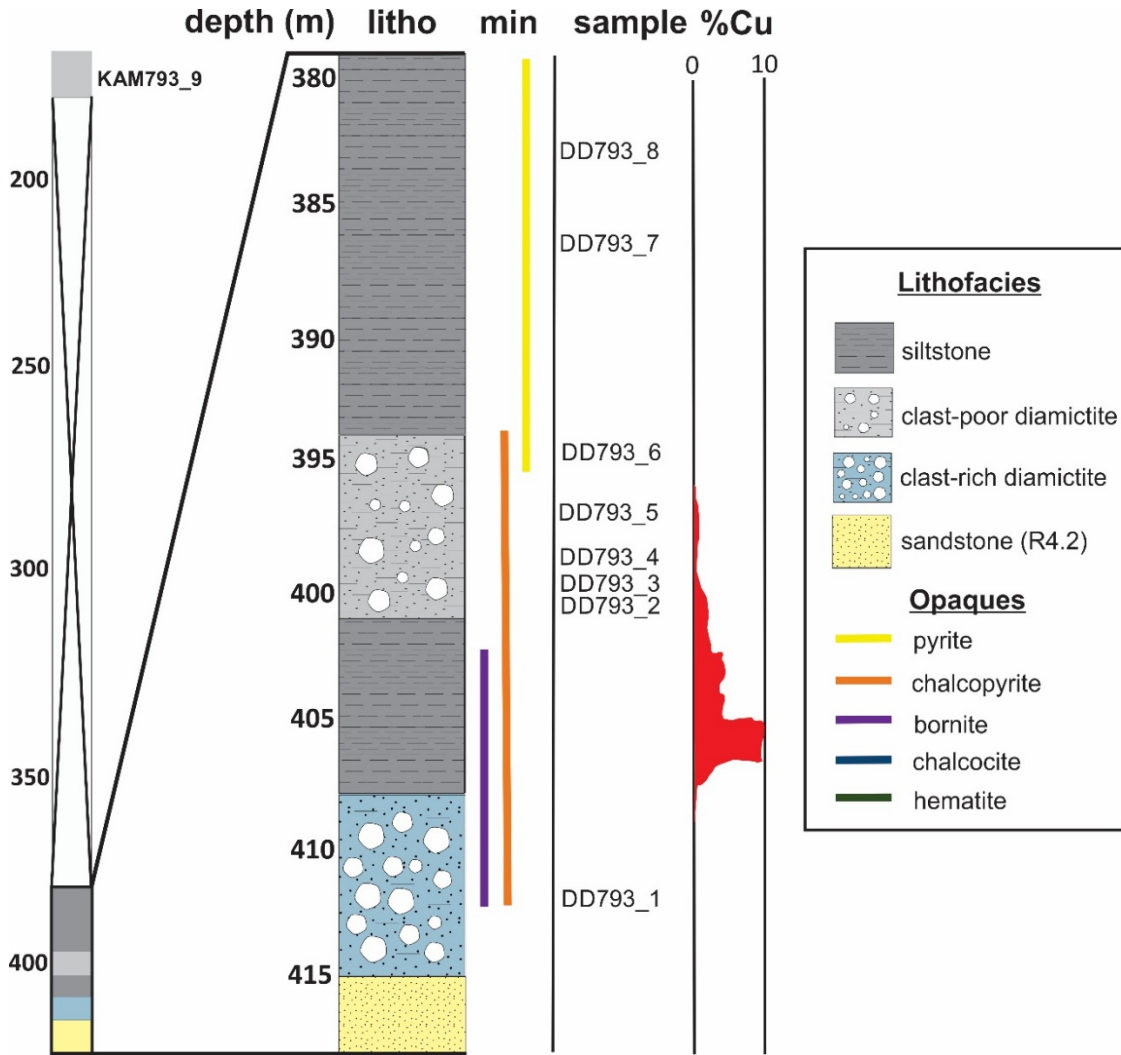


Figure 11: Stratigraphic log of high-grade drill-hole DKMC_DD793 at Kamoia, with focus on the ore-zone. This log includes sedimentary facies, sample IDs and locations, and approximate copper grades (% Cu) from Ivanhoe Mines Ltd. assay results. The opaque mineral phases and their approximate stratigraphic distributions are based on their presence, rather than abundance and copper grade. The presence bornite, chalcopyrite, and pyrite has been approximated from visual logging, petrography, and Ivanhoe Mines Ltd. assay results. Diamictite and siltstone belong to the grand conglomérat, whereas the sandstone belongs to the Mwashya subgroup (R4.2). Samples examined under the SEM are in bold.

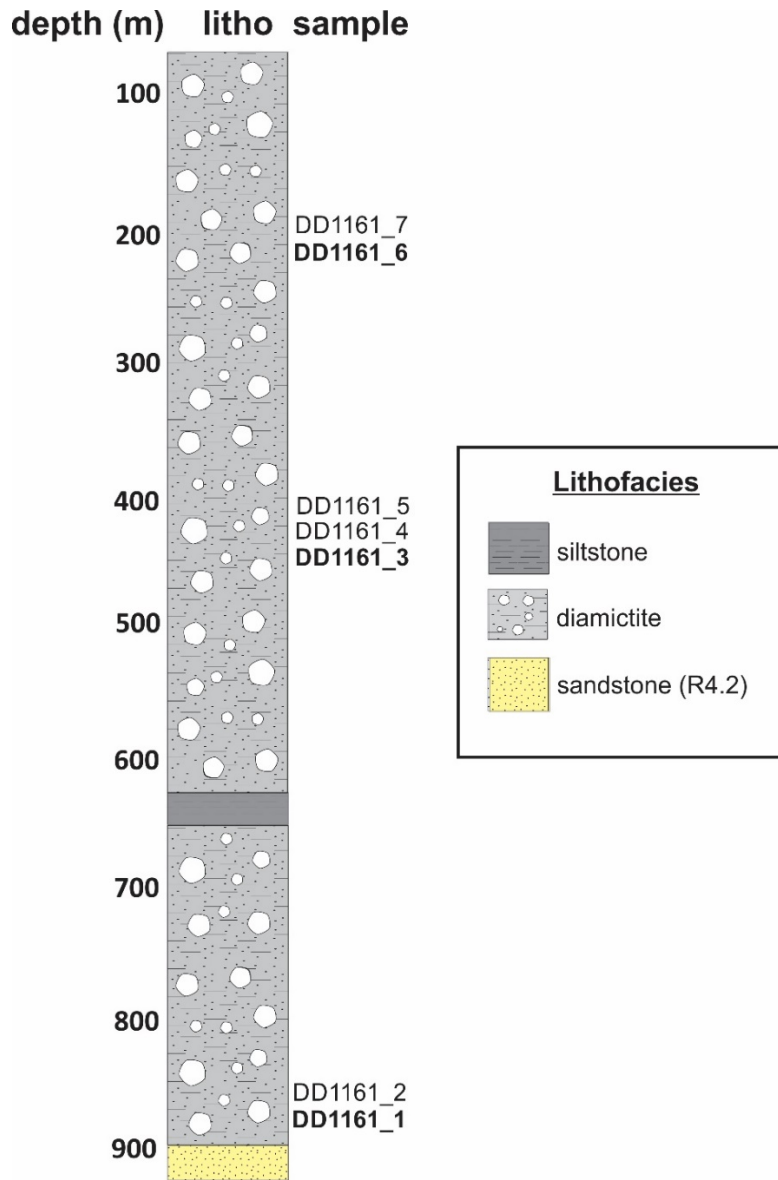


Figure 12: Stratigraphic log of low-grade drill-hole DKMC_DD1161 at Kakula. No detailed logging was conducted on this drill-hole. This log includes the sedimentary facies based on Ivanhoe Mines Ltd.'s geology logs. Sample IDs and locations are included, and those examined under the SEM are in bold. Diamictite and siltstone belong to the grand conglomérat, whereas the sandstone belongs to the Mwashya subgroup (R4.2). The lowermost two samples were collected from the basal diamictite (Ng.1.1.1), whereas the middle three samples and the uppermost two samples are from the middle diamictite (Ng.1.1.3) and the upper diamictite (Ng.1.1.5), respectively.

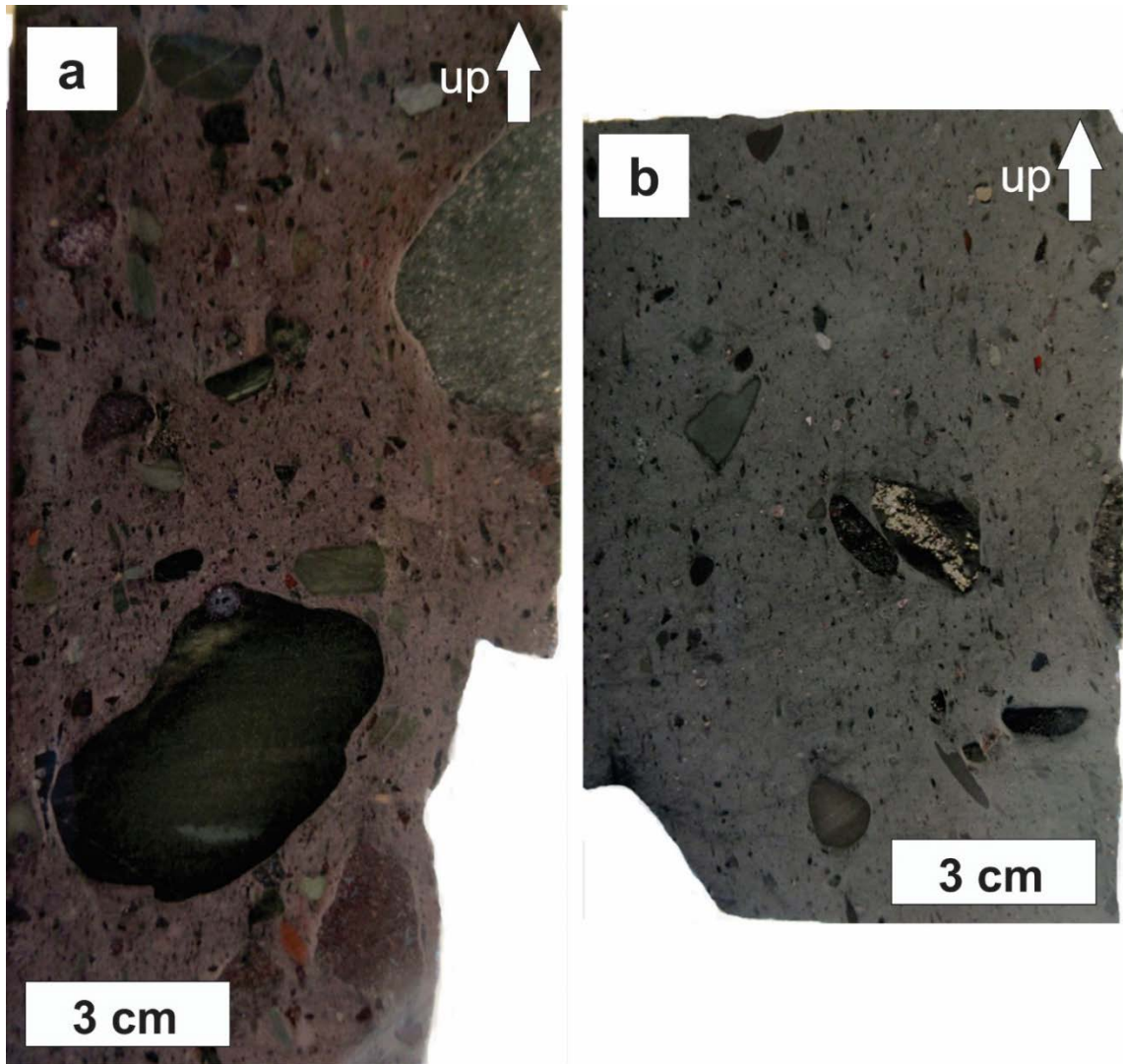


Figure 13: Oriented drill-core samples of the basal diamictite at Kakula from low-grade drill-hole DKMC_DD975. (a) clast-rich diamictite sample DKMC-DD975_3 at 255 m depth with disseminated hematite and chalcocite. (b) Clast-poor diamictite sample DKMC-DD975_8 at 197 m depth (top of the ore-zone) with disseminated pyrite and minor chalcopyrite. The clast-rich diamictite contains 20 - 40% clasts (≥ 2 mm), whereas the clast-poor diamictite contains $\leq 20\%$ clasts (≥ 2 mm). Diamictite is generally textureless with clasts of various sizes in fine-grained matrix. The most abundant clast types are quartzite, siltstone, and altered mafic rock. Generally, clast-rich diamictite is poorly mineralised compared to clast-poor diamictite. The fine-grained nature of opaque minerals in the matrix makes estimating grade from hand sample difficult.

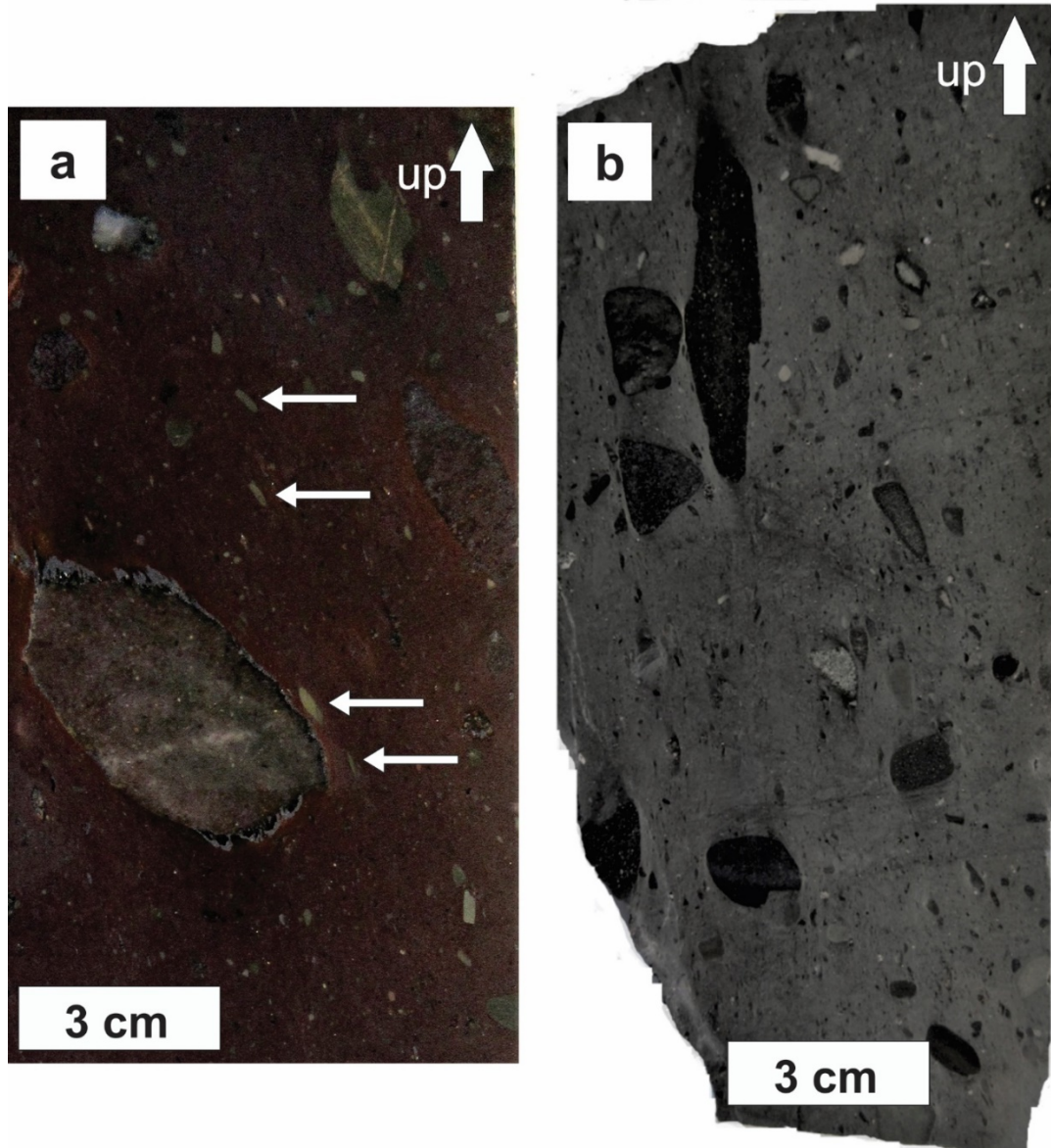


Figure 14: Oriented drill-core samples from Kakula of the basal diamictite of clast-poor diamictite from high-grade drill-hole DKMC_DD1012. (a) Sample DD1012_5 from 337 m depth has maroon matrix colour with disseminated chalcocite and hematite. (b) Sample DD1012_11 at 304 m depth has grey to green-grey matrix colour with disseminated pyrite. Although the diamictite is generally textureless, a sub-vertical fabric defined by aligned and elongated matrix components, and sometimes larger clasts (white arrows), is locally evident. The maroon colour is conferred by fine-grained disseminated hematite in the matrix, which is also associated with stratigraphic levels containing chalcocite and lesser bornite.

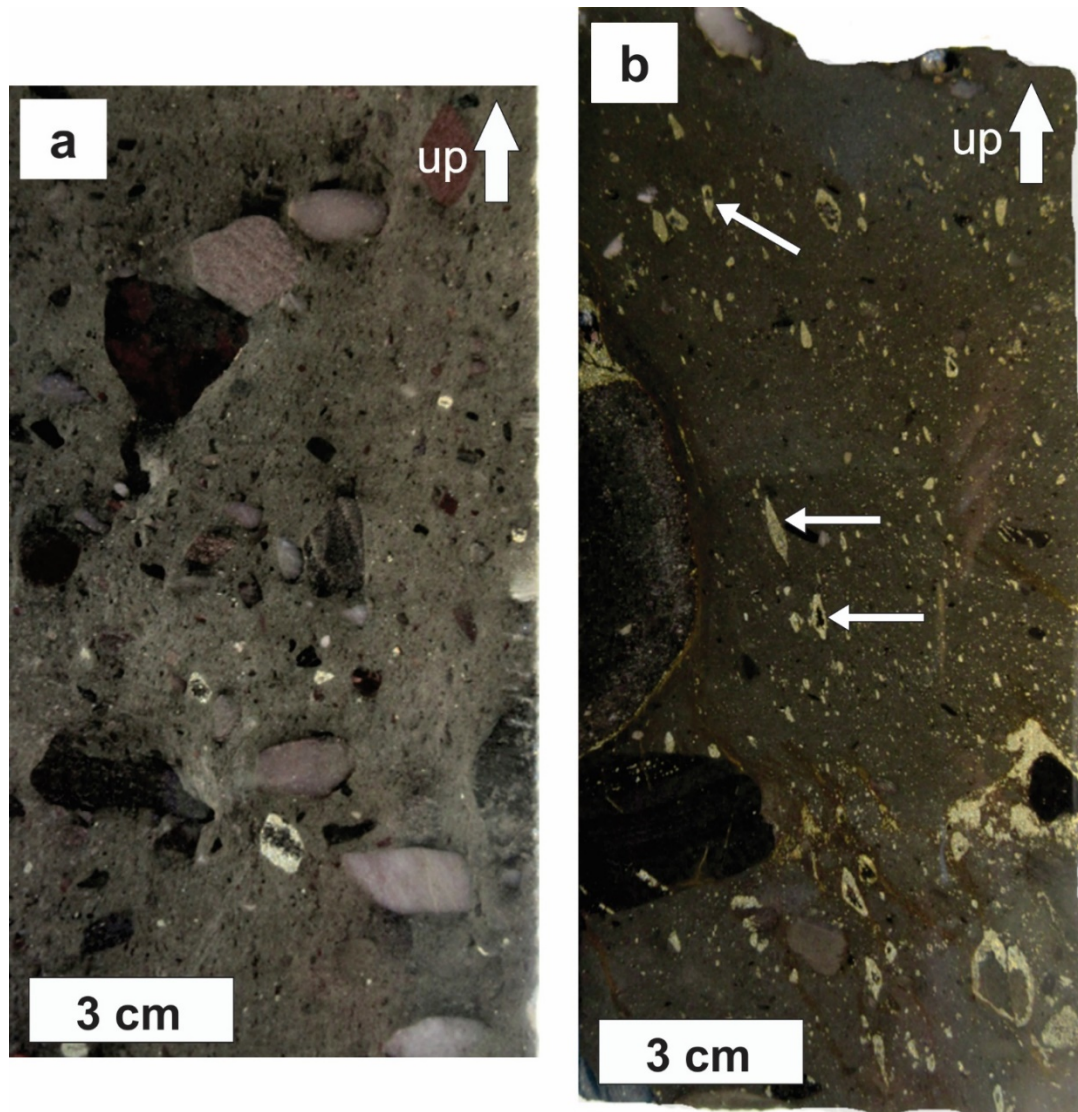


Figure 15: Oriented drill-core samples from the basal diamictite at Kamo. (a) clast-rich diamictite sample DD627_2 at 500 m depth from drill-hole DKMC_DD627 with minor chalcopyrite. (b) Clast-poor diamictite sample DD793_3 at 399 m depth from drill-hole DKMC_DD793 with abundant chalcopyrite. Mineralisation is predominantly fine-grained and hard to see with the unaided eye but is also present as coarse grains and caps on relatively larger clasts. Chalcopyrite, like other matrix minerals, locally expresses alignment and elongation (white arrows) parallel to matrix fabric. As at Kakula, the clast-rich diamictite contains 20 - 40% clasts (≥ 2 mm), whereas the clast-poor diamictite contains $\leq 20\%$ clasts (≥ 2 mm). In diamictite containing copper-sulphides, grey and green-grey matrix colours dominate at Kamo, whereas maroon colours are more commonly observed at Kakula.



Figure 16: Oriented drill-core sample DD1012_16 at 74 m depth from Kakula of the middle diamictite from drill-hole DKMC_DD1012, approximately 250 m above the ore-zone. The diamictite is generally textureless with clasts of various sizes in fine-grained matrix. In hand sample, the middle diamictite appears to have characteristics similar to diamictite of the basal diamictite for clast composition, sizes, and percentages. The middle diamictite is generally green-grey to grey like the basal diamictite outside of hematite-rich zones.

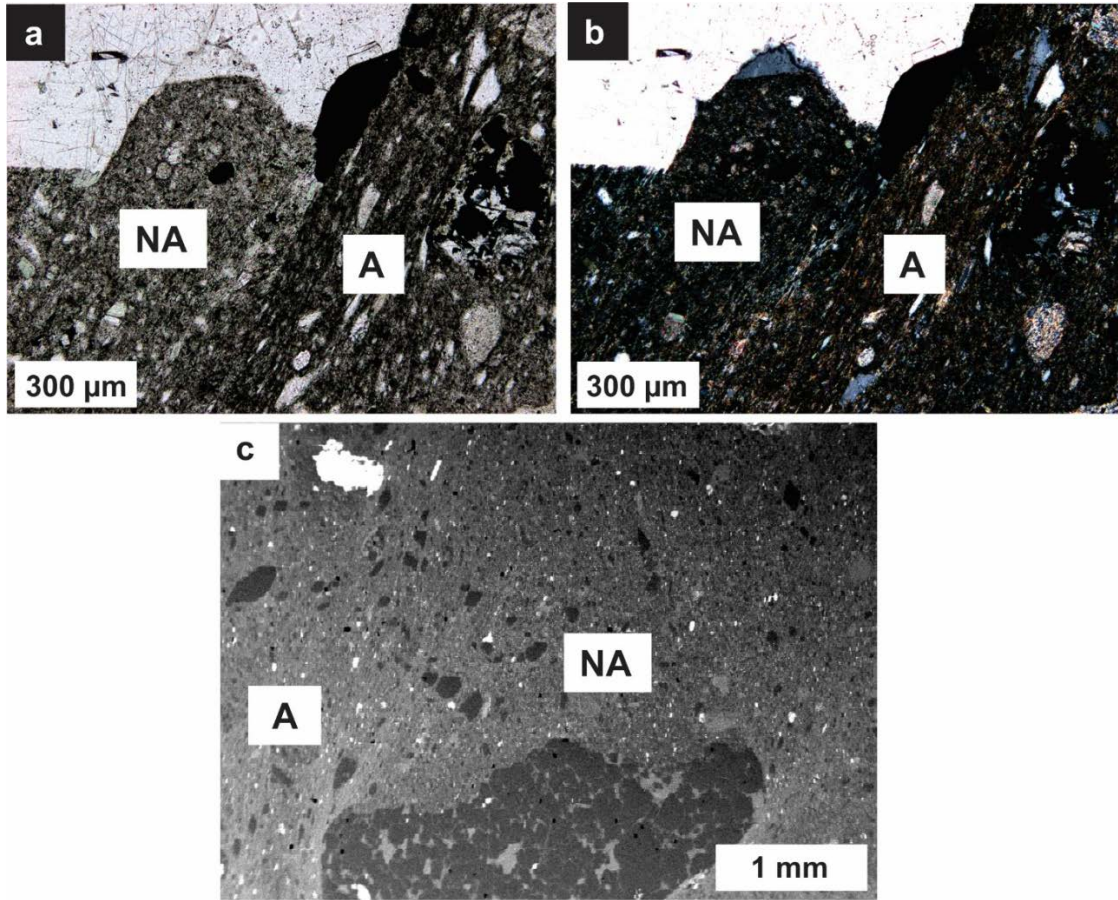


Figure 17: Aligned (A) and non-aligned (NA) matrix textures in the vicinity of large clasts in the basal diamictite at Kakula. The aligned matrix is defined by elongated, aligned matrix minerals. Matrix alignment is generally stronger near the margins of large diamictite clasts. (a) Oriented plane-polarised light photomicrograph of sample DD1012_7 (326 m depth) and on lower right side of a large clast, and (b) the same photomicrograph in cross-polarised light. Aligned matrix has more colourful birefringent material than non-aligned matrix. (c) Oriented BS-SEM image of matrix from the same sample (DD1012_7). Dark (quartz) and grey (muscovite, chlorite, biotite, K-feldspar, dolomite) shades indicate lower-density matrix components, whereas bright spots are denser minerals (copper-sulphides and hematite).

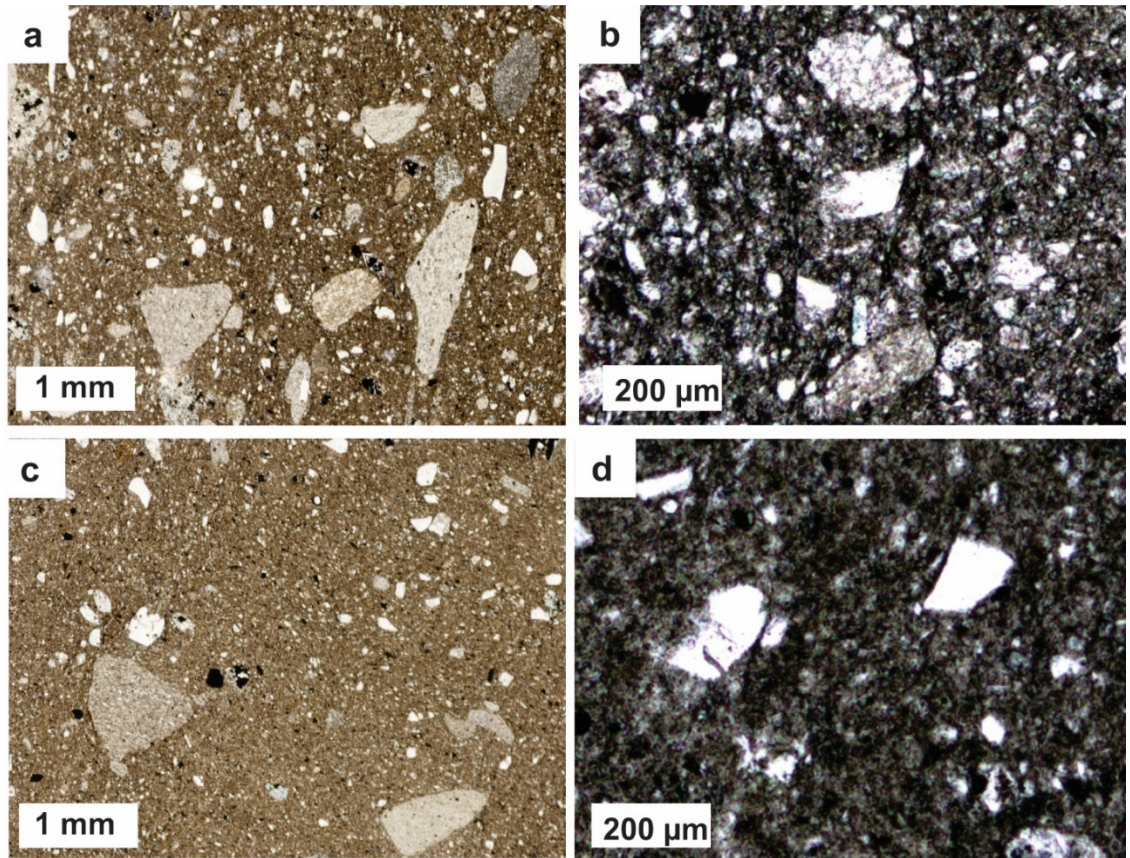


Figure 18: Oriented plane-polarised photomicrographs showing differences in matrix grain sizes, shapes, and abundances between clast-poor and clast-rich varieties of the basal diamictite at Kakula. (a) Sample DD975_3 (255 m depth) of clast-rich diamictite at low magnification and (b) high magnification highlighting abundance of sand-sized quartz clasts. (c) Sample DD975_6 (218 m depth) of clast-poor diamictite at low magnification and (d) high magnification showing comparatively low abundance of sand-sized quartz grains. Although only the percentage of clasts ≥ 2 mm is used in the distinction between clast-poor and clast-rich diamictite, the clast-rich diamictite also generally has relatively higher sand component than clast-poor diamictite. Regardless of the diamictite variety, diamictite matrix has a full spectrum of grain sizes from clay- to coarse silt-sized.

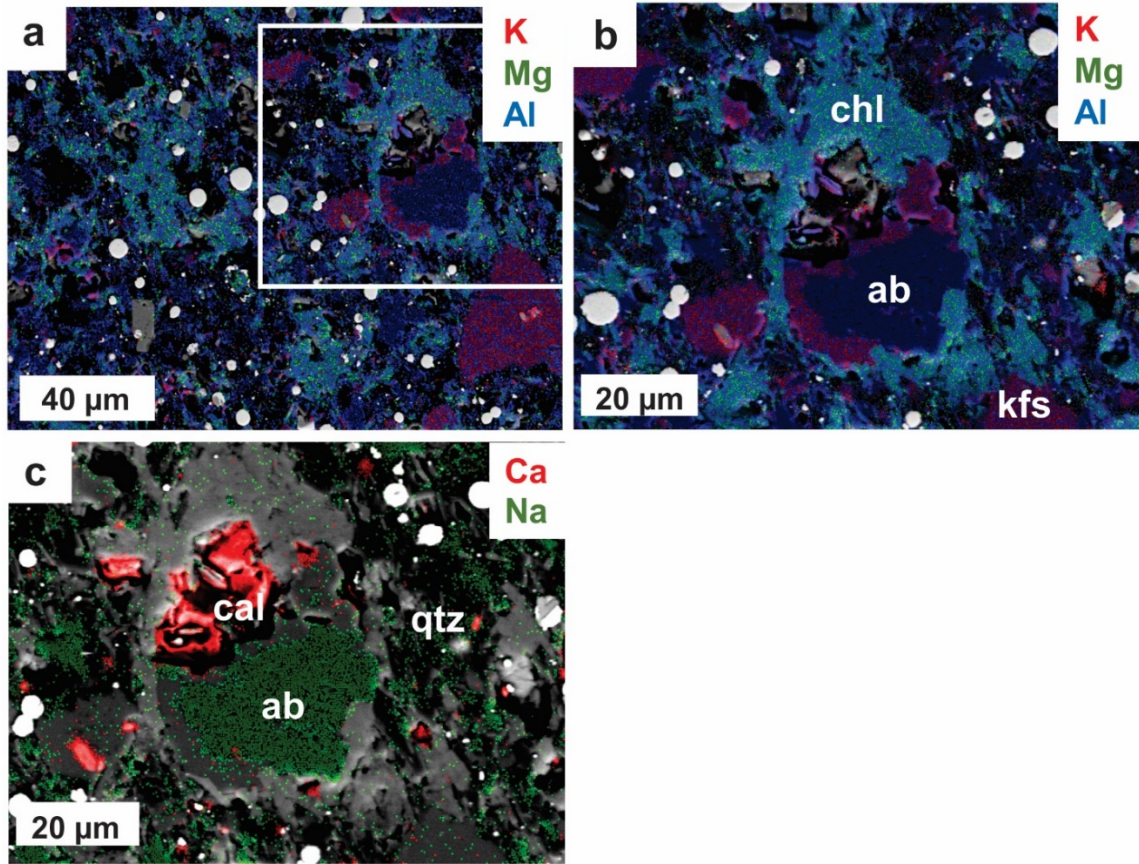


Figure 19: Composition and texture of least-altered matrix from sample DD1012_16 (74 m depth) of the middle diamictite at Kakula, approximately 250 m above the copper-sulphide zone. (a) Oriented SEM-EDS element map (K, Mg, Al). (b) High-magnification SEM-EDS element map (K, Mg, and Al) from a. (c) High-magnification SEM-EDS element map (Ca and Na) showing the composition of the matrix. The matrix consists of albite (ab), K-feldspar (kfs), calcite (cal), quartz (qtz), chlorite (chl), and framboidal pyrite (white). Chlorite locally present surrounding K-feldspar, albite, and calcite. Localised replacement of albite by K-feldspar is present along grain edges. Calcite appears to have been partially dissolved (porous; black). Unlike ore-zone matrix, this sample contains albite and calcite but no muscovite or biotite.

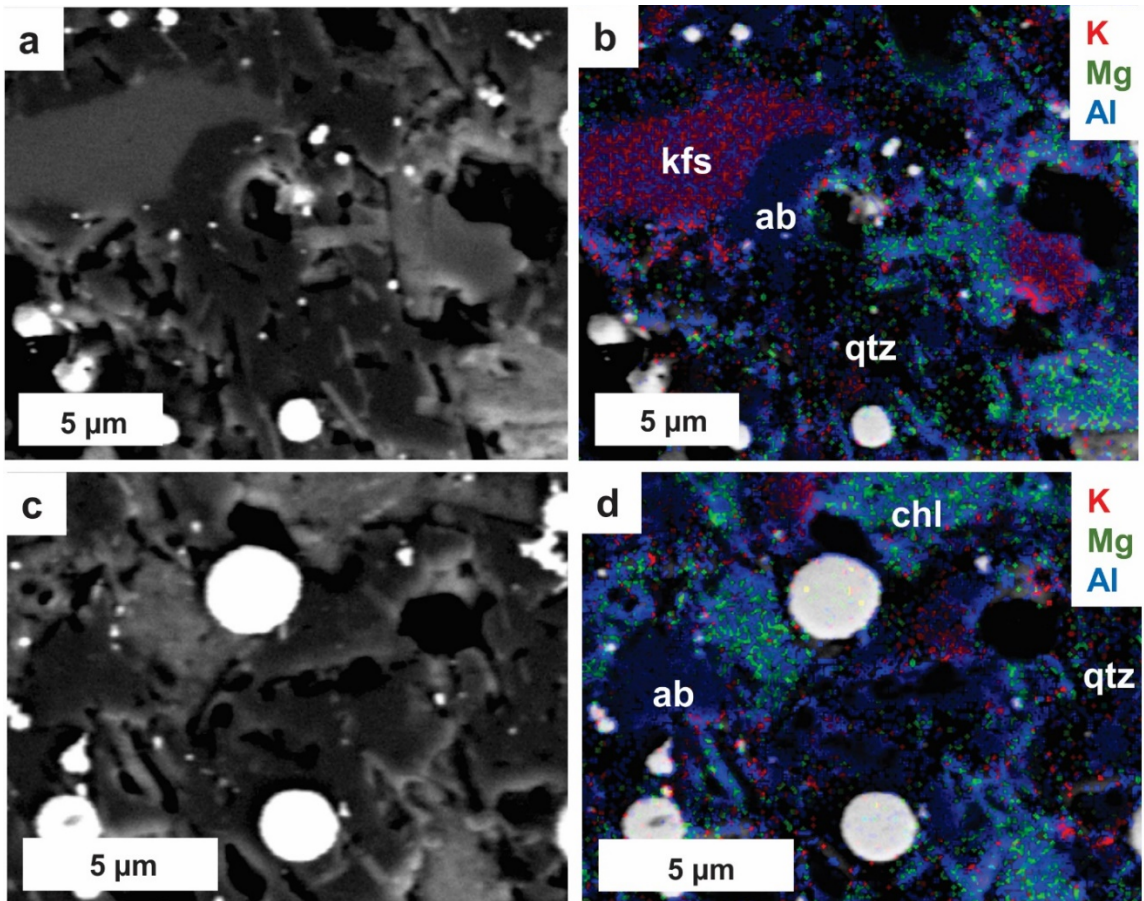


Figure 20: Composition and texture of least-altered matrix from sample DD1012_16 (74 m depth) of the middle diamictite at Kakula at high magnification. (a) Oriented BS-SEM image and (b) oriented SEM-EDS element map (K, Mg, Al) showing the composition of the least-altered matrix to be K-feldspar (kfs), albite (ab), chlorite (chl), quartz (qtz), and pyrite (white). Quartz appears to surround K-feldspar and albite locally, and grain boundaries among matrix components are locally indistinct. (c) Oriented BS-SEM image and (d) oriented SEM-EDS element map (K, Mg, Al) showing pyrite, other matrix minerals, and porosity (black). Pyrite is predominantly framboidal and locally present at the edges of pore space, but locally appears to be enclosed by other matrix minerals.

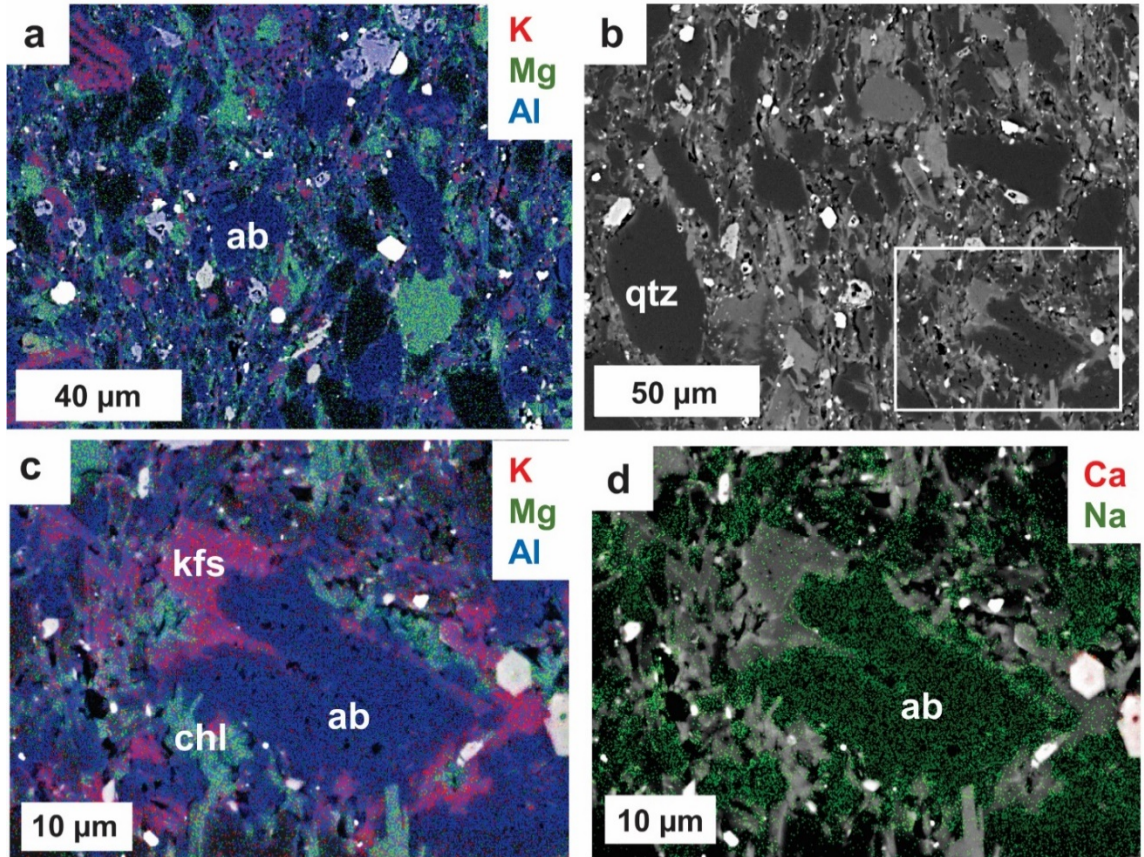


Figure 21: Composition and texture of least-altered matrix from sample DD1161_3 (452 m depth) of the middle diamictite at Kakula. (a) Oriented SEM element map (K, Mg, Al) and (b) oriented SEM image showing the composition of the least-altered matrix. The matrix consists of K-feldspar (kfs), albite (ab), chlorite (chl), quartz (qtz), and pyrite (white). Although not visible in these images, ferroan dolomite is also present in relatively low abundances in this sample and is present instead of calcite. (c) Oriented SEM image and (d) oriented SEM element map (Ca and Na) showing the replacement of an albite grain by K-feldspar and possibly chlorite.

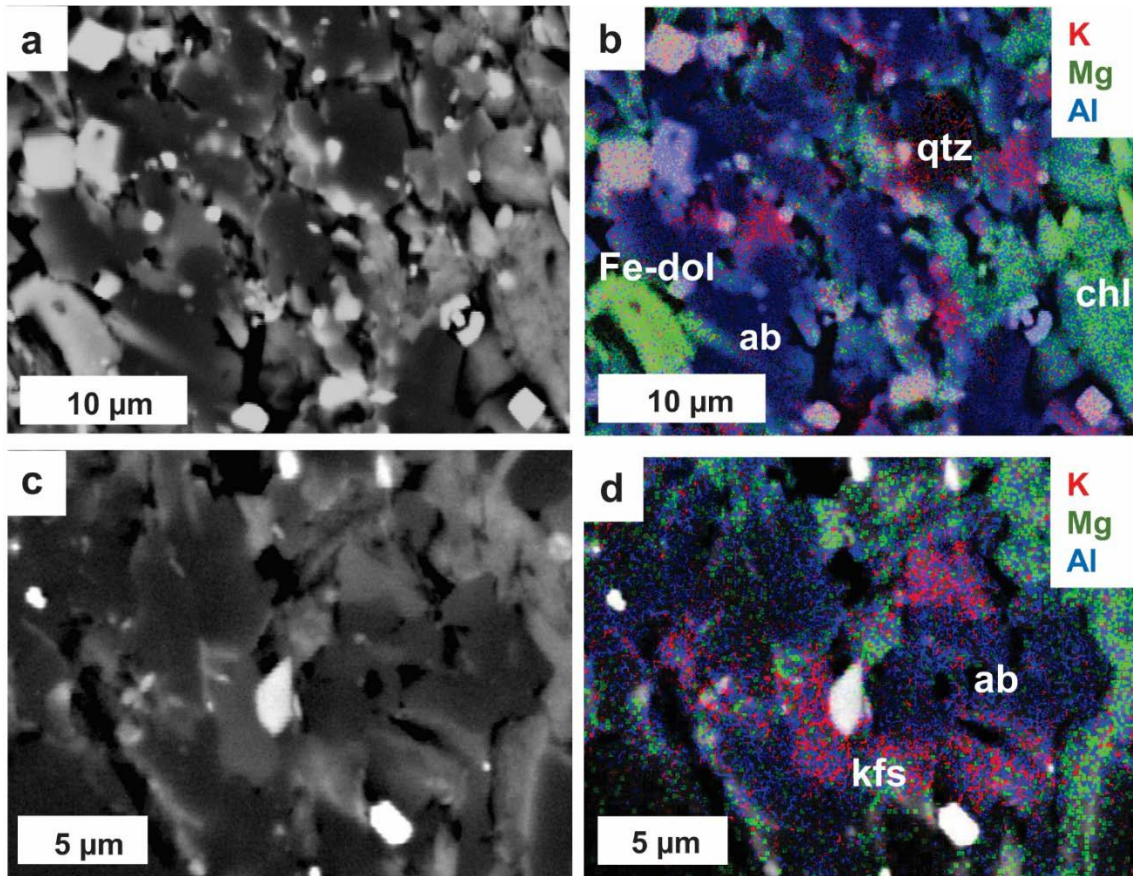


Figure 22: Composition and texture of least-altered matrix from sample DD1161_3 (452 m depth) of the middle diamictite at Kakula. (a) Oriented SEM image and (b) oriented SEM element map (K, Mg, Al) showing the composition of least-altered matrix to be K-feldspar (kfs), albite (ab), chlorite (chl), ferroan dolomite (Fe-dol), quartz (qtz), and pyrite (white) at higher magnification. Albite, quartz, and K-feldspar are commonly subrounded and are probably of detrital origin. (c) Oriented BS-SEM image and (d) oriented SEM_EDS element map (K, Mg, Al), showing matrix porosity (black) and matrix composition. Pyrite is predominantly framboidal but is locally euhedral, and is locally present along the edges of pore space, whereas other pyrite crystals appear to be enclosed by other matrix minerals such as quartz.

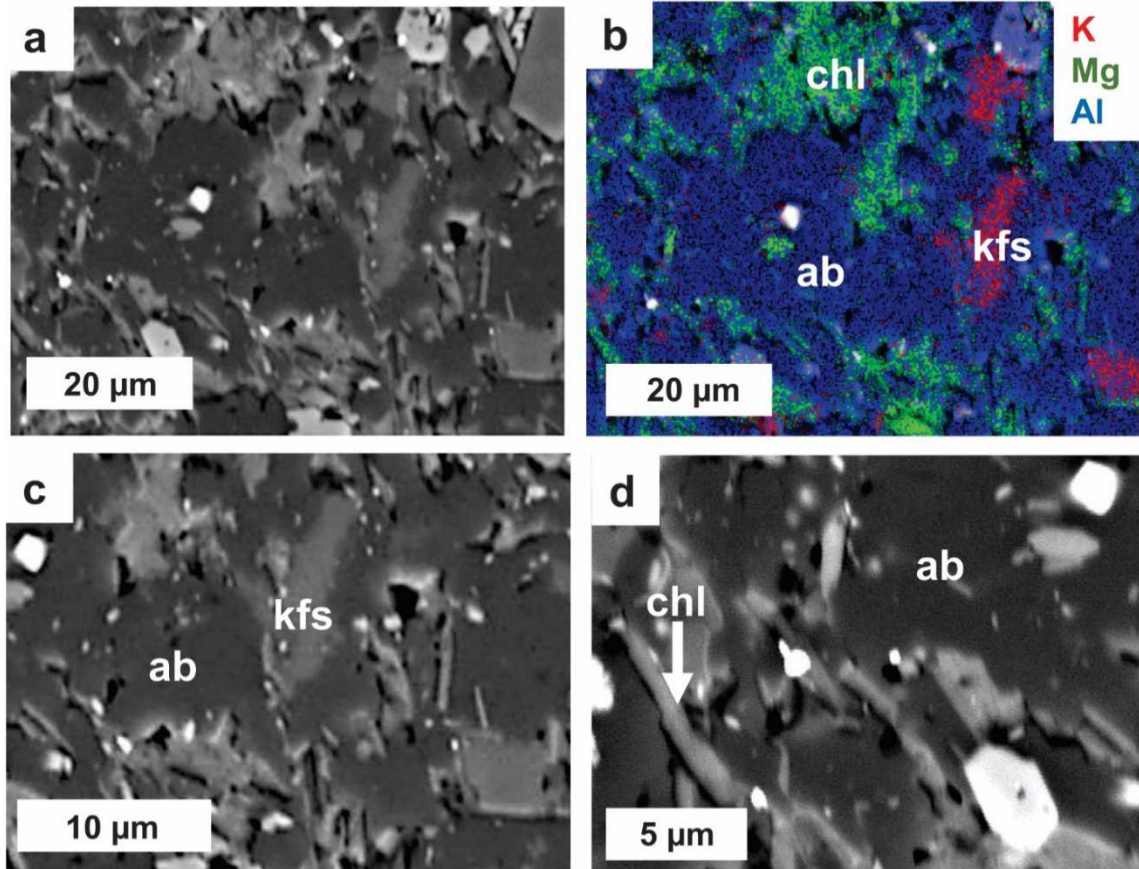


Figure 23: Composition and texture of least-altered matrix from sample DD1161_6 (211 m depth) of the upper diamictite at Kakula. This sample is considered to be farthest from the ore-zone both laterally and vertically. (a) Oriented BS-SEM image and (b) oriented SEM-EDS element map (K, Mg, Al) showing composition of the least-altered matrix. The matrix consists predominantly of albite (ab), with K-feldspar (kfs), chlorite (chl), and pyrite (white) in lower abundance. Ferroan dolomite and quartz are also present in the sample but in lower abundances and not shown in these images. (c and d) Oriented SEM images showing indistinct boundaries among matrix components, which locally gives the matrix a “cemented” appearance.

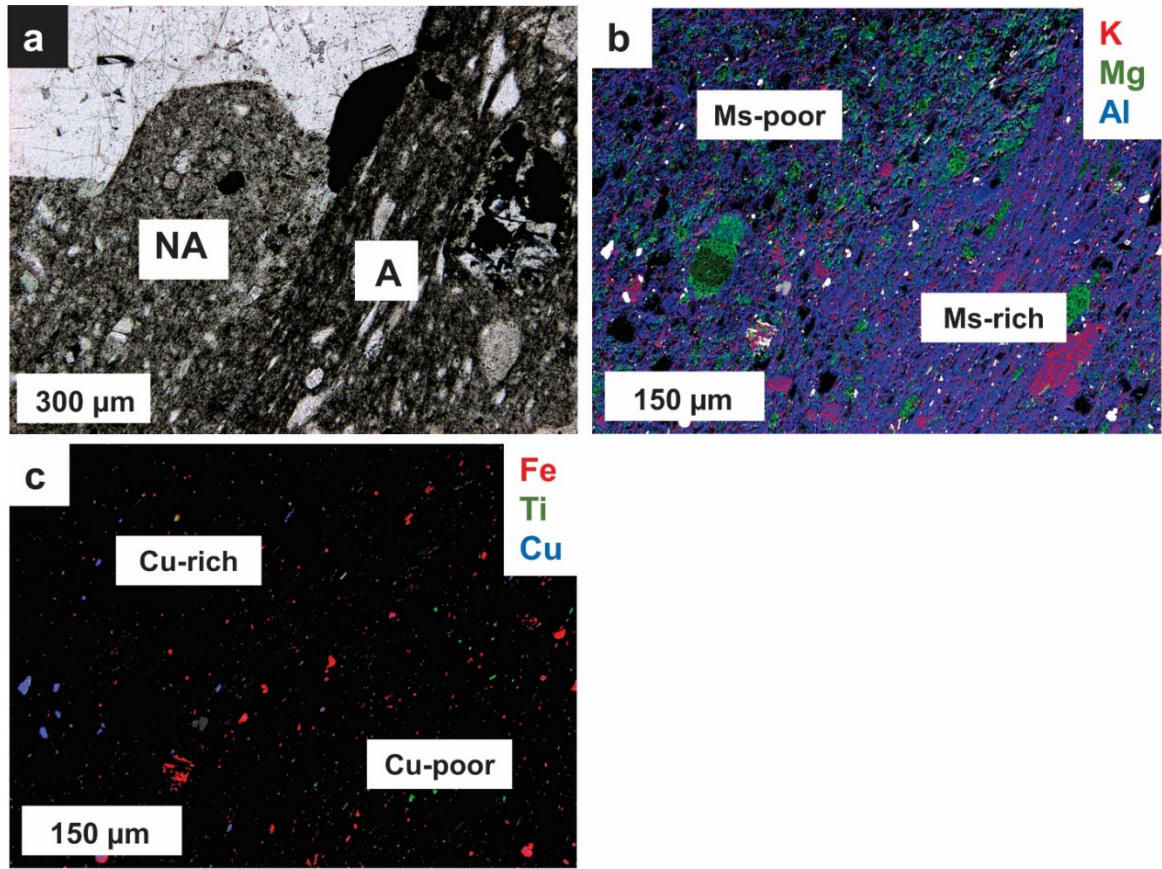


Figure 24: Composition of aligned and non-aligned matrix of ore-zone matrix of basal diamictite at Kakula from sample DD1012_7 (326 m depth). These images are taken at the lower-right side of a large clast. (a) Oriented plane-polarised light photomicrograph showing aligned (A) and non-aligned (NA) matrix at Kakula. (b) Oriented SEM-EDS element map of K, Mg, and Al showing that aligned matrix is muscovite-rich (ms-rich; purple) relative to non-aligned matrix (ms-poor). (c) Oriented SEM-EDS element map of Fe, Ti, and Cu of the same SEM image showing that areas of aligned matrix are copper-poor (Cu-poor) relative to non-aligned matrix (Cu-rich). Notably, there is more hematite (red) and rutile (green) in aligned matrix than non-aligned matrix. Lower copper-sulphide concentrations in aligned matrix suggests that some copper-sulphides were dissolved and possibly replaced during the alignment process, and areas of aligned matrix appear to have been favourable for hematite (and rutile) formation.

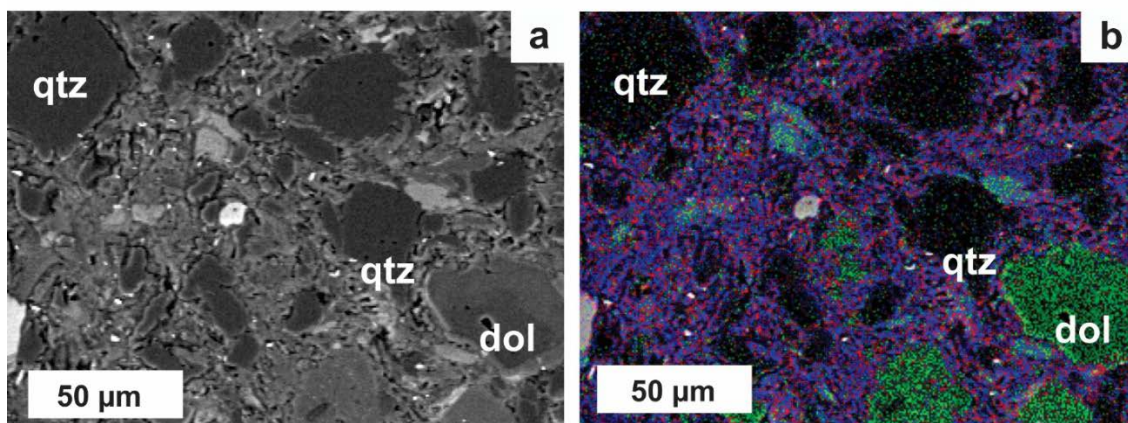


Figure 25: Relatively large, rounded quartz and dolomite in the matrix of sample DD975_3 (255 m depth) in ore-zone matrix of the basal diamictite at Kakula. (a) Oriented backscattered SEM image. (b) Oriented SEM-EDS element map of K, Mg, and Al. The relatively large size and rounded morphology of the quartz suggest a detrital origin. Other minerals visible in the matrix include muscovite, dolomite, and chlorite.

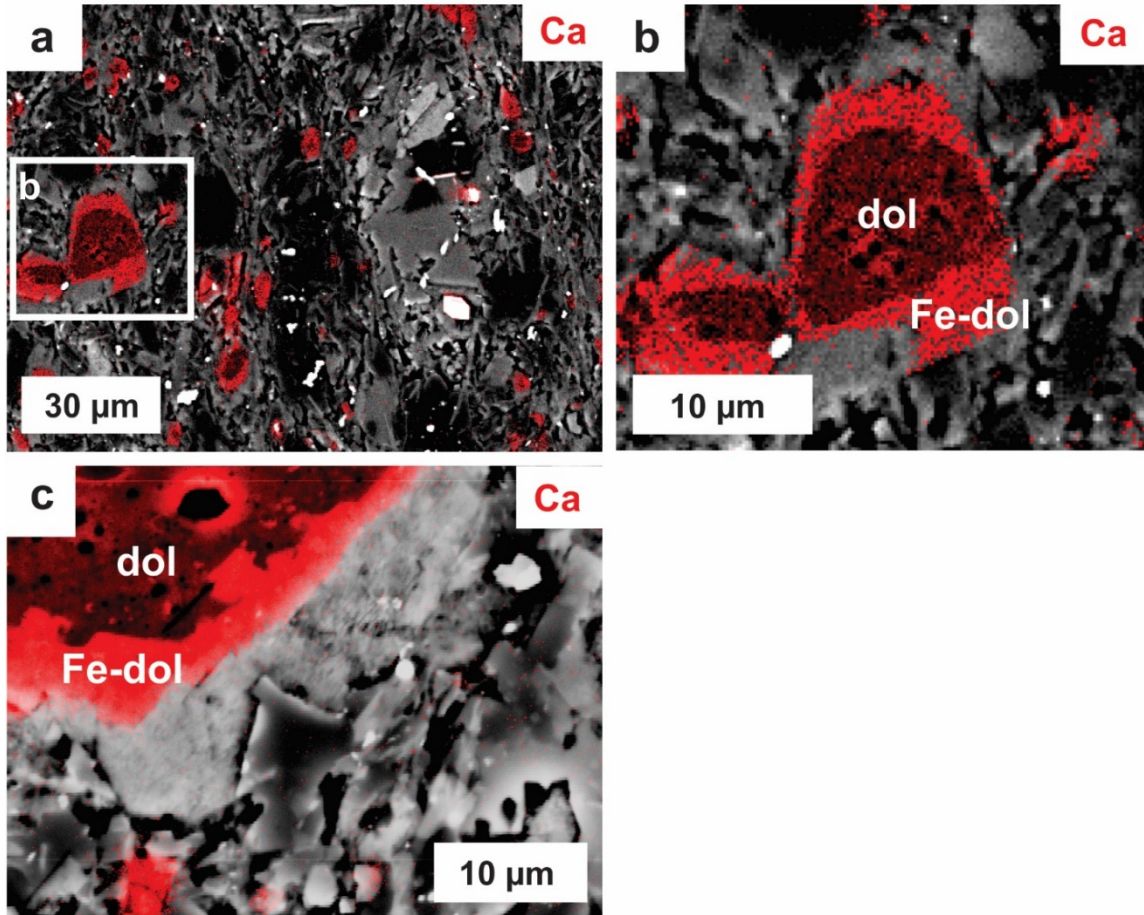


Figure 26: Pure dolomite (dol) and ferroan dolomite (Fe-dol) overgrowths in ore-zone matrix of basal diamictite at Kakula. (a and b) Oriented SEM-EDS element maps of Ca from sample DD975_3 (255 m depth). Pure dolomite (dark red) has ferroan-dolomite overgrowths (bright red). Subrounded to rounded morphologies of pure dolomite suggests a detrital origin. Ferroan dolomite is also present without pure dolomite cores in the matrix, but no pure dolomite has been identified without at least some associated ferroan-dolomite. (c) Oriented SEM-EDS element map of Ca for sample DD975_10 (166 m depth). This image shows ferroan dolomite (Fe-dol) overgrowth on a silt-sized pure dolomite (dol) grain in the matrix. The boundary between pure dolomite (porous) and ferroan dolomite overgrowth (not porous) is irregular.

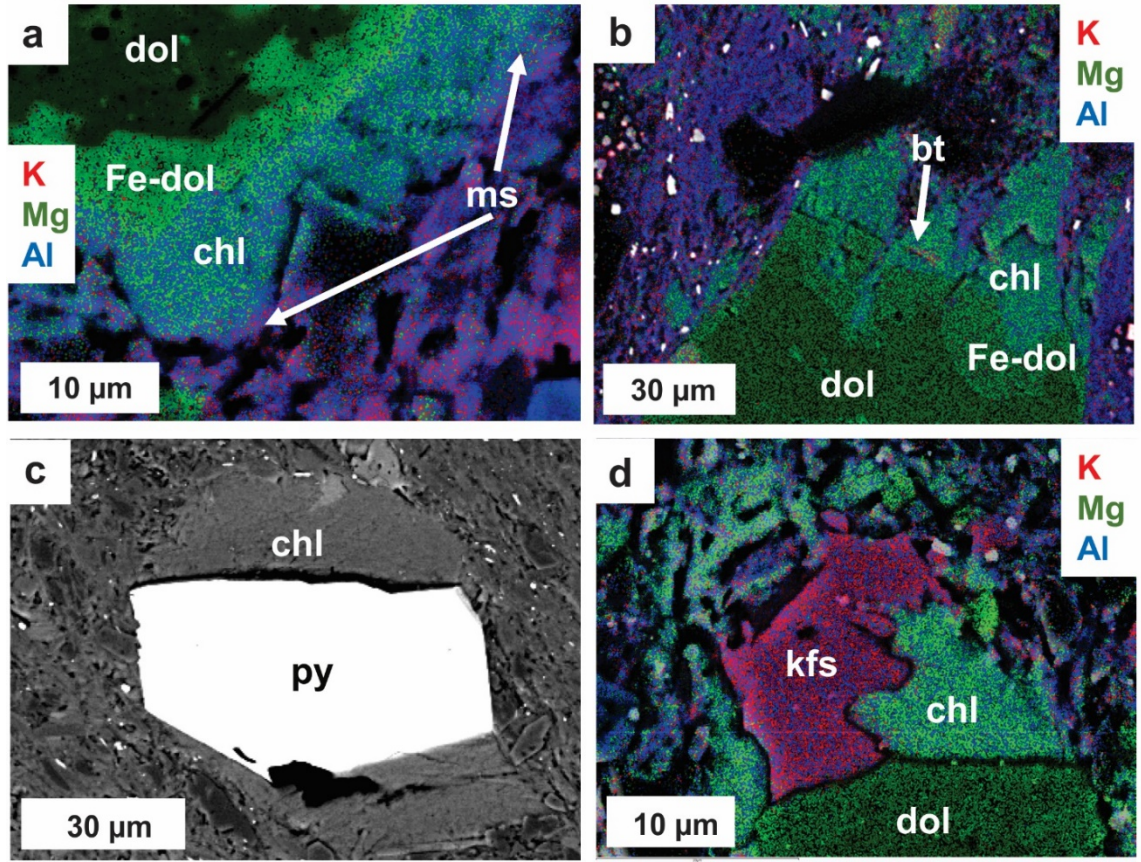


Figure 27: Paragenetic relationships, characteristics, and associations of ore-zone matrix components of basal diamictite at Kakula. (a) Oriented SEM element map (K, Mg, Al) of sample DD975_10 (186 m depth) showing chlorite (chl) overgrowths on ferroan-dolomite (Fe-dol) overgrowths on a matrix silt-sized pure dolomite (dol) grain. Muscovite (Ms) also replaces or overgrows the edges of chlorite (white arrows). (b) Oriented SEM element map (K, Mg, Al) sample DD1012_9 (317 m depth) showing chlorite and minor biotite (bt) on a ferroan dolomite (Fe-dol) overgrowth on a fine-sand-sized pure dolomite (dol) grain. (c) Oriented backscattered SEM image of sample DD1012_9 (317 m depth) showing chlorite (chl) growth on a euhedral pyrite (py), illustrating that chlorite formed after pyrite. (d) Oriented SEM element map (K, Mg, Al) of sample DD975_10 (186 m depth) of a matrix silt-sized dolomite grain being overgrown by chlorite (chl) and K-feldspar (kfs). The chlorite and K-feldspar appear to have formed at approximately the same time.

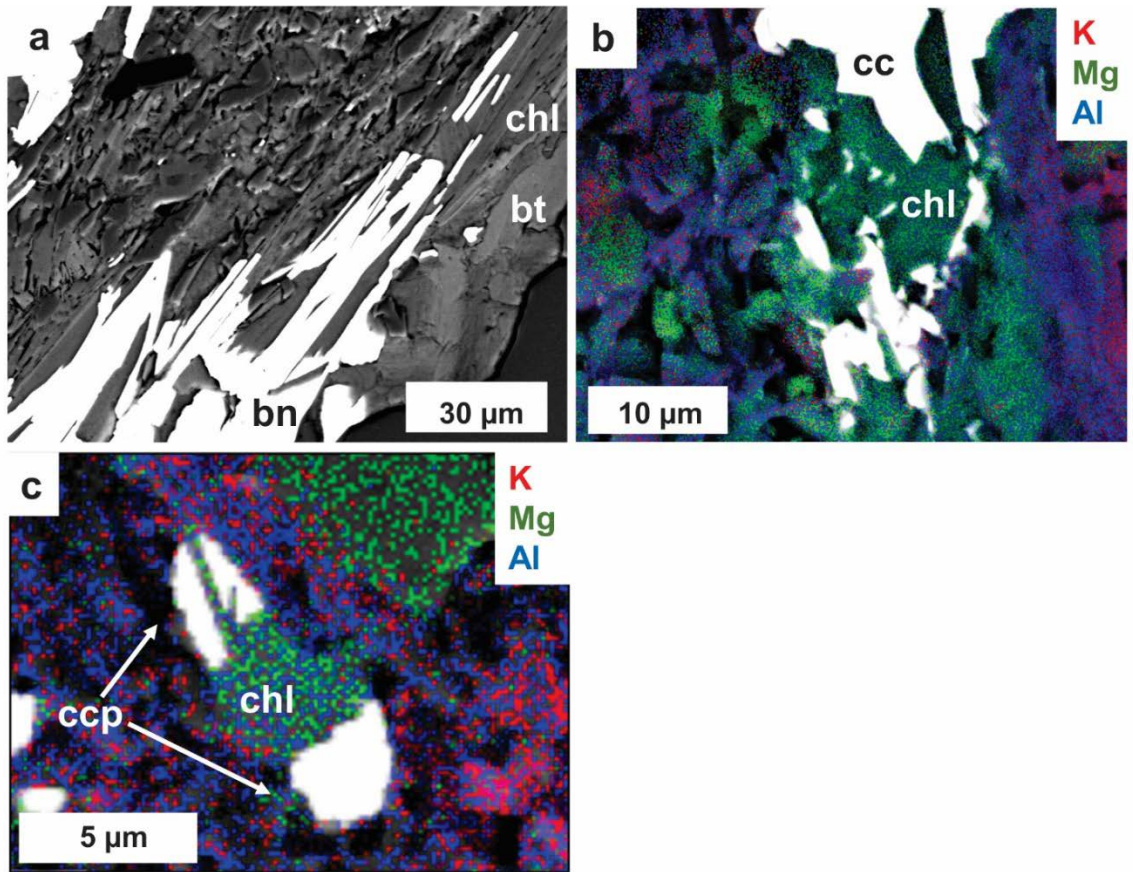


Figure 28: Paragenetic relationships among matrix components and copper-sulphides of ore-zone matrix of the basal diamictite at Kakula. (a) Oriented backscattered SEM image from sample DD1012_7 (326 m depth) of bornite (bn), chlorite (chl), and biotite (bt) as a small cap above a quartz-rich sand-sized clast. Bornite is present along chlorite mineral cleavage and appears to have formed at the same time as chlorite based on their spatial relationship and composition. (b) Oriented SEM-EDS element map (K, Mg, Al) from sample DD975_3 (255 m depth) showing the spatial association of chlorite (chl) with copper-sulphides in the matrix, in this case chalcocite (cc). (c) Oriented SEM element map (K, Mg, Al) from sample DD975_6 (218 m depth) showing the association of chlorite with copper-sulphides, in this case chalcopyrite (ccp). Although it is not entirely clear at this small scale, chalcopyrite appears to have formed along chlorite mineral cleavage and formed around the same time as chlorite.

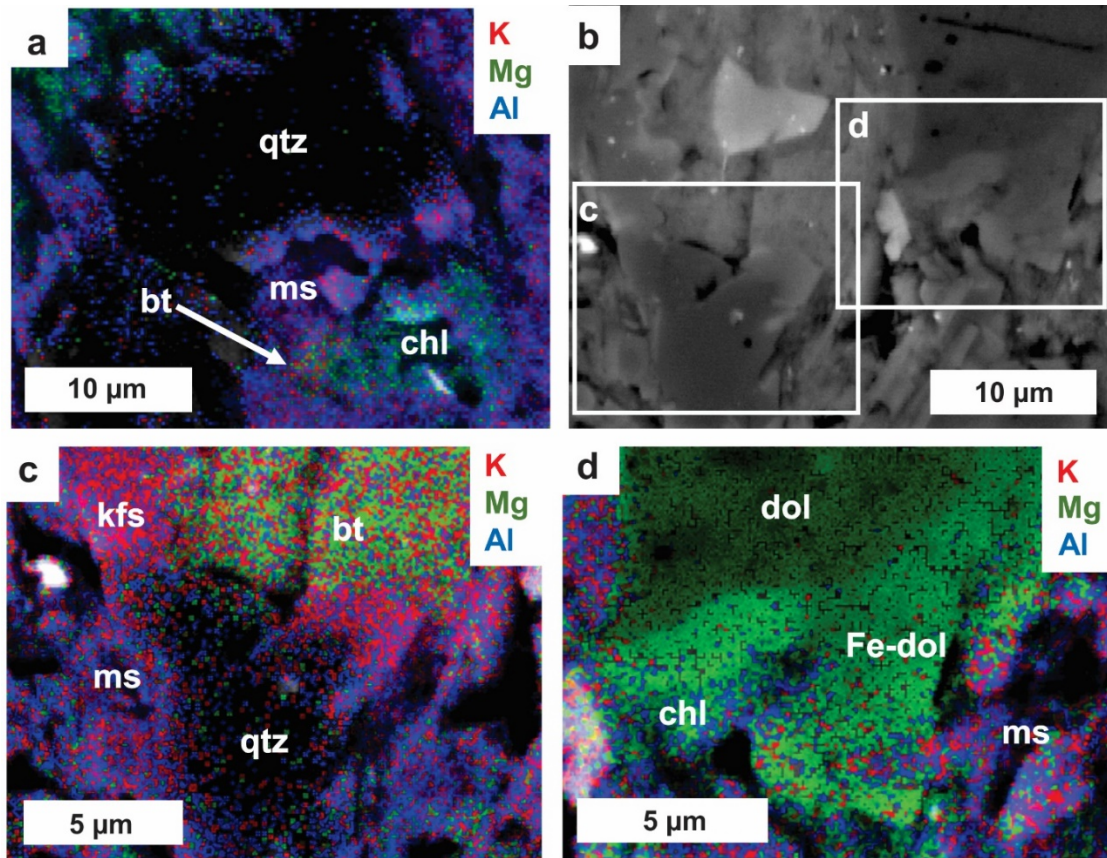


Figure 29: Paragenetic relationships, characteristics, and associations of ore-zone matrix components of the basal diamictite from Kakula from sample DD975_3 (255 m depth). (a) Oriented SEM-EDS element map (K, Mg, Al) showing quartz (qtz) and chlorite (chl) ± biotite (bt) overgrown and/or replaced by muscovite (ms). (b) Oriented SEM image of matrix with two areas of interest for paragenetic relationships. (c) Oriented SEM-EDS element map (K, Mg, Al) showing biotite (bt) that appears to have been locally replaced or overgrown by quartz (qtz) and K-feldspar (kfs). Quartz and K-feldspar are in turn replaced or overgrown by muscovite (ms). (d) Oriented SEM-EDS element map (K, Mg, Al) showing the edges of ferroan dolomite (Fe-dol) and dolomite (dol) being overgrown and/or replaced by muscovite (ms).

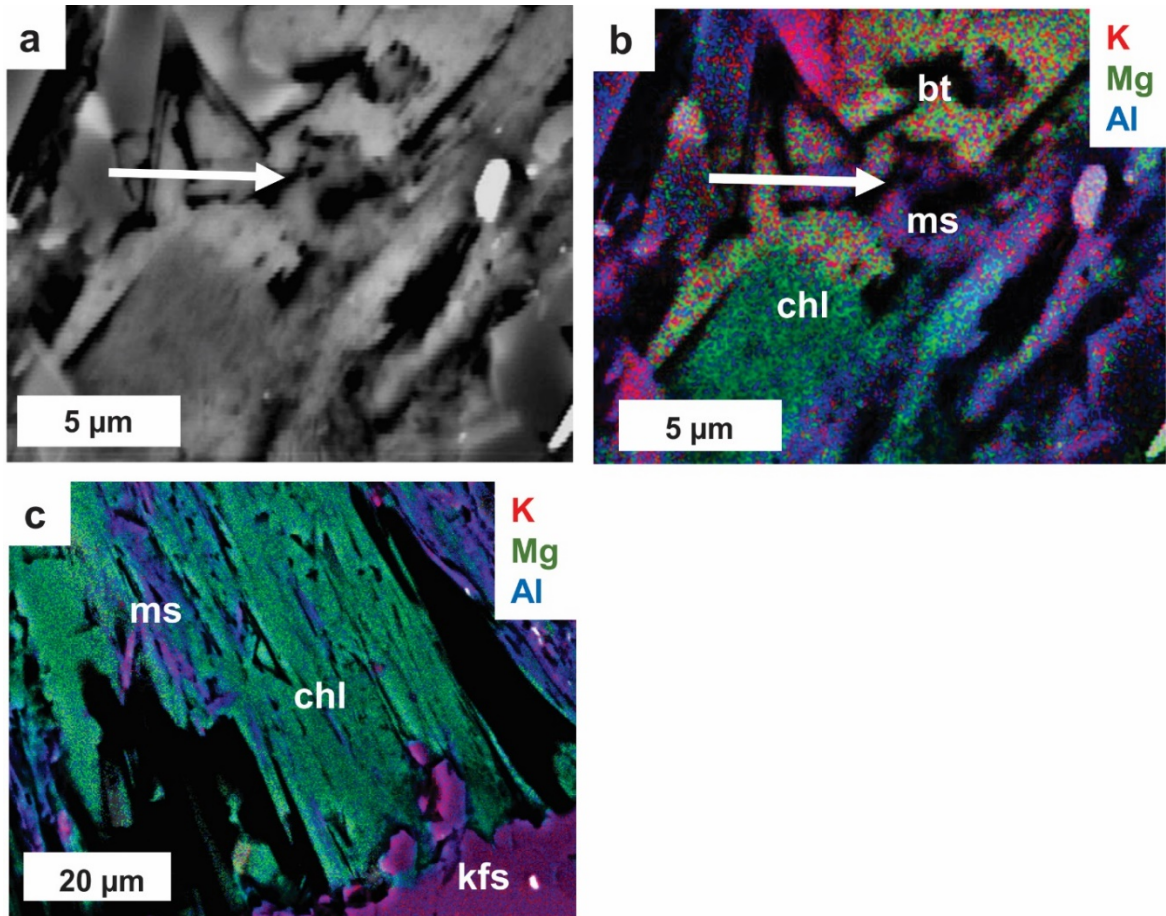


Figure 30: Paragenetic relationships, characteristics, and associations of ore-zone matrix components of the basal diamictite at Kakula. (a) Oriented BS-SEM image of DD1012_7 (326 m depth); white arrow points to area of ragged pores (black) in biotite, possibly caused by dissolution. (b) Oriented SEM-EDS element map (K, Mg, Al) showing what appears to be biotite (bt) ± chlorite (chl) dissolution and the formation of muscovite (ms) and pores (black) at the site of dissolution. (c) Oriented SEM element map (K, Mg, Al) of sample DD975_3 (255 m depth) showing chlorite (chl) on sand-sized detrital K-feldspar (kfs) grain. Chlorite is replaced along mineral cleavage by paragenetically late muscovite. Porosity (black) is also present along chlorite mineral cleavage.

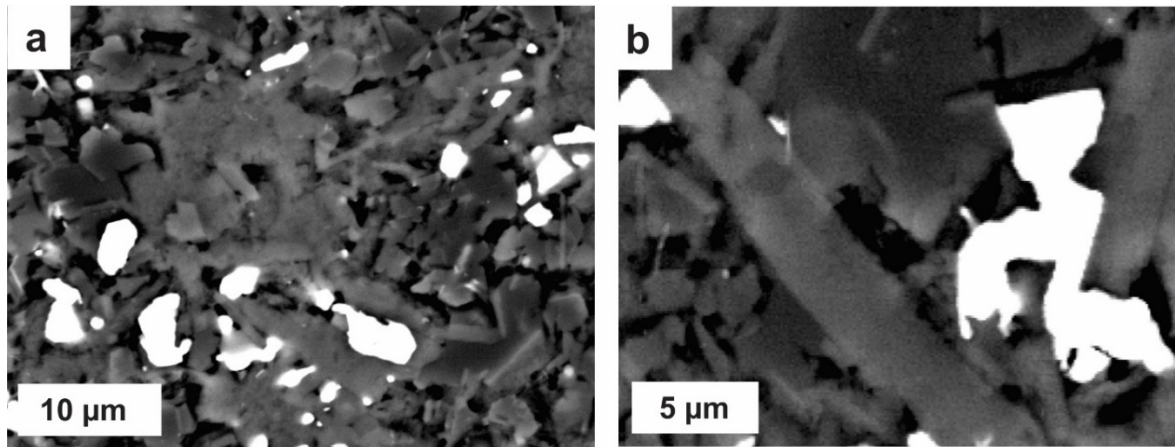


Figure 31: Disseminated copper-sulphides (white) in non-aligned (textureless) matrix at high magnification in ore-zone matrix of the basal diamictite at Kakula. (a) Oriented BS-SEM image of sample DD1012_6 (335 m depth) showing disseminated chalcocite (white) in the matrix. (b) Oriented backscattered SEM image of sample DD975_3 (255 m depth) showing disseminated chalcocite in the matrix. The measured porosity in image a and image b are 11.9 and 11.6%, respectively. The average porosity volume varies between 8 and 12.5% in non-aligned matrix. Copper-sulphide minerals have diverse shapes and sizes but are typically $\leq 5 \mu\text{m}$ and not elongated unless present in aligned matrix. Copper-sulphide minerals are locally rounded, but elsewhere have irregular shapes and appear to form along the edges of or inside matrix pores. In this case, there is a pronounced lack of copper-sulphide minerals with morphologies indicating direct replacement of framboidal pyrite.

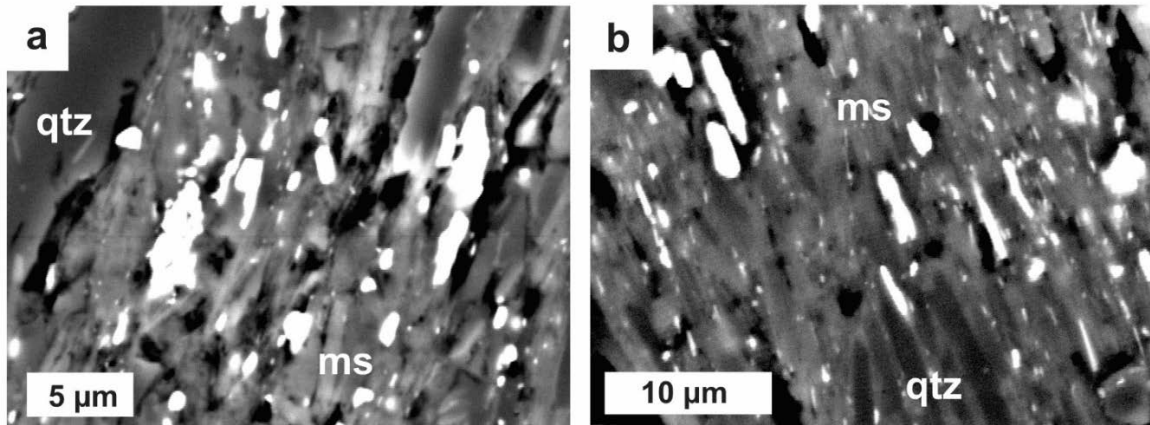


Figure 32: Disseminated copper-sulphide minerals (white) in aligned matrix at high magnification of ore-zone matrix of the basal diamictite at Kakula. (a) Oriented backscattered SEM image of sample DD1012_6 (335 m depth). (b) Oriented backscattered SEM image of sample DD1012_7 (326 m depth). In areas of relatively strong matrix alignment, copper-sulphide minerals and other minerals, such as quartz (qtz) and muscovite (ms) are commonly elongated. Minor hematite and rutile is also present. The porosity was measured at 7.4% in figure a, and 4% in figure b, which is noticeably lower than the porosity measured for non-aligned matrix figures from figure 31. Although it cannot be confirmed if copper-sulphide grains are completely enclosed by individual matrix minerals, they appear to be, at least, tightly surrounded.

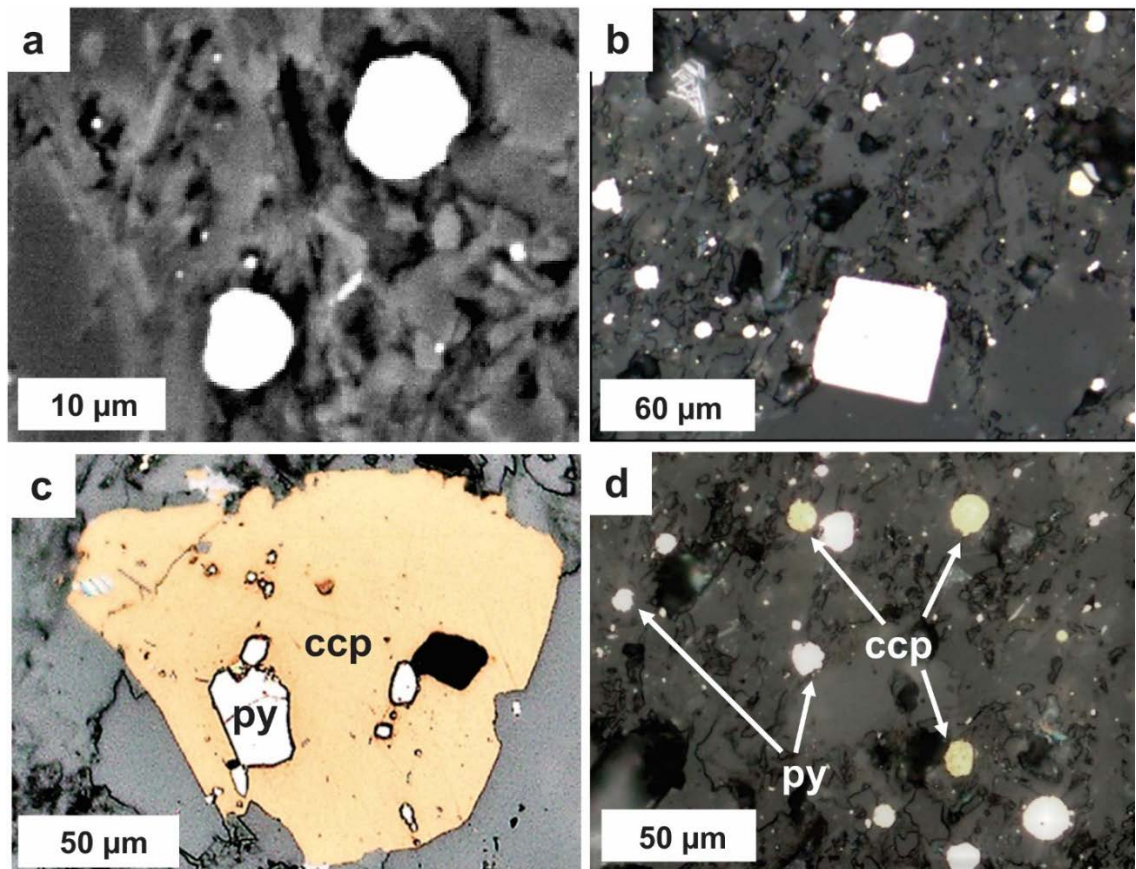


Figure 33: Pyrite and chalcopyrite relationships and morphologies of ore-zone matrix of the basal diamictite at Kakula. Although pyrite is rare in copper-sulphide zones, it locally coexists with chalcopyrite in low-grade sections. (a) Oriented BS-SEM image from sample DD975_10 (186 m depth) showing framboidal pyrite (white). Pyrite locally appears to be present at the edges of matrix porosity. (b) Oriented reflected light photomicrograph of sample DD1012_11 (304 m depth) of pyrite framboids and euhedra (white). Euhedral pyrite is commonly larger than framboidal pyrite. (c) Oriented reflected-light photomicrograph from sample DD1161_1 (889 m depth) showing euhedral and framboidal pyrite (py) overgrown by chalcopyrite (ccp). It is not clear if the chalcopyrite replaces matrix or represents an individual matrix grain. (d) Oriented reflected light photomicrograph of sample DD1012_11 (304 m depth) of framboidal pyrite (py) and chalcopyrite (ccp). The similar size and shape of framboidal pyrite to chalcopyrite suggests the replacement of pyrite by chalcopyrite.

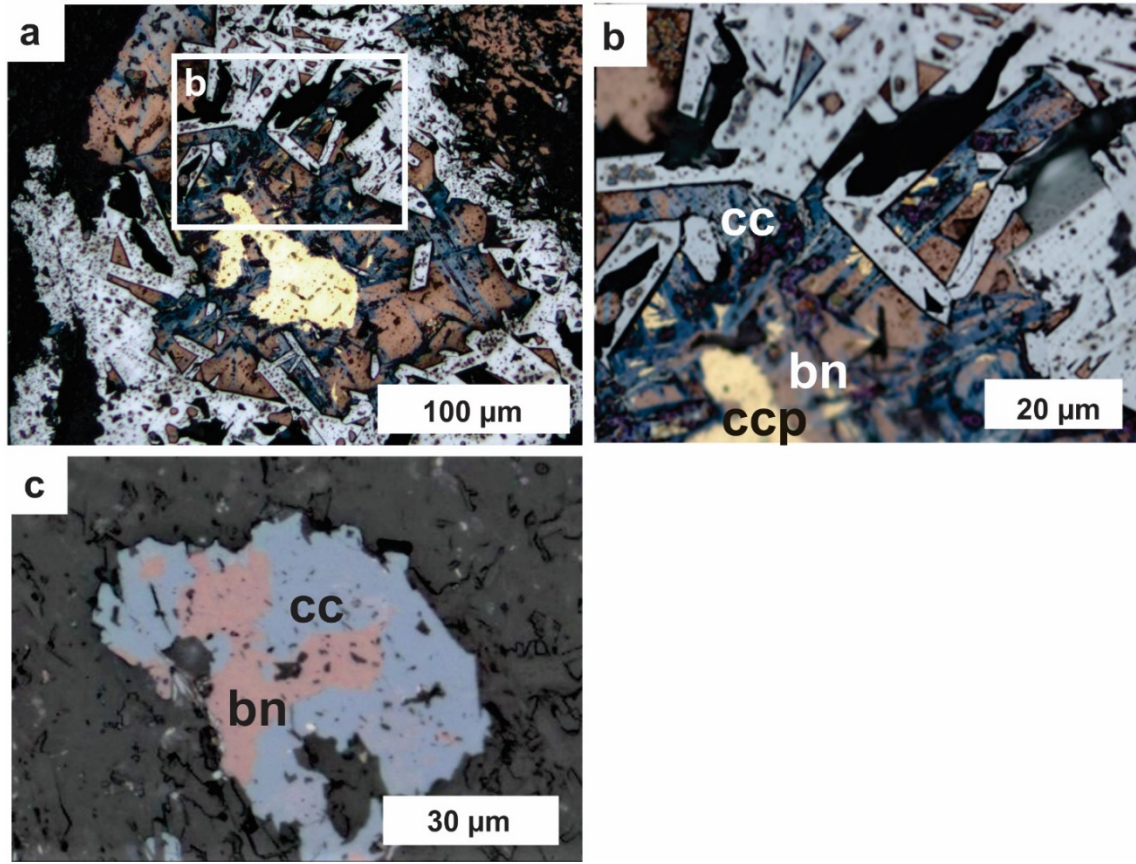


Figure 34: Paragenetic relationships of hematite and copper-sulphides of ore-zone matrix of the basal diamictite. (a and b) Oriented reflected-light photomicrographs of sample DD975_5 (225 m depth) showing the progressive replacement of copper-sulphides by more copper-rich copper-sulphides and later hematite. Chalcopyrite (ccp) is replaced by bornite (bn), in turn replaced by chalcocite (cc). Hematite (hem) has a bladed morphology and replaces, cross-cuts, and encloses copper-sulphides, especially bornite. It is not clear if the copper-sulphide minerals replace matrix or represent an individual matrix grain. (c) Oriented reflected light photomicrograph in of sample DD975_4 (240 m depth) of silt-sized bornite (bn) enclosed by chalcocite (cc). Bornite may have been replaced or overgrown by chalcocite (cc), predominantly on its outer edges.

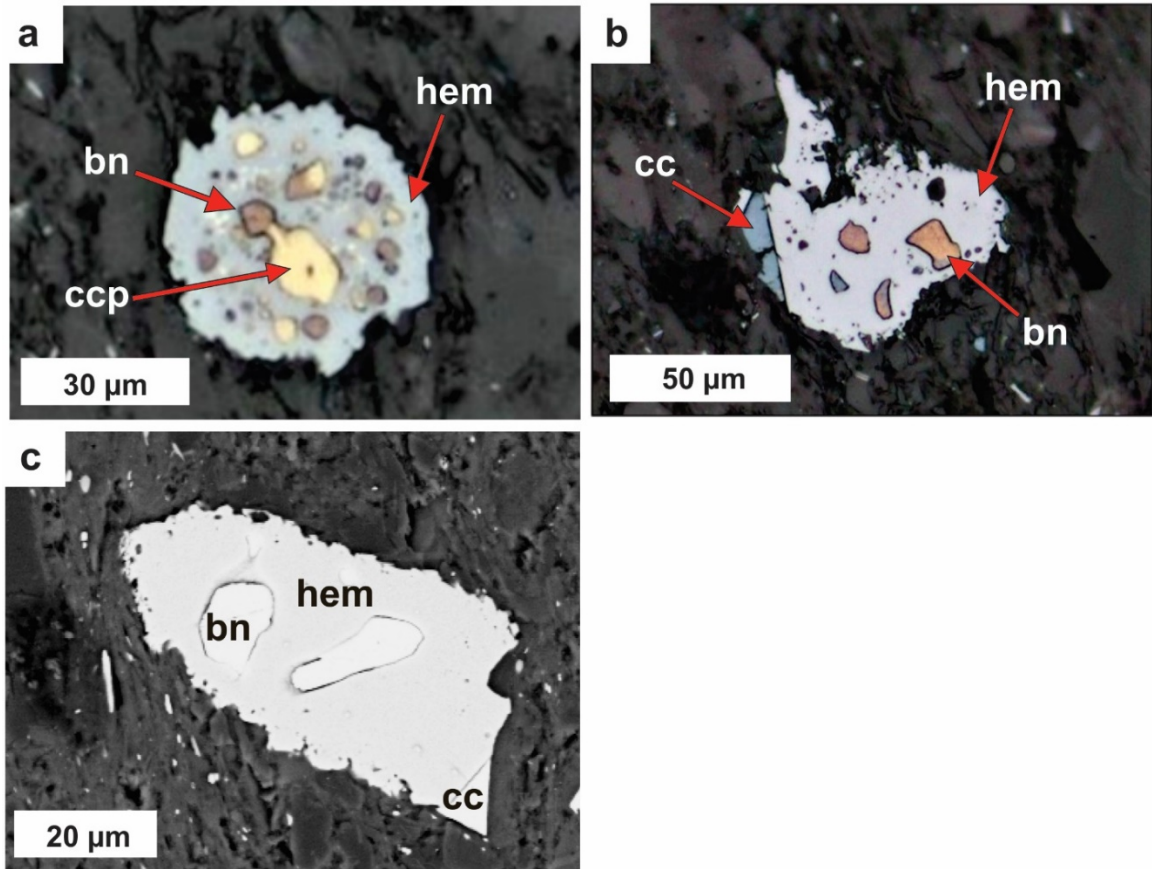


Figure 35: Paragenetic relationships of hematite and copper-sulphides of ore-zone matrix of the basal diamictite at Kakula. (a) Oriented reflected light photomicrograph of sample DD975_6 (218 m depth) showing sphaeroidal hematite (hem) enclosing bornite and chalcopyrite inclusions. Hematite coexists predominantly with chalcocite and lesser bornite; it rarely coexists with chalcopyrite and has not been identified in zones where chalcopyrite is the only copper-sulphide species. (b) Oriented reflected light photomicrograph of sample DD1012_7 (326 m depth) and showing bornite (bn) ± chalcocite (cc) inclusions in hematite (hem). Chalcocite (cc) appears to have formed with hematite. (c) Oriented SEM image of sample DD1012_7 (326 m depth) of rounded bornite (bn) inclusions in hematite (hem). Copper-sulphides and hematite are typically smaller than shown here.

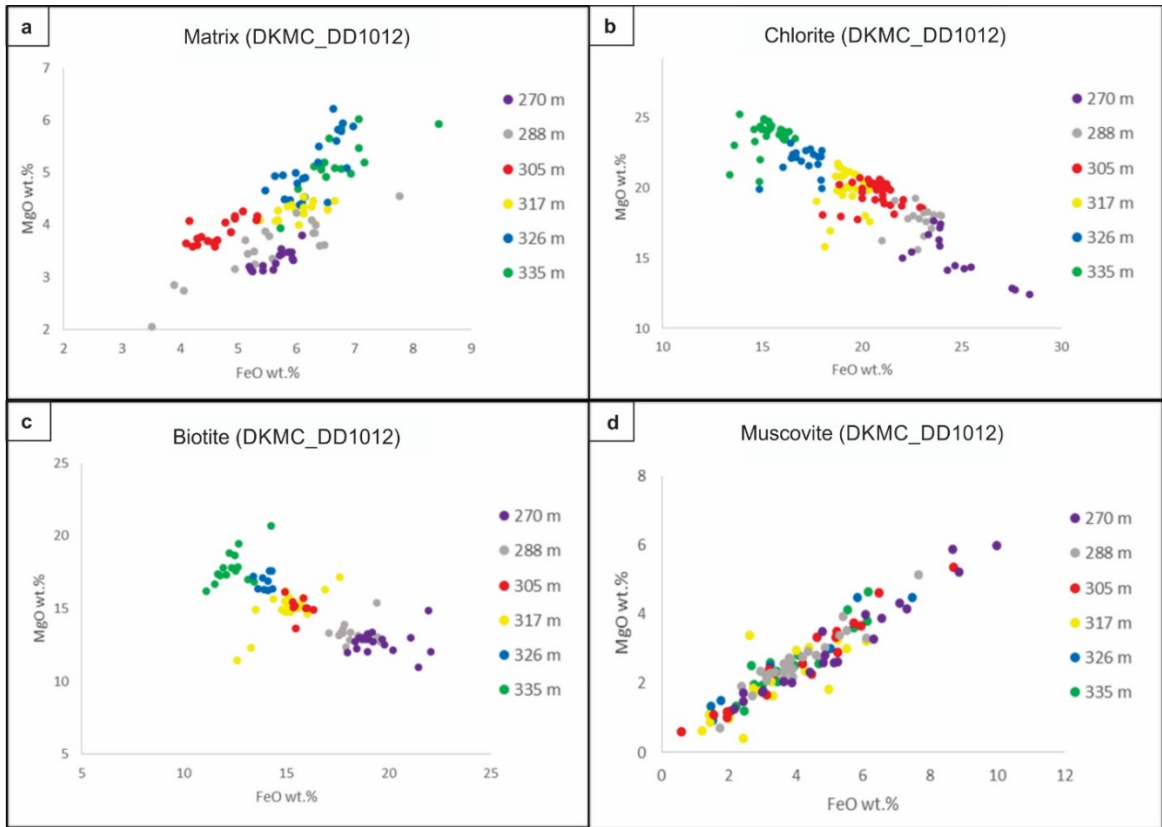


Figure 36: Chemical analyses of FeO versus MgO wt% for six samples of diamictite from the high-grade drill-hole DKMC_DD1012 of ore-zone matrix of the basal diamictite at Kakula for (a) “bulk” matrix of non-aligned matrix, (b) chlorite, (c) biotite, and (d) muscovite. The colours correspond to each sample analysed and their corresponding depths. The scatter plots illustrate the progression from relatively Mg-rich to relatively Fe-rich chlorite and biotite up-section, which happens over short vertical distances irrespective of “bulk” matrix FeO to MgO wt% ratios. The composition of chlorite and biotite is more likely controlled, primarily, by the composition and characteristics of a migrating fluid rather than bulk-rock composition; relatively Mg-rich chlorite and biotite in relatively high-copper grade zones suggest strong correlation among chlorite, biotite, and copper-sulphides (\pm hematite). Moreover, chlorite and biotite composition is essentially homogeneous in a given sample, which is consistent with one single generation of chlorite and biotite. Muscovite also contains notable FeO and MgO wt%, but its composition is heterogeneous and does not show a stratigraphic trend as do biotite and chlorite. These relationships suggest that muscovite did not form at the same time as chlorite and biotite. The variability in muscovite composition may be because muscovite formed through replacement and breakdown of a variety of different minerals.

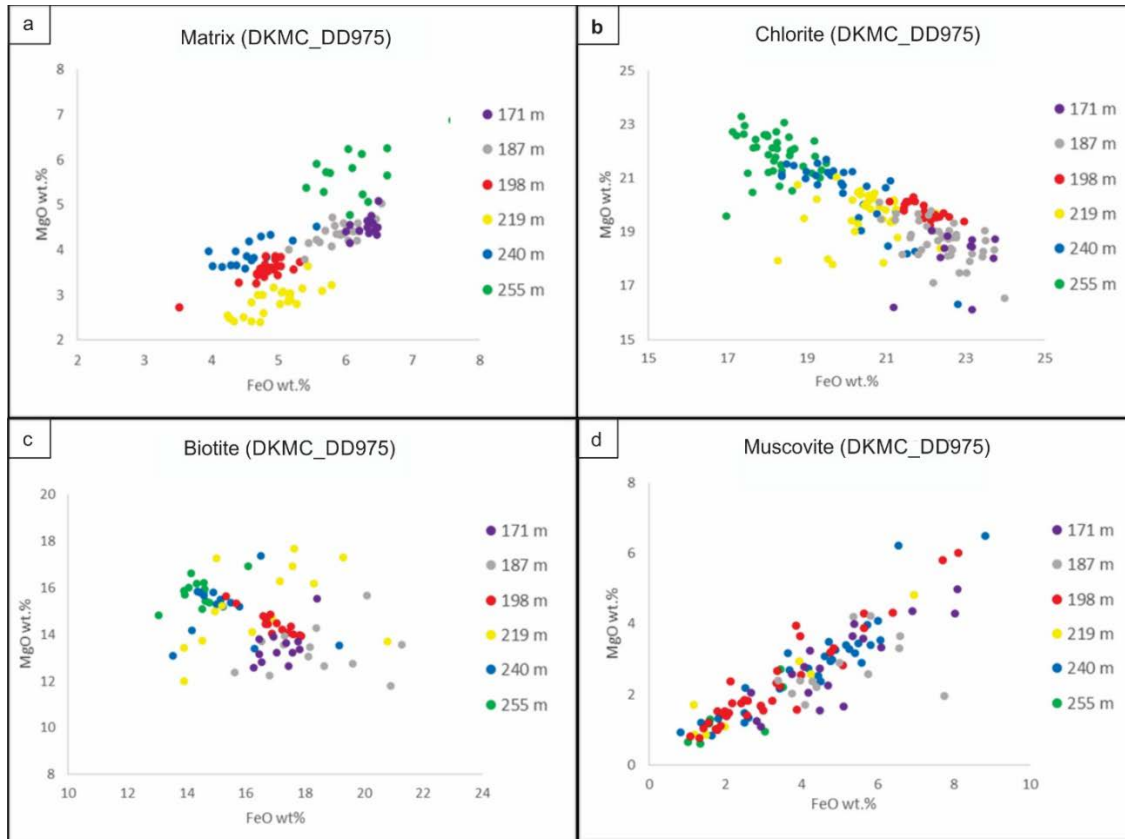


Figure 37: Chemical analyses of FeO versus MgO wt% for six samples of diamictite from the low-grade drill-hole DKMC_DD975 of ore-zone matrix of the basal diamictite at Kakula for (a) “bulk” matrix of non-aligned matrix, (b) chlorite, (c) biotite, and (d) muscovite. The colours correspond to each sample analysed and their corresponding depths. Although the systematic trend in FeO and MgO wt% in chlorite and biotite is not as drastic as in DKMC_DD1012, the observations and interpretations are the same. Moreover, the observations for “bulk” matrix and muscovite are also consistent with what was observed in DKMC_DD1012.

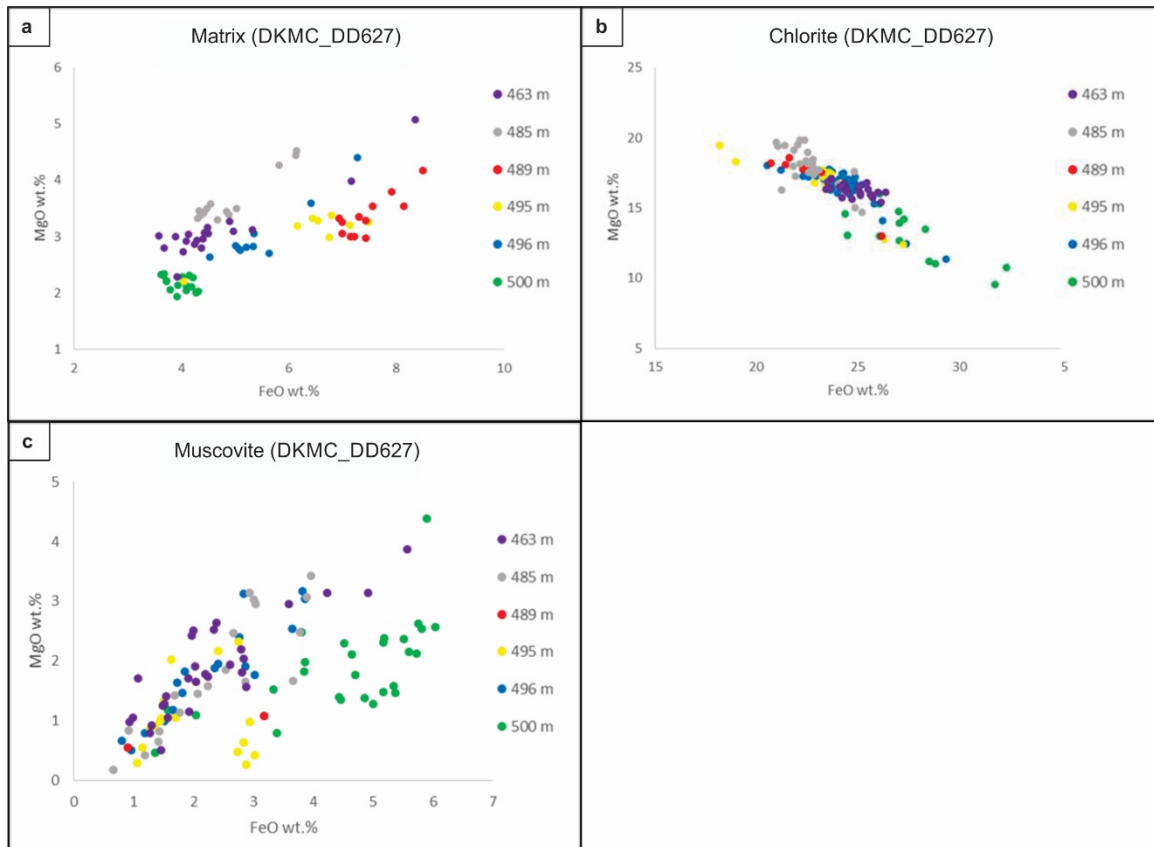


Figure 38: Chemical analyses of FeO versus MgO wt% for six samples of diamictite from the high-grade drill-hole DKMC_DD627 of ore-zone matrix of the basal diamictite at Kamoia for (a) “bulk” matrix of non-aligned matrix, (b) chlorite, and (d) muscovite. Not enough biotite could be identified in every sample to document compositional trends. The colours correspond to each sample analysed and their corresponding depths. Similar to Kakula, chlorite MgO and FeO wt% ratios change over short vertical distances irrespective of “bulk” matrix FeO to MgO wt% ratios. However, chlorite is more Fe-rich in the lowermost relatively copper-poor, clast-rich diamictite sample, becomes Mg-rich in the copper-rich, clast-poor diamictite samples, and then becomes Fe-rich upwards away from mineralisation. This trend further illustrates the association of copper-sulphides and MgO and FeO wt% ratios in chlorite. Muscovite also contains significant FeO and MgO wt%, has heterogeneous composition, and does not show a trend like biotite and chlorite. However, there appears to be more variability in the FeO to MgO wt% ratio of muscovite at Kamoia than at Kakula.

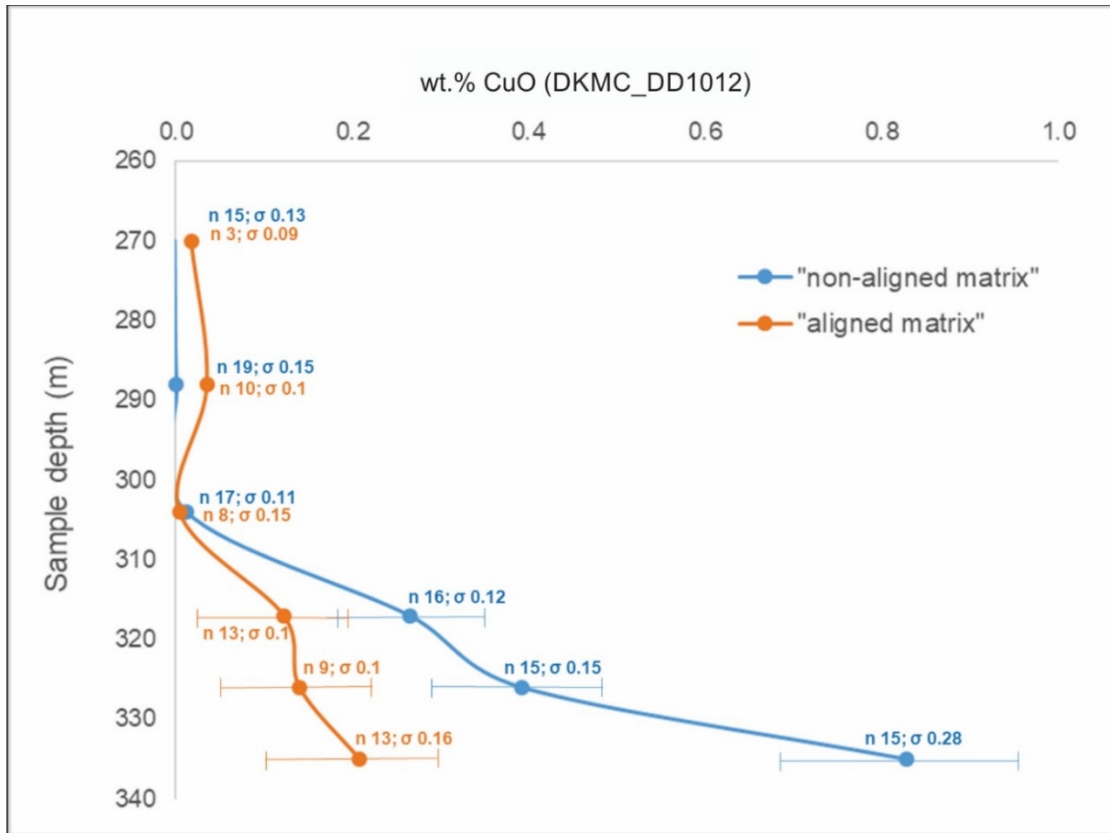


Figure 39: Chemical analysis showing the average copper concentration (CuO wt%) of aligned and non-aligned matrix versus depth from six samples of high-grade drill-hole DKMC_DD1012 in ore-zone matrix of the basal diamictite at Kakula. This graph illustrates two important phenomena: (1) there is a steady up-section decrease in copper grade, and (2) non-aligned matrix has relatively high copper concentrations compared to aligned matrix. The relatively low copper concentrations in aligned matrix relative to non-aligned matrix suggests that copper-sulphides were dissolved during the alignment process. Instrument error, # of analyses (n), and standard deviations (σ) are indicated.

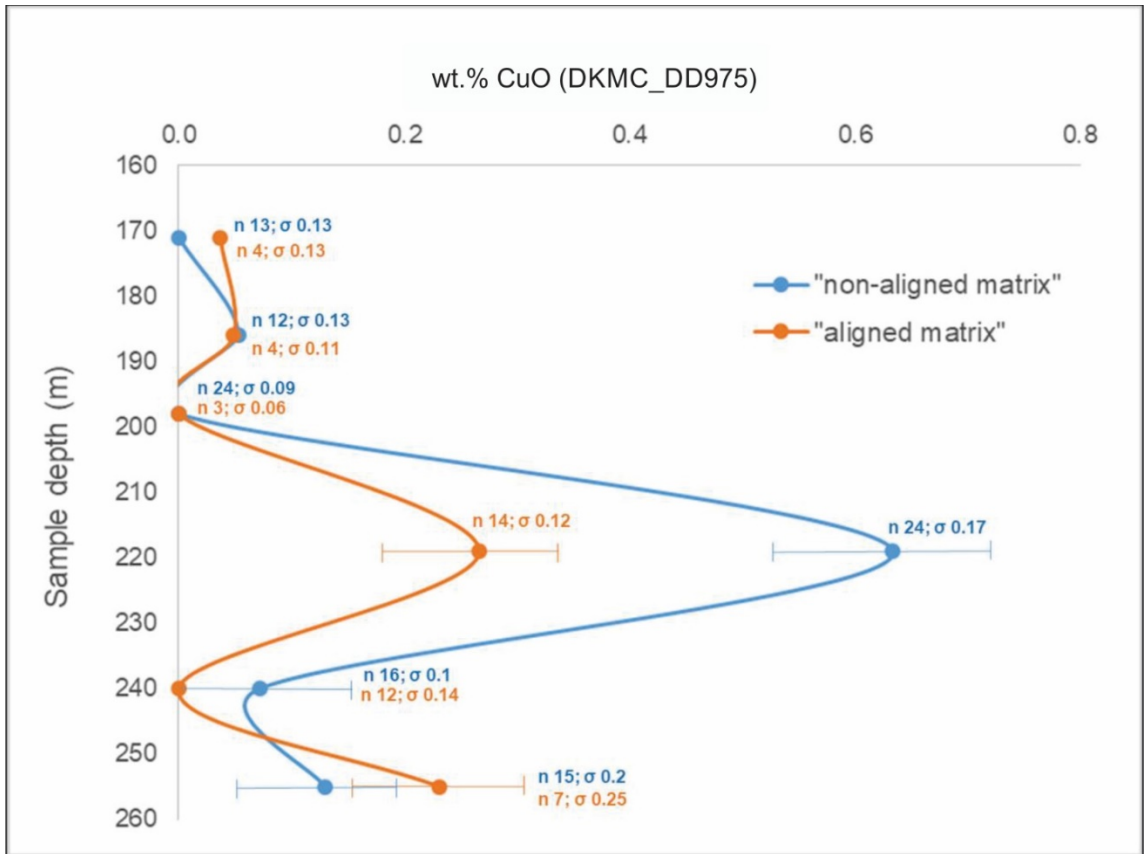


Figure 40: Chemical analysis showing the average copper concentration (CuO wt%) of aligned and non-aligned matrix versus depth from six samples of low-grade drill-hole DKMC_DD975 in ore-zone matrix of the basal diamictite at Kakula. This graph illustrates that non-aligned matrix has a relatively high copper concentration relative to aligned matrix. This is not true for the sample at 255 m depth, but the analyses fall within statistical error. The relatively low copper concentrations in aligned matrix relative to non-aligned matrix suggests that copper-sulphides were dissolved during the alignment process. This graph also illustrates how copper grades are relatively low in the two lowermost samples, which are samples of clast-rich diamictite of the lower basal diamictite unit. Instrument error, # of analyses (n), and standard deviations (σ) are indicated.

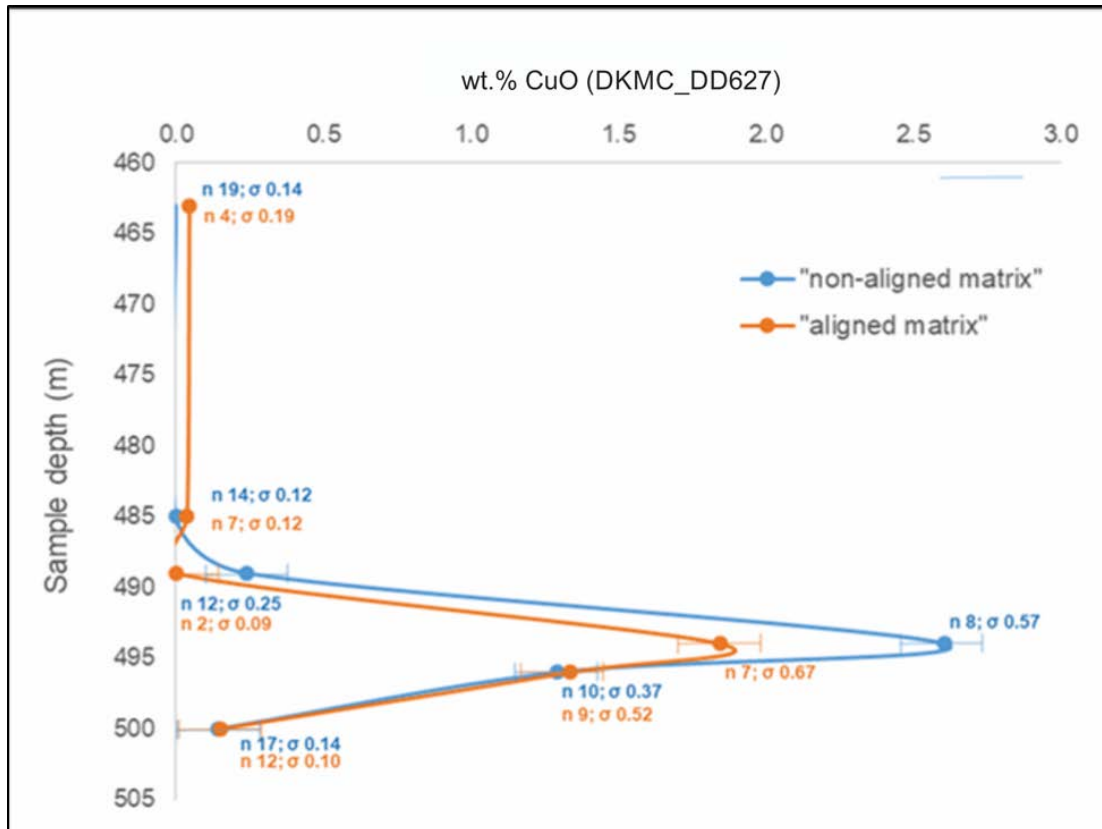


Figure 41: Chemical analysis showing the average copper concentration (CuO wt%) of aligned and non-aligned matrix versus depth from six samples of high-grade drill-hole DKMC_DD627 in ore-zone matrix of the basal diamictite at Kamo. This graph illustrates that non-aligned matrix has a relatively high copper concentration relative to aligned matrix, but this phenomenon is not as striking as at Kakula and is only statistically significant for the sample at 494 m depth. The relatively low copper concentrations in aligned matrix relative to non-aligned matrix suggests that copper-sulphides were dissolved during the alignment process. This graph also illustrates that the copper grade is lower in the lowermost sample at 500 m depth, which is clast-rich diamictite. Instrument error, # of analyses (n), and standard deviations (σ) are indicated.

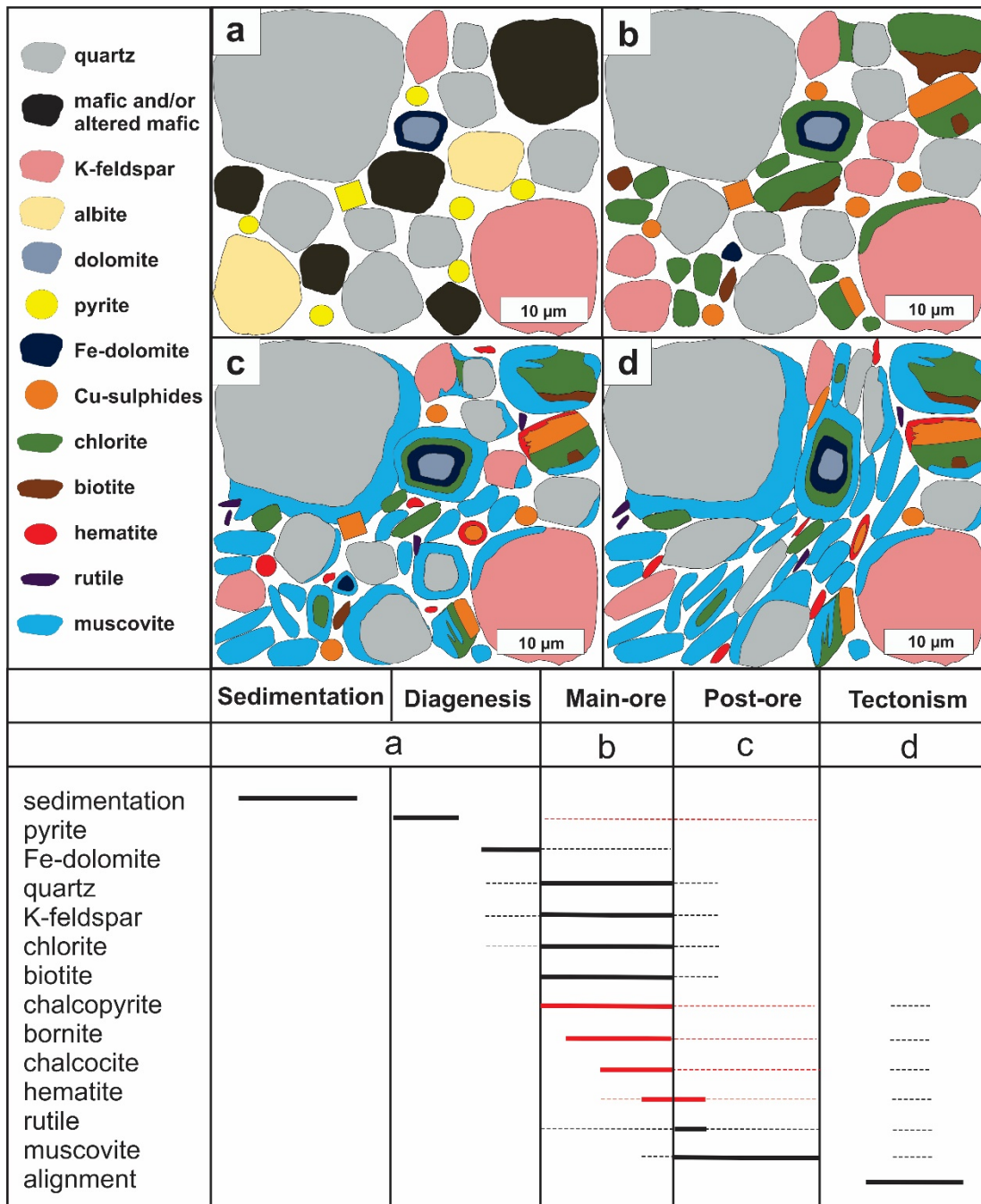


Figure 42: Paragenetic table and summary diagram illustrating the evolution of ore-zone diamictite matrix at Kakula. The summary diagram depicts alteration of mafics taking place after sediment deposition, whereas mafic rock may have been altered prior to sediment deposition. Heavy lines in the paragenetic table represent paragenetic episodes with high certainty, whereas pale, dashed lines represent areas of uncertainty or speculation. Black lines represent matrix components that are present in all parts of the ore-zone matrix, regardless of stratigraphic position. Red lines represent main-ore opaque minerals that are limited in presence and abundance to certain parts of the stratigraphy and ore-zone. The absolute timing and extent of the different phases and overlap from one into the other is not to scale and remains somewhat unclear. Subaqueous debris flow deposition is thought to have had an overwhelming component of fine-grained quartz and mafic and/or altered mafic minerals, and lesser carbonate and felsic minerals. Copper-sulphides (chalcopyrite, bornite, chalcocite) ± hematite fit into a paragenetic sequence between pre-ore diagenetic pyrite (earliest post-depositional mineral) and muscovite (latest paragenetic mineral), and they are associated with relatively Mg-rich chlorite and biotite, and broadly coincident with ferroan dolomite, K-feldspar, and quartz. The original makeup of the matrix at the time of sedimentation is estimated but difficult to determine. Mafic (pyroxene, anorthite) and/or altered mafic minerals (e.g., albite) were broken down and/or altered during the main-ore phase into an assemblage of chlorite and smaller amounts of biotite and Fe-dolomite, whereas albite was broken down and altered to K-feldspar. The formation of muscovite resulted from increasingly acidic conditions following the copper mineralising event and resulted in the breakdown of other matrix minerals such as chlorite, biotite, quartz, and K-feldspar. Hematite replaced Cu-sulphides and may have formed during the progressive replacement of Cu-sulphides, more so during chalcocite formation, and from the breakdown of biotite and chlorite. Rutile may have formed from the hydrothermal breakdown of biotite. Matrix alignment took place relatively late and is defined by relatively high muscovite content and relatively low content of other matrix minerals, including copper-sulphides, which were partly dissolved during weak tectonism. The textural and compositional information used to develop the ore-zone matrix paragenesis is consistent in all drill-holes studied at Kakula.

Tables

Table 1: Sample list and information about their location, depth, lithofacies, what samples were made into thin sections, and what analytical techniques were performed on different samples.

Drill-hole	Sample ID	Start depth (m)	End depth (m)	Lith	Thin-section ID	SEM analysis	XRD and WR-geochem
DKMC_DD 1012	DD101 2_1	349.57	349.48	Sands tone	n.a	n.a	
DKMC_DD 1012	DD101 2_2	347.45	347.35	Diamic tite	n.a	n.a	
DKMC_DD 1012	DD101 2_3	346.1	346.2	Diamic tite	n.a	n.a	
DKMC_DD 1012	DD101 2_3.5	345.50	345.60	Siltstone	DD1012_3.5	YES	
DKMC_DD 1012	DD101 2_4	340.75	340.65	Diamic tite	DD1012_4	n.a	
DKMC_DD 1012	DD101 2_5	337.68	337.59	Diamic tite	DD1012_5	n.a	
DKMC_DD 1012	DD101 2_6	335.87	335.69	Diamic tite	DD1012_6	YES	
DKMC_DD 1012	DD101 2_7	326.8	326.65	Diamic tite	DD1012_7	YES	YES
DKMC_DD 1012	DD101 2_8	321.55	321.4	Diamic tite	DD1012_8	n.a	
DKMC_DD 1012	DD101 2_9	317.19	317.03	Diamic tite	DD1012_9	YES	
DKMC_DD 1012	DD101 2_10	313.92	313.8	Diamic tite	n.a	n.a	
DKMC_DD 1012	DD101 2_11	304.77	304.64	Diamic tite	DD1012_11	YES	
DKMC_DD 1012	DD101 2_12	296.62	296.45	Diamic tite	DD1012_12	n.a	
DKMC_DD 1012	DD101 2_13	288.5	288.36	Diamic tite	DD1012_13	YES	YES
DKMC_DD 1012	DD101 2_14	270.35	270.55	Diamic tite	DD1012_14	YES	
DKMC_DD 1012	DD101 2_15	75.70	75.80	Diamic tite	DD1012_15	n.a	
DKMC_DD 1012	DD101 2_16	74.35	74.45	Diamic tite	DD1012_16	YES	YES
DKMC_DD 975	DD975 _1	263.8	263.67	Sands tone	n.a	n.a	
DKMC_DD 975	DD975 _2	258.84	258.73	Diamic tite	n.a	n.a	
DKMC_DD 975	DD975 _3	255.32	255.21	Diamic tite	DD975_3	YES	

DKMC_DD 975	DD975 _4	240.36	240.27	Diamic tite	DD975_4	YES	YES
DKMC_DD 975	DD975 _5	225.82	225.96	Diamic tite	DD975_5	n.a	
DKMC_DD 975	DD975 _6	218.95	218.8	Diamic tite	DD975_6	YES	
DKMC_DD 975	DD975 _7	209.25	209.13	Diamic tite	DD975_7	n.a	
DKMC_DD 975	DD975 _8	197.78	197.65	Diamic tite	DD975_8	YES	
DKMC_DD 975	DD975 _9	196	195.87	Diamic tite	DD975_9	n.a	
DKMC_DD 975	DD975 _10	186.83	186.92	Diamic tite	DD975_10	YES	YES
DKMC_DD 975	DD975 _11	171.40	171.50	Diamic tite	DD975_11	YES	
DKMC_DD 1001	DD100 1_1	280.2	280.38	Diamic tite	DD1001_1	n.a	
DKMC_DD 1001	DD100 1_2	275.08	275.19	Diamic tite	DD1001_2	n.a	
DKMC_DD 1001	DD100 1_3	265.69	265.57	Diamic tite	DD1001_3	n.a	
DKMC_DD 1001	DD100 1_4	246.41	246.29	Diamic tite	DD1001_4	n.a	
DKMC_DD 1001	DD100 1_5	233.42	233.62	Diamic tite	DD1001_5A , 5B	n.a	
DKMC_DD 1001	DD100 1_6	222.98	222.8	Diamic tite	DD1001_6	n.a	
DKMC_DD 1001	DD100 1_7	217.78	217.68	Diamic tite	n.a	n.a	
DKMC_DD 1001	DD100 1_8	204.7	204.6	Diamic tite	DD1001_8	n.a	
DKMC_DD 1161	DD116 1_1	889.17	889.08	Diamic tite	DD1161_1	YES	
DKMC_DD 1161	DD116 1_2	871.81	871.94	Diamic tite	DD1161_2	n.a	
DKMC_DD 1161	DD116 1_3	452.58	452.70	Diamic tite	DD1161_3	YES	YES
DKMC_DD 1161	DD116 1_4	434.19	434.25	Diamic tite	DD1161_4	n.a	
DKMC_DD 1161	DD116 1_5	402.60	402.74	Diamic tite	DD1161_5	n.a	
DKMC_DD 1161	DD116 1_6	211.40	211.51	Diamic tite	DD1161_6	YES	YES
DKMC_DD 1161	DD116 1_7	201.25	201.38	Diamic tite	n.a	n.a	
DKMC_DD 627	DD627 _1	502.67	502.56	Sands tone	n.a	n.a	
DKMC_DD 627	DD627 _2	500.65	500.49	Diamic tite	DD627_2	YES	
DKMC_DD 627	DD627 _3	497.21	497.13	Diamic tite	n.a	n.a	
DKMC_DD 627	DD627 _4	496.22	496.1	Diamic tite	DD627_4A, 4B	YES (4B)	

DKMC_DD 627	DD627 _5	495.85	495.65	Diamic tite	DD627_5A, 5B	n.a
DKMC_DD 627	DD627 _6	495.47	495.37	Diamic tite	DD627_6	n.a
DKMC_DD 627	DD627 _7	494.85	494.73	Diamic tite	DD627_7	YES
DKMC_DD 627	DD627 _8	492.48	492.3	Diamic tite	n.a	n.a
DKMC_DD 627	DD627 _9	491.97	491.84	Diamic tite	DD627_9	n.a
DKMC_DD 627	DD627 _10	489.5	489.38	Diamic tite	DD627_10	YES
DKMC_DD 627	DD627 _11	485.57	485.38	Diamic tite	DD627_11	YES
DKMC_DD 627	DD627 _12	477.87	477.77	Siltsto ne	n.a	n.a
DKMC_DD 627	DD627 _13	474.73	474.57	Siltsto ne	n.a	n.a
DKMC_DD 627	DD627 _14	472.4	472.27	Siltsto ne	n.a	n.a
DKMC_DD 627	DD627 _15	463.25	463.35	Diamic tite	DD627_15	YES
DKMC_DD 793	DD793 _1	411.4	411.25	Diamic tite	DD793_1	n.a
DKMC_DD 793	DD793 _2	400.45	400.36	Diamic tite	n.a	n.a
DKMC_DD 793	DD793 _3	399.9	399.77	Diamic tite	DD793_3	n.a
DKMC_DD 793	DD793 _4	399.37	399.13	Diamic tite	DD793_4	n.a
DKMC_DD 793	DD793 _5	396.96	396.81	Diamic tite	DD793_5	n.a
DKMC_DD 793	DD793 _6	394.36	394.24	Diamic tite	n.a	n.a
DKMC_DD 793	DD793 _7	386	385.89	Diamic tite	n.a	n.a
DKMC_DD 793	DD793 _8	383.62	383.52	Diamic tite	n.a	n.a
DKMC_DD 793	DD793 _9	171.5	171.4	Diamic tite	DD793_9	YES

Table 2: Diamictite grain size percentages (clay-silt, sand, larger) and measured matrix porosity percentages for different samples analysed with the SEM. Matrix percentage has been corrected for porosity (matrix – porosity) to total 100%. Matrix elemental Cu concentration was calculated from SEM compositional analyses of bulk matrix.

Sample ID	Depth (m)	Lith	Type	Clast %	Sand %	Matrix %	Porosity %	Total	Matrix Cu %
DD975_3	255.3	Diamictite	clast-rich	25	32.5	33.9	8.6	100	0.09
DD975_4	240.3	Diamictite	clast-rich	20	22.5	45.3	12.2	100	0.05
DD975_6	218.9	Diamictite	clast-poor	12	12.5	65	10.5	100	0.47
DD975_8	198.7	Diamictite	clast-poor	8	17.5	62	12.5	100	0.00
DD975_10	186.9	Diamictite	clast-poor	15	22.5	50.3	12.2	100	0.00
DD975_11	171.5	Diamictite	clast-poor	10	17.5	62.4	10.1	100	0.00
DD1012_3.5	345.5	Siltstone	n.a	n.a	n.a	n.a	13.8	100	4.99
DD1012_6	335.8	Diamictite	clast-poor	8	22.5	58	11.5	100	0.60
DD1012_7	326.8	Diamictite	clast-poor	15	25	48.9	11.1	100	0.30
DD1012_9	317.1	Diamictite	clast-poor	15	17.5	57.6	9.9	100	0.20
DD1012_11	304.7	Diamictite	clast-poor	10	20	59.8	10.2	100	0.00
DD1012_13	288.4	Diamictite	clast-poor	17	25	48.5	9.5	100	0.00
DD1012_14	270.4	Diamictite	clast-poor	15	20	55.3	9.7	100	0.00
DD1012_16	74	Diamictite	clast-poor	8	20	63.7	8.3	100	0.00
DD627_2	500.6	Diamictite	clast-rich	22	37.5	31.8	8.7	100	0.11
DD627_4	496.2	Diamictite	clast-poor	8	22.5	60.7	8.8	100	0.98
DD627_7	494.8	Diamictite	clast-poor	15	20	54.1	10.8	100	2.03
DD627_10	489.5	Diamictite	clast-poor	8	20	63.3	8.7	100	0.19
DD627_11	485.5	Diamictite	clast-poor	5	17.5	67.2	10.3	100	0.00
DD627_15	463.3	Diamictite	clast-poor	10	17.5	64	8.5	100	0.00

Table 3: Diamictite matrix average grain size calculations for samples analysed with the SEM. The average matrix size was calculated by taking the average of 100 point analyses for each samples.

Sample ID	Depth (m)	Lith	Type	n	Matrix Size Avg (μm)	Std.dev (p)
DD975_3	255.3	Diamictite	clast-rich	100	7.43	7.83
DD975_4	240.3	Diamictite	clast-rich	100	5.93	5.18
DD975_6	218.9	Diamictite	clast-poor	100	6.24	5.35
DD975_8	198.7	Diamictite	clast-poor	100	5.21	4.59
DD975_10	186.9	Diamictite	clast-poor	100	5.48	4.75
DD975_11	171.5	Diamictite	clast-poor	100	5.62	5.15
DD1012_3.5	345.5	Siltstone	n.a	100	3.54	2.64
DD1012_6	335.8	Diamictite	clast-poor	100	5.36	4.73
DD1012_7	326.8	Diamictite	clast-poor	100	5.17	3.84
DD1012_9	317.1	Diamictite	clast-poor	100	4.88	4.29
DD1012_11	304.7	Diamictite	clast-poor	100	4.49	3.43
DD1012_13	288.4	Diamictite	clast-poor	100	5.06	3.73
DD1012_14	270.4	Diamictite	clast-poor	100	4.47	3.77
DD1012_16	74	Diamictite	clast-poor	100	7.61	6.24
DD627_2	500.6	Diamictite	clast-rich	100	7.47	6.35
DD627_4	496.2	Diamictite	clast-poor	100	4.6	4.08
DD627_7	494.8	Diamictite	clast-poor	100	4.87	4.27
DD627_10	489.5	Diamictite	clast-poor	100	5.01	3.56
DD627_11	485.5	Diamictite	clast-poor	100	4.62	4.03
DD627_15	463.3	Diamictite	clast-poor	100	5.8	4.63

Table 4: Summary for minerals present in least-altered matrix in non-aligned and aligned matrix. Mineral common size ranges, typical percent volumes, and typical shapes and rounding are provided. Note that matrix alignment is weak in least-altered matrix and was only identified in least-altered sample DD1012_16.

Mineral phase	Least-altered matrix (non-aligned)				Least-altered matrix (aligned)			
	Typical size range	Typical % vol	Typical shape	Typical rounding	Typical size range	Typical % vol	Typical shape	Typical rounding
quartz	1-65 μm	30-60%	equant	rounded to subangular	1-65 μm	30-60%	equant	subrounded to subangular
chlorite	1-20 μm	15-40%	elongate	subangular to angular	1-10 μm	15-40%	elongate	subangular to angular
Fe-dolomite	1-20 μm	0-5%	equant to elongate	rounded to angular	1-10 μm	0-5%	equant	subrounded to subangular
K-feldspar	1-65 μm	5-15%	equant	rounded to subangular	1-65 μm	5-15%	equant, elongate	subrounded to subangular
albite	1-65 μm	15-50%	equant	rounded to subangular	1-65 μm	10-50%	equant, elongate	subrounded to subangular
calcite	1-20 μm	0-5%	equant	subrounded to angular	1-5 μm	0-5%	equant, elongate	subrounded to angular
pyrite	≤ 5 μm	1-5%	equant	rounded or blocky	1-5 μm	1-5%	equant	variable
rutile	≤ 1 μm	$\leq 1\%$	elongate	angular	≤ 1 μm	$\leq 1\%$	elongated	angular

Table 5: Summary of minerals present in ore-zone matrix in non-aligned and aligned matrix. Mineral common size ranges, typical percent volumes, and typical shapes and rounding are provided.

Mineral phase	Ore-zone matrix (non-aligned)				Ore-zone matrix (aligned)			
	Typical size range	Typical % vol	shape	rounding	Size range	Typical % vol	Shape	rounding
quartz	1-65 μm	30-40%	equant	rounded to subangular	1-65 μm	20-30%	equant to elongate	rounded to angular
muscovite	1-10 μm	40-60%	elongate	angular	1-10 μm	50-80%	elongate	angular
chlorite	1-20 μm	10-20%	elongate	subangular to angular	1-65 μm	5-15%	elongate	subangular to angular
Fe-dolomite	1-20 μm	1-5%	equant	rounded to angular	1-65 μm	1-5%	equant to elongate	subangular to angular
dolomite	1-65 μm	1-5%	equant to elongate	rounded to subrounded	1-65 μm	1-5%	equant to elongate	rounded to angular
K-feldspar	1-65 μm	10-20%	equant	rounded to subangular	1-65 μm	5-15%	equant to elongate	rounded to angular
biotite	1-20 μm	$\leq 3\%$	elongate	angular	1-5 μm	$\leq 2\%$	elongate	angular
pyrite	$\leq 5 \mu\text{m}$	0-5%	equant	rounded or blocky	1-5 μm	0-5%	equant to elongate	variable
chalcocite	$\leq 5 \mu\text{m}$	0-5%	equant to elongate	variable	1-5 μm	0-5%	equant to elongate	variable
bornite	$\leq 5 \mu\text{m}$	0-5%	equant to elongate	variable	1-5 μm	0-5%	equant to elongate	variable
chalcopyrite	$\leq 5 \mu\text{m}$	0-5%	equant to elongate	variable	1-5 μm	0-5%	equant to elongate	variable
hematite	$\leq 5 \mu\text{m}$	0-5%	equant to elongate	variable	1-5 μm	0-5%	equant to elongate	variable
rutile	$\leq 1 \mu\text{m}$	$\leq 1\%$	elongate	angular	$\leq 1 \mu\text{m}$	$\leq 1\%$	elongate	angular

Table 6: Summary of typical mineral distributions and associations in least-altered matrix.

Mineral phase	Least-altered matrix	
	Typical distribution	Typical association
quartz	widespread	Quartz locally overgrows K-feldspar and albite. Detrital quartz is overgrown by other minerals
chlorite	widespread	Along edges of albite, quartz, and K-feldspar. Overgrows K-feldspar, albite, and calcite
Fe-dolomite	localised	Locally associated with chlorite and present between larger grains
K-feldspar	widespread	Locally overgrows albite and locally overgrown by calcite, chlorite, and quartz
albite	widespread	Locally overgrown or altered to K-feldspar and quartz
calcite	localised	Partially dissolved, contains pores, and locally overgrown by chlorite
pyrite	widespread	Locally overgrown by quartz and albite. Locally at the margins of pores

Table 7: Summary of typical mineral distributions and associations in ore-zone matrix.

Mineral phase	Ore-zone matrix	
	Typical distribution	Typical mineral associations
quartz	widespread	Typically detrital and overgrown by other minerals
muscovite	widespread	Overgrows and replaces all other minerals and locally encloses Cu-sulphides
chlorite	widespread	Overgrows Fe-dolomite and commonly intergrown and spatially associated with biotite, chalcocite, bornite, chalcopyrite
Fe-dolomite	widespread	Overgrows dolomite and commonly overgrown by chlorite
dolomite	widespread	Overgrown by Fe-dolomite
K-feldspar	widespread	Spatially associated with biotite and locally overgrown by or altered to muscovite
biotite	localised	Intergrown with chlorite or along edges of K-feldspar
pyrite	localised	In contact with other minerals or in pore space, locally overgrown by muscovite
chalcocite	localised	Replaces bornite, intergrown with chlorite, and replaced by hematite. Spatially associated with chlorite
bornite	localised	Replaces chalcopyrite, intergrown with chalcocite and spatially associated with chlorite
chalcopyrite	localised	Intergrown with chlorite, locally replaces pyrite, and replaced by bornite. Spatially associated with chlorite
hematite	localised	Spatially associated with and replaces chalcocite, bornite
rutile	widespread	May be associated with the breakdown of biotite

Table 8: SEM average oxide concentrations from high-grade drill-hole DKMC_DD1012 at Kakula. Oxide concentrations are in wt.% and normalised to 100%. Negative values and values below the general SEM detection limit of 0.15 wt.% are not reliable or meaningful. Sample descriptions, sample depths, sample IDs, and number of analyses (n) are provided.

Description	Depth	Sample	n	Na2O	MgO	Al2O3	SiO2	SO3	K2O	CaO	TiO2	MnO	FeO	CuO	Total
Siltstone (non-aligned)	345m	DD1012_3.5	14	0.13	3.50	13.60	60.92	3.31	7.01	0.23	0.96	0.01	3.81	6.50	100
Non-aligned matrix	335m	DD1012_6	15	0.13	5.21	12.96	63.23	0.49	6.59	2.92	0.85	0.10	6.71	0.83	100
Non-aligned matrix	326m	DD1012_7	15	0.24	5.09	14.41	63.26	0.39	6.97	1.93	0.95	0.11	6.26	0.39	100
Non-aligned matrix	317m	DD1012_9	16	0.20	4.26	12.91	67.06	0.28	6.52	1.54	0.86	0.06	6.04	0.27	100
Non-aligned matrix	304m	DD1012_11	17	0.23	3.87	13.48	67.45	0.51	6.37	2.55	0.78	0.09	4.65	0.01	100
Non-aligned matrix	288m	DD1012_13	19	0.22	3.55	12.18	69.92	0.60	5.60	1.50	0.78	0.08	5.56	0.00	100
Non-aligned matrix	270m	DD1012_14	15	0.13	3.33	14.22	66.83	0.77	7.20	0.93	0.88	0.06	5.64	0.00	100
Non-aligned matrix	74m	DD1012_16	9	1.47	3.60	10.80	59.97	6.99	2.61	2.21	0.64	0.11	11.63	-0.03	100
Siltstone (Aligned)	345m	DD1012_3.5	n.a	n.a	n.a	n.a	n.a	n.a	n.a	n.a	n.a	n.a	n.a	n.a	100
Aligned matrix	335m	DD1012_6	13	0.10	5.34	16.26	57.61	0.22	8.35	2.64	1.31	0.10	7.87	0.21	100
Aligned matrix	326m	DD1012_7	9	0.21	5.24	20.25	52.86	0.12	9.80	2.35	1.58	0.06	7.39	0.14	100
Aligned matrix	317m	DD1012_9	13	0.18	4.39	15.56	62.32	0.19	8.00	1.41	1.11	0.08	6.63	0.12	100
Aligned matrix	304m	DD1012_11	8	0.22	4.04	17.75	60.56	0.67	8.29	2.04	1.02	0.07	5.34	0.00	100
Aligned matrix	288m	DD1012_13	10	0.28	3.53	15.50	64.43	0.87	7.36	1.38	1.03	0.10	5.49	0.04	100
Aligned matrix	270m	DD1012_14	3	0.19	3.71	17.03	60.68	1.25	8.49	1.05	1.15	0.02	6.41	0.02	100
Aligned matrix	74m	DD1012_16	7	1.09	6.16	14.16	47.92	8.13	3.00	0.82	1.08	0.14	17.49	0.01	100
Chlorite	345m	DD1012_3.5	32	0.10	22.86	19.61	29.90	0.09	0.74	0.00	0.13	0.15	14.17	0.26	88

Chlorite	335m	DD1012_6	30	0.09	23.77	19.15	28.86	0.07	0.27	0.07	0.08	0.13	15.35	0.16	88
Chlorite	326m	DD1012_7	19	0.15	21.92	19.48	28.46	0.08	0.46	0.07	0.10	0.14	17.10	0.03	88
Chlorite	317m	DD1012_9	24	0.15	19.91	19.59	28.37	0.03	0.46	0.06	0.09	0.13	19.23	-0.02	88
Chlorite	304m	DD1012_11	43	0.13	19.68	19.31	27.65	0.09	0.18	0.06	0.06	0.12	20.78	-0.06	88
Chlorite	288m	DD1012_13	19	0.17	17.72	19.36	27.28	0.10	0.25	0.05	0.03	0.17	22.95	-0.09	88
Chlorite	270m	DD1012_14	15	0.18	15.12	20.94	26.33	0.08	0.45	0.01	0.13	0.18	24.69	-0.10	88
Chlorite	74m	DD1012_16	17	0.32	13.61	19.43	25.84	0.19	0.02	0.10	0.07	0.21	28.24	-0.03	88
Biotite	345m	DD1012_3.5	6	0.08	17.68	14.29	41.83	0.09	12.18	0.05	1.25	0.06	10.29	0.21	98
Biotite	335m	DD1012_6	18	0.07	17.83	15.77	40.13	0.03	10.54	0.02	1.18	0.07	12.39	-0.02	98
Biotite	326m	DD1012_7	5	0.30	16.85	14.24	39.44	0.09	11.48	-0.03	1.53	0.05	13.98	0.06	98
Biotite	317m	DD1012_9	22	0.22	15.12	15.17	40.00	0.07	10.69	0.06	1.47	0.08	15.14	-0.03	98
Biotite	304m	DD1012_11	9	0.07	15.13	14.41	39.38	0.14	11.63	0.02	1.60	0.05	15.63	-0.07	98
Biotite	288m	DD1012_13	16	0.13	13.33	14.67	38.84	0.06	10.79	0.12	1.83	0.09	18.25	-0.11	98
Biotite	270m	DD1012_14	21	0.14	12.73	14.13	38.23	0.03	11.08	0.13	2.03	0.05	19.52	-0.06	98
Biotite	74m	DD1012_16	n.a	n.a	n.a	n.a	n.a	n.a	n.a	n.a	n.a	n.a	n.a	n.a	n.a
Muscovite	345m	DD1012_3.5	22	0.14	3.61	24.79	48.61	0.08	12.67	-0.03	0.68	0.01	5.14	0.31	96
Muscovite	335m	DD1012_6	15	0.17	2.67	27.22	47.96	0.05	12.81	0.01	1.11	0.03	3.96	0.00	96
Muscovite	326m	DD1012_7	9	0.21	2.44	29.46	47.00	0.04	12.67	0.00	0.55	0.04	3.50	0.08	96
Muscovite	317m	DD1012_9	18	0.30	2.01	27.67	49.51	0.05	12.39	0.01	0.64	0.01	3.41	0.00	96
Muscovite	304m	DD1012_11	18	0.29	2.59	25.68	50.30	0.18	12.18	0.01	0.70	-0.02	4.09	0.01	96
Muscovite	288m	DD1012_13	29	0.26	2.62	28.47	47.51	0.08	12.34	0.01	0.70	0.02	4.01	-0.02	96
Muscovite	270m	DD1012_14	21	0.36	3.10	25.05	51.06	0.13	10.32	0.00	0.74	0.02	5.27	-0.06	96
Muscovite	74m	DD1012_16	n.a	n.a	n.a	n.a	n.a	n.a	n.a	n.a	n.a	n.a	n.a	n.a	n.a

Table 9: Standard deviations for the SEM compositional analysis of high-grade drill-hole DKMC_DD1012 at Kakula.

Analysis	Depth	Sample	n	Na2O	MgO	Al2O3	SiO2	SO3	K2O	CaO	TiO2	MnO	FeO	CuO
Siltstone (non-aligned)	345m	DD1012_3.5	14	0.06	0.13	0.22	0.69	0.26	0.11	0.05	0.11	0.05	0.09	0.55
Non-aligned matrix	335m	DD1012_6	15	0.07	0.50	1.85	3.97	0.19	1.05	0.70	0.19	0.07	0.58	0.28
Non-aligned matrix	326m	DD1012_7	15	0.11	0.56	0.93	1.60	0.10	0.60	0.39	0.16	0.06	0.42	0.15
Non-aligned matrix	317m	DD1012_9	16	0.09	0.16	1.11	1.91	0.08	0.58	0.22	0.12	0.06	0.33	0.12
Non-aligned matrix	304m	DD1012_11	17	0.08	0.23	0.65	0.88	0.11	0.26	0.47	0.12	0.07	0.38	0.11
Non-aligned matrix	288m	DD1012_13	19	0.15	0.56	0.96	2.50	0.22	0.60	0.39	0.14	0.12	1.00	0.15
Non-aligned matrix	270m	DD1012_14	15	0.08	0.19	0.45	1.08	0.13	0.22	0.12	0.09	0.07	0.28	0.13
Non-aligned matrix	74m	DD1012_16	9	0.05	0.54	0.77	2.95	0.51	0.19	0.63	0.09	0.06	1.14	0.09
Siltstone (aligned)	345m	DD1012_3.5	n.a	n.a	n.a	n.a	n.a	n.a	n.a	n.a	n.a	n.a	n.a	n.a
Aligned matrix	335m	DD1012_6	13	0.10	0.29	2.39	4.63	0.14	1.21	0.43	0.42	0.05	0.93	0.16
Aligned matrix	326m	DD1012_7	9	0.05	0.62	1.34	2.33	0.09	0.69	0.64	0.18	0.05	0.47	0.10
Aligned matrix	317m	DD1012_9	13	0.10	0.43	2.52	4.34	0.10	1.27	0.48	0.34	0.08	0.58	0.10
Aligned matrix	304m	DD1012_11	8	0.09	0.27	2.17	3.06	0.36	0.83	0.67	0.14	0.07	0.44	0.15
Aligned matrix	288m	DD1012_13	10	0.07	0.40	2.43	3.90	0.23	1.00	0.32	0.36	0.12	0.54	0.10
Aligned matrix	270m	DD1012_14	3	0.06	0.08	0.42	0.49	0.25	0.20	0.00	0.08	0.04	0.07	0.09
Aligned matrix	74m	DD1012_16	7	0.07	0.57	0.99	2.47	0.70	0.63	0.38	0.27	0.06	0.77	0.08
Chlorite	345m	DD1012_3.5	32	0.06	1.22	0.84	1.29	0.07	0.53	0.04	0.10	0.05	0.98	0.08
Chlorite	335m	DD1012_6	30	0.11	1.02	1.84	1.01	0.14	0.53	0.10	0.11	0.08	0.79	0.30
Chlorite	326m	DD1012_7	19	0.09	0.89	1.00	1.04	0.11	0.53	0.14	0.13	0.07	0.82	0.19
Chlorite	317m	DD1012_9	24	0.11	1.47	1.49	0.95	0.08	0.46	0.07	0.07	0.07	0.66	0.12

Chlorite	304m	DD1012_11	43	0.12	0.80	0.72	0.83	0.12	0.31	0.08	0.09	0.08	0.94	0.11
Chlorite	288m	DD1012_13	19	0.14	0.93	0.93	0.61	0.15	0.46	0.08	0.13	0.11	0.76	0.13
Chlorite	270m	DD1012_14	15	0.11	1.66	2.05	1.91	0.09	0.41	0.07	0.10	0.08	1.82	0.12
Chlorite	74m	DD1012_16	17	0.06	0.61	0.79	1.42	0.10	0.05	0.06	0.07	0.07	1.42	0.13
Biotite	345m	DD1012_3.5	6	0.06	0.72	1.32	0.83	0.04	0.38	0.06	0.12	0.03	1.00	0.04
Biotite	335m	DD1012_6	18	0.10	1.13	3.29	1.43	0.06	2.87	0.08	0.41	0.10	0.77	0.21
Biotite	326m	DD1012_7	5	0.28	0.51	0.45	0.47	0.11	0.79	0.07	0.19	0.06	0.30	0.09
Biotite	317m	DD1012_9	22	0.17	1.21	2.70	1.66	0.06	1.81	0.10	0.44	0.08	1.09	0.12
Biotite	304m	DD1012_11	9	0.12	0.65	2.68	0.51	0.09	1.38	0.08	0.44	0.06	0.41	0.09
Biotite	288m	DD1012_13	16	0.17	0.68	2.14	0.80	0.07	1.56	0.25	0.44	0.08	0.74	0.16
Biotite	270m	DD1012_14	21	0.12	0.74	1.15	0.76	0.07	1.33	0.22	0.22	0.06	1.18	0.08
Biotite	74m	DD1012_16	n.a	n.a	n.a	n.a	n.a	n.a	n.a	n.a	n.a	n.a	n.a	n.a
Muscovite	345m	DD1012_3.5	22	0.13	0.84	1.58	2.09	0.15	1.07	0.06	0.53	0.04	1.00	0.32
Muscovite	335m	DD1012_6	15	0.07	0.95	2.86	1.64	0.06	0.57	0.12	2.02	0.07	1.32	0.08
Muscovite	326m	DD1012_7	9	0.11	1.28	3.72	0.57	0.06	0.44	0.05	0.36	0.06	2.07	0.09
Muscovite	317m	DD1012_9	18	0.24	0.94	5.91	5.61	0.08	1.16	0.09	0.46	0.07	1.46	0.09
Muscovite	304m	DD1012_11	18	0.27	1.29	5.96	5.97	0.38	2.02	0.05	0.63	0.09	1.99	0.16
Muscovite	288m	DD1012_13	29	0.17	0.76	2.10	1.26	0.08	0.55	0.09	0.76	0.07	1.17	0.06
Muscovite	270m	DD1012_14	21	0.54	1.38	6.12	7.02	0.14	3.46	0.08	0.50	0.07	2.18	0.10
Muscovite	74m	DD1012_16	n.a	n.a	n.a	n.a	n.a	n.a	n.a	n.a	n.a	n.a	n.a	n.a

Table 10: SEM average oxide concentrations from high-grade drill-hole DKMC_DD975 at Kakula. Oxide concentrations are in wt.% and normalised to 100%. Negative values and values below the general SEM detection limit of 0.15 wt.% are not reliable or meaningful. Sample descriptions, sample depths, sample IDs, and number of analyses (n) are provided.

Description	Depth	Sample	n	Na2O	MgO	Al2O3	SiO2	SO3	K2O	CaO	TiO2	MnO	FeO	CuO	Total
Non-aligned matrix	255m	DD975_3	15	0.10	5.72	13.04	63.72	0.07	6.56	3.42	0.92	0.18	6.14	0.13	100
Non-aligned matrix	240m	DD975_4	16	0.20	3.94	14.11	65.84	0.15	7.56	2.45	1.03	0.08	4.57	0.07	100
Non-aligned matrix	219m	DD975_6	24	0.22	2.87	12.30	70.35	0.60	6.64	0.57	0.83	0.03	4.95	0.63	100
Non-aligned matrix	198m	DD975_8	24	0.16	3.55	13.58	66.80	0.40	7.64	2.00	1.03	0.07	4.81	-0.03	100
Non-aligned matrix	186m	DD975_10	12	0.32	4.37	11.54	67.21	0.68	5.75	3.23	0.77	0.17	5.90	0.05	100
Non-aligned matrix	171m	DD975_11	13	0.11	4.52	12.31	66.73	0.54	6.34	2.19	0.88	0.13	6.31	-0.06	100
Aligned matrix	255m	DD975_3	7	0.17	5.38	17.18	56.47	0.22	8.89	2.54	1.79	0.16	6.95	0.23	100
Aligned matrix	240m	DD975_4	12	0.28	3.99	20.78	55.43	0.07	10.79	1.06	1.92	0.06	5.63	-0.03	100
Aligned matrix	219m	DD975_6	14	0.29	3.83	16.52	62.75	0.38	8.39	0.59	1.15	0.00	5.83	0.27	100
Aligned matrix	198m	DD975_8	3	0.18	4.07	16.38	61.25	0.41	8.72	2.37	1.13	0.17	5.41	-0.08	100
Aligned matrix	186m	DD975_10	4	0.39	5.39	15.35	58.42	0.85	7.18	2.87	1.35	0.15	7.99	0.05	100
Aligned matrix	171m	DD975_11	4	0.20	5.19	14.32	62.29	0.62	6.97	1.72	0.82	0.06	7.77	0.04	100
Chlorite	255m	DD975_3	40	0.14	21.88	18.68	28.51	0.03	0.21	0.03	0.10	0.13	18.22	0.07	88
Chlorite	240m	DD975_4	30	0.19	20.40	19.17	27.75	0.10	0.14	0.03	0.05	0.13	20.02	0.02	88
Chlorite	219m	DD975_6	35	0.16	19.66	18.69	28.35	0.07	0.27	0.05	0.11	0.11	20.49	0.04	88
Chlorite	198m	DD975_8	21	0.12	19.67	18.50	27.39	0.08	0.01	0.02	0.02	0.12	22.16	-0.11	88
Chlorite	186m	DD975_10	41	0.21	18.67	18.76	27.51	0.07	0.15	0.08	0.11	0.11	22.40	-0.06	88
Chlorite	171m	DD975_11	11	0.07	18.10	19.18	27.15	0.11	0.25	0.10	0.11	0.16	22.80	-0.04	88

Biotite	255m	DD975_3	14	0.05	15.82	13.70	40.22	0.05	11.99	0.01	1.70	0.05	14.46	-0.06	98
Biotite	240m	DD975_4	14	0.14	15.09	13.64	39.66	0.07	12.39	0.05	1.65	0.05	15.34	-0.07	98
Biotite	219m	DD975_6	14	0.30	15.26	17.74	39.01	0.10	7.54	0.13	1.21	0.13	16.53	0.05	98
Biotite	198m	DD975_8	16	0.11	14.48	13.57	38.99	0.08	12.03	0.01	1.73	0.10	16.94	-0.04	98
Biotite	186m	DD975_10	13	0.28	13.31	16.66	38.53	0.06	9.10	0.09	1.53	0.12	18.38	-0.06	98
Biotite	171m	DD975_11	13	0.12	13.50	15.16	39.27	0.00	11.10	0.00	1.67	0.05	17.22	-0.07	98
Muscovite	255m	DD975_3	7	0.61	1.37	31.44	47.47	0.05	12.39	-0.04	0.43	0.01	2.23	0.05	96
Muscovite	240m	DD975_4	31	0.30	2.82	25.37	50.77	0.06	11.60	-0.03	0.86	0.01	4.27	-0.04	96
Muscovite	219m	DD975_6	7	0.61	2.12	26.35	51.54	0.10	11.99	-0.04	0.38	-0.03	3.00	-0.03	96
Muscovite	198m	DD975_8	36	0.52	2.30	29.67	47.46	0.07	12.18	0.14	0.40	0.03	3.29	-0.06	96
Muscovite	186m	DD975_10	13	0.27	2.76	23.41	50.71	1.05	11.29	0.01	1.43	-0.02	5.14	-0.05	96
Muscovite	171m	DD975_11	18	0.23	2.86	26.47	48.00	0.04	12.88	-0.02	0.54	0.00	4.95	0.05	96

Table 11: Standard deviations for the SEM compositional analysis of high-grade drill-hole DKMC_DD975 at Kakula.

Analysis	Depth	Sample	n	Na2O	MgO	Al2O3	SiO2	SO3	K2O	CaO	TiO2	MnO	FeO	CuO
----------	-------	--------	---	------	-----	-------	------	-----	-----	-----	------	-----	-----	-----

Non-aligned matrix	255m	DD975_3	15	0.13	0.53	1.34	1.86	0.15	0.75	0.85	0.17	0.11	0.54	0.20
Non-aligned matrix	240m	DD975_4	16	0.13	0.28	1.57	2.67	0.06	0.60	0.35	0.10	0.04	0.41	0.10
Non-aligned matrix	219m	DD975_6	24	0.08	0.30	0.67	1.39	0.15	0.26	0.11	0.11	0.05	0.41	0.17
Non-aligned matrix	198m	DD975_8	24	0.08	0.23	0.43	1.18	0.12	0.23	0.19	0.11	0.06	0.33	0.09
Non-aligned matrix	186m	DD975_10	12	0.14	0.26	0.78	1.74	0.16	0.43	0.37	0.13	0.11	0.33	0.13
Non-aligned matrix	171m	DD975_11	13	0.05	0.22	0.35	0.71	0.11	0.28	0.15	0.07	0.10	0.16	0.13
Aligned matrix	255m	DD975_3	7	0.06	0.68	3.17	4.74	0.12	1.54	0.88	0.71	0.16	0.76	0.25
Aligned matrix	240m	DD975_4	12	0.13	0.32	2.80	4.29	0.05	1.00	0.42	0.39	0.06	0.50	0.14
Aligned matrix	219m	DD975_6	14	0.12	0.69	2.12	4.03	0.13	0.94	0.14	0.25	0.07	0.88	0.12
Aligned matrix	198m	DD975_8	3	0.06	0.14	0.35	0.35	0.06	0.18	0.19	0.11	0.03	0.20	0.06
Aligned matrix	186m	DD975_10	4	0.17	0.28	0.66	1.74	0.14	0.36	0.53	0.24	0.09	0.38	0.11
Aligned matrix	171m	DD975_11	4	0.05	0.14	0.50	0.81	0.14	0.19	0.28	0.11	0.11	0.32	0.13
Chlorite	255m	DD975_3	40	0.12	0.78	0.47	0.54	0.13	0.29	0.09	0.24	0.11	0.63	0.18
Chlorite	240m	DD975_4	30	0.12	1.23	1.17	0.80	0.08	0.22	0.09	0.08	0.07	1.05	0.24
Chlorite	219m	DD975_6	35	0.10	0.83	0.59	1.17	0.08	0.38	0.08	0.08	0.09	0.85	0.19
Chlorite	198m	DD975_8	21	0.19	0.53	0.35	0.41	0.09	0.09	0.07	0.08	0.07	1.05	0.17
Chlorite	186m	DD975_10	41	0.12	0.74	0.70	0.63	0.10	0.19	0.08	0.28	0.07	0.75	0.12
Chlorite	171m	DD975_11	11	0.09	0.96	1.26	0.80	0.09	0.41	0.09	0.10	0.10	0.72	0.13
Biotite	255m	DD975_3	14	0.11	0.55	0.56	0.79	0.08	0.76	0.10	0.49	0.07	0.66	0.10
Biotite	240m	DD975_4	14	0.09	1.12	1.02	1.19	0.05	0.92	0.07	0.17	0.08	1.32	0.11
Biotite	219m	DD975_6	14	0.17	1.68	3.24	3.35	0.09	2.84	0.13	1.05	0.07	2.01	0.19
Biotite	198m	DD975_8	16	0.09	0.49	0.25	0.55	0.09	0.28	0.07	0.21	0.07	0.70	0.14
Biotite	186m	DD975_10	13	0.19	0.98	4.20	0.63	0.09	2.86	0.16	0.69	0.07	1.64	0.08
Biotite	171m	DD975_11	13	0.16	0.73	3.20	1.03	0.10	2.62	0.13	0.57	0.07	0.63	0.14

Muscovite	255m	DD975_3	7	0.27	0.74	3.25	3.46	0.10	0.69	0.09	0.12	0.04	0.99	0.14
Muscovite	240m	DD975_4	31	0.42	1.30	6.15	7.06	0.10	3.05	0.06	1.07	0.08	1.73	0.10
Muscovite	219m	DD975_6	7	0.51	1.34	7.41	6.61	0.09	2.28	0.09	0.17	0.05	2.00	0.13
Muscovite	198m	DD975_8	36	0.25	1.32	5.08	3.09	0.10	1.31	0.55	0.20	0.07	1.74	0.11
Muscovite	186m	DD975_10	13	0.15	0.80	4.95	5.79	1.89	2.13	0.11	1.49	0.07	1.26	0.07
Muscovite	171m	DD975_11	18	0.12	1.12	3.74	3.86	0.13	1.29	0.22	0.29	0.10	1.55	0.12

Table 12: SEM average oxide concentrations from high-grade drill-hole DKMC_DD627 at Kamoā. Oxide concentrations are in wt.% and normalised to 100%. Negative values and values below the general SEM detection limit of 0.15 wt.% are not reliable or meaningful. Sample descriptions, sample depths, sample IDs, and number of analyses (n) are provided.

Analysis	Depth	Sample	n	Na2O	MgO	Al2O3	SiO2	SO3	K2O	CaO	TiO2	MnO	FeO	CuO	Total
Non-aligned matrix	500m	DD627_2	17	0.21	2.16	11.58	73.28	0.26	5.42	2.09	0.79	0.09	3.98	0.14	100
Non-aligned matrix	496m	DD627_4	10	0.30	3.04	12.94	67.19	2.92	5.48	0.40	0.92	0.03	5.49	1.29	100
Non-aligned matrix	494m	DD627_7	8	0.10	3.10	12.24	62.71	5.52	5.33	0.93	0.93	0.09	6.42	2.61	100
Non-aligned matrix	489m	DD627_10	12	0.17	3.36	12.32	60.05	8.84	5.47	1.11	0.91	0.07	7.47	0.24	100
Non-aligned matrix	485m	DD627_11	14	0.14	3.64	13.47	68.22	1.49	5.47	1.60	1.03	0.12	4.88	-0.07	100
Non-aligned matrix	463m	DD627_15	19	0.12	3.11	12.45	70.79	1.31	4.49	2.36	0.62	0.07	4.67	0.00	100
Aligned matrix	500m	DD627_2	12	0.23	2.46	13.56	68.93	0.34	6.24	2.42	1.12	0.09	4.48	0.15	100
Aligned matrix	496m	DD627_4	9	0.22	4.45	14.74	60.84	2.95	5.71	1.72	0.92	0.11	7.00	1.34	100
Aligned matrix	494m	DD627_7	7	0.15	2.51	13.56	65.17	3.58	6.25	0.96	1.19	0.00	4.78	1.85	100
Aligned matrix	489m	DD627_10	2	0.08	3.42	13.48	58.86	8.61	5.93	1.07	0.80	0.13	7.67	-0.04	100
Aligned matrix	485m	DD627_11	7	0.19	4.08	13.40	66.50	1.61	5.34	1.46	1.56	0.15	5.66	0.04	100
Aligned matrix	463m	DD627_15	4	0.11	5.55	9.28	62.43	1.06	4.06	11.23	0.74	0.35	5.14	0.05	100
Chlorite	500m	DD627_2	16	0.23	13.24	20.27	25.90	0.08	0.24	0.11	0.14	0.12	27.66	0.00	88
Chlorite	496m	DD627_4	42	0.12	16.61	19.96	26.77	0.08	0.07	0.04	0.05	0.10	24.20	0.01	88
Chlorite	494m	DD627_7	14	0.21	16.76	20.66	26.52	0.13	0.04	0.01	0.04	0.24	23.26	0.13	88
Chlorite	489m	DD627_10	9	0.16	17.46	20.47	26.82	0.12	0.06	0.15	0.07	0.13	22.59	-0.04	88
Chlorite	485m	DD627_11	32	0.12	17.97	19.78	27.14	0.07	0.03	0.05	0.04	0.10	22.75	-0.04	88

Chlorite	463m	DD627_15	23	0.16	16.23	20.26	26.24	0.01	0.07	0.05	0.03	0.11	24.86	-0.03	88
Biotite	500m	DD627_2	16	0.16	9.31	13.83	37.13	0.01	10.74	0.17	2.22	0.00	24.47	-0.05	98
Biotite	496m	DD627_4	1	0.15	13.13	14.03	38.74	0.22	10.96	0.12	1.74	-0.01	19.14	-0.22	98
Biotite	494m	DD627_7	n.a	n.a	n.a	n.a	n.a	n.a	n.a	n.a	n.a	n.a	n.a	n.a	n.a
Biotite	489m	DD627_10	n.a	n.a	n.a	n.a	n.a	n.a	n.a	n.a	n.a	n.a	n.a	n.a	n.a
Biotite	485m	DD627_11	n.a	n.a	n.a	n.a	n.a	n.a	n.a	n.a	n.a	n.a	n.a	n.a	n.a
Biotite	463m	DD627_15	n.a	n.a	n.a	n.a	n.a	n.a	n.a	n.a	n.a	n.a	n.a	n.a	n.a
Muscovite	500m	DD627_2	27	0.37	1.89	28.39	47.33	0.05	12.32	0.09	1.03	0.02	4.53	0.00	96
Muscovite	496m	DD627_4	17	0.45	1.82	27.58	52.09	0.09	11.15	-0.04	0.50	-0.01	2.30	0.08	96
Muscovite	494m	DD627_7	16	0.67	1.02	30.91	49.29	0.08	11.50	0.00	0.38	0.02	2.00	0.12	96
Muscovite	489m	DD627_10	2	1.09	0.82	33.86	45.32	0.18	12.07	-0.02	0.56	0.01	2.03	0.07	96
Muscovite	485m	DD627_11	20	0.49	1.93	28.35	51.12	0.11	11.11	-0.04	0.51	-0.02	2.47	-0.03	96
Muscovite	463m	DD627_15	29	0.39	1.92	29.48	49.35	0.05	11.71	0.05	0.50	0.01	2.48	0.06	96

Table 13: Standard deviations for the SEM compositional analysis of high-grade drill-hole DKMC_DD627 at Kamoia.

Analysis	Depth	Sample	n	Na2O	MgO	Al2O3	SiO2	SO3	K2O	CaO	TiO2	MnO	FeO	CuO
Non-aligned matrix	500m	DD627_2	17	0.11	0.13	0.94	1.66	0.13	0.54	0.27	0.19	0.04	0.23	0.14
Non-aligned matrix	496m	DD627_4	10	0.06	0.52	0.66	1.96	0.80	0.42	0.60	0.20	0.06	0.75	0.37
Non-aligned matrix	494m	DD627_7	8	0.06	0.36	0.94	2.21	1.48	0.70	0.29	0.14	0.08	0.98	0.57
Non-aligned matrix	489m	DD627_10	12	0.14	0.35	0.64	1.49	1.01	0.35	0.27	0.14	0.04	0.47	0.25
Non-aligned matrix	485m	DD627_11	14	0.12	0.41	0.89	2.12	0.19	0.24	0.24	0.36	0.09	0.64	0.12
Non-aligned matrix	463m	DD627_15	19	0.11	0.55	0.48	1.15	0.29	0.33	0.56	0.12	0.09	1.16	0.14
Aligned matrix	500m	DD627_2	12	0.07	0.37	2.04	3.57	0.09	0.92	0.96	0.27	0.09	0.41	0.10
Aligned matrix	496m	DD627_4	9	0.07	1.16	1.03	3.45	1.06	0.82	2.76	0.23	0.17	1.20	0.52
Aligned matrix	494m	DD627_7	7	0.10	0.33	0.92	1.72	1.18	0.44	0.17	0.17	0.05	0.71	0.67
Aligned matrix	489m	DD627_10	2	0.01	0.08	0.01	1.19	0.89	0.07	0.34	0.06	0.04	0.03	0.09
Aligned matrix	485m	DD627_11	7	0.12	0.22	0.67	0.88	0.19	0.23	0.31	0.08	0.07	0.29	0.12
Aligned matrix	463m	DD627_15	4	0.11	0.31	0.55	0.68	0.37	0.19	0.62	0.18	0.13	0.38	0.19
Chlorite	500m	DD627_2	16	0.12	2.11	3.02	1.58	0.13	0.31	0.16	0.12	0.12	2.80	0.15
Chlorite	496m	DD627_4	42	0.12	1.26	0.97	0.96	0.14	0.12	0.09	0.10	0.11	1.43	0.19
Chlorite	494m	DD627_7	14	0.09	1.85	1.27	1.41	0.13	0.08	0.09	0.08	0.30	2.25	0.26
Chlorite	489m	DD627_10	9	0.08	1.61	1.14	0.89	0.12	0.07	0.12	0.06	0.08	1.46	0.15
Chlorite	485m	DD627_11	32	0.13	1.21	1.70	1.18	0.11	0.09	0.09	0.10	0.11	1.10	0.18
Chlorite	463m	DD627_15	23	0.15	0.41	0.52	0.60	0.12	0.16	0.10	0.10	0.12	0.86	0.14

Biotite	500m	DD627_2		16	0.10	0.77	1.06	1.93	0.15	1.04	0.23	0.16	0.11	2.64	0.16
Biotite	496m	DD627_4		1	n.a	n.a	n.a	n.a	n.a	n.a	n.a	n.a	n.a	n.a	n.a
Biotite	494m	DD627_7	n.a		n.a	n.a	n.a	n.a	n.a	n.a	n.a	n.a	n.a	n.a	n.a
Biotite	489m	DD627_10	n.a		n.a	n.a	n.a	n.a	n.a	n.a	n.a	n.a	n.a	n.a	n.a
Biotite	485m	DD627_11	n.a		n.a	n.a	n.a	n.a	n.a	n.a	n.a	n.a	n.a	n.a	n.a
Biotite	463m	DD627_15	n.a		n.a	n.a	n.a	n.a	n.a	n.a	n.a	n.a	n.a	n.a	n.a
Muscovite	500m	DD627_2		27	0.26	0.75	3.24	3.19	0.12	1.20	0.50	0.60	0.10	1.26	0.11
Muscovite	496m	DD627_4		17	0.36	0.81	6.19	7.07	0.11	1.89	0.06	0.69	0.06	0.94	0.14
Muscovite	494m	DD627_7		16	0.39	0.63	6.73	8.60	0.11	2.14	0.07	0.17	0.05	0.72	0.25
Muscovite	489m	DD627_10		2	0.48	0.26	2.21	0.12	0.16	1.03	0.02	0.03	0.00	1.14	0.02
Muscovite	485m	DD627_11		20	0.37	1.11	4.67	4.21	0.12	1.36	0.10	0.40	0.11	1.02	0.23
Muscovite	463m	DD627_15		29	0.31	0.86	4.28	4.26	0.14	1.72	0.16	0.29	0.09	1.51	0.17

Table 14: SEM average oxide concentrations from high-grade drill-hole DKMC_DD1161 at Kakula. Oxide concentrations are in wt.% and normalised to 100%. Negative values and values below the general SEM detection limit of 0.15 wt.% are not reliable or meaningful. Sample descriptions, sample depths, sample IDs, and number of analyses (n) are provided.

Analysis	Depth	Sample	n	Na2O	MgO	Al2O3	SiO2	SO3	K2O	CaO	TiO2	MnO	FeO	CuO	Total
Non-aligned matrix	889m	DD1161_1	8	0.20	3.98	16.67	62.82	0.26	7.93	1.31	0.86	0.10	5.68	0.20	100
Non-aligned matrix	452m	DD1161_3	18	3.26	2.84	12.35	69.56	0.79	3.24	1.20	0.80	0.06	5.88	0.00	100
Non-aligned matrix	211m	DD1161_6	10	5.97	4.71	15.34	58.42	0.21	2.09	2.92	1.24	0.11	9.03	0.04	100
Aligned Matrix	889m	DD1161_1	n.a	n.a	n.a	n.a	n.a	n.a	n.a	n.a	n.a	n.a	n.a	n.a	n.a
Aligned Matrix	452m	DD1161_3	n.a	n.a	n.a	n.a	n.a	n.a	n.a	n.a	n.a	n.a	n.a	n.a	n.a
Aligned Matrix	211m	DD1161_6	n.a	n.a	n.a	n.a	n.a	n.a	n.a	n.a	n.a	n.a	n.a	n.a	n.a
Chlorite	889m	DD1161_1	7	0.35	20.97	19.91	28.28	0.08	0.38	0.03	0.10	0.14	17.84	-0.08	88
Chlorite	452m	DD1161_3	24	0.16	17.13	18.40	27.17	0.06	0.04	0.04	0.04	0.46	24.59	0.10	88
Chlorite	211m	DD1161_6	8	0.24	18.50	17.85	27.39	0.09	0.23	0.05	0.04	0.40	23.37	0.16	88
Biotite	889m	DD1161_1	13	0.23	15.56	14.74	39.21	0.11	11.36	-0.05	1.61	0.04	15.15	0.04	98
Biotite	452m	DD1161_3	n.a	n.a	n.a	n.a	n.a	n.a	n.a	n.a	n.a	n.a	n.a	n.a	n.a
Biotite	211m	DD1161_6	n.a	n.a	n.a	n.a	n.a	n.a	n.a	n.a	n.a	n.a	n.a	n.a	n.a
Muscovite	889m	DD1161_1	18	0.20	2.58	27.68	48.11	0.15	11.89	-0.03	0.63	0.03	4.71	0.06	96
Muscovite	452m	DD1161_3	n.a	n.a	n.a	n.a	n.a	n.a	n.a	n.a	n.a	n.a	n.a	n.a	n.a
Muscovite	211m	DD1161_6	n.a	n.a	n.a	n.a	n.a	n.a	n.a	n.a	n.a	n.a	n.a	n.a	n.a

Table 15: Standard deviations for the SEM compositional analysis of high-grade drill-hole DKMC_DD1161 at Kakula.

Analysis	Depth	Sample	n	Na2O	MgO	Al2O3	SiO2	SO3	K2O	CaO	TiO2	MnO	FeO	CuO
Non-aligned matrix	889m	DD1161_1	8	0.03	0.27	0.93	0.93	0.02	0.49	0.68	0.06	0.03	0.47	0.07
Non-aligned matrix	452m	DD1161_3	18	0.08	0.09	0.24	0.55	0.04	0.21	0.08	0.07	0.04	0.23	0.07
Non-aligned matrix	211m	DD1161_6	10	0.34	0.17	0.41	0.70	0.05	0.15	0.15	0.08	0.06	0.35	0.06
Aligned Matrix	889m	DD1161_1	n.a	n.a	n.a	n.a	n.a	n.a	n.a	n.a	n.a	n.a	n.a	n.a
Aligned Matrix	452m	DD1161_3	n.a	n.a	n.a	n.a	n.a	n.a	n.a	n.a	n.a	n.a	n.a	n.a
Aligned Matrix	211m	DD1161_6	n.a	n.a	n.a	n.a	n.a	n.a	n.a	n.a	n.a	n.a	n.a	n.a
Chlorite	889m	DD1161_1	7	0.03	0.89	0.72	0.69	0.02	0.18	0.06	0.05	0.02	0.7	0.07
Chlorite	452m	DD1161_3	24	0.13	0.26	0.24	0.43	0.03	0.06	0.03	0.03	0.06	1.42	0.06
Chlorite	211m	DD1161_6	8	0.09	0.2	0.27	0.17	0.04	0.23	0.04	0.02	0.07	0.62	0.08
Biotite	889m	DD1161_1	13	0.06	1.03	0.42	0.56	0.04	0.73	0.03	0.06	0.04	1.77	0.09
Biotite	452m	DD1161_3	n.a	n.a	n.a	n.a	n.a	n.a	n.a	n.a	n.a	n.a	n.a	n.a
Biotite	211m	DD1161_6	n.a	n.a	n.a	n.a	n.a	n.a	n.a	n.a	n.a	n.a	n.a	n.a
Muscovite	889m	DD1161_1	18	0.08	0.82	1.75	1.29	0.04	1.09	0.06	0.22	0.04	1.92	0.09
Muscovite	452m	DD1161_3	n.a	n.a	n.a	n.a	n.a	n.a	n.a	n.a	n.a	n.a	n.a	n.a
Muscovite	211m	DD1161_6	n.a	n.a	n.a	n.a	n.a	n.a	n.a	n.a	n.a	n.a	n.a	n.a

Table 16: SEM average oxide concentrations for various minerals at Kakula. Oxide concentrations are in wt.% and normalisation was to 52% for dolomite and Fe-dolomite and 52% to calcite because carbon was not analysed, whereas normalisation was to 95% for pumpellyite to account for H₂O. Negative values and values below the general SEM detection limit of 0.15 wt.% are not reliable or meaningful. Sample descriptions, sample depths, sample IDs, and number of analyses (n) are provided.

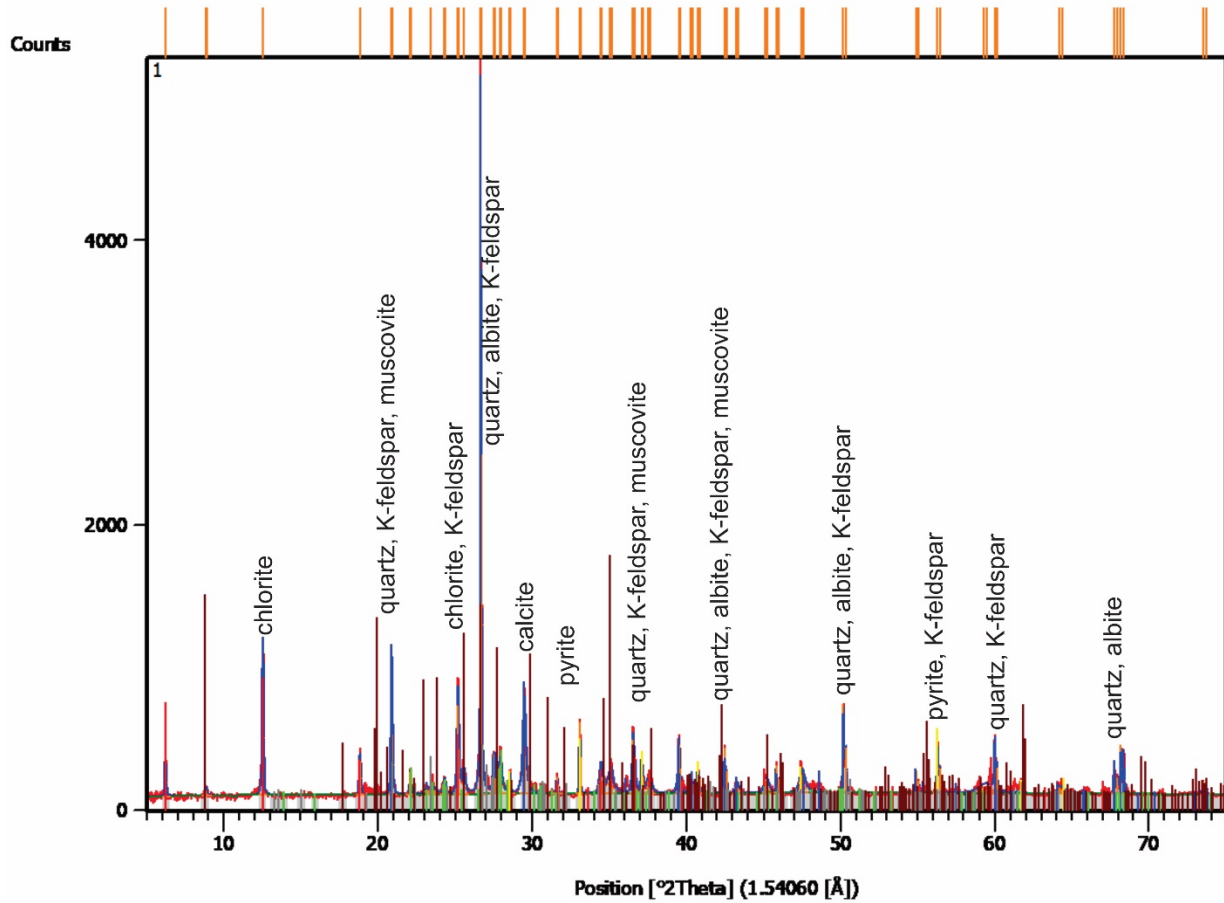
Analysis	Depth	Sample	n	Na2O	MgO	Al2O3	SiO2	SO3	K2O	CaO	TiO2	MnO	FeO	CuO	Total
K-feldspar	335m	DD1012_6	6	0.21	0.17	17.52	62.53	0.10	19.06	-0.09	0.07	0.01	0.34	0.09	100
Fe-dolomite	335m	DD1012_6	15	0.04	16.42	0.04	0.40	-0.01	0.03	29.14	0.06	1.32	4.50	0.05	52
Dolomite	326m	DD1012_7	4	0.05	20.25	0.07	0.21	0.05	0.12	30.89	-0.01	0.07	0.27	0.04	52
Albite	74m	DD1012_16	4	11.57	0.21	19.82	67.52	0.32	0.01	0.20	0.02	0.00	0.26	0.06	100
Calcite	74m	DD1012_16	8	0.06	0.12	0.18	0.57	0.25	0.18	53.45	0.04	0.54	0.65	-0.05	56
Pumpellyite?	211m	DD1161_6	5	0.40	0.02	18.17	39.22	0.05	0.09	21.88	0.48	0.10	14.70	-0.12	95

Table 17: Standard deviations for the SEM compositional analysis of various minerals Kakula.

Analysis	Depth	Sample	n	Na2O	MgO	Al2O3	SiO2	SO3	K2O	CaO	TiO2	MnO	FeO	CuO
K-feldspar	335m	DD1012_6	6	0.12	0.29	0.50	1.19	0.05	0.90	0.06	0.08	0.06	0.20	0.15
Fe-dolomite	335m	DD1012_6	16	0.07	1.26	0.13	0.58	0.07	0.08	0.53	0.06	0.17	1.15	0.14
Dolomite	326m	DD1012_7	4	0.04	0.43	0.07	0.10	0.09	0.06	0.35	0.09	0.07	0.17	0.05
Albite	74m	DD1012_16	4	0.19	0.08	0.33	0.40	0.11	0.06	0.12	0.06	0.04	0.09	0.06
Calcite	74m	DD1012_16	8	0.14	0.12	0.19	0.40	0.18	0.12	0.91	0.04	0.26	0.15	0.06
Pumpellyite?	211m	DD1161_6	5	0.59	0.07	0.73	1.65	0.10	0.13	1.10	0.32	0.11	0.99	0.13

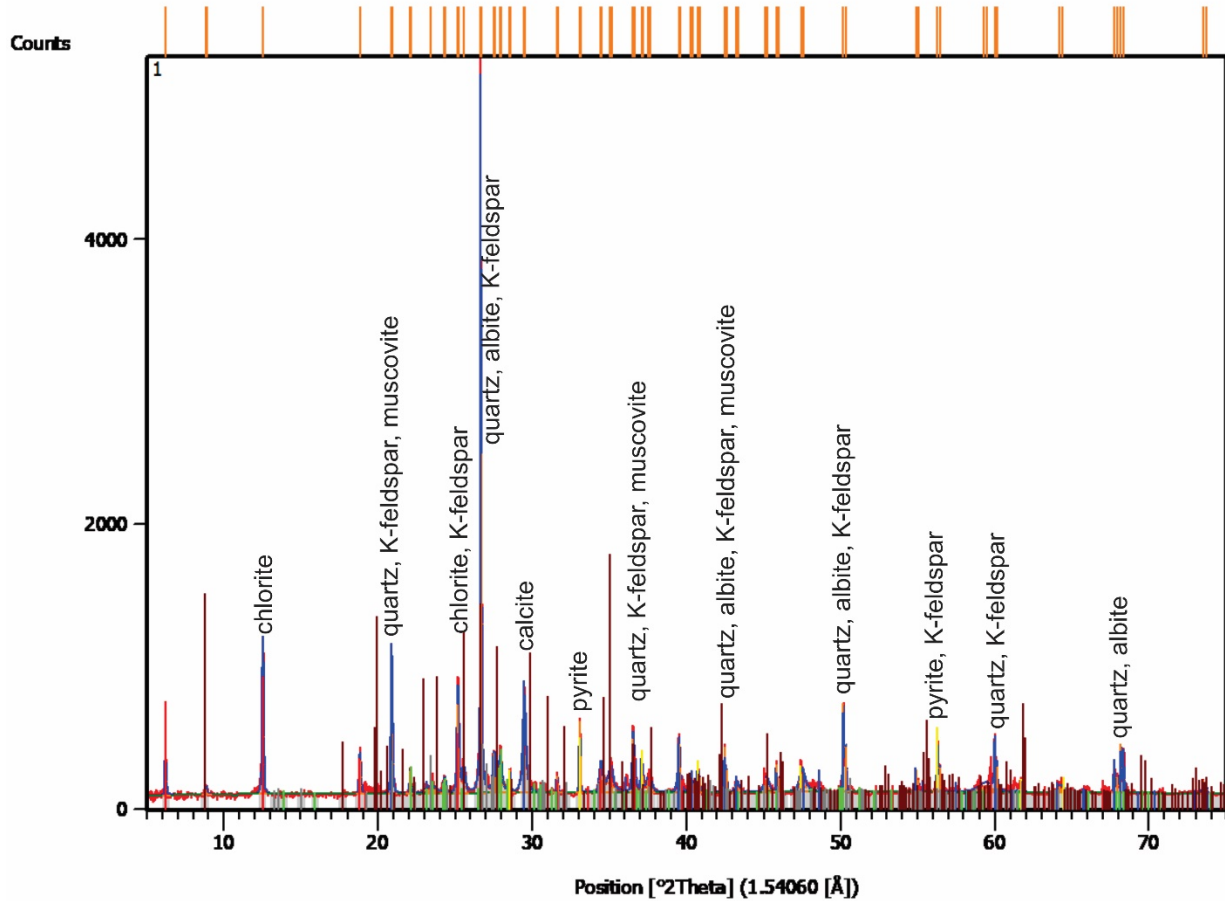
Appendix A

Figure A.1: XRD pattern and mineral identification of sample DD1012_16 of least-altered diamictite matrix at Kakula.



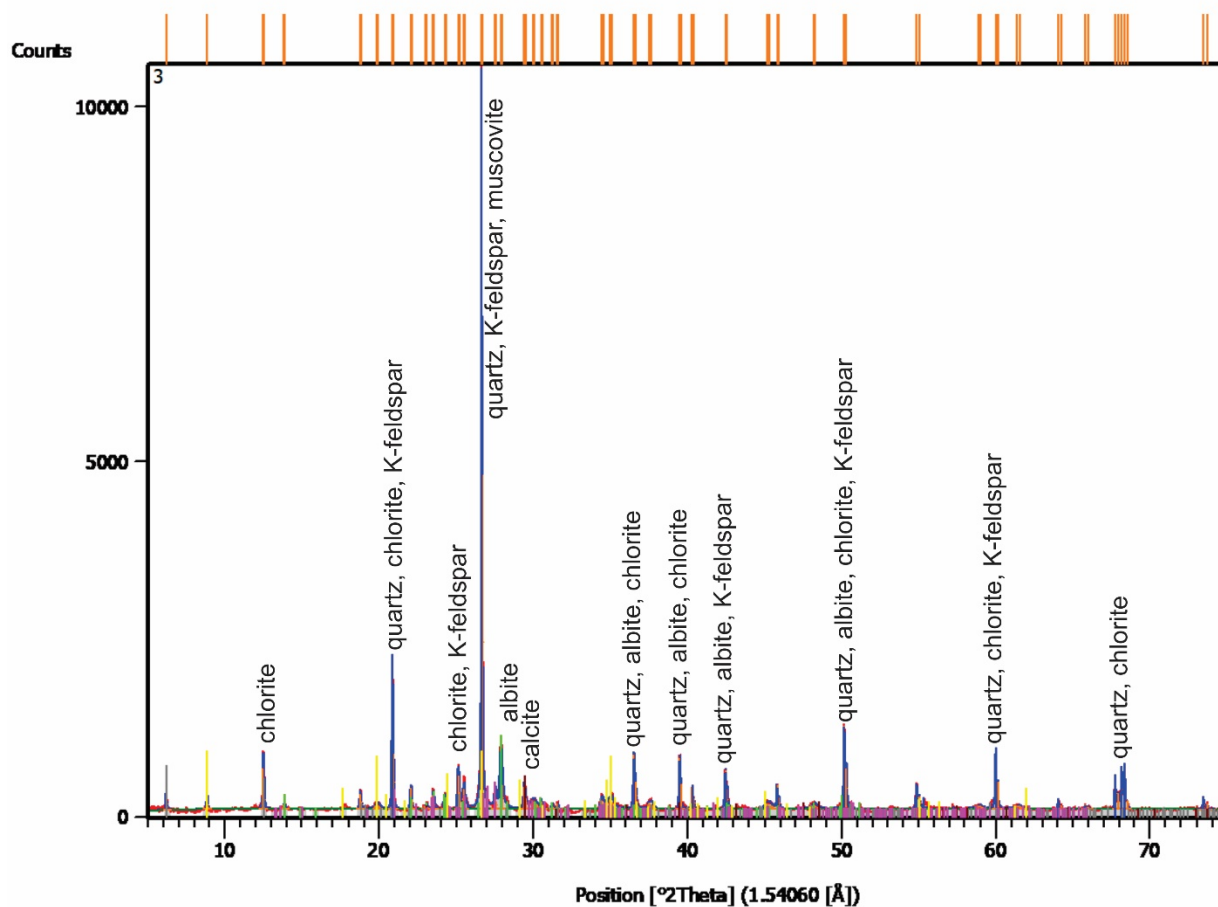
Visible	Ref. Code	Score	Mineral Name	Chemical Formula
*	01-079-1910	73	Quartz	Si O ₂
*	00-006-0710	55	Pyrite, syn	Fe S ₂
*	00-007-0076	55	Clinocllore, ferroan	(Mg _{2.8} Fe _{1.7} Al _{1.2}) (Si _{2.8} Al _{1.2}) O ₁₀ (O H) ₈
*	01-083-0578	37	Calcite	Ca (C O ₃)
*	00-020-0554	24	Albite, ordered	Na Al Si ₃ O ₈
*	01-076-0823	20	Potassium-Feldspar P2B	K Al Si ₃ O ₈
*	01-074-2428	12	Muscovite	K Al ₃ Si ₃ O ₁₀ (O H) ₂

Figure A.2: XRD pattern and mineral identification of sample DD1161_6 of least-altered diamictite matrix at Kakula.



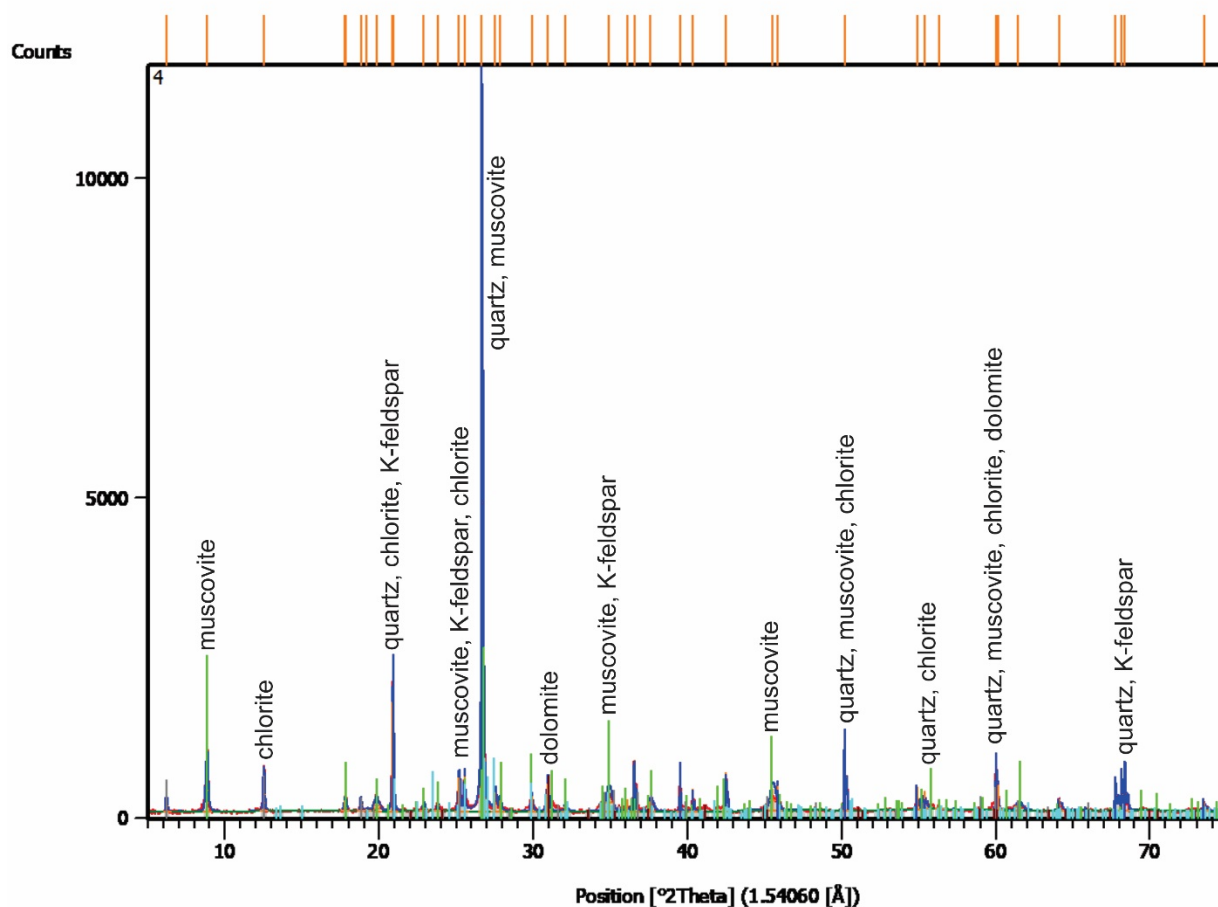
Visible	Ref. Code	Score	Mineral Name	Chemical Formula
*	01-079-1910	62	Quartz	Si O ₂
*	00-009-0466	57	Albite, ordered	Na Al Si ₃ O ₈
*	00-007-0078	37	Clinochlore- 1\ITM#I#b\RG, ferrian	(Mg , Fe , Al) ₆ (Si , Al) ₄ O ₁₀ (O H) ₈
*	00-019-0467	38	Ferropargasite, syn	Na Ca ₂ Fe ₄ Al (Si ₆ Al ₂) O ₂₂ (O H) ₂
*	00-041-0586	18	Ankerite	Ca (Fe , Mg) (C O ₃) ₂
*	01-076-0824	29	Potassium-Feldspar P2A	K _{0.931} Na _{0.055} Ca _{0.009} Ba _{0.005} Al _{0.97} Si _{3.03} O ₈
*	01-073-1658	19	Phlogopite	K Mg ₃ Al Si ₃ O ₁₀ O H F

Figure A.3: XRD pattern and mineral identification of sample DD1161_3 of least-altered diamictite matrix at Kakula.



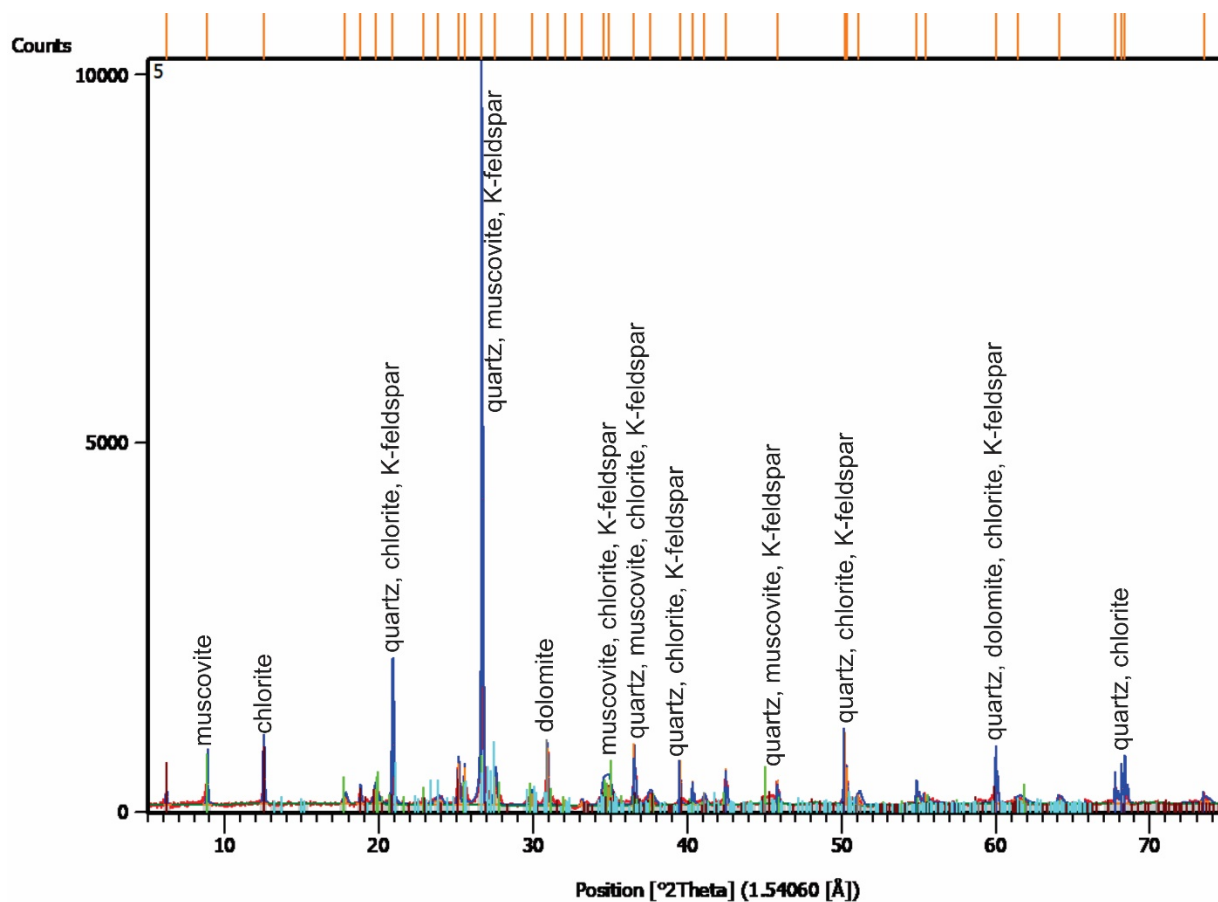
Visible	Ref. Code	Score	Mineral Name	Chemical Formula
*	01-078-2315	75	Quartz	Si O ₂
*	00-009-0466	48	Albite, ordered	Na Al Si ₃ O ₈
*	01-072-1234	25	Chlorite	Mg _{2.5} Fe _{1.65} Al _{1.5} Si _{2.2} Al _{1.8} O ₁₀ (O H) ₈
*	01-083-0578	21	Calcite	Ca (C O ₃)
*	01-076-0827	24	Potassium-Feldspar A1D	K _{.904} Na _{.085} Ca _{.005} Ba _{.006} Al _{0.95} Si _{3.05} O ₈
*	00-007-0025	23	Muscovite-1\ITM\RG, syn	K Al ₂ Si ₃ Al O ₁₀ (O H) ₂

Figure A.4: XRD pattern and mineral identification of sample DD1012_13 of ore-zone diamictite matrix at Kakula.



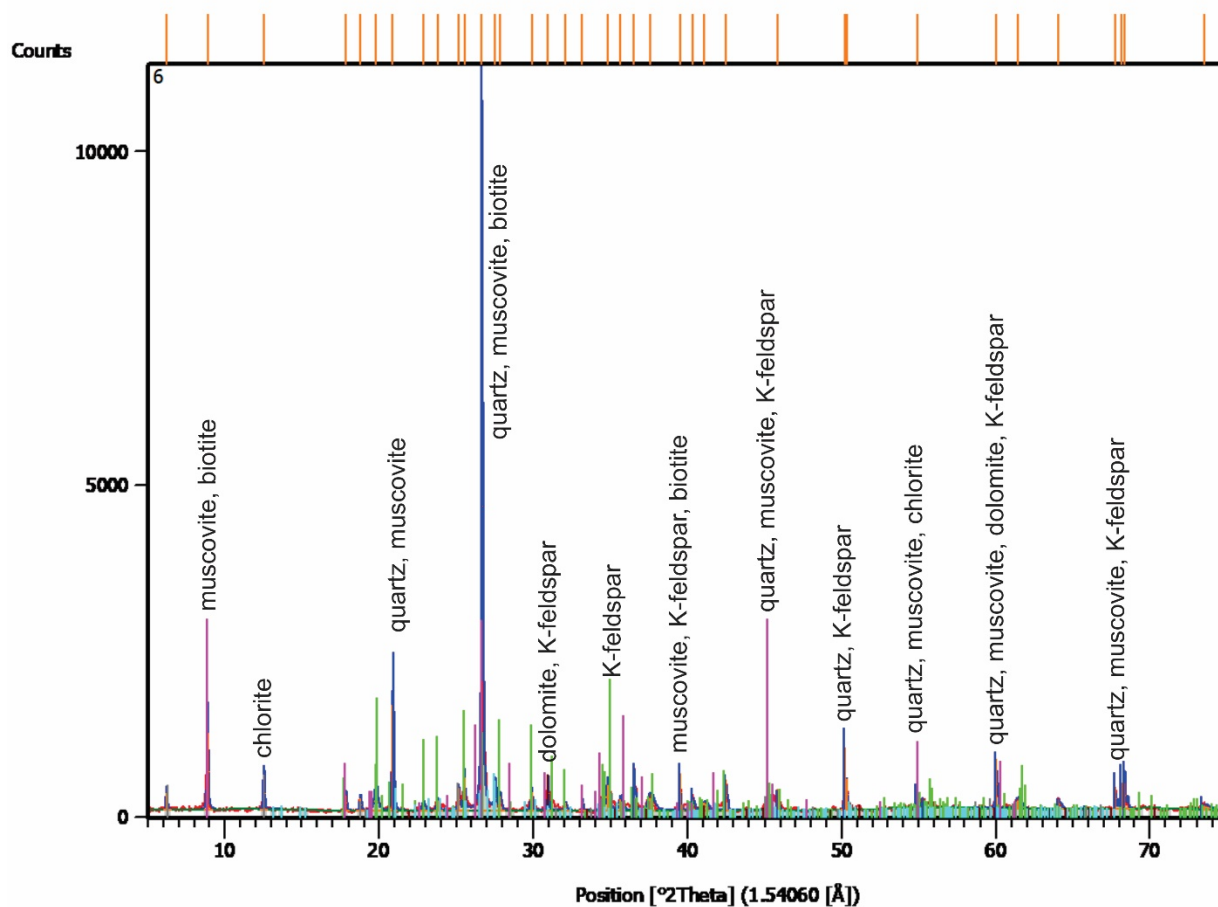
Visible	Ref. Code	Score	Mineral Name	Chemical Formula
*	01-079-1910	76	Quartz	Si O ₂
*	00-006-0263	34	Muscovite-2\ITM#1\RG	K Al ₂ (Si ₃ Al) O ₁₀ (O H , F) ₂
*	00-046-1323	41	Clinochlore-1\ITM#I#I#b-2\RG	(Mg , Al , Fe) ₆ (Si , Al) ₄ O ₁₀ (O H) ₈
*	00-036-0426	28	Dolomite	Ca Mg (C O ₃) ₂
*	01-071-1540	16	Orthoclase	K Si ₃ Al O ₈

Figure A.5: XRD pattern and mineral identification of sample DD975_10 of ore-zone diamictite matrix at Kakula.



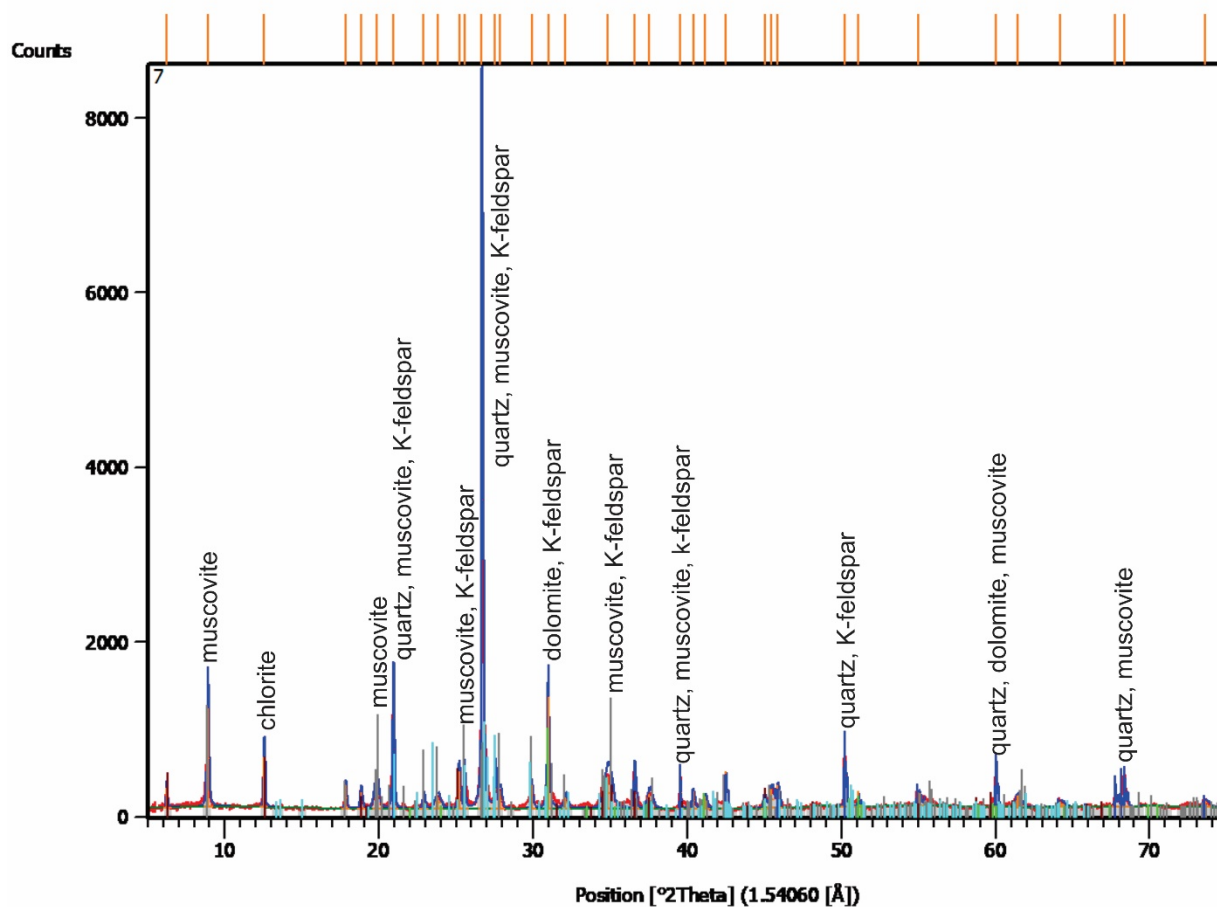
Visible	Ref. Code	Score	Mineral Name	Chemical Formula
*	01-078-2315	74	Quartz	Si O ₂
*	00-007-0032	33	Muscovite 2M1, syn	K Al ₂ Si ₃ Al O ₁₀ (O H) ₂
*	00-036-0426	40	Dolomite	Ca Mg (C O ₃) ₂
*	01-079-1270	39	Clinochlore	(Mg _{2.96} Fe _{1.55} Fe _{.136} Al _{1.275}) (Si _{2.622} Al _{1.376} O ₁₀) (O H) ₈
*	01-076-0830	22	Potassium-Feldspar RC2OC	K _{0.92} Na _{0.08} Al _{0.99} Si _{3.01} O ₈

Figure A.6: XRD pattern and mineral identification of sample DD1012_7 of ore-zone diamictite matrix at Kakula.



Visible	Ref. Code	Score	Mineral Name	Chemical Formula
*	01-083-0539	54	Quartz	Si O ₂
*	01-072-1503	27	Muscovite	K Al ₂ (Si ₃ Al) O ₁₀ (O H) ₂
*	00-045-1321	34	Clinochlore-1\ITM#I#I#b\RG, manganoan	Mg ₃ Mn ₂ Al Si ₃ Al O ₁₀ (O H) ₈
*	00-005-0622	31	Dolomite	Ca Mg (C O ₃) ₂
*	01-076-0831	18	Potassium-Feldspar CA1E	K _{0.94} Na _{0.06} Al _{1.01} Si _{2.99} O ₈
*	00-010-0492	17	Phlogopite-3\ITT\RG	K Mg ₃ (Si ₃ Al) O ₁₀ (O H) ₂

Figure A.7: XRD pattern and mineral identification of sample DD975_4 of ore-zone diamictite matrix at Kakula.



Visible	Ref. Code	Score	Mineral Name	Chemical Formula
*	01-079-1910	73	Quartz	Si O ₂
*	00-036-0426	43	Dolomite	Ca Mg (C O ₃) ₂
*	01-072-1503	31	Muscovite	K Al ₂ (Si ₃ Al) O ₁₀ (O H) ₂
*	00-045-1321	39	Clinochlore- 1\ITM#I#I#b\RG, manganooan	Mg ₃ Mn ₂ Al Si ₃ Al O ₁₀ (O H) ₈
*	01-076-0824	25	Potassium-Feldspar P2A	K.931 Na0.055 Ca.009 Ba.005 Al0.97 Si3.03 O8

Appendix B

Table B.1: Whole-rock geochemistry analyses with major oxide concentrations from different samples, average concentrations, and estimates of abundance of major oxides by Pakiser and Robinson (1967) in silicic rock, mafic rock, and continental crust.

Sample	Description	SiO ₂ %	TiO ₂ %	Al ₂ O ₃ %	Fe ₂ O ₃ %	MgO %	CaO %	Na ₂ O %	K ₂ O %
DD1012_16	least-altered matrix	49.20	0.73	11.50	15.55	4.67	5.28	0.99	2.19
DD1161_6	least-altered matrix	55.80	1.19	14.10	11.65	4.98	2.63	4.09	1.88
DD1161_3	least-altered matrix	63.50	0.85	13.90	8.26	3.71	1.35	2.46	2.96
DD1012_13	ore-zone matrix	63.00	0.85	14.40	6.88	4.02	1.30	0.09	5.19
DD975_10	ore-zone matrix	59.40	0.83	13.05	7.66	5.14	2.32	0.07	4.82
DD1012_7	ore-zone matrix	57.80	0.86	13.90	7.12	4.74	1.97	0.08	5.27
DD975_4	ore-zone matrix	58.80	0.80	13.50	7.42	6.25	1.70	0.08	5.45
DD975_4_M	mafic clast (diamictite)	48.10	1.66	10.65	13.20	12.60	2.19	0.03	0.67
DD627_4	mafic clast (diamictite)	43.40	0.39	15.00	16.60	11.10	1.20	0.03	1.56
DD1161_2	mafic clast (diamictite)	47.40	0.59	15.25	11.85	10.15	0.15	0.03	3.72
DLKE_6	local mafic (flow)	49.70	1.75	15.10	12.05	7.12	4.17	4.80	0.81
DKLE_2	local mafic (flow)	39.60	1.53	13.00	6.70	3.24	15.70	5.15	0.11
DKMC_12	local mafic (flow)	50.20	1.63	13.55	11.35	5.87	11.10	2.97	0.55
DKMC_32	local mafic (flow)	57.50	0.90	17.25	8.71	3.53	6.54	0.12	3.87
DKMC_72	local mafic (basement)	47.10	0.61	15.30	9.88	6.95	10.15	3.09	0.23
DPLB_4	local mafic (basement)	53.70	0.56	13.65	9.61	6.90	9.19	1.43	1.20
DLFP_8	local mafic (basement)	51.10	0.47	14.95	8.80	8.39	11.25	1.44	0.58

average	least-altered matrix	56.17	0.92	13.17	11.82	4.45	3.09	2.51	2.34
average	ore-zone matrix	59.75	0.84	13.71	7.27	5.04	1.82	0.08	5.18
average	mafic clasts (diamictite)	49.84	1.06	14.69	9.59	6.00	9.73	2.71	1.05
average	local mafics	46.30	0.88	13.63	13.88	11.28	1.18	0.03	1.98
reference	silicic rock	69.30	0.50	14.60	4.20	1.10	2.60	3.90	3.80
reference	mafic rock	48.80	1.80	15.60	11.90	8.70	10.80	2.30	0.70
reference	continental crust	57.90	1.20	15.20	8.40	5.30	7.10	3.00	2.10

Table B.2: Whole-rock geochemistry analyses with trace element concentrations from different samples, average concentrations, and estimates of abundance of trace elements for MORB (mid-ocean ridge basalt; Taylor and McLennan, 1985; 2001), continental crust, upper continental crust, (Taylor and McLennan, 1995; 2001) and average sediment (McLennan and Murray, 1999; Taylor and McLennan, 2001). Plotting order of elements was according to the North American shale composite (NASC) by Gromet et al. (1984).

SAMPLE	DESCRIPTION	V ppm	Cr ppm	Rb ppm	Sr ppm	Y ppm	Zr ppm	Nb ppm	Cs ppm	Ba ppm	La ppm	Ce ppm
DD1012_16	least-altered matrix	178.0	140.0	61.0	98.4	25.3	153.0	13.7	0.9	319.0	28.3	58.0
DD1161_6	least-altered matrix	281.0	90.0	65.0	196.5	37.2	199.0	18.5	2.1	415.0	37.8	76.4
DD1161_3	least-altered matrix	181.0	110.0	122.0	116.0	33.1	253.0	16.9	3.2	524.0	39.0	81.3
DD1012_13	ore-zone matrix	158.0	90.0	203.0	50.5	31.3	224.0	20.5	9.2	485.0	53.1	105.0
DD975_10	ore-zone matrix	206.0	90.0	173.0	60.0	26.5	192.0	14.7	6.7	457.0	40.5	82.7
DD1012_7	ore-zone matrix	170.0	100.0	193.0	55.8	32.7	212.0	20.2	7.1	556.0	43.5	86.2
DD975_4	ore-zone matrix	128.0	190.0	199.5	49.2	24.4	173.0	21.1	9.3	398.0	29.8	59.3
DD975_4_M	mafic clast (diamictite)	190.0	800.0	40.5	46.4	12.4	122.0	13.2	5.0	23.5	15.9	33.9
DD627_4	mafic clast (diamictite)	140.0	390.0	55.6	53.6	4.9	46.0	3.8	3.0	233.0	1.4	3.0
DD1161_2	mafic clast (diamictite)	225.0	310.0	139.5	583.0	9.2	60.0	4.2	7.8	>1000	3.9	7.2
DLKE_6	local mafic (flow)	337.0	220.0	38.5	131.0	22.2	109.0	13.8	6.0	113.0	13.2	30.7
DKLE_2	local mafic (flow)	269.0	190.0	2.6	127.5	20.1	101.0	10.9	0.2	18.6	5.4	15.0
DKMC_12	local mafic (flow)	329.0	200.0	9.9	559.0	21.1	106.0	11.0	0.6	116.0	11.8	26.5
DKMC_32	local mafic (flow)	195.0	160.0	164.0	376.0	40.8	205.0	14.0	8.1	601.0	50.0	102.0
DKMC_72	local mafic (basement)	272.0	220.0	5.6	93.9	20.7	92.0	5.0	0.5	50.1	14.8	30.3
DPLB_4	local mafic (basement)	225.0	510.0	39.8	119.5	22.4	104.0	5.4	0.8	292.0	16.8	33.8
DLFP_8	local mafic (basement)	245.0	360.0	29.7	105.0	12.5	50.0	2.7	3.9	142.5	6.9	14.3
average	least-altered matrix	213.3	113.3	82.7	137.0	31.9	201.7	16.4	2.1	419.3	35.0	71.9

average	ore-zone matrix	165.5	117.5	192.1	53.9	28.7	200.3	19.1	8.1	474.0	41.7	83.3
average	mafic clasts (diamictite)	185.0	500.0	78.5	227.7	8.8	76.0	7.1	5.3	128.3	7.1	14.7
average	local mafics	267.4	265.7	41.4	216.0	22.8	109.6	9.0	2.9	190.5	17.0	36.1
reference	average MORB	250.0	270.0	1.5	115.0	32.0	80.0	2.2	20.0	15.0	3.7	11.5
reference	average sediment	110.0	74.0	110.0	385.0	21.0	210.0	17.0	4.5	480.0	28.3	58.9
reference	average crust	230.0	185.0	37.0	260.0	20.0	100.0	11.0	1.5	250.0	16.0	33.0
reference	average upper crust	110.0	85.0	112.0	350.0	22.0	190.0	12.5	4.8	550.0	30.0	64.0

Table B.2 (continued)

SAMPLE	DESCRIPTION	Nd ppm	Sm ppm	Eu ppm	Tb ppm	Yb ppm	Lu ppm	Hf ppm	Ta ppm	W ppm	Th ppm	U ppm
DD1012_16	least-altered matrix	25.0	5.2	1.0	0.7	2.4	0.4	4.0	0.9	1.0	7.3	2.1
DD1161_6	least-altered matrix	34.4	7.1	1.7	1.1	3.6	0.6	5.5	1.1	1.0	9.6	2.1
DD1161_3	least-altered matrix	35.2	7.3	1.3	0.9	3.5	0.6	7.1	1.1	2.0	13.0	3.3
DD1012_13	ore-zone matrix	44.2	8.7	1.6	1.0	3.2	0.5	6.6	1.2	2.0	13.4	3.4
DD975_10	ore-zone matrix	35.1	6.7	1.3	0.8	2.9	0.4	5.3	0.9	2.0	10.4	2.2
DD1012_7	ore-zone matrix	35.8	7.1	1.5	1.0	3.4	0.5	6.1	1.2	2.0	11.4	3.0
DD975_4	ore-zone matrix	25.0	5.1	1.1	0.7	2.3	0.4	5.2	1.3	1.0	9.9	4.0
DD975_4_M	mafic clast (diamictite)	18.3	4.1	1.1	0.5	1.0	0.2	3.3	0.5	4.0	2.8	1.2
DD627_4	mafic clast (diamictite)	1.7	0.6	0.1	0.1	0.5	0.1	1.3	0.2	1.0	1.9	0.6
DD1161_2	mafic clast (diamictite)	3.2	0.9	0.1	0.2	0.8	0.2	2.0	0.2	1.0	3.2	1.0
DLKE_6	local mafic (flow)	18.5	4.4	1.4	0.7	1.9	0.3	2.8	0.7	<1	1.1	0.3
DKLE_2	local mafic (flow)	11.1	3.5	1.0	0.6	1.9	0.3	2.6	0.6	20.0	1.0	0.9
DKMC_12	local mafic (flow)	16.0	3.7	1.5	0.7	1.8	0.3	2.7	0.6	<1	0.9	0.2

DKMC_32	local mafic (flow)	45.6	8.7	1.8	1.3	4.1	0.6	5.5	0.9	2.0	12.6	3.5
DKMC_72	local mafic (basement)	14.1	3.1	0.9	0.6	2.2	0.3	2.5	0.3	1.0	4.5	1.1
DPLB_4	local mafic (basement)	15.2	3.3	0.7	0.6	2.3	0.3	2.8	0.3	1.0	5.2	1.4
DLFP_8	local mafic (basement)	7.2	1.6	0.6	0.3	1.3	0.2	1.6	0.2	<1	2.1	0.6
average	least-altered matrix	31.5	6.5	1.3	0.9	3.1	0.5	5.5	1.0	1.3	10.0	2.5
average	ore-zone matrix	35.0	6.9	1.4	0.9	3.0	0.5	5.8	1.2	1.8	11.3	3.2
average	mafic clasts (diamictite)	7.7	1.9	0.4	0.3	0.8	0.1	2.2	0.3	2.0	2.6	0.9
average	local mafics	18.2	4.1	1.1	0.7	2.2	0.3	2.9	0.5	6.0	3.9	1.2
reference	average MORB	10.0	3.3	1.3	0.9	3.7	0.6	2.5	0.2	0.0	0.2	0.1
reference	average sediment	24.9	4.2	0.9	0.6	2.1	0.3	5.5	1.5	2.1	10.4	2.3
reference	average crust	16.0	3.5	1.1	0.6	2.2	0.3	3.0	1.0	1.0	4.2	1.1
reference	average upper crust	26.0	4.5	0.9	0.6	2.2	0.3	5.8	1.1	2.0	10.7	2.8

Figure B.1: Concentrations (log scale) of major oxides for the average of least-altered and ore-zone matrix samples. The data are given in Table B.1.

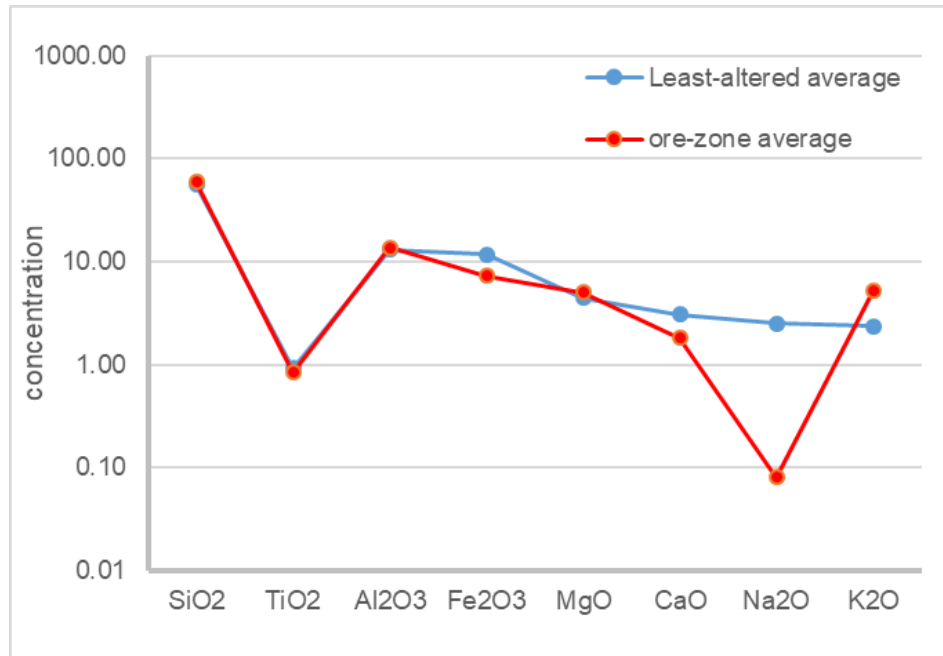


Figure B.2 : Concentrations (log scale) of major oxides for the average of least-altered and ore-zone matrix samples normalised to local mafic rock. The data and normalising values are given in Table B.1.

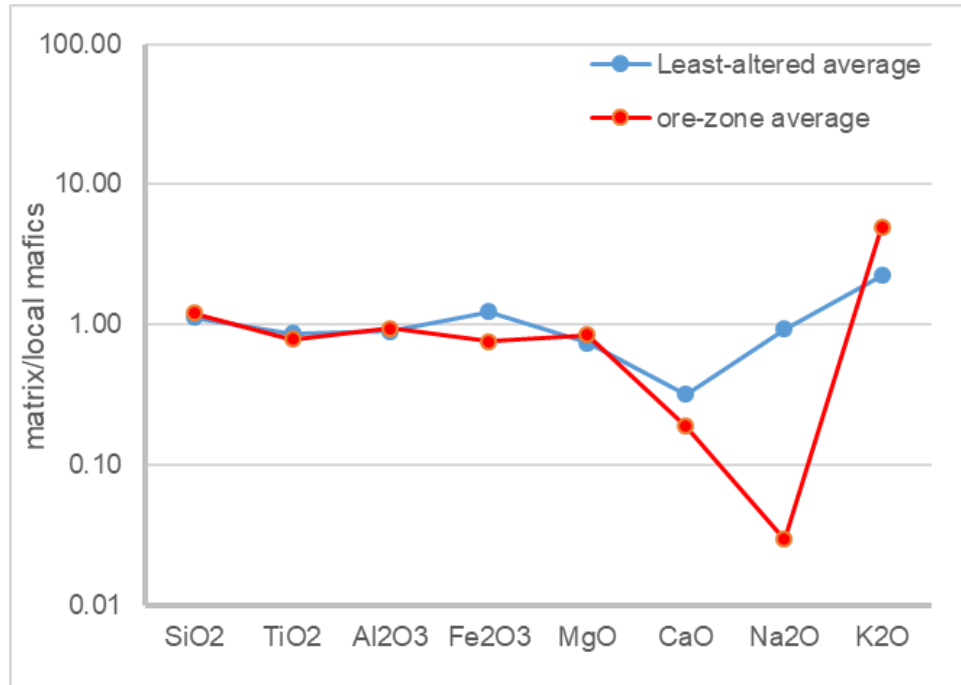


Figure B.3: Concentrations (log-scale) of major oxides for the average of least-altered and ore-zone matrix samples normalised to mafic clasts. The data and normalising values are given in Table B.1.

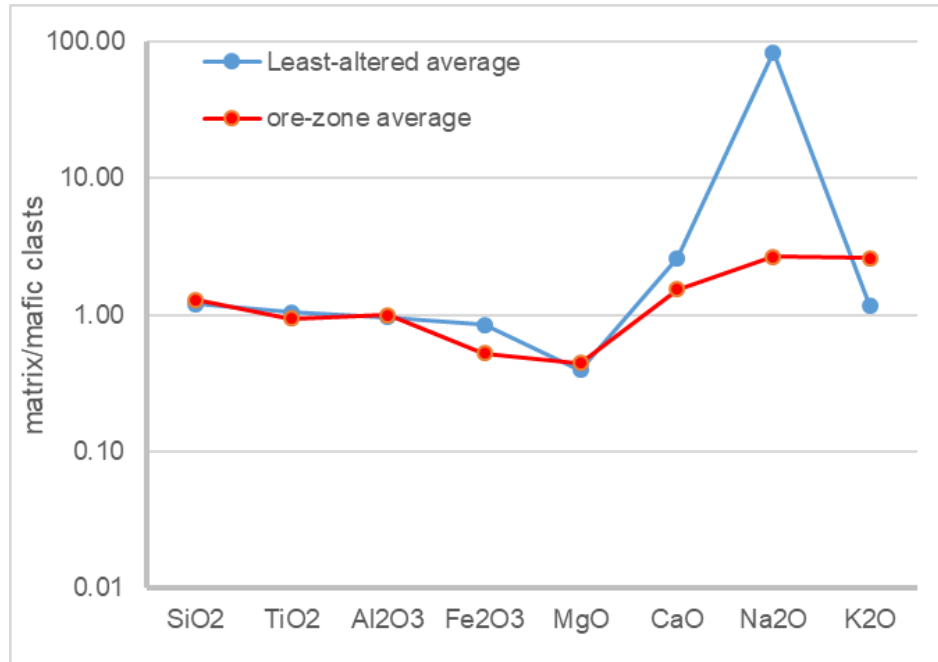


Figure B.4: Concentrations (log-scale) of major oxides for the average of least-altered and ore-zone matrix samples normalised to average crust. The data and normalising values are given in Table B.1.

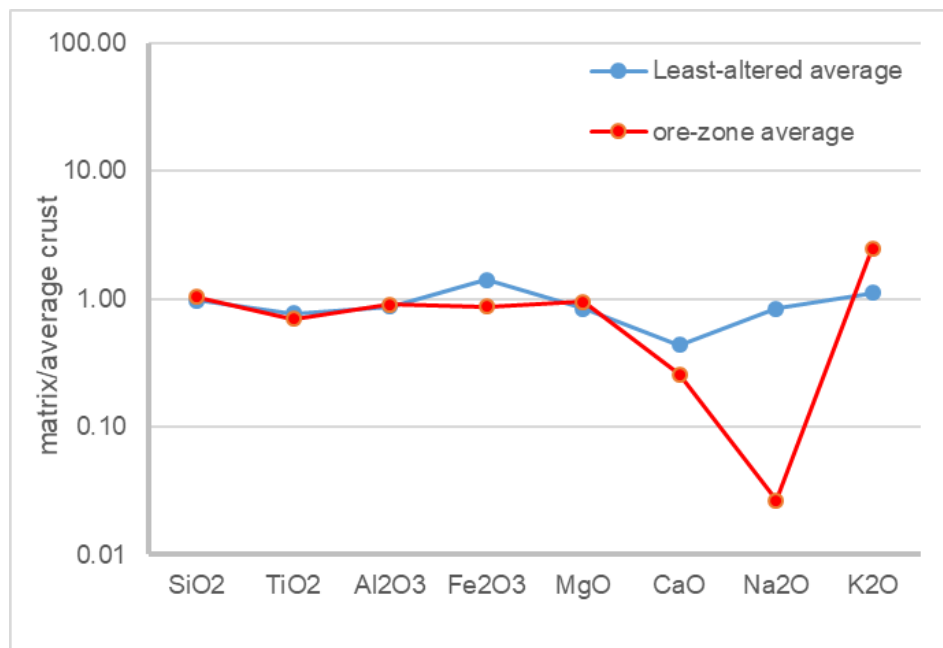


Figure B.5: Concentrations (log-scale) of major oxides for the average of least-altered and ore-zone matrix samples normalised to mafic rock. The data and normalising values are given in Table B.1.

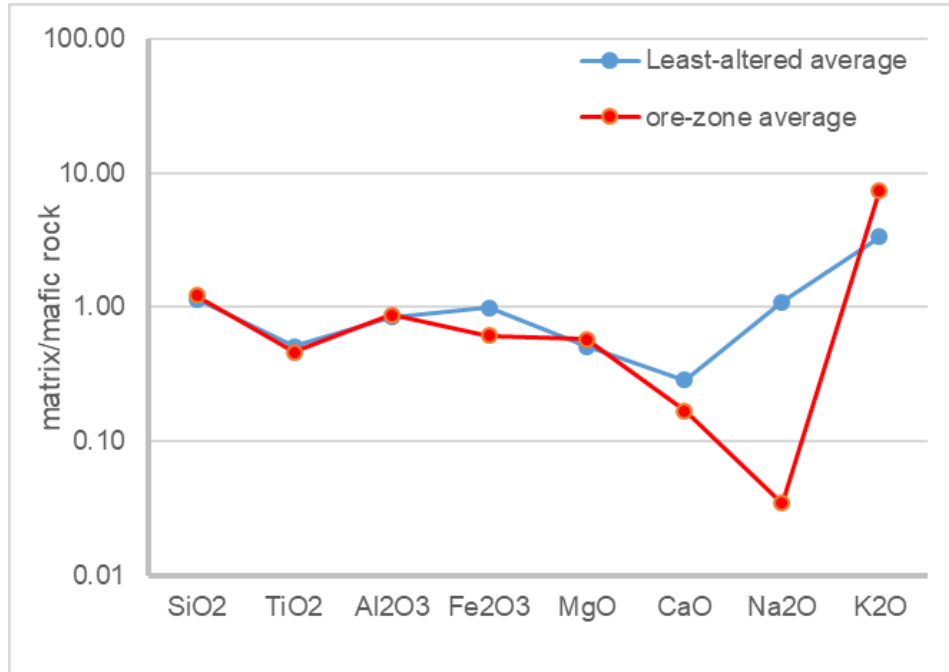


Figure B.6: Concentrations (log-scale) of major oxides for the average of least-altered and ore-zone matrix samples normalised to silicic rock. The data and normalising values are given in Table B.1.

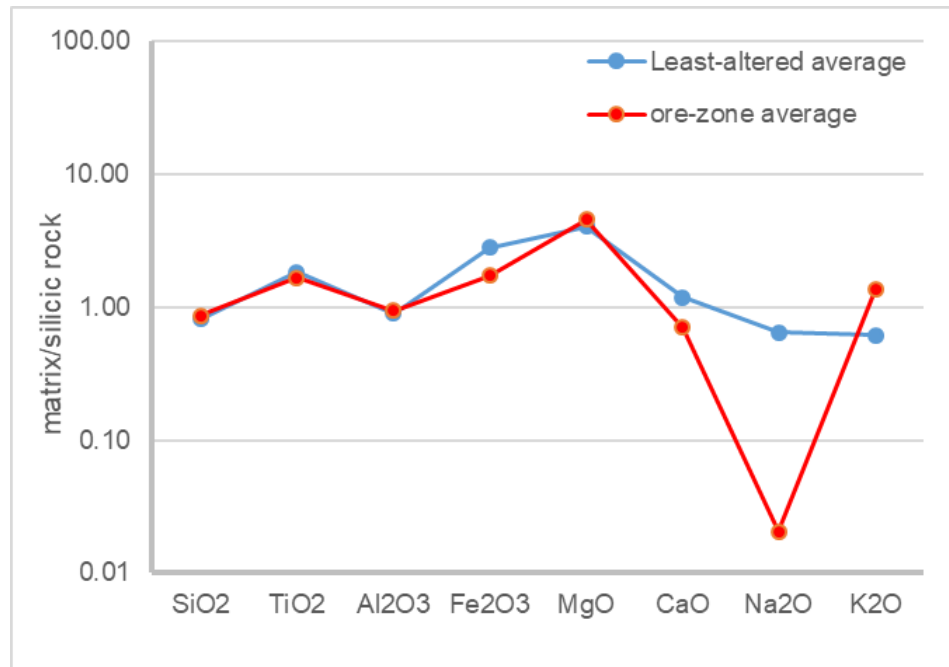


Figure B.7: Concentrations (log-scale) of trace elements for the average of least-altered and ore-zone matrix samples. The data are given in Table B.2.

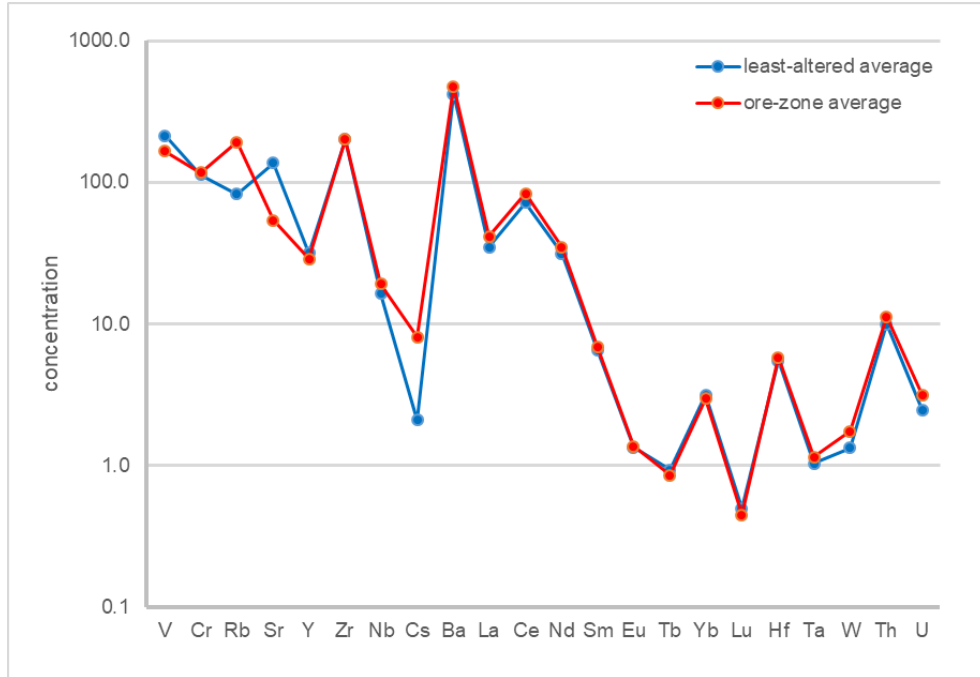


Figure B.8: Concentrations (log-scale) of trace elements for the average of least-altered and ore-zone matrix samples normalised to MORB. The data and normalising values are given in Table B.2.

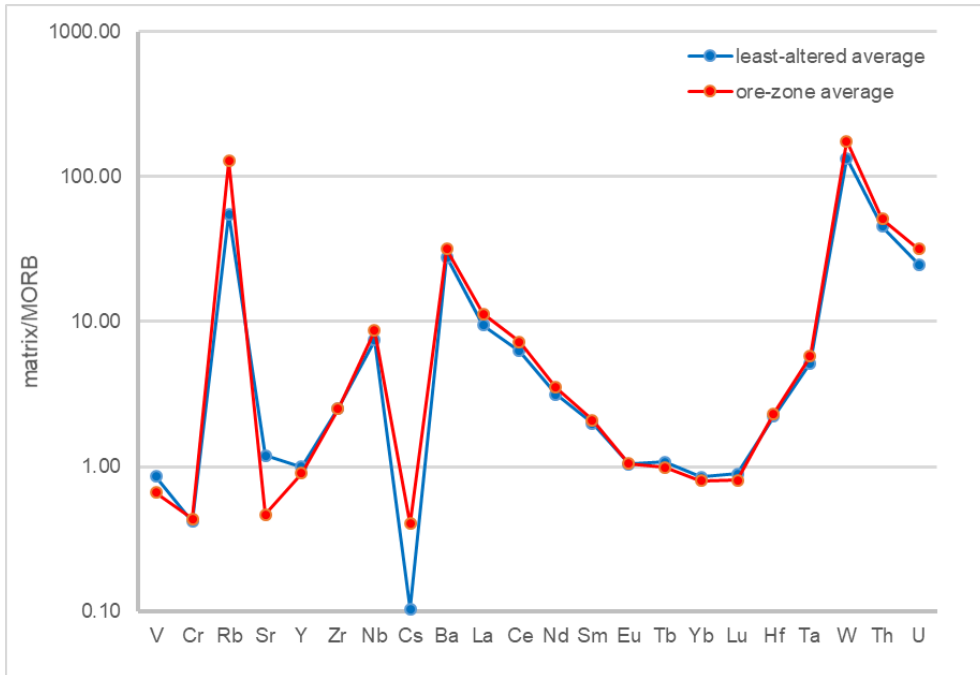


Figure B.9: Concentrations (log-scale) of trace elements for the average of least-altered and ore-zone matrix samples normalised to local mafics. The data and normalising values are given in Table B.2.

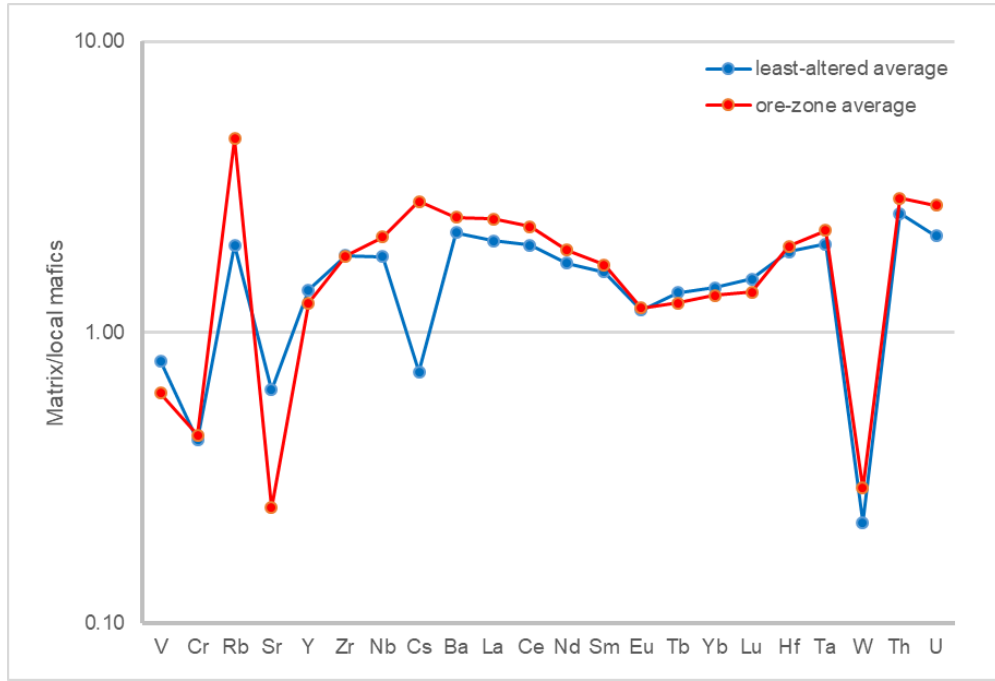


Figure B.10: Concentrations (log-scale) of trace elements for the average of least-altered and ore-zone matrix samples normalised to mafic clasts. The data and normalising values are given in Table B.2.

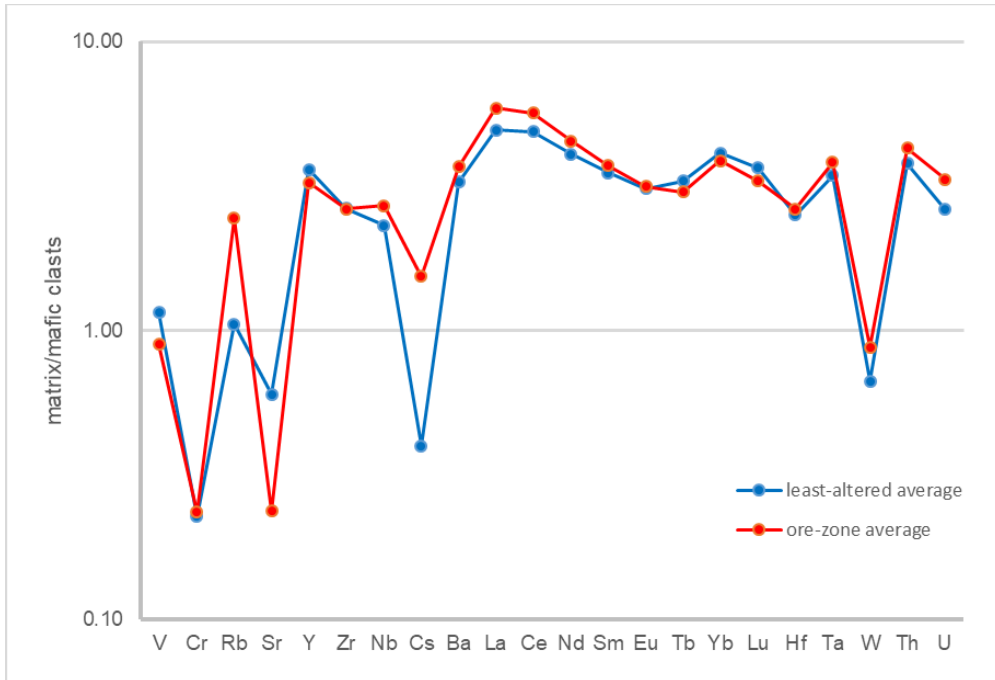


Figure B.11: Concentrations (log-scale) of trace elements for the average of least-altered and ore-zone matrix samples normalised to bulk crust. The data and normalising values are given in Table B.2.

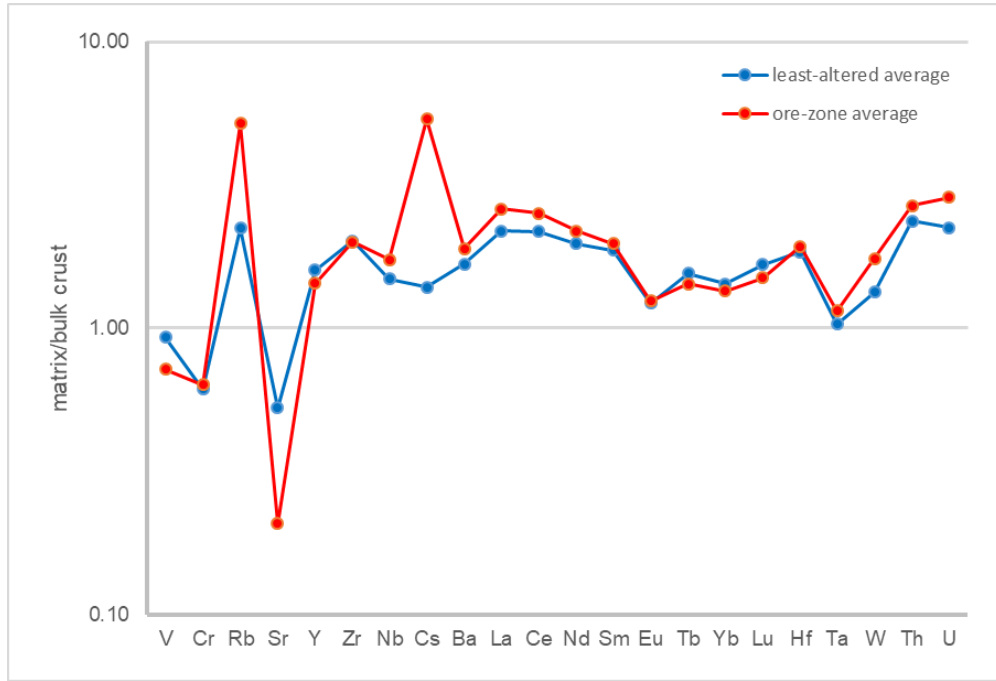


Figure B.12: Concentrations (log-scale) of trace elements for the average of least-altered and ore-zone matrix samples normalised to average sediment. The data and normalising values are given in Table B.2.

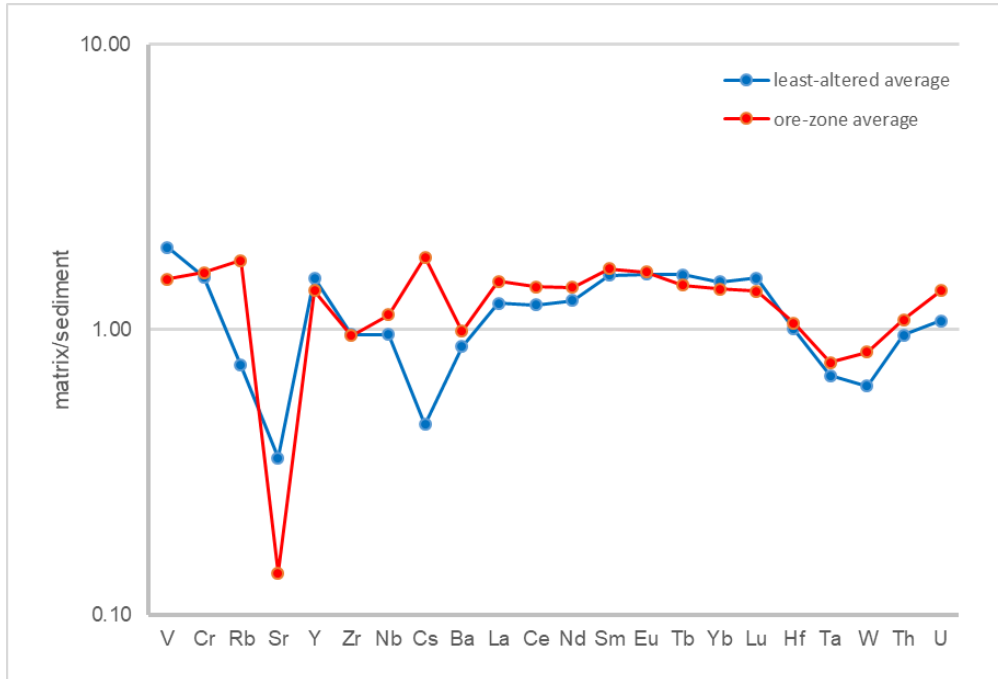


Figure B.13: Concentrations (log-scale) of trace elements for the average of least-altered and ore-zone matrix samples normalised to upper crust. The data and normalising values are given in Table B.2.

